PHYSIK-DEPARTMENT

Polymeric PEDOT:PSS electrodes for organic electronics: Understanding the conductivity-structure relation

Dissertation

von

Dipl.-Phys. (Univ.)
Claudia Maria Palumbiny

TECHNISCHE UNIVERSITÄT
MÜNCHEN

TECHNISCHE UNIVERSITÄT MÜNCHEN

Physik-Department
Lehrstuhl für Funktionelle Materialien

Polymeric PEDOT:PSS electrodes for organic electronics: Understanding the conductivity-structure relation

Dipl.-Phys.(Univ.) Claudia Maria Palumbiny

Vollständiger Abdruck der von der Fakultät für Physik der Technischen Universität München zur Erlangung des akademischen Grades eines

Doktors der Naturwissenschaften (Dr. rer. nat.)

genehmigten Dissertation.

Vorsitzender:	Univ.-Prof. Dr. Martin Zacharias
Prüfer der Dissertation:	1. apl.-Prof. Dr. Peter Müller-Buschbaum
	2. apl. Prof. Dr. Martin S. Brandt

Die Dissertation wurde am 10.11.2015 bei der Technischen Universität München eingereicht und durch die Fakultät für Physik am 18.12.2015 angenommen.

Abstract / Zusammenfassung

Abstract

In this thesis, polymer-based thin films are examined for their application as electrodes in organic electronic devices. The morphology of the initially low-conducting polymer blend PEDOT:PSS is modified by doping with high boiling point co-solvents (secondary doping). With this method, highly conductive thin films are obtained. It is shown that the characteristic structure sizes influence the electronic performance of the polymeric electrodes and the respective photovoltaic device characteristics. This thesis demonstrates, how secondary doping tailors the morphology of PEDOT:PSS polymeric electrodes and thus their electrical properties. Understanding the conductivity-structure relation enables optimizing and tuning the properties of polymeric electrodes.

Zusammenfassung

In dieser Dissertation werden polymerbasierte Dünnschichten für die Anwendung in organischer Elektronik untersucht. Die Morphologie des ursprünglich schwach leitenden Polymergemisches PEDOT:PSS wird durch Dotierung mittels hochsiedender Lösungsmittelzusätze modifiziert (Sekundärdotierung). Mit dieser Methode werden hochleitfähige Dünnschichten erzielt. Es wird gezeigt, dass die charakteristischen Strukturgrößen die elektronische Effizienz der Polymerelektroden sowie die Charakteristik der entsprechenden Photovoltaikzellen beeinflussen. In dieser Arbeit wird dargelegt, wie durch Sekundärdotierung die Morphologie und damit die elektronischen Eigenschaften von PEDOT:PSS-Elektroden angepasst werden können. Das Verstehen des Zusammenspiels von Leitfähigkeit und Struktur ermöglicht die Optimierung und Anpassung der Eigenschaften von Polymerelektroden.

Contents

Chapter 1

Introduction

The ever increasing energy consumption, which is stimulated by the world-wide industrialization and electrification, provides a huge market potential and likewise a strong challenge for the semiconductor industry. The first theoretical principle of a device similar to a field effect transistor was predicted 1925 in a patent by J. E. Lilienfeld followed by the basic theoretical description of the Schottky-Diode 1939 by E. W. Schottky. The first realization of a bipolar transistor in the Bell Laboratories in 1947 led to the Nobel Prize in physics for Bardeen, Brettain and Shockley in 1956. This paved the way for the semiconductor industry in the early 1960s.
With the increase of decentralized energy supply caused by the growing alternative energy contribution, promising new markets for semiconductor devices are arising. Within the last few decades a trend towards mechanically flexible and light weight electronic products can be observed. Flexible mobile phone displays, for example, consist of organic light-emitting diode (OLED) arrays, the so-called AMOLED (active-matrix organic light-emitting diode). These organic electronic devices are based on organic semiconductors, such as conducting polymers. The conductivity of organic polymers was discovered 1997 and awarded the Nobel Prize in chemistry 2000 to Heeger, MacDiarmid and Shirakawa. [1,2] Conducting polymers are carbon-based polymers and provide strong mechanical flexibility and light weight of these materials and thus of OEs. Organic electronics (OE) have exhibited a new market potential and quickened the development of organic semiconductors in the recent years (OE).
Within the field of organic electronics, semiconducting polymers are typically applied as a photoactive layer or as a functional charge-selective blocking layer, e.g. in organic photovoltaic (OPV) devices. The photoactive and the functional layers are sandwiched between one charge collecting metal electrode and one charge collecting transparent electrode (TE), whereby the latter allows the incoming light to pass through for absorption in the sandwiched photoactive layer. Widely-used is the application of indium tin oxide

(ITO) as the TE. However, the ITO base element indium is a chemical element that is rarely available. Further, the strongest market share of indium is its production to ITO for the use in touchscreens and displays, with increasing demand. The lack of the indium mineral deposits causes an increase of the production cost of ITO as well as a strong discussion on the mineral resource of indium. These facts make the metal-oxide electrode ITO to one of the limiting factors for volume production of OEs. Further, ITO is a brittle metal-oxide which limits its applicability in flexible OE devices.[3,4] Based on the mentioned arguments, it is desirable to find ways for replacing the ITO electrode. This thesis presents the development a polymeric electrode, which assures availability, low cost as well as flexibility and thus can replace the ITO electrode.

In the above-discussed context, the attention is directed to the organic polymer poly(3,4-ethylene-dioxythiophene):poly(styrene-sulfonate) (PEDOT:PSS).[3–6] PEDOT:PSS is already widely established as a functional selective-charge blocking layer in OEs such as organic photovoltaics (OPV), OLEDs and organic field effect transistors (OFET). The present thesis is oriented towards the modification of PEDOT:PSS by doping with high boiling point co-solvents (secondary doping). Secondary doping does not alter the chemistry of the PEDOT:PSS, but enables to tune the morphology and structure within the film. Several methods of secondary doping of PEDOT:PSS can be used, ranging from doping the initial PEDOT:PSS solution to post-treating the solidified PEDOT:PSS thin film. By this method, the initially low conduction of PEDOT:PSS is increased by up to three orders of magnitude to the one of ITO.[5–7] Thereby, highly conductive PEDOT:PSS films and thus PEDOT:PSS electrodes are obtained. However, a clear picture of the underlying mechanisms that lead to the conductivity increase are still under debate. This thesis is assigned to identify different mechanisms that impact the film conductivity of PEDOT:PSS. The focus is put on the relation of the electronic, spectroscopic and structural properties of PEDOT:PSS thin films and their application as polymeric electrodes. It is shown how characteristic structure sizes within the PEDOT:PSS thin films influence the electronic performance of the polymeric electrodes and the respective photovoltaic device characteristics. It is demonstrated, how secondary doping tailors the morphology of PEDOT:PSS polymeric electrodes and thus their electrical properties. By understanding the conductivity-structure relation, a powerful tool for optimizing and tuning the properties of polymeric electrodes is developed. With these electrodes flexible and roll-to-roll printable[8] OEs can be optimized. Further, modification of PEDOT:PSS with the correspondent choice of co-solvent makes the material highly adaptable to hydrophilic or hydrophobic surfaces.
In the first chapter of this thesis (chapter 2) the theoretical aspects are explained with

a focus on the basic principles of conducting polymers, their application in OPV devices and the basics of the structure-investigation technique used (X-ray scattering), before providing a description of all used experimental characterization methods in chapter 3. The sample preparation of PEDOT:PSS thin films and their secondary doping is detailed in chapter 4 together with a description of the materials involved in the process. Further, this chapter provides an overview on the preparation of OPV devices. These fundamental chapters are followed by a detailed description of the different research highlights in chapters 5 to 7. The thesis is summarizing and an outlook provided in chapter 8. Figure 1.1 provides a schematic overview on the featured research topics discussed in this thesis, which are introduced shortly in the following.

In chapter 5.1 (represented as figure 1.1a) several secondary doping methods, i.e. treating the PEDOT:PSS film with co-solvents, are verified to identify the ideal processing parameters. Besides the processing parameters, the choice of co-solvent, the processing time and the number of treatment cycles are investigated in terms of thin film conductivity, absorption coefficient and vertical film composition. The spectroscopic and morphological thin film properties are thereby related to the final electronic properties. As it turns out that the film morphology has a great impact on the electric properties of the resulting films (chapter 5.2, represented as figure 1.1b), a contiguous study with controlled increase in the dopant concentration is performed to relate morphological changes to changes in the film conductivity. Further, additional post-treatment of all films assists to compare these two secondary doping methods, i.e. doping and post-treatment in terms of structure-conductivity relation. An optimized inner film morphology is assumed to enhance the intergrain conductivity within the thin films. Further, the orientation of molecules within the crystallites is assumed to influence the intragrain conductivity as the conductivity through the conducting PEDOT crystallites is asymmetric.
Another aspect promising a versatile application of PEDOT:PSS thin films is its modification using a surfactant as the solvent additive. With this, the PEDOT:PSS electrodes, which are coated from a water-based solution, can additionally be applied on hydrophobic surfaces. This enables further application of the material, e.g. in silicon-based photovoltaic devices (see outlook in chapter 8). In chapter 6 (represented as figure 1.1c) the suitability of surfactant-modified PEDOT:PSS as transparent electrodes is investigated in terms of their transmission and their sheet resistance. Surfactants interact between hydrophilic and hydrophobic parts, in this case between the PSS and the PEDOT phases of the polymer blend. Hence, the impact of the surfactant on the phase separation and the film morphology of the polymer blend is examined. As in chapter 5 the morphology is shown to influence the film conductivity, in this chapter also the inner film structure is

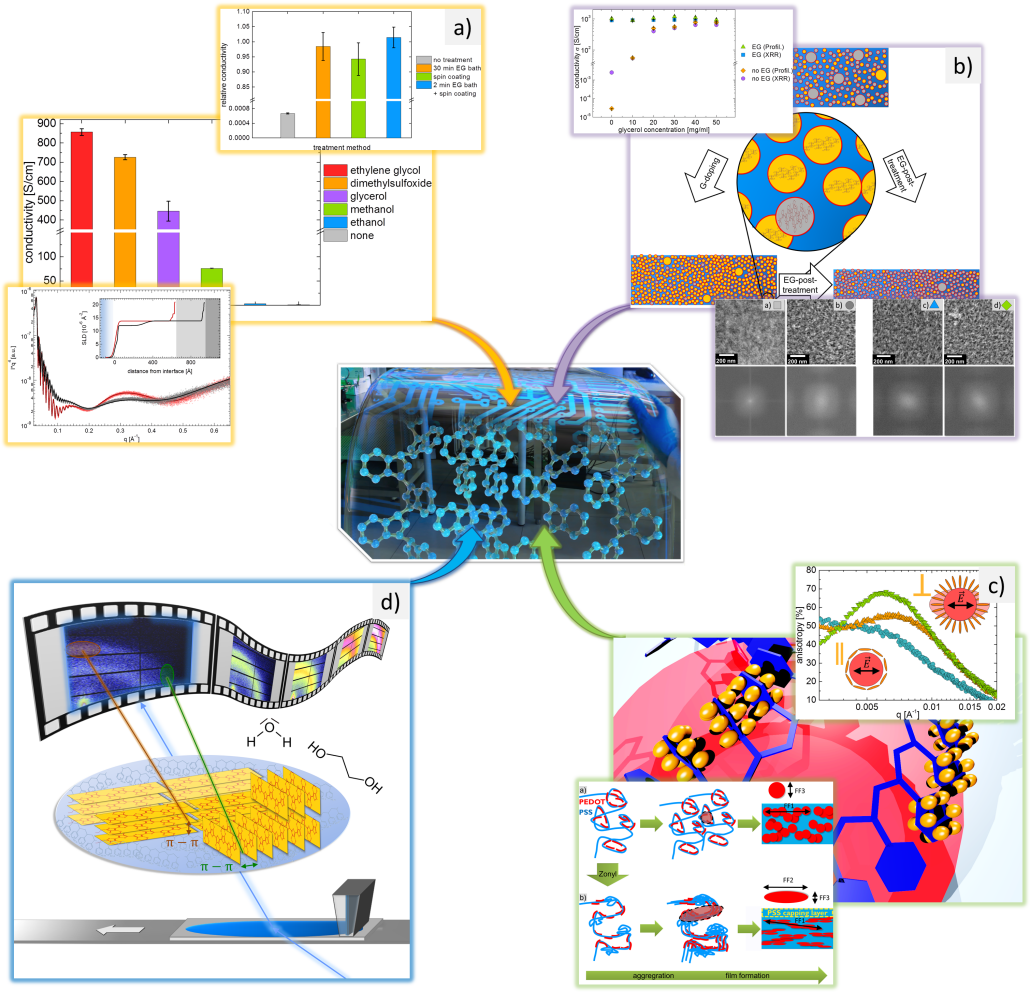

Figure 1.1: Schematic overview of the different research topics addressed in the present thesis. Their results lead to highly conductive, transparent and printable polymeric PEDOT:PSS electrodes of tunable electric properties as sketched in the center. (a) Influence of different treatment parameters on the thin film properties. This chapter deals with treatment parameters such as the treatment time, the choice of solvent or the treatment cycle number and investigates the effect of these parameters on the electric, spectroscopic and structure characteristics of the final PEDOT:PSS film. (b) Exploring the conductivity-structure relation by two promising treatment processes for PEDOT:PSS. Detailed investigation of the inner film structure, crystalline nature and molecular orientation of the thin films. (c) Possibilities of tuning the phase separation and interface orientation of molecules within the two-component polymer matrix PEDOT:PSS. (d) In-situ structure investigation of printed PEDOT:PSS electrodes. This chapter provides unique insight to the film formation processes with high applicability for industrial roll-to-roll printing processes of organic electronics.

investigated and related to the sheet resistance. Further, the question arises if surfactant-modified PEDOT:PSS can be applied in OPV devices. Therefore, the application of surfactant modified PEDOT:PSS layers in OPV devices is investigated and the impact of the surfactant modification on the resulting device characteristics is discussed.
The conductivity increase of PEDOT:PSS films is related to the inner film morphology, which develops in fast kinetic processes during the film formation. The film formation is hence expected to be strongly dependent on the thin film processing method. However, most scientific investigations are based on laboratory-based deposition methods which differ from industrial processing methods. The results shown in chapter 7 (represented as figure 1.1d) provide answers to the question if the results obtained by laboratory-based deposition techniques also hold for industrial thin film processing methods such as printing. Therefore, the PEDOT:PSS thin film preparation, including the optimized secondary doping processes of doping and post-treatment shown in chapter 5, is transferred to the industrial deposition method of slot-died printing. The fast kinetic processes in the structure evolution of the films are tracked with in-situ X-ray investigations. Thereby, monitoring the film evolution during the process of thin film solidification reveals new insight to the underlying processes, e.g. insight on how the evaporation of the involved solvents influence the inner film structures and thus the film conductivity. Therein, important parameters such as the molecular stacking distances are tracked with film formation time. The final film conductivities are related to important thin film properties such as the size of crystallites and the molecular stacking distances. By controlling these parameters, the PEDOT:PSS polymeric electrodes can be tuned to their desired applications.
The above-posed questions on the conductivity-structure relation of polymeric PEDOT:PSS electrodes are tackled in the corresponding chapters of this thesis. The results obtained in the framework of this thesis are summarized in chapter 8, answering all raised questions of the present section. Based on the findings, a short outlook to future projects is given at the end of chapter 8.

Chapter 2

Principles and Theory

In this thesis, the possibility of utilizing polymer blends for the application in organic electronics is investigated. Therein, the systems are studied and directed towards the function as transparent electrodes. In this chapter, the theoretical background of the materials and their tractability related to their potential application in organic photovoltaics is introduced together with the basics on structure investigation using X-ray scattering methods. The chapter opens with the theoretical background of polymers (section 2.1) with a special focus on the crystallization, phase separation and conductivity in polymer blends. The crystallization and phase separation mechanisms play a crucial role for the film formation of the investigated PEDOT:PSS polymeric blend system and are further shown in this thesis to strongly impact the conductivity of the resulting final films. The main application of polymer blends shown in this thesis are organic photovoltaics. Therefore, in section 2.2 the working mechanism and the kinetic processes during the operation of organic photovoltaic devices are presented together with the main device architectures used in this work. Lastly, the theoretical aspects about the structure-investigation technique of X-ray scattering is introduced in section 2.3. This section provides theoretical details on the variety of possibilities in X-ray scattering, from reflection and diffraction to grazing incidence and resonant soft X-ray scattering.

2.1 Polymer basics

In the following, the general properties and the most important definitions of polymers are presented in section 2.1.3. After this introduction to polymer basics, the basic theoretical aspects of polymer crystallization is explained in section 2.1.2 and the phase separation of polymer blends is presented in section 2.1.3 before focussing on conducting polymers in section 2.1.4. Therein, the band structure and charge carrier types in polymer systems are

discussed along with charge transport mechanisms in such systems. Further, two types of polymer doping for conductivity increase are presented.

2.1.1 General properties and definitions

Polymers, as well as *macromolecules* or *oligomers*, consist of repeated units of monomers. These monomers typically consist of carbon atoms plus other light atoms, such as hydrogen, oxygen or sulfur. In a polymer, the cores of the monomer units, which are covalently bound to each other are referred to as the *polymer backbone*. The resulting polymer thereby has a backbone unit to which polymer side chains can be attached, depending on the initial monomer. The number of monomeric units n of which the polymer consists, is the degree of polymerization. The degree of polymerization itself relates directly to the molecular weight M by which the following three classes are defined:

- Macromolecules with $M < 1000\,\mathrm{g/mol}$
- Oligomers with $M = 1000 - 10\,000\,\mathrm{g/mol}$
- Polymers with $M > 10\,000\,\mathrm{g/mol}$

Each covalently bound chain has an end, which chemically differs in the interaction with its surroundings from the rest of the chain. For macromolecules and oligomers this influence of their chain ends is not negligible whereas for polymers it may not be negligible. In principle, polymers are indicated in chemical notations, e.g. covalently linked styrene monomers are abbreviated as PS and their chemical formula is written as $(C_8H_8)_n$, where n denotes the *degree of polymerization*. For further possible notations it is referred to the International Union for Pure Applied Chemistry (IUPAC).

In this thesis, solely man-made polymers are used, so-called *synthetic polymers*. Synthetic polymers are synthesized by a polymerization reaction. This results in polymers of different *degree of polymerization*, i.e. polymers of different length. Therefore, polymers are described by statistical mean values. An arithmetic mean, i.e. the first central moment of the statistical distribution, of the individual polymeric molecules is the *number average molecular mass* M_n.

$$M_n = \frac{\sum_i n_i \cdot M_i}{\sum_i n_i} \tag{2.1}$$

with M_i the molar mass of a component and n_i the number of chains of component i. The *weight average molar mass* M_w, also named as the molecular weight, is the ratio of the second to the first central moment of the statistical distribution

$$M_w = \frac{\sum_i n_i \cdot M_i^2}{\sum_i n_i \cdot M_i} = \frac{\sum_i w_i \cdot M_i}{\sum_i w_i} \tag{2.2}$$

where w_i is the total mass of macromolecules of component i, i.e. $w_i = n_i \cdot M_i$. The statistical distribution of the degree of polymerization of polymers is the width of the distribution, the so-called *polydispersity*. A measure for the polydispersity is the *polydispersity index* PI

$$PI = \frac{M_w}{M_n} = U + 1 \tag{2.3}$$

which is the width of the distribution of the molar masses with U the *inconsistency*. The inconsistency is a measure for the polydispersity, where $U = 0$ ($PI = 1$) is the measure for a fully monodisperse polymer. All synthetic polymers, that means also all polymers used in this thesis are synthetic polymers, which means that they always have a polydispersity greater than one ($PI > 1$).

The final properties of synthesized polymers often depend strongly on their polydispersity. Therefore, different polymerization routes are used dependent on the desired application of the polymer. A very cost-effective production, which is e.g. widely used in industry, is the step-growth polymerization or also referred to as the polycondensation, where already linked monomers are condensed. This synthesis route results in a wide distribution, the so-called *Schulz-Zimm distribution function*. In this work, and in general for scientific use, a synthesis route based on a step by step growth is used, the *chain polymerization*. Therein, the reactive sides react only with monomers and are moved to the end of the polymer after a new monomer was successfully attached to the polymer chain. This synthesis route results in a narrow Poisson distribution function, in the ideal case with a polydispersity index of $PI = \frac{1}{M_n} + 1$, where $U = \frac{1}{M_n}$ and $M_w = 1$.

2.1.2 Crystallization of polymers

In contrast to small molecules or to oligomers, polymers do not translate into a perfectly crystalline state. Full crystallization of polymers is hindered by two criteria. The first criterion is the need of complete disentanglement before full crystallization becomes possible. This is the reason for a high entropic activation barrier as the time scale for full disentanglement is beyond the film formation time. The second criterion which hinders the full crystallization of polymers is the polydispersity of synthetic polymers, where the polymers consist of chains of different lengths. These variation of chain lengths comes along with coiled polymer chains of a varying degree of entanglement. The crystallization

of polymers hence results in a semicrystalline state. This state is not in thermal equilibrium and is hence driven by kinetics. The state is characterized by polymer crystals which are separated by amorphous intermediate ranges of the same polymer.

The crystallinity in polymer systems is described as the volume fraction which is occupied by the crystalline part of the polymer matrix, i.e. the volume of the crystalline part divided by the total volume according to

$$\phi_c = \frac{v_c}{v_a + v_c} \tag{2.4}$$

with v_a the fraction of the polymer matrix which is occupied by the amorphous phase, chain ends, impurities etc. The crystallization of a polymer matrix results in a layered structure of thickness $d(T)$ and length $l(T)$ perpendicular to the thickness which can expand up to several micrometers in contrast to $d(T)$. In this aspect, it is noted that the crystallinity depends on the temperature however not on the average molecular weight M_w.

As the crystallinity of polymers is temperature dependent, the physical properties of a polymer matrix are likewise temperature dependent. The crystallization of polymers can be classified by a multi-stage growth model introduced by Strobl wherein several temperatures identify the transition of the characteristic growth states. [9,10]

Nucleation

Before crystallization starts the system is in the amorphous state, which is also referred to as the amorphous melt. When the crystallization process starts, regions of enhanced order form within this amorphous phase (figure 2.1a) on the basis of thermal fluctuations or the presence of impurities with a nucleation rate τ_{nuc} which is proportional to the volume of crystallizable polymer domains with $\tau_{nuc} \propto v^{-1}$. Further, the nucleation rate can be described by a thermodynamical approach [11] according to

$$\tau_{nuc}^{-1} \propto exp\left(-\frac{\Delta U + \Delta F_c}{k_B \cdot T}\right) \tag{2.5}$$

with k_B the Boltzmann constant and T the temperature. The dominating term at low temperatures is ΔU, which is the activation energy barrier for polymer diffusion across the phase boundary. At high temperatures, the nucleation leads to a gain in free energy, which is described by the second term, the critical free energy barrier for primary nucleation ΔF_c. The maximal nucleation rate is found at mediate temperatures changing with the chain length of the polymer matrix. [12,13]

Mesophase

The crystallization of polymers shows three characteristic temperatures which are assigned to the transition of crystalline growth phases. Therefore, in the growth model suggested by Strobl, the so-called mesophase or mesomorphic phase is introduced to explain these three characteristic temperatures.[10] It characterized the transition from amorphous to crystalline phases. Therein, neighboring chains of a single polymer chain fold themselves to reach an ordered arrangement of polymer chains. This polymer crystal growth stage is depicted in figure 2.1b.

Crystalline phase

Within the crystalline phase the phase of native crystals (figure 2.1c) is distinguished from the phase of stabilized crystals (figure 2.1d). At a certain thickness of the mesomorphous core the phase solidifies forming a crystal block. Further, polymers at the surface of this core order according to the crystalline core, which stabilizes the crystal.

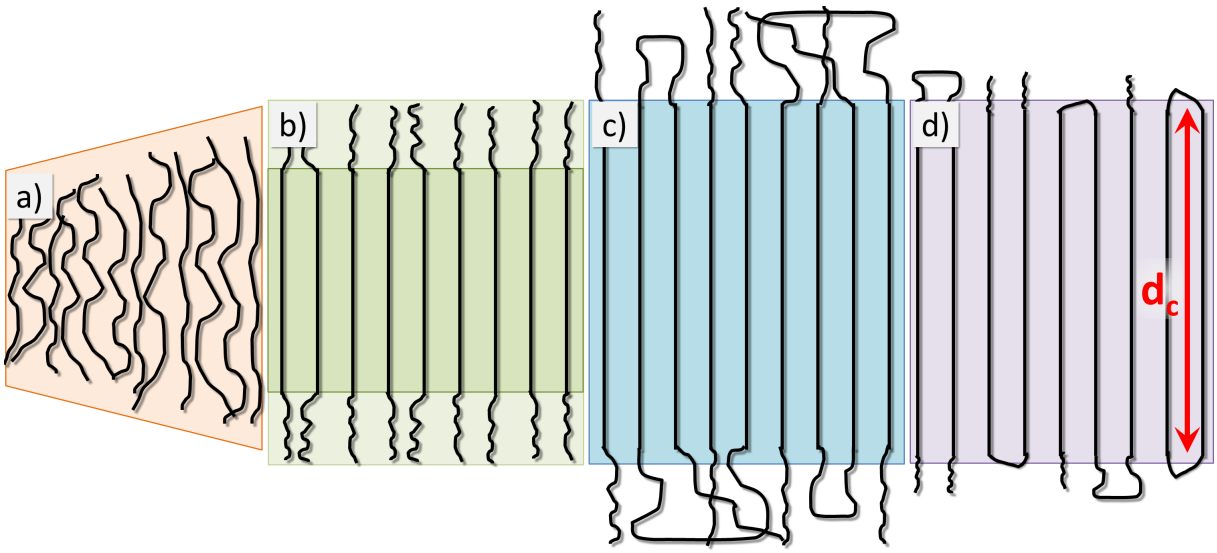

Figure 2.1: Polymer crystallization model introduced by Strobl.[10] The scheme adapted from[10] shows the different stages of crystal growth for synthetic polymers, a) the nucleation, b) the mesophase, c) the crystalline phase and d) the stabilized crystal phase.

2.1.3 Phase separation in polymer blends

So far, the crystallization of polymers was described. In organic electronics (OE) typically organic blends consisting of two phases are used. The active layers in an organic light emitting diode or in an organic solar cell is typically a mixture of a small molecule phase

and a polymer phase or of two organic molecule phases. Further, the polymer electrodes which are investigated in this thesis, are a polymer-polymer mixture of two different polymers of different polydispersities. When the two materials are dissolved, phase separation occurs due to low miscibility on the molecular level. As a consequence of the phase separation, the inter-facial area between the two components changes, which has an impact on the charge carrier generation of the active layer. Further, phase separation causes a change in the percolation paths for charge carrier transport within each component. With this, the need of phase separation control becomes clear for optimizing the spectroscopic and electronic properties of the individual layers of an OE device.

In general the phase separation in polymer blends can be described by the Flory-Huggins (FH) theory, which is based on a mean field approach.[14,15] This theory holds for polymer solutions and blend solutions of coil-like polymers. However, the conjugated polymers, which are used in OEs are rod-like and have the tendency to crystallize during solidification. For these kind of polymers, the FH theory is extended on the basis of coil-like and rod-like polymer. In the following the classical FH theory is sketched before the modified FH approach is introduced. Further, the influence of polymer crystallization on phase separation of polymer blends is discussed.

Phase separation of coil-like polymer blends

In the mean field approach of the FH theory, the Gibbs free energy of mixing ΔG_{mix} describes the phase separation of the mixed polymer components by

$$\Delta G_{mix} = G_{AB} - (G_A + G_B) \tag{2.6}$$

with G_{AB} the Gibbs free energy of the mixture, and G_A and G_B the Gibbs free energy of the pure components A and B. Further, G_{AB} can be expressed as the sum of the changes in entropy ΔS_{mix} and enthalpy ΔE_{mix}, which occurs due to mixing.

$$\Delta G_{mix} = -T \cdot \Delta S_{mix} + \Delta E_{mix} \tag{2.7}$$

With $\Delta S_{mix} = -k_B \cdot n \left[\frac{\phi_A}{N_A} \cdot ln\left(\phi_A\right) + \frac{\phi_B}{N_B} \cdot ln\left(\phi_B\right)\right]$ and $\Delta E_{mix} = n \cdot k_B \cdot T \cdot \chi \cdot \phi_A \cdot \phi_B$ the Gibbs free energy of the mixture is expressed by the degree of polymerization of the two components (N_A, N_B), the volume ratio of the two components (ϕ_A, ϕ_B) and the FH interaction parameter χ normalized to one mole ($n = N$).

$$\Delta G_{mix} = k_B \cdot N \cdot T \cdot \left[\frac{\phi_A}{N_A} \cdot ln\left(\phi_A\right) + \frac{\phi_B}{N_B} \cdot ln\left(\phi_B\right) + \chi \cdot \phi_A \cdot \phi_B\right] \tag{2.8}$$

Therein, k_B is the Boltzmann constant, n the number of molecules on the lattice model of the mean field approach, N the Avogadro number and T the temperature. Within the

FH theory the mean field approach is applied, where the system is incompressible and χ is independent of the molecular weight of the polymers, the composition of the blend, the chemical structure of the chain and the system pressure. It was experimentally shown that χ can be expressed by an enthalpy (χ_E) and an entropy (χS) term, similar to the Gibbs free energy of the mixture ΔG_{mix}.[9]

$$\chi = \chi_S + \frac{\chi_E}{T} \tag{2.9}$$

Phase separation in conjugated rod- and coil-like polymer blends

Conjugated polymers are elongated and additionally have the tendency to crystallize as discussed in the last section. As mentioned above, the classical FH theory is modified to describe the phase separation of an elongated crystalline and a flexible polymer chain. The two chains are described by rod-like (R) and coil-like (C) polymer, respectively.[16] Further, a degree of disorder is added to the crystalline component to account for partial crystallization. The rod-like polymer is represented by m rod-like chain segments of equal length x_R which are freely joined. The disorientation of the chain segments y equals x_R for complete disorder. The ratio of disorientation and the segment length $\frac{y}{x_R}$ is hence a measure for the degree of disorder. Further, the contour of the coil-like polymer is x_C. The two lengths $m \cdot x_R$ and $m \cdot x_C$ are interpreted as the degree of polymerization and ϕ_R and ϕ_C are the volume fractions of the two corresponding polymers.

The Gibbs free energy of mixing of the above-discussed classical FH approach is modified by adding an enthalpic contribution $\Delta G_{crystal}$ to account for the influence of crystallized polymers in a polymer matrix. Equation 2.8 hence extends to[16]

$$\Delta G_{mix,crystal} = \Delta G_{mix} + \Delta G_{crystal} \tag{2.10}$$

with the enthalpic contribution of crystallized polymers $\Delta G_{crystal}$ defined as

$$\Delta G_{crystal} = \frac{\phi_R}{m \cdot x_R} \cdot ln\left(\frac{1}{m \cdot x_R}\right) - \left[1 - \phi_R \cdot \left(1 - \frac{y}{x_R}\right)\right] \cdot ln\left[1 - \phi_R \cdot \left(1 - \frac{y}{x_R}\right)\right] + \\ - \frac{\phi_R}{m \cdot x_R} \cdot \left[m \cdot ln\left(y^2\right) - m \cdot y + 1\right] \tag{2.11}$$

High crystallized fractions of a polymer matrix consequently lead to a stronger impact of $\Delta G_{crystal}$ (equation 2.10) and to an increased Gibbs free energy of mixing $\Delta G_{mix,crystal}$ (equation 2.11). Consequently, for a completely disordered system y equals x_R and hence $\Delta G_{crystal}$ equals zero. In this case, the Gibbs free energy of mixing is ΔG_{mix} of the classical FH theory according to equation 2.8.

2.1.4 Conductivity in polymers

Polymers are known because of their variety of applications, which is based on their tunable mechanical and electrical isolating properties as well as their light weight. The possibility of doping polymers, such that these show conductive properties was first discovered in 1997 for polyacetylene and awarded with a Nobel Prize in chemistry in 2000 for Shirakawa, Mac Diarmid and Heeger. Conducting polymers form $\pi - \pi$ bonds which leads to the formation of bonding π- and anti-bonding π^* bands. In a classic semiconductor physics these are referred to as the valence and conduction band. In polymer physics, the bonding and anti-bonding bands are named as the highest occupied molecular orbital and the lowest unoccupied molecular orbital, respectively. In these bands electrons are delocalized and can move freely along the polymer backbone chain. Typically the polymer backbone consists of alternating single and double bonds, the so-called conjugated double bonds or conjugated backbone.

Band structure

The band structure of polymers with alternating single and double bonds is described by the Peierls instability.[17] In this model the bands of a one-dimensional metal chain are filled up to the Fermi energy (E_F), which lies in the center of the band as shown in figure 2.2a. If a 1D metal lattice is disturbed, it is described as a flexible lattice. In this transition, dimerization occurs and influences the nature of the band structure. The formation of a band gap reduces the total energy of the system as depicted in figure 2.2b and figure 2.2c within one Brioullin zone. This transition is the Peierls instability, which is also referred to as the metal-insulator transition. In comparison to metals, the Peierls instability for polymers is much stronger than in metals with typical band gaps of 1.5-3 eV.

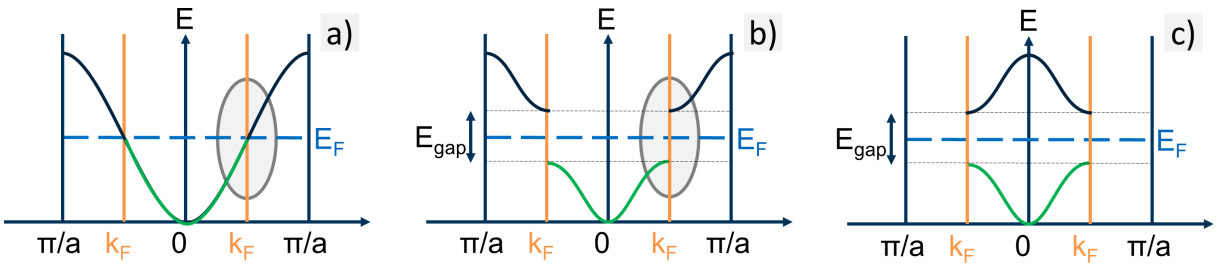

Figure 2.2: Illustration of the band structure in polymers with the band structure according to Peierls instability a) of an one-dimensional chain and b) the band structure after dimerization. The phase transition is shown for a one-dimensional chain. The circles in a) and b) indicate the formation of a band gap with dimerization. In c) the band structure is shown within one Brioullin zone.

The distortion of the lattice, which leads to the formation of a band gap is schematically shown in figure 2.3a. In the middle row the undisturbed lattice is shown with a lattice periodicity of a. The top and the bottom row depict two possibilities of lattice distortion. The distorted lattices have a superstructure with a periodicity of $2a$. The undisturbed lattice has a continuous band structure while the disturbed lattices form a band gap. A close-up to the band structure for the region around the E_F is depicted in figure 2.3b.

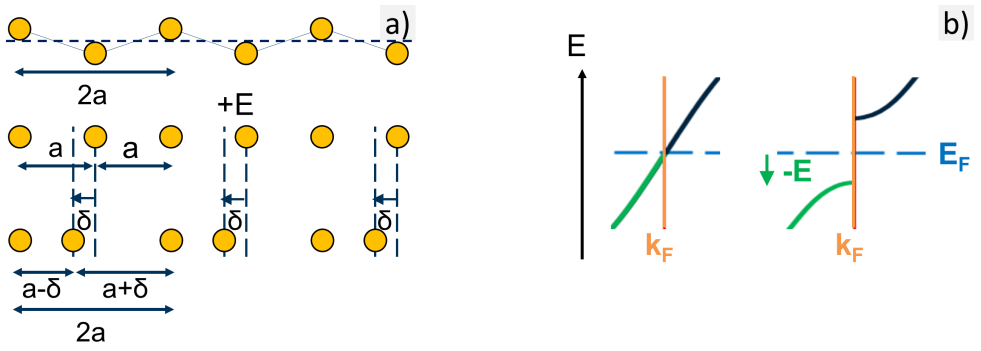

Figure 2.3: The phase transition on the basis of the Peierls instability is shown on a one-dimensional chain of atoms. a) Before transition the atoms are equally spaced with a periodicity of a. After distortion of the lattice, the periodicity of the superstructure is $2a$ as depicted. In b) the corresponding shift in energy is depicted.

Charge carriers

The transport of charge carriers within polymers is described by quasiparticles (QP). In the following, these QPs are described on the example of polyacethylene, which acts as a simple role-model for polymers with a conjugated backbone such as the polymers used in this thesis. In general, charge carriers are generated by doping or by excitation with light. The ionization of the polymer follows by a structural relaxation of the molecule as depicted in figure 2.4. Hence, charge transport in polymers leads to local lattice distortion. The conduction of a charge within polymers are therefore described by QPs.

The three types of existing QPs are depicted in figure 2.5. These QPs are present in systems which consist of two degenerated ground states.[18] Solitons (figure 2.5a) exist in three variation, a neutral soliton S^0 and a positive S^+ and a negative S^- soliton.[19] In contrast, polarons (figure 2.5b) and bipolarons (figure 2.5c) exist as positively (P^+, P^-) and negatively (B^+, B^-) charged QPs. Each of the QPs is characterized by charges and spins. Neutral solitons have a spin of 1/2 whereas charged solitons are spin-less. Polarons and bipolarons exist only as charges QPs where polarons have a spin of 1/2 and bipolarons are spin-less.

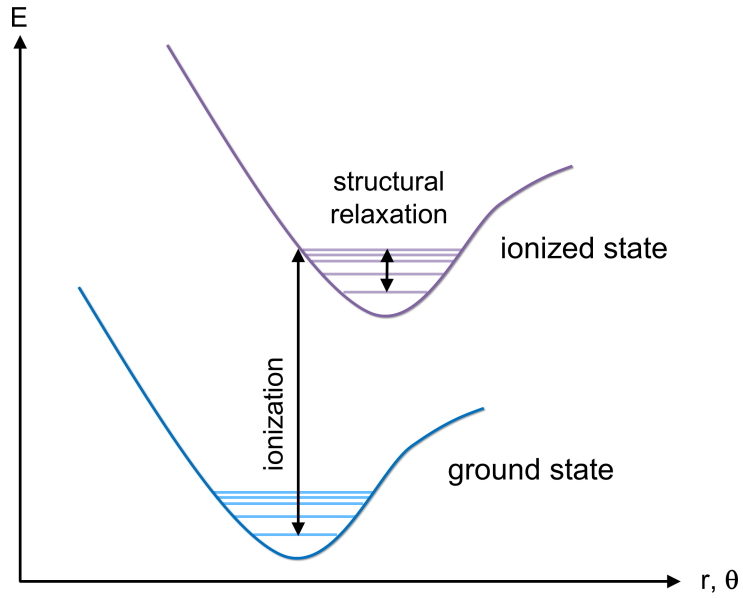

Figure 2.4: Energetic diagram of the ground and the ionized state depending on the binding distance r and the angle θ. After ionization the excited system relaxes structurally as depicted. Modified from Bredas et al.[18]

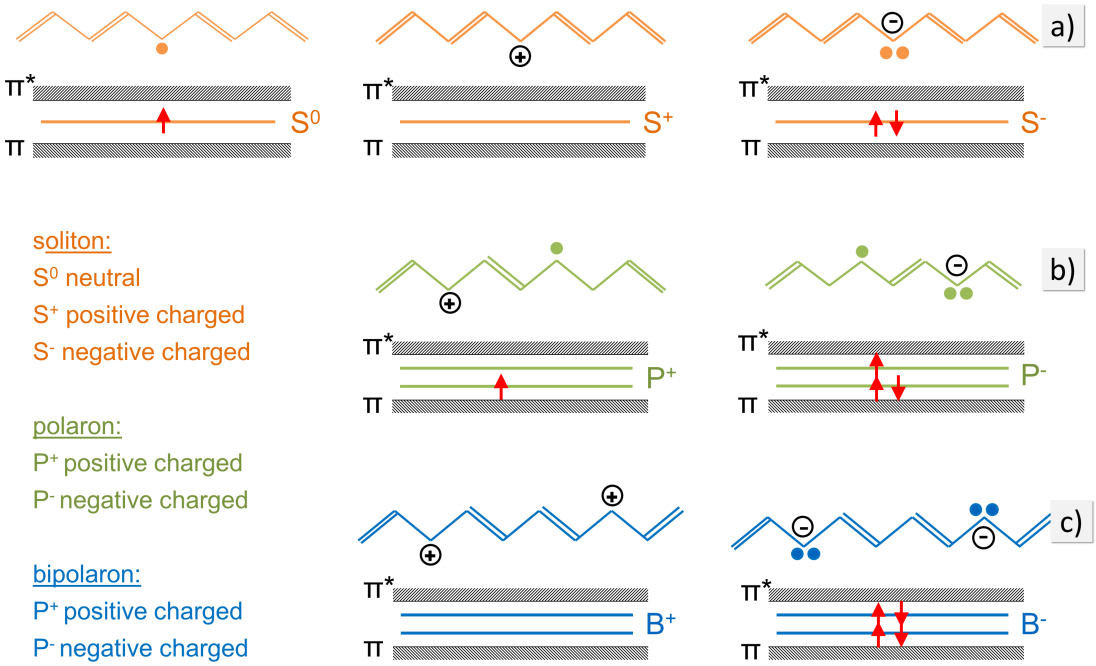

Figure 2.5: Quasiparticles (QP) as they can be present in conductive polymers, here shown for polyacetylene. Soliton (top row) exist as neutral or charged QPs. Polyrons and bipolarons exist only as charges QPs. The type of QP is defined by a charge and a spin of the particle. Their energy states lie within the band gap, i.e. between the HOMO and the LUMO.[19]

Solitons, polarons and bipolarons extend over several atoms such as shown in figure 2.6 for the example of polyacetylene. The top row shows the PA chain as depicted in figure 2.5 with an A and a B structure part. The lower row shows how the soliton actually expands over 14 carbon atoms. Further, on one polymer chain more than one type of QP can exist. Depending on the doping concentration, these QPs can meet. When two QPs meet, they either combine or annihilate.[20]

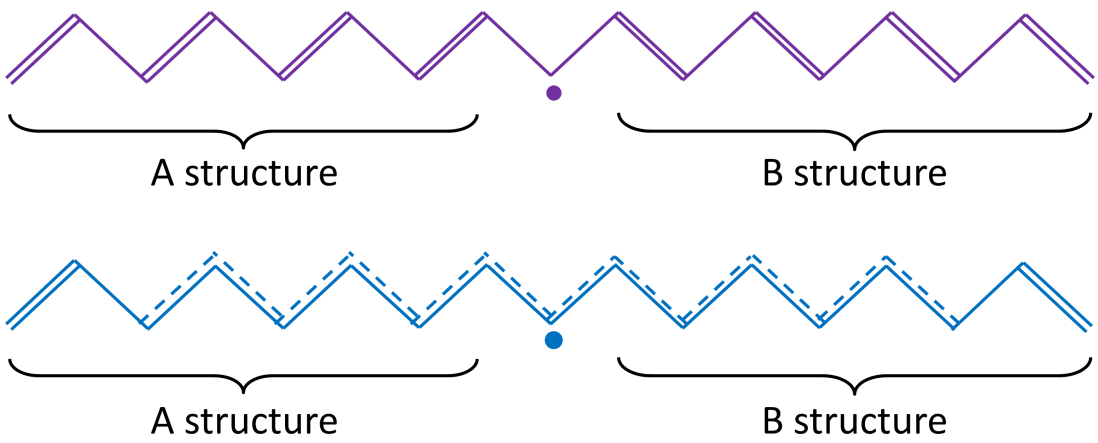

Figure 2.6: Expansion of solitons. In polyacetylene the soliton expands over 14 carbon atom with an effective mass of $6\,m_e$. The A and B structures are interconverted by a charge carrier, the soliton. The soliton is either a charged or neutral defect or a kink in the chain which propagates down the chain carrying a net charge with it.

Figure 2.7 shows the possibilities of QP combination when two QPs meet on a polymer chain. The combination of a neutral and a charged soliton leads to a polaron of the same charge as depicted in figure 2.7a. Two solitons or two polaron of the same charge combine by forming a bipolaron of the same charge as seen in figure 2.7b and in figure 2.7c, respectively.

Two QPs can either combine and form a new QP or annihilate as shown in figure 2.8. Annihilation occurs if two neutral solitons (figure 2.8a) or two soliton of opposite charge (figure 2.8b) meet on a polymer chain. Also, the combination of polarons (figure 2.8c) and bipolarons (figure 2.8d) of opposite charge leads to the annihilation of the QPs.

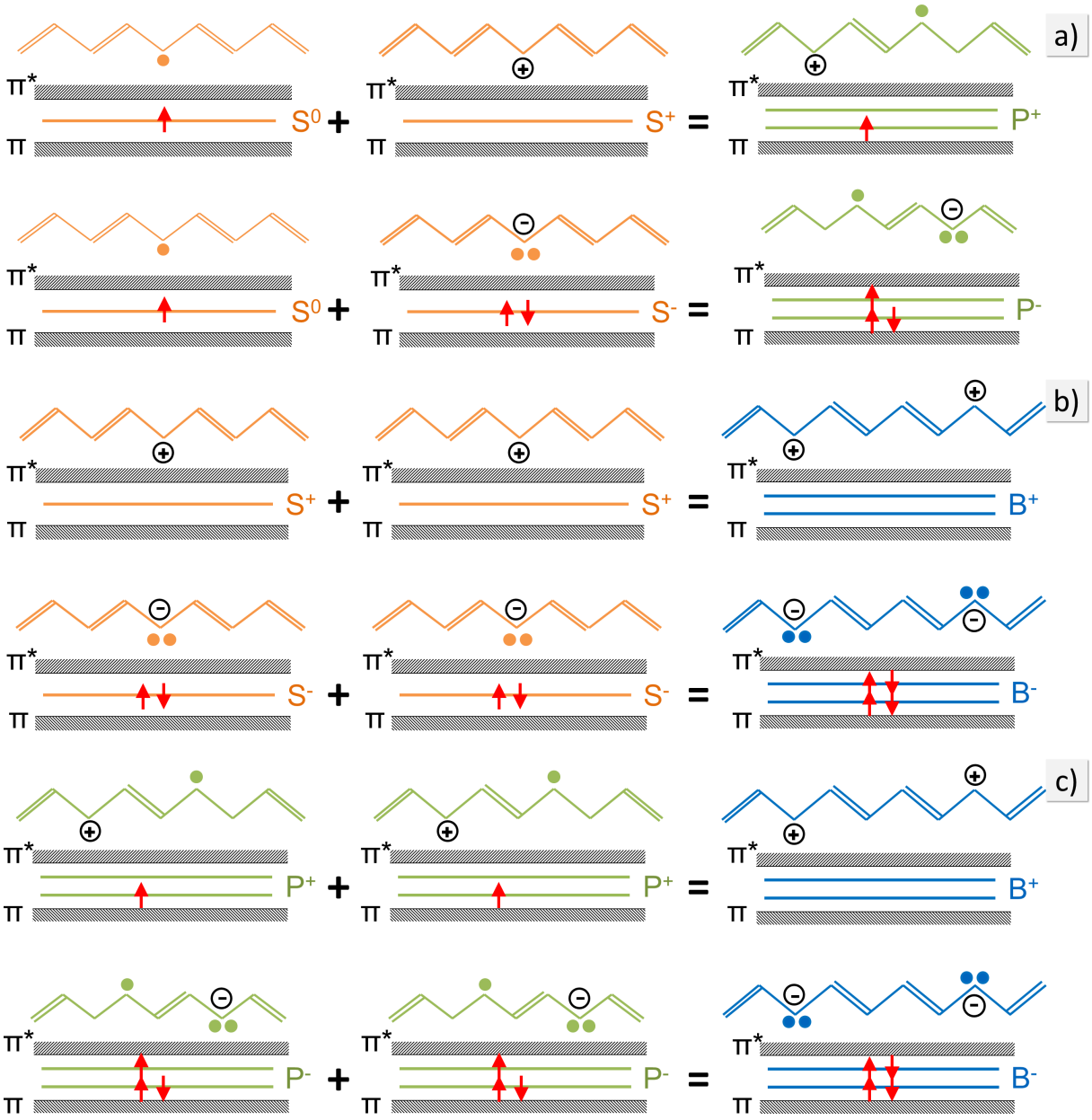

Figure 2.7: Combination of quasiparticles when they converge in the same polymer chain. a) a neutral and a charged soliton form a polaron of same charge, b) two solitons of same charge form a bipolaron of same charge and c) two polarons of same charge converge to a bipolaron of same charge.

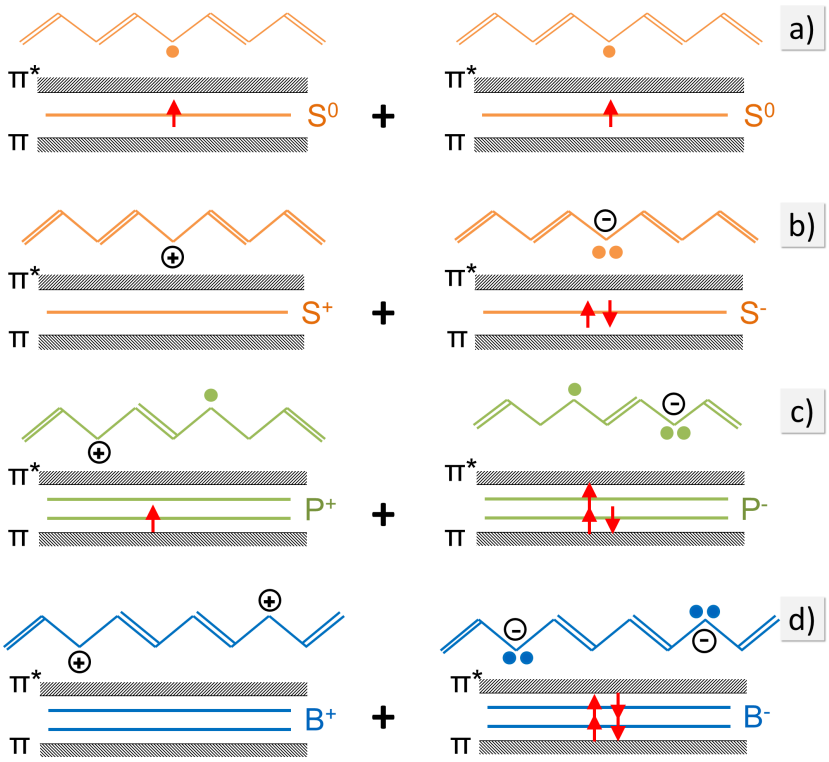

Figure 2.8: Annihilation of quasiparticles when they converge on the same polymer chain. Annihilation occurs for a) two neutral solitons, b) two solitons of opposite charge, c) two polarons of opposite charge and d) for two bipolarons of opposite charge.

Doping

To obtain conducting polymers, the initial polymer is either primary or secondary doped. Doping leads to a conductivity enhancement from 10×10^{-11}-10×10^{-7} S/cm for isolating polymers and 10×10^{-3}-10×10^{3} S/cm for semiconducting and conducting polymers. While for inorganic materials doping is done via incorporation of doping atoms and thereby holes in the valence band or addition of electrons in the conduction band, for polymers counter ions are simultaneously inserted into the polymer matrix. Therein, the doped polymer is referred to as the polymeric organic salt and the doping agent is the oxidizing or reducing agent which converts the polymer to a polymer salt. Further, the concentration of doping for polymer systems is much lower than for inorganic materials. In polymers only a ppm concentration is necessary that the dopant counter ion and the conjugated polymer neutralize the extra charge. A strong potential is the variety of chemical species that are available for doping polymers. Although the doping process for polymer systems differs strongly from the one for inorganic materials, the term doping is justified by the following reasons. The process increases the conductivity, changes the oxidation state, leads to the diffusion of charge carriers as the conduction mechanism and higher dopant concentrations are used for a stronger mobility of the charge carriers.

Primary doping is a chemical doping process. The addition of small nonstoichiometric quantities of a material to the conductive polymer leads to a strong increase in conductivity of the polymers. For the doping process, a redox agent can be used which oxidized (p-doping) or reduces (n-doping) the polymer chain. For the example of PA shown in figure 2.9, the addition of iodine (I_3^-) leads to polymer oxidation. After the addition of I_3^-, the positive QP and the I_3^- are ionically bound. In the case, that a neutral soliton was present on the PA chain before interaction with the I_3^-, a positively charged soliton forms as depicted in figure 2.9a. In the case of an undisturbed PA chain before interaction with the I_3^-, a positively charged polaron forms as illustrated in figure 2.9b. The amount of charge carriers thereby defines the resulting type of QPs. E.g. for a higher density of charge carriers bipolarons are dominant such as for the polymer P3HT, which is one of the most common polymers used for the production of organic solar cells.

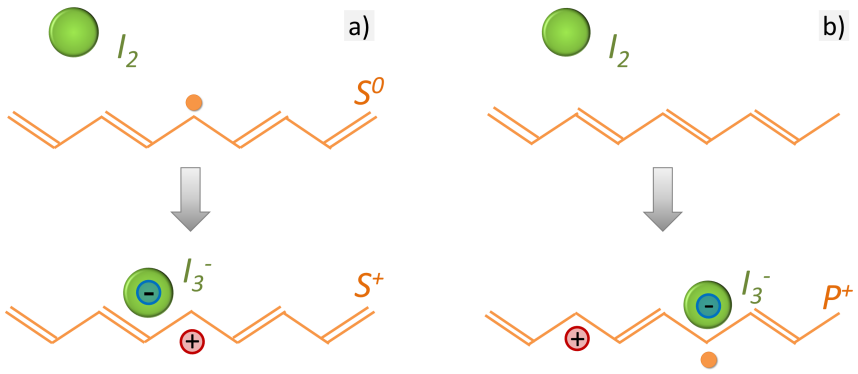

Figure 2.9: Doping of polyacetylene with iodine. a) shows the doping process when a neutral soliton is present on the polymer chain when the interaction with iodine occurs. b) shows the doping process if the polymer chain is undisturbed before interaction with the iodine molecules.

Secondary doping is a doping of structural and crystalline nature rather than of the addition of a redox agent.[21,22] For secondary doping, typically an additive solvent is added to the already primary doped polymer. This increases the conductivity further by up to several orders of magnitude. Typical additive solvents are co-solvents such as alcohols of high boiling point solvents as discussed in chapters 5 to 7, plasticizers or even acids. Primary doping is in principle reversible, while secondary doping is permanent and remains even when the additive is removed, eg. by evaporation of the additive co-solvent.

Charge transport

Within polymer systems, the conduction of charges along the backbone is the most efficient. However, conduction along the side chain of polymer is also possible, however

with lower conductivity than along the polymer backbone. In general, for conductivity through a polymer matrix, the charges need to be transported along polymer chains and from chain to chain. Further, the conductivity in amorphous and semicrystalline phases are fundamentally different than in crystalline phases. The charge transport along an undisturbed polymer chain is described by the introduced QPs which are free to move along the polymer chain. Further, charge transport also occurs from chain to chain or along disturbed chains via the so-called hopping transport. This transport mechanism is a fundamentally different mechanism and the limiting factor for the mobility of the whole polymeric system.

The transport in polymer systems is described by the Su-Schieffer-Heeger (SSH) model.[23] Therein, the soliton transfer, e.g. in PA, is described by an effective Hamiltonian. Within the model the following assumptions are made

- a one-dimensional chain of carbon atoms is assumed,
- electrons are treated in the tight-binding approximation,
- the interaction between the polymer chain and the p-electrons allow for the calculation of structural relaxation and
- no electron-electron interactions are present.

With this, the SSH Hamiltonian $\mathcal{H}_{SSH}$ reads as follows

$$\mathcal{H}_{SSH} = \mathcal{H}_e + \mathcal{H}_{e-ph} + \mathcal{H}_{ph} \tag{2.12}$$

where $\mathcal{H}_e$ is the electron transfer Hamiltonian, $\mathcal{H}_{e-ph}$ is the electron-phonon interaction Hamiltonian and $\mathcal{H}_{ph}$ is the phonon Hamiltonian. The different Hamiltonian describe the different transport mechanism, which are present for electrical transport in polymer systems, i.e. band transport, band and hopping transport and pure hopping transport.

Band transport occurs for ordered crystals where the π-orbitals overlap and form band on which the charge carriers can move freely along the polymer backbone with high mobility. For this transport mechanism the conductivity decreases with increasing temperature due to the emergence of lattice vibration (phonon), on which the transported charges can scatter.

Hopping transport occurs as soon as the static disorder (localized charge carriers) have a large effect on the charge carrier transport. This is typically the case for amorphous

regions or for crystalline regions with defects and impurities. The domains of crystalline order form thereby energetic states of varying size and spatial distribution which leads to a Gaussian distribution of states as depicted in figure 2.10a. The QPs are then transported by hopping from state to state if the thermal excitation (phonon interaction) is strong enough. Therefore, the conductivity increases with increasing temperature for hopping transport. The total density of state (DOS) (figure 2.10a) is proportional to $\delta^2 \cdot (k_B \cdot T)^{-1}$ with $2\,\delta$ the width of the Gaussian distribution, the so-called disorder parameter. Consequently, for low temperatures, the transported charge carriers relax at states of low energy where they get trapped. For hopping transport however, the wave function of different states need to overlap. This is more likely the case at high temperatures where the charges are not trapped due to the overlap of the individual DOSs as depicted in the red box of figure 2.10b. The situation for $k_B \cdot T = 0$ and for $k_B \cdot T > 0$ are depicted in figure 2.10b.

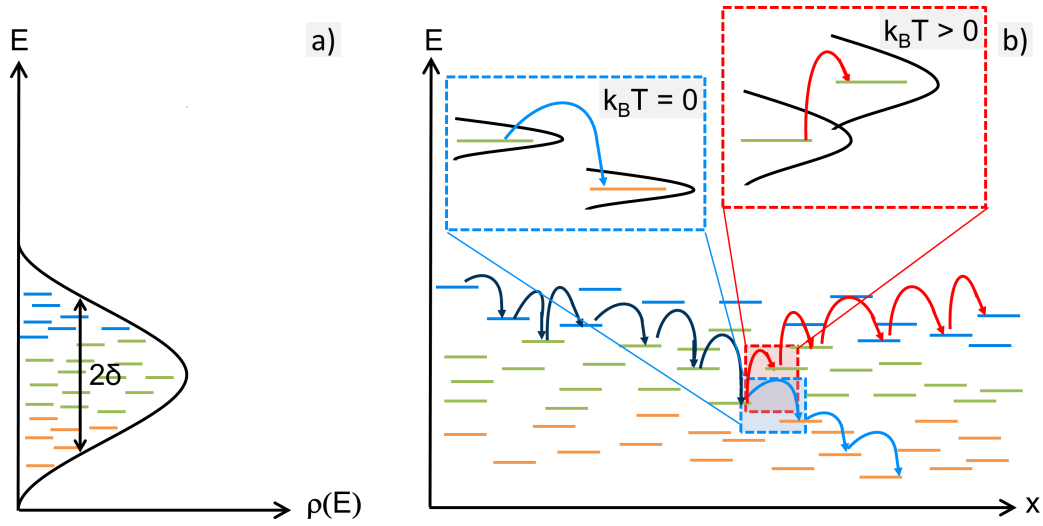

Figure 2.10: Hopping transport in polymer systems. In a) the total density of states (DOS) is depicted. The single lines depict the possible states for charge carriers. In b) the transport mechanism in a polymeric system is shown. The transport path for low and high temperatures is illustrated. The detailed description is found in the text. Adapted from [24] and [25]

As the charge carriers in polymer systems are described as QPs, the hopping transport between polymer chain occurs by hopping of QPs, the so-called interchain crossing. [26] Soliton transfer, also referred to as intersoliton-hopping, is only possible if a neutral and a charged soliton meet as depicted in figure 2.11a. If a charged soliton meets an undisturbed chain, the soliton transfer is suppressed as depicted in figure 2.11b. Polarons are

transferred as a superposition of two solitons from a charged soliton to an undisturbed polymer chain as shown in figure 2.11c-d. Hence, for polaron transfer, no QP is needed on the other chain. For solitona and polarons the hopping between the chains occurs without changing bond alternation. For bipolarons, only the bonds between charged solitons shift their pattern as depicted in figure 2.11e-f.

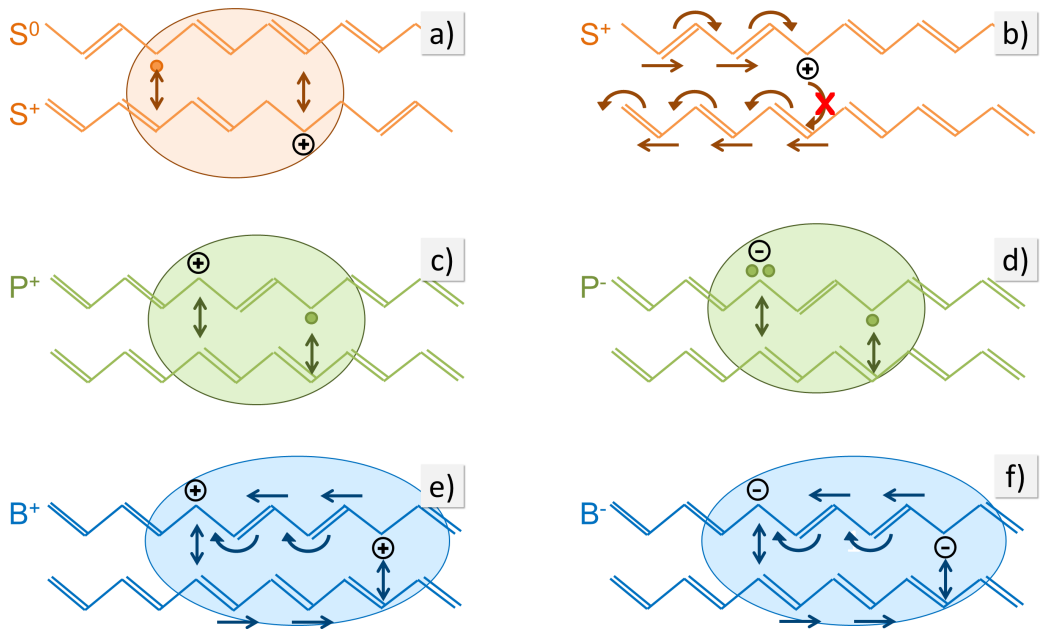

Figure 2.11: Interchain crossing of quasiparticles. In a) a neutral and a charged soliton lead to intersoliton -hopping while the intersoliton-hopping of a charged soliton and an undisturbed polymer chain is suppressed. For polarons and bipolarons interchain crossing occurs with undisturbed polymer chains. The interchain crossing of an undisturbed polymer chain and c) a positive polaron, d) a negative polaron, e) a positive bipolaron and f) a negative bipolaron is depicted.

The resulting mobility and conductivity can be described by a drift velocity $\vec{v}$, an applied electric field $\vec{E}$, a current density $\vec{j}$, a charge carrier density n and an elementary charge q. The charge carrier mobility μ thereby connects the charge carriers to the applied field

$$\vec{v} = \mu \cdot \vec{E} \tag{2.13}$$

and the macroscopic conductivity σ defines the current due to motion of charge carriers with

$$\vec{j} = \sigma \cdot \vec{E} = n \cdot q \cdot \mu \cdot \vec{E}. \tag{2.14}$$

2.2 Organic photovoltaic (OPV) devices

Photovoltaic (PV) devices are optoelectronic devices, which convert light into electricity. In organic PV (OPV) devices the active layer (AL) of the device, which is responsible for absorbing and converting the incident light into electricity, consists purely of organic semiconductors. In the present thesis, the AL is a blend of a polymer and a small molecule as described in chapter 4, sections 4.3 and 4.1.1. As the AL in OPV usually consists of a heterojunction of two materials this leads to some peculiarities in OPV compared to their inorganic counterparts. In the device architecture, the AL is sandwiched between a metal electrode, the so-called top electrode, and a transparent electrodes (TE), the so-called bottom electrode as depicted in figure 2.12. The TE allows light to pass through to the AL, where the light is then converted to electricity. Typically this TE consists of a selective electrode material, in this thesis PEDOT:PSS, and an inorganic metal oxide layer, which is widely used but also one of the limiting factors of OPV regarding flexibility and cost (see chapter 1 for discussion on this point). This thesis is assigned to investigate the possibility of replacing this inorganic metal oxide by a highly conductive version of the selective electrode PEDOT:PSS.

In the following, the device architecture and the basic mechanism of the operating principle of an OPV device is explained in section 2.2.1. Further, the possible recombination mechanisms are shortly discussed in section 2.2.2, including the recombination mechanisms at the interface of AL and selective electrode.

2.2.1 Working principle of OPV

The conversion from light to electricity in an OPV device can be described by five mechanisms starting with (1) the absorption and formation of excitons, followed by (2) the diffusion and (3) the dissociation of the excited excitons, (4) the transport of the charge carriers to the electrodes and finally (5) the extraction of the charge carriers at the electrodes. These four mechanism are depicted in figure 2.12.

(1) Absorption of light and exciton formation
The absorption of light by the organic semiconductors follows the Lambert-Beer law

$$I_T(\lambda) = I_0(\lambda)\, \mathrm{e}^{-\alpha(\lambda)\, d} \tag{2.15}$$

with $I_T(\lambda)$ the transmitted intensity, $I_0(\lambda)$ the incident intensity, α the material specific absorption coefficient and d the thickness of the layer. The absorption of the incident

photons occurs if its energy is larger than the energy gap of the absorbing molecules E_{gap}.

$$E = \lambda\,\nu = \frac{h\,c}{\lambda} > E_{gap} \tag{2.16}$$

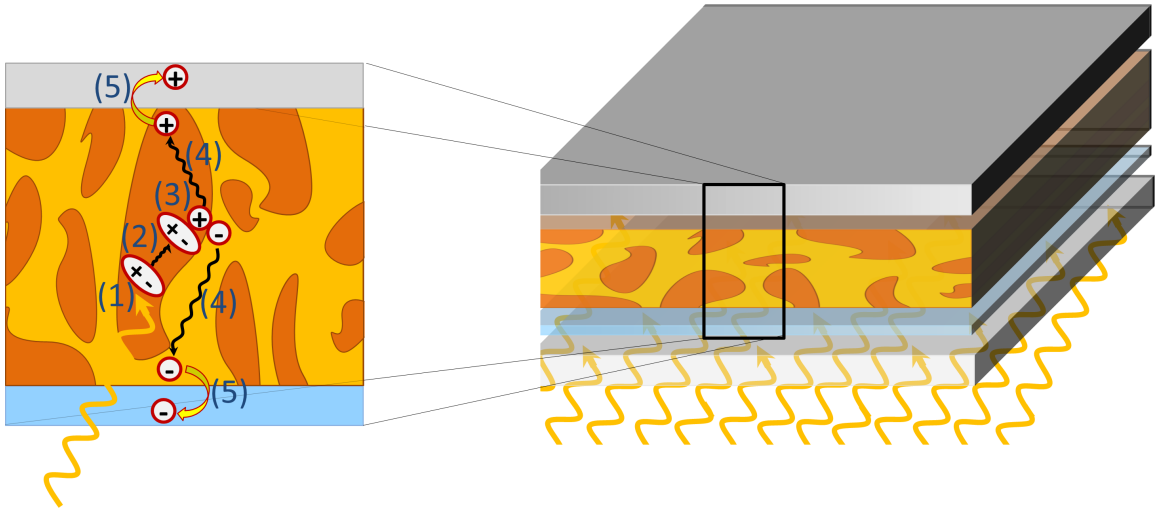

Figure 2.12: Cross section through an organic photovoltaic device. The light is injected from the bottom through the transparent electrode (depicted in blue) into the active layer blend of a donor and an acceptor material (depicted in yelllow and orange). The conversion from light to electricity is described the 5 steps which are indicated in the scheme here and described in detail in the text: (1) Absorption of light and Exciton formation, (2) Exciton dissusion, (3) Charge carrier (polaron pair) dissociation, (4) Charge transport, (5) Charge extraction at electrodes.

Thereby the electron is excited from the highest occupied molecular orbital (HOMO) to the lowest unoccupied molecular orbital (LUMO). The missing electron in the HOMO is described by a quasiparticle with equivalent charge, the so-called hole. After excitation, the electron and the hole are still bound by their Coulomb interaction. This excited, bound state is called exciton. In classical inorganic semiconductors, due to a low binding energy these excitons expand much further, than in organic semiconductors and often dissociate at room temperature. The exciton in an inorganic semiconductor is referred to as the Wannier-Mott exciton, while the exciton in an organic semiconductor is referred to as the Frenkel exciton which is localized, exhibits a strong binding of typically 0.35 eV-0.5 eV as a result of the low permittivity of these materials ($\epsilon \approx 3-4$) and has a weak screening.[27] Caused by this strong binding, the probability to recombine from the excited back to the ground state, is relatively large for Frenkel excitons. The lifetime of excitons in organic semiconductor is hence typically in the order of ns.[28] Due to the short lifetime,

also the diffusion length of the excitons is low with $l_{diff} \approx 10\,\text{nm}$.

(2) Exciton diffusion

After absorption of light in one material of the AL, the created exciton needs to diffuse to the interface with the second material. At this interface, the exciton is dissociated into free charge carriers. The diffusion of excitons does not go along with charge transport, as an exciton is a bound pair and has no net charge. Hence, the exciton diffusion is described by two energy transfer processes between the donor and acceptor molecules, the classical energy transfer-process and the Förster transfer-process.

For relatively large distances ($R > 10\,\text{nm}$) between the donor and the acceptor molecules, the energy transfer-process dominates. In the energy transfer-process, the donor emits a photon (flourescence) which is then reabsorbed by the acceptor. Thereby, an exciton is created in the acceptor material. By this process the lifetime of the initial exciton is increased.[26] The transfer rate K_{D-A}^{ET} of this process is inversely proportional to the squared distance R^{-2} between the donor and the acceptor molecules

$$K_{D-A}^{ET} \propto R^{-2} \tag{2.17}$$

For shorter distances between the donor and the acceptor molecules ($R < 10\,\text{nm}$), the Förster transfer is the dominating process. This process is also known as the fluorescence resonant energy transfer (FRET). In this process, dipole-dipole coupling between the donor and the acceptor leads to the radiation-less energy transfer. For Förster transfer to occur, the emission spectrum of the donor and the acceptor has to overlap slightly. Further, the probability of a Förster transfer process is maximized if the dipoles in the acceptor and in the donor materials are aligned parallel to each other. The transfer K_{D-A}^{FRET} rate is

$$K_{D-A}^{FRET} = \frac{1}{\tau_D}\left(\frac{R_0}{R}\right)^6 \tag{2.18}$$

with τ_D the decay time and R_0 the critical transfer distance at which the rate of the energy transfer equals the decay rate.[29]

The diffusion itself can be described by random hopping with a diffusion length l_D, which is proportional to the square route of the exciton lifetime with $l_D \propto \sqrt{\tau_D}$. As the exciton lifetime is typically in the order of ns[30], this leads to diffusion lengths in conjugated polymer systems of 4–14 nm.[31,32]

$$l_D = \sqrt{2\,d\,D\,\tau_D}, \tag{2.19}$$

(3) Charge charrier (polaron pair) dissociation

In the ALs used in this thesis, the exciton is typically excited in the polymer materials

(donor) and dissociated at the interface to the small molecule (acceptor). An exciton, which was created in the donor, diffuses through the donor until it reaches the interface to the acceptor material. For an interface, where the energy levels of the HOMO and the LUMO match, the exciton dissociation is with $\approx 10\,\mathrm{fs}$ faster than the exciton decay time. Splitting of the exciton at the donor-acceptor interface either occurs by direct electron transfer from the donor to the acceptor or first by energy transfer from the donor to the acceptor followed by hole transfer from the acceptor back to the donor. This exciton dissociation is also referred to as polaron pair dissociation, as the charge carriers are not free but exist as polarons within molecules.

One model, which describes the dissociation of polaron pairs is the Braun-Onsager model based on two oppositely charged ions with the help of an electric field.[33,34] In this model, the rate of polaron pair recombination is $k_r \propto \tau_r^{-1}$ with τ_r the polaron pair lifetime and the rate of dissociation $k_d(F)$ is field dependent.[35] The field dependent polaron pair separation yield $P(F)$ is then given by

$$P(F) = \frac{k_d(F)}{k_d(F) + k_r} \tag{2.20}$$

and can further by expressed with the substitution $k_d(F) = \mu\,\kappa_d$ by the mobility μ with

$$P(F) = \frac{\kappa_d(F)}{\kappa_d(F) + (\mu\,\tau_r)^{-1}} \tag{2.21}$$

In total, the polaron pair separation yield and hence the charge carrier generation depends on the mobility of the materials and the lifetime of the polaron pairs.[35]

(4) Charge transport

Due to the high disorder in organic semiconductor compared to classical semiconductors, the transport of charges, or rather, quasiparticles such as polaron, is described by hopping mechanism as discussed in section 2.1.4. The hopping transport describes the transport from one localized state to the next by the weak overlap of their wavefunctions. The hopping rate can be described by tunneling and thermal activation. Besides the description by Marcus[36,37], the hopping rate ν_{ij} is described by Millera and Abrahams[38] with

$$\nu_{ij} = \nu_0 \mathrm{e}^{-\gamma' r_{ij}} \begin{cases} \mathrm{e}^{-\Delta E_{ij}/(k\,T)} & \Delta E_{ij} > 0 \quad \text{(hopping up)} \\ 1 & \Delta E_{ij} \leq 0 \quad \text{(hopping down).} \end{cases} \tag{2.22}$$

with ν_0 the maximum hopping rate, γ' the inverse localization radius, ΔE_{ij} the energy difference and r_{ij} the distance between the two localized states i and j.

The Miller-Abrahams model described the mesoscopic hopping of charges. To describe the macroscopic hopping transport, Bässler extended the Miller-Abrahams model using a Monte-Carlo simulation and describing the density of states as Gaussian distributions.[39] Thereby it was found that the mobility μ_B for macroscopic hopping transport depends on the temperature as well as on the electric field

$$\mu_B = \mu_\infty \mathrm{e}^{-\left(\frac{2\,\sigma}{3\,k\,T}\right)^2 + C\left(\left(\frac{\sigma}{k\,T}\right)^2 - \Sigma\right) F^{1/2}} \tag{2.23}$$

with $2\,\sigma$ the energetic width and Σ the spatial width of the Gaussian distributions, i.e. the respective disorder parameters (see section 2.1.4). The two dependencies $ln(\mu) \propto F^{1/2}$ and $ln(\mu) \propto 1/T^2$ were also found experimentally, confirming the approach.[40,41] As discussed in section 2.1.4, the charge transport in organic semiconductors is in general described by band and hopping transport with Gaussian distributed densities of state. The center of the Gaussian distribution is the so-called transport energy around which the hopping transport is possible. For charges below this energy, the chance for charge carrier trapping in deep trap sites become more likely which hinders charge carrier transport (see also figure 2.10 in section 2.1.4).

(5) Charge extraction at electrodes

The mechanism of charge carrier extraction at electrodes is still under debate. Among others, Scott et al. e.g. reported a model in which the mechanism of charge carrier injection and recombination at electrodes is discussed.[35] In general, the charge carrier extraction at the electrodes strongly depends on the device architecture and energy level alignment as also shortly discussed in chapter 6, sections 6.2 and 6.2.2. Further, the charge carrier concentrations near the electrodes influence the recombination at the interfaces and therefore also the charge extraction. Last but not least, the extraction depends on the hole and electron mobilities of the two AL materials. In case the hole and electron mobilities differ strongly, recombination close to the electrode interface is more likely.

2.2.2 Loss mechanisms

The loss mechanisms which lead to a internal quantum efficiency below 100 % are of various origin and range from incomplete absorption of the light to recombination mechanisms within the AL or at the interfaces to the outer electrodes. Within a typical heterojunction AL of the OPV device the excited exciton recombines if no interface between the absorber materials is available within the exciton diffusion length, which is typically in the order of *nm*.[30] If exciton, i.e. polaron pair, dissociation is too slow, so-called geminate recombination occurs, i.e. recombination of polarons within the same molecule.[35]

However, recombination can also occur for polarons, which are already separated, which is the referred to as non-geminate recombination.[35] During the transport of charge carriers through the organic semiconductor, the charge carriers can be trapped in deep trap states, i.e. low energetic states within the band gap, impurities or structural defects.[42,43] In this case, the trapped charges recombine with mobile transported charges.

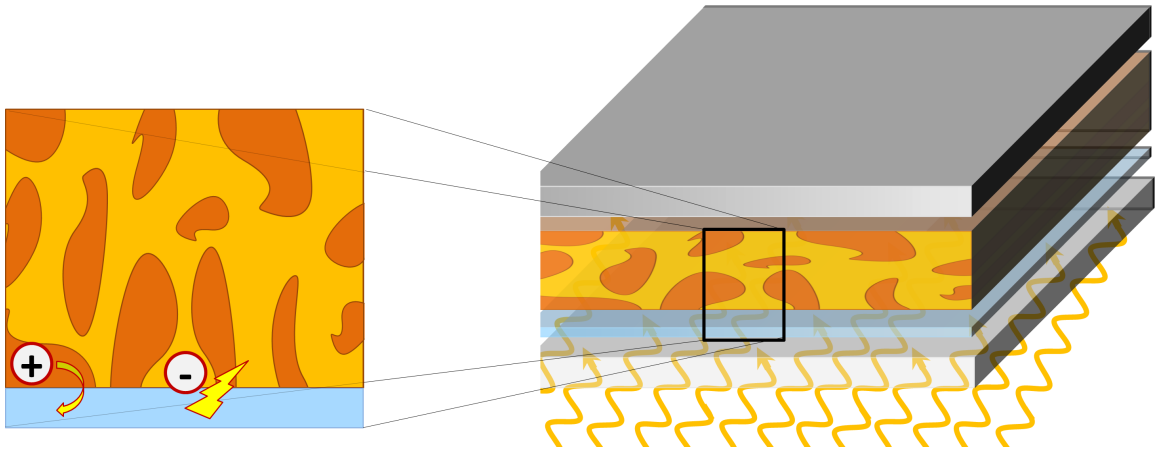

Figure 2.13: The schematic shows a cross section through an organic photovoltaic device. The active layer consists of an electron and a hole conducting material. At the interfece between to the anode, holes from the hole conducting material are extracted to the anode. If an electron from the electron conducting materials happens to be present at the interface to the anode, it will recombine with the holes present in the anode.

The charge carriers can also recombine at the interface to the electrodes, where the charge carriers are injected to after successful generation and transport through the AL. Two types of recombination can occur at the interface to the electrodes, e.g. the PEDOT:PSS electrode, which is examined in this thesis. Scott et al.[44], treated the charge recombination at the interface to a metal by a hopping process in the image potential and thereby are able to determine the surface recombination rate, the infection current and the net current, i.e. the injected minus the recombination current. Further, the AL is a blend of two semiconductors of which one is the electron donator and one the electron acceptor. This blend morphology has the drawback the also the electron accepting material has an interface to the hole collecting electrode, i.e. the „wrong“ electrode. If now an electron from the electron conducting materials is present near the interface to the anode, the electron from the active layer recombines with the holes of the anode (see Figure 2.13). Vice versa the same can happen for holes in the hole conducting semiconductor of the active layer near the interface to the cathode. In this case the hole from the active layer recombines with electrons from the cathode.

2.3 Scattering basics

In this thesis, the conductivity-structure relation of highly conductive PEDOT:PSS thin films is investigated by X-ray scattering techniques. X-ray scattering techniques are powerful methods to probe large film areas obtaining statistically relevant information about structures of the inner film volume. Depending on the method, different length scales of sample morphology are probed, from crystalline lattice distances to structural arrangement on the mesoscale. The present section discusses general theoretical aspects of elastic X-ray scattering. For elastic scattering the energies of the incoming and the scattered photons are always equal ($E_i = E_f$). The X-ray scattering techniques that are applied for sample investigations in this thesis range from reflectivity to grazing incidence and soft X-ray scattering. After introducing the general definitions, an introduction to the theory of reflection (section 2.3.2), grazing incidence (section 2.3.3) and soft X-ray scattering (section 2.3.4) is provided.

2.3.1 General definitions

The incident photons with a wave vector of $k = \left|\vec{k_i}\right| = \frac{2\,\pi}{\lambda}$ and a wavelength λ are described by an electromagnetic wave traveling through a medium with a refractive index $n(\vec{r})$. In general, the electric field vector of a plane electromagnetic wave is described by:

$$\vec{E}(\vec{r}) = \vec{E_0}\,\mathrm{e}^{i\,\vec{k_i}\cdot\vec{r}}, \tag{2.24}$$

whereby $\vec{r}$ denotes the position vector and $\vec{E_0}$ involves the amplitude and polarization direction of the electric field. With this, the propagation of an electromagnetic wave is described by the Helmholtz equation[45]:

$$\Delta\vec{E}(\vec{r}) + k^2\,n^2(\vec{r})\,\vec{E}(\vec{r}) = 0 \tag{2.25}$$

Scattering contrast

Scattering occurs if a change in refractive index is given. As the refractive index $n(\vec{r})$ of matter is just slightly smaller than one for investigations with X-rays, $n(\vec{r})$ is given by:

$$n(\vec{r}) = 1 - \delta(\vec{r}) + i\,\beta(\vec{r}) \tag{2.26}$$

where, $\delta(\vec{r})$ represents the dispersion and $\beta(\vec{r})$ represents the absorption, each as the sum over N atoms per unit volume according to:

$$\delta(\vec{r}) = \frac{\lambda^2}{2\,\pi}\,r_e\,\rho(\vec{r})\,\sum_{j=1}^{N}\frac{f_j^0 + f_j^{'}(E)}{Z} = \frac{\lambda^2}{2\,\pi}\,\rho(\vec{r}) \tag{2.27}$$

and

$$\beta(\vec{r}) = \frac{\lambda^2}{2\,\pi}\, r_e\, \rho(\vec{r})\, \sum_{j=1}^{N} \frac{f_j''(E)}{Z} = \frac{\lambda}{4\,\pi}\, \mu(\vec{r}). \tag{2.28}$$

whereby $\mu(\vec{r})$ denotes the absorption coefficient if the investigated material. With the position dependent electron density $\rho(\vec{r})$, also referred to as the real part of the scattering length density, which is given by:

$$\rho(\vec{r}) = r_e\, \rho_e(\vec{r}) \tag{2.29}$$

with the classical electron radius $r_e = e^2/(4\,\pi\,\epsilon_0\,m\,c^2) = 2.814 \times 10^{-5}\,\text{Å}$ and the electron density $\rho_e(\vec{r})$ of the material under investigation. The contrast between two phases within the same film is given by:

$$\Delta\delta^2 + \Delta\beta^2 = (\delta_1 - \delta_2)^2 + (\beta_1 - \beta_2)^2 \tag{2.30}$$

With this, the scattering contrast in X-ray scattering experiments also depends on the difference in scattering length density of the investigated materials, i.e. according to equation 2.29 on the difference in electron density.

Principle definitions

The principle of scattering is schematically depicted in figure 2.14a for specular scattering and in figure 2.14b for diffuse scattering. For both cases, the incident beam $\vec{k_i}$ impinges the sample under an incident angle α_i. After interaction with the material under investigation, the reflected beam $\vec{k_f}$ exits the under the final angle of α_f. Hence, the scattering vector is defined as indicated in figure 2.14 by:

$$\vec{q} = \vec{k_f} - \vec{k_i} \tag{2.31}$$

whereby the modulus of both incoming and outgoing wavevectors equal to $k = 2\pi/\lambda$ for elastic scattering, as it is the case for the investigations shown in the present thesis.
In the case of specular reflection the final angle α_f equals the incident angle α_i and further remains within the xz-plane. In the case of diffuse scattering, the reflected beam does not necessarily remain in the xz-plane but exhibits an additional out of plane angle ψ_f in the xy-plane as depicted in figure 2.14.

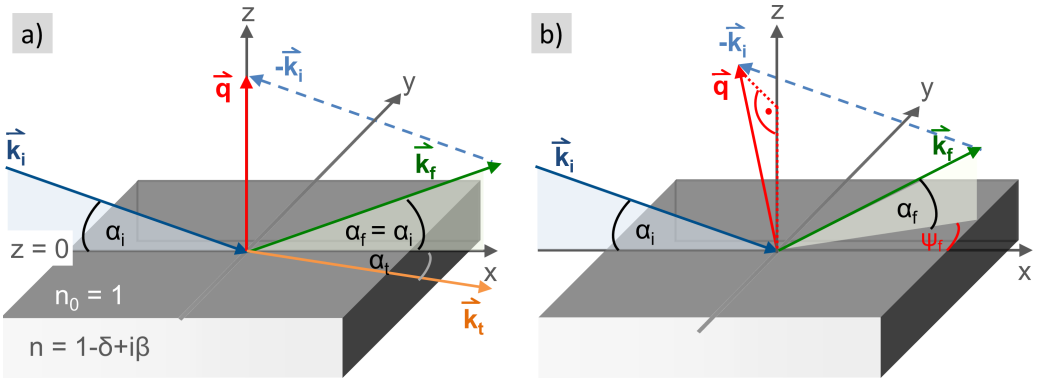

Figure 2.14: Definition of scattering vectors and angles for a) specular and b) diffuse scattering from the scattering plane, which is defined by the surface of the investigated film.

After interaction of the incident beam with the material, the beam can be transmitted or reflected as depicted in figure 2.14a, depending on the incident angle as well as on the refractive indices. The angle of the transmitted beam is described by the Snell's law, which establishes that:

$$cos(\alpha_i) = n\, cos(\alpha_t). \tag{2.32}$$

For X-ray scattering ($\delta > 0$) from air ($n = 1$) to matter ($n < 1$) and with the small angle approximation, the critical angle for total reflection is given by

$$\alpha_c = \alpha_i \approx \sqrt{2\,\delta} = \lambda \sqrt{\frac{\rho}{\pi}}. \tag{2.33}$$

The critical angle depends on the wavelength of the incident photons as well on the scattering length density of the material under investigation. For all incident angles below the critical angle ($\alpha_i < \alpha_c$), the beam is reflected totally.

2.3.2 Reflectivity

The reflectivity of a thin film, e.g. the PEDOT:PSS electrodes in this thesis, is measured by X-ray reflectivity (XRR), where the specular scattering is measured as a function of the incident angle α_i. For specular scattering, the incident angle equals the exit angle with $\alpha_i = \alpha_f$ and $\psi_f = 0$. Therefore, only the z-component of the scattering vector q differs from 0 ($q_z \neq 0$) and is given by[46]:

$$q_z = \frac{4\,\pi}{\lambda}\, sin(\alpha_i). \tag{2.34}$$

The incident beam is partially reflected and partially transmitted at interfaces depending on equation 2.32 described in section 2.3.1. Furthermore, the amplitudes of the reflected

and the transmitted beams can be described by the Fresnel reflection coefficient r^F and the Fresnel transmission coefficient t^F. With this, the reflectivity and transmittivity are given by the square of the respective coefficients[46]

$$R^F = \left|r^F\right|^2 \quad \text{and} \quad T^F = \left|t^F\right|^2 \tag{2.35}$$

From XRR analysis, the vertical film composition as well as the total film thickness and the film roughness can be extracted. The polymer films measured in the present thesis, typically exhibit a different density at the interface to air than at the interface to the substrate. Hence, the vertical film composition is described by several stacked layers of different refractive indices n. A model describing the final reflectivity was developed by Parratt using a recursive algorithm.[47] In this model, N layers are assumed, each of a refractive index $n_j(z)$ and a thickness d_j. The thin film is sandwiched between an infinite thick layer of air on top side and an infinite thick layer of silicon or glass on the bottom side. Each interface within the thin film is described by the ratio of its reflectivity and transmission according to:

$$X_j = \frac{R_j}{T_j} \tag{2.36}$$

whereby R_j and T_j are calculated by the above-defined Fresnel coefficients. The Parratt algorithm can be extended by the Névot-Crocet factor to account for non-ideal, meaning not perfectly flat interfaces. Therefore, the root mean square roughness

$$\sigma_{rms} = \sqrt{\frac{1}{N_{\sigma_{rms}}} \sum_{i=1}^{N_{\sigma_{rms}}} \Delta z_i^2} \tag{2.37}$$

is introduced to the Parratt algorithm by an exponential function to the Fresnel coefficients. The limit of the roughness σ_{rms} is the total film thickness. Therein, $N_{\sigma_{rms}}$ is the number of measured points, i.e. sampling points, along the interface and Δz_i is the deviation from the mean interface at the sampling point i. A detailed description can be found in the corresponding reference[46].
Figure 3.2 in section 3.3.1 exemplary shows a normalized reflectivity curve of a PEDOT:PSS thin film including the corresponding fit. At low incident angles below the critical angle of the materials, the intensity is normalized to unity ($I = 1$ and $log(I) = 0$) as there the condition for total reflection is fulfilled with $\alpha_i < \alpha_c$. At slightly higher incident angles, a slight decrease in the reflectivity is seen, which indicate the critical angles of the film components ($\alpha_i = \alpha_c$), in this case of PEDOT $\alpha_{c,PEDOT}$ and PSS $\alpha_{c,PSS}$. At the critical angel of silicon or glass $\alpha_{c,Si/glass}$, the intensity of the reflectivity exhibits a strong decrease with a decay proportional to q^{-4}, which is even steeper for higher roughness. The decay is modulated by the so-called Kiessig fringes, whose spacing depend on the total

film thickness. Therefore, the total film thickness is proportional to the inverse spacing of the Kiessig fringes and approximated by[48]:

$$d \approx 2\,\pi/\Delta q_z \tag{2.38}$$

Lastly, fitting of the full reflectivity curve according to the aforementioned description, the profile of the refractive index and with this the scattering length density profile can be extracted, describing the vertical film composition as shown for PEDOT:PSS films in chapter 5, section 5.1.

2.3.3 Grazing incidence scattering

Diffuse scattering of thin films, such as investigated in the present thesis, is typically measured in grazing incidence geometry and at fixed incident angle α_i. As in this geometry the footprint of the beam on the film surface is larger than in transmission geometry, this allows for good statistics despite of low film thicknesses. A two dimensional detector is used, to detect the diffuse scattering which originates either from rough interfaces or, more important for the results shown in this thesis, from lateral arrangement of phases or domains. The scattering vector q, which describes the nature of the scattering at these structures depends on the wavelength λ, the incident angle α_i as well as on the exit angles in-plane α_f and out of plane ψ_f. Thereby in-plane and out-of-plane refers to the xz-plane, the so-called scattering plane, which is perpendicular to the xy-plane, the so-called sample plane (see figure 2.14). The scattering vector q is given by:

$$q = \frac{2\,\pi}{\lambda} \begin{pmatrix} cos(\psi_f)\,cos(\alpha_f) - cos(\alpha_f) \\ sin(\psi_f)\,cos(\alpha_f) \\ sin(\alpha_i) + sin(\alpha_f) \end{pmatrix}. \tag{2.39}$$

Grazing incidence small angle X-ray scattering (GISAXS)

In this thesis, GISAXS is used to describe the diffuse scattering of X-rays after interaction with PEDOT:PSS thin films. With the small angle geometry (see chapter 3, section 3.3.2 for experimental details), lateral length scales of the films are measured, which correspond to the meso-morphology of the inner film, i.e. material clusters in the range of several nanometers up to micrometers. In scattering theory, the scattering is described as the perturbation of an ideal system. Thereby, the ideal system is an ideally smooth interface whereas the perturbations are the film roughness and the lateral structures. The first order perturbation is used to calculate the differential scattering cross section of the incident beam of wavelength λ with the material according to

$$\left.\frac{d\sigma}{d\Omega}\right|_{diff} = \frac{C\,\pi^2}{\lambda^4}\left(1-n^2\right)^2 \left|t_i^F\right|^2 \left|t_f^F\right|^2 P_{diff}(\vec{q}) \propto P_{diff}(\vec{q}) \tag{2.40}$$

with the illuminated surface area C, the respective Fresnel transmission coefficients t_i^F and t_f^F and the diffuse scattering factor $P_{diff}(\vec{q})$.[49] As the Fresnel transmission coefficients exhibit a their maximum if the incident angle or the exit angle equal to the critical angle of the measured material, at these angles the scattering intensity is strongly increased. This increase in intensity at $\alpha_i = \alpha_c$ or $\alpha_f = \alpha_c$ is the so-called material sensitive Yoneda peak.[50] Nevertheless, the intensity of the scattered wavevector is proportional to $P_{diff}(\vec{q})$ and the Fresnel transmission coefficients are just an overall scaling factor for the scattering intensity.[51] In general, the scattering pattern is described by two terms: 1) objects of a certain size within the film and 2) an interference function, which describes the distance between the objects. For N objects of the same kind of random orientation, the diffuse scattering factor is proportional to these two terms

$$P_{diff}(\vec{q}) \propto N\, S(\vec{q})\, F(\vec{q}) \tag{2.41}$$

with the form factor $F(\vec{q})$ being the Fourier transformation of the electron distribution of the objects, and with the interference function $S(\vec{q})$ describing the spatial arrangement of the objects.[52] To analyze the diffuse scattering pattern, in this thesis five additional approximations are made as qualitatively described in the following

(1) The diffuse scattering in GISAXS is typically described in the distorted wave Born approximation (DWBA).[53,54] In the DWBA, the scattering is described as discussed above, by the perturbation of an ideal system. The DWBA takes four terms into account, whereby each corresponds to a different scattering event: (a) scattering of the incident beam in the bulk material. (b) reflection of the incident beam at the substrate followed by scattering in the bulk of the investigated material, (c) scattering of the incident beam in the bulk followed by reflection at the substrate, (d) succeeding reflection at the film surface followed by scattering in the bulk followed by another reflection at the substrate. The form factor of the scattering event is then the coherent interference these terms.

(2) In thesis solely the lateral structures are analyzed from GISAXS measurements, i.e. only the q_y information. Therefore, the effective surface approximation is justified.[55] With this approximation, scattering is assumed to occur at only one specific surface, which allows to decouple the height from the radii of the scattering objects.

(3) The shape of the lateral structures is simplified to either cylinders of spheres. This assumption is based on the fact that the samples investigated in this thesis are rotationally isotropic equally to the assumed shape of the objects.

(4) The spatial arrangement, described by the interference function $S(\vec{q})$ is approximated by a one-dimensional paracrystalline lattice (1DDL). The 1DDL describes the lateral structure as a periodical arrangement of objects. In this approximation only short range order is taken into account by an increasing deviation from the theoretical position for objects with larger distance from the origin of the lattice. This assumption is valid, as the structures within the investigated PEDOT:PSS thin films do not exhibit a long range order. Further, in the 1DDL approximation no two-dimensional ordering is taken into account as the arrangement of the objects is independent of the direction within the system as mentioned above.[56]

(5) The distribution of sizes is described in the local monodisperse approximation (LMA). All object sizes are thereby described with a Gaussian distribution for the sizes. In the approximation, coherent scattering is only allowed for objects of the same kind, i.e. scattering from objects of different form and structure factor is prohibited. With this assumption, different structures present in the same film, are independent of each other. Typically, two to three form and corresponding structure factors are used to model the investigated PEDOT:PSS thin films.

(5) With in the small angle approximation the scattering vector can be approximated to:

$$q = \frac{2\pi}{\lambda} \begin{pmatrix} 0 \\ 2\,\psi_f \\ \alpha_i + \alpha_f \end{pmatrix}. \tag{2.42}$$

Grazing incidence wide angle X-ray scattering (GIWAXS)

In the present thesis, GIWAXS measurements are used to parametrize the crystalline structure of films. The setup is similar to the one in GISAXS measurements just with a much shorter sample-detector distance. For experimental details it is referred to chapter 3, section 3.3.3. Furthermore, the incident angle in GIWAXS measurements is chosen to be above the critical angle of the investigated materials and below the one of the substrate to suppress scattering originating from the substrate. The origin of scattering intensity is the same as for typical diffraction. Crystals within the investigated material are described by the lattice of the crystal, which is a periodic grating for the incident X-ray beam whose wavelength is in the order of the lattice dimensions. If the Bragg condition is fulfilled at a certain exit angle, coherent scattering leads to increased scattering intensity for the corresponding exit wavevector.

As discussed above, X-rays scatter with the electrons of the investigated material. These electrons are located around the atom cores, which are themselves located at the crystal

lattice points. The structure factor $S(\vec{q})$ described the arrangement of N atoms in a crystal by

$$S(\vec{q}) = \sum^{N} f_j e^{2\pi i (h x_j + k y_j + l z_j)} \tag{2.43}$$

where (h, k, l) describes the scattering vector $\vec{q}$ and (x_j, x_j, z_j) describes the position vector $\vec{r}$. f_j are the individual atomic form factors, which are described by the Fourier transformed electron density distribution $\rho_e(\vec{r})$

$$f_j(\vec{q}) = \int_V \rho_e(\vec{r})\, e^{2\pi i (\vec{q}\vec{r})}\, dV. \tag{2.44}$$

If the reciprocal lattice vector $\vec{G}$ equals the scattering vector $\vec{q}$ ($\vec{G} = \vec{q}$), the form factor $F(\vec{q}) \neq 0$. The maximum of the scattering intensity is thereby described by the Laue equation. Further, the Bragg equation defines the condition for which constructive interference occurs and hence, a scattering intensity is detected:

$$2\, d_{hkl}\, sin(\alpha_i) = n\, \lambda \tag{2.45}$$

with d_{hkl} the lattice spacing, α_i the incident angle and λ the wavelength of the beam. The geometry and definitions of the vectors and an angles are given in figure 2.15. It shows, that depending on the angle between the incident and the exit beam, the difference in the path length s leads to constructive or destructive interference with d_{hkl}.

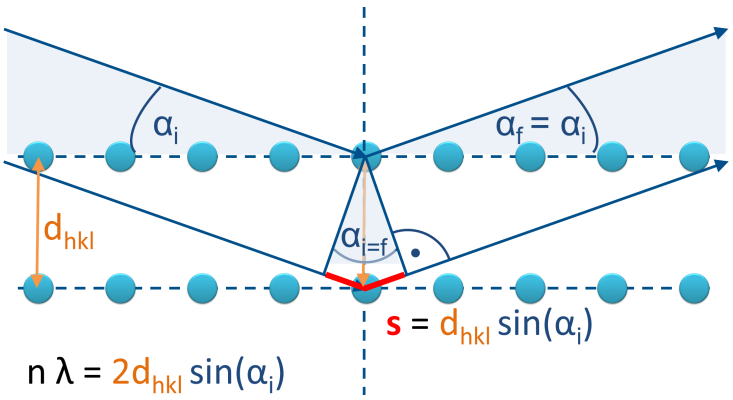

Figure 2.15: Sketch of the Bragg condition at a periodic crystal lattice of plane spacing d_{hkl}. The incident X-ray beam k_i impinges under the incident angle α_i and scatters (k_f)at the electron clouds of the atoms. The difference in path length $2s$ defines if the beam scatters constructive or destructive.

The polycrystalline, i.e. partially crystalline, films investigated in this thesis exhibit crystals, which have no preferred orientation in the sample plane, similar to powder diffraction. Figure 3.7a in chapter 3, section 3.3.3 shows a typical 2D GIWAXS image. From

the width of a scattering peak in the radial direction, the crystal size can be estimated by the Scherrer equation

$$D_{hkl} = \frac{K\,\lambda}{\Delta(2\,\theta)\,cos(\theta_0)} \tag{2.46}$$

with $K = 0.9$ the Scherrer form factor, $\Delta(2\,\theta)$ the full width at half maximum (FWHM) of the Bragg peak at θ_0.[57]

As polymer crystals exhibit an asymmetric conductivity, the orientation of the crystals within the films have a strong impact on the intragrain conductivity and hence also on the direction dependent film conductivity. As figure 3.6 in chapter 3, section 3.3.3 shows, the intensity distribution along one of the observed scattering rings provides information on the orientation of crystals, which cannot be observed in transmission geometry measurements or classical X-ray diffraction (XRD) measurements. A entirely random orientation of crystals leads to a uniform scattering ring in corrected 2D GIWAXS images (for the corrections see chapter 3, section 3.3.4). For crystal planes, which are oriented perpendicular to the substrate plane, the reflection that originated from the repeated stacking distance of these planes appears in the horizontal direction of the 2D patterns. Consequently, crystal planes, which are oriented parallel to the substrate plane, lead to reflection in the vertical direction of the 2D image. It is important to mention, that due to the fixed incident angle, the area where $q_x \approx 0$ and $q_y \approx 0$ is not measured. Hence, the raw 2D images have to be corrected as described in chapter 3, section 3.3.4. For a detailed description of the analysis of GIWAXS patterns in general, it is referred to chapter 3, section 3.3.3.

2.3.4 Resonant soft X-ray scattering

In soft X-ray scattering, the energy of the impinging X-ray beam is much lower than for hard X-rays and lies within the range of 50-2000 eV.[58] For these energies, no inelastic scattering occurs. Benefits of measuring with soft X-rays are the elemental and chemical sensitivity of this technique, allowing for contrast matching by the choice of measuring energy. Compared to hard X-ray investigations, the absorption of the investigated materials is much higher for interaction with soft X-rays. Therefore, the absorption has a strong contribution to the resulting scattering contrast in such experiments. The absorption is defined via the complex index of refraction and the definition of electromagnetic waves. The complex refractive index is given by:

$$n(E) = 1 - \delta(E) + i\,\beta(E) \quad \text{with} \quad E \in \mathbb{R}. \tag{2.47}$$

This leads to the description of the electromagnetic wave using the complex refractive index

$$\vec{E}(\vec{x},t) = \vec{E}_0 \mathrm{e}^{i\,(n\,\vec{k}\cdot\vec{x}-\omega\,t)} = \vec{E}_0 \mathrm{e}^{i\,((1-\delta(E)+i\,\beta(E))\,\vec{k}\cdot\vec{x}-\omega\,t)} = \vec{E}_0 \mathrm{e}^{-\beta(E)\,\vec{k}\cdot\vec{x}}\,\mathrm{e}^{i((1-\delta(E))\,\vec{k}\vec{x}-\omega\,t)} \quad (2.48)$$

with $\mathrm{e}^{-\beta(E)\,\vec{k}\cdot\vec{x}}$ describing the absorption and $\mathrm{e}^{i((1-\delta(E))\,\vec{k}\cdot\vec{x}-\omega\,t)}$ describing the extinction of the electromagnetic wave. Therefore, the imaginary part of the refractive index describes the absorption, which can be measured directly with soft X-ray near edge X-ray absorption fine structure (NEXAFS) spectroscopy. The imaginary part of the complex refractive index can further be linked to the real part by using the Kramers-Kronig relation. With the atomic scattering factor:

$$f(E) = f_\delta(E) - i\,f_\beta(E) \quad (2.49)$$

whereby

$$\delta(E) = a\,f_\delta(E), \quad \beta(E) = a\,f_\beta(E) \quad \text{and} \quad a = \frac{n_a\,r_e\,\lambda^2}{2\,\pi}, \quad (2.50)$$

the Kramers-Kronig relation is given by:

$$f_\delta(E) = Z - \frac{2}{\pi}\,P_c \int_0^\infty \frac{u}{u^2-\omega^2}\,f_\beta(u)\,du. \quad (2.51)$$

n_a is the atomic density, r_e the electron radius, λ the wavelength, Z is a constant factor, P_c is the Cauchy Principal Value, u the angular frequency as integrating variable and ω the angular frequency of the beam. The absorption of X-rays is given by

$$\bar{I}(E,\vec{r}) = \bar{I}_0\,\mathrm{e}\left(-\frac{4\,\pi\,\beta(E)}{\lambda}\right)\vec{r} \quad (2.52)$$

In this thesis, soft X-rays are used to investigate the inner film structure of the polymeric blend PEDOT:PSS, with a focus on the orientation of PSS molecules to the interface to PEDOT. The scattering contrast between the two materials is described by the difference in their dispersion and their absorption

$$\Delta\delta^2 + \Delta\beta^2 = (\delta_2-\delta_1)^2 + (\beta_2-\beta_1)^2\,, \quad (2.53)$$

where δ_1, δ_2 and β_1, β_2 are the dispersion and absorption of the two involved materials.[58] If the measurement energy is varied, the dispersion and the absorption show strong changes near the absorption edge of an atom, e.g. near 285 eV for carbon atoms. These changes can be described by a damped forced oscillator in a semi-classical model of atoms. If the natural frequency equals to the driving frequency, the amplitude of the oscillator exhibits a maximum amplitude. In the case of soft X-ray scattering, The X-ray energy is the

driving frequency, while the excitation of a core electron to an empty state is the natural frequency. Typically at the absorption edge of an atom the X-ray energy equals the excitation energy of the electron, which leads to the so-called resonant scattering as depicted in figure 2.16a. As the excitation depends not only on the atom but also on the bonds, which this atom has with neighboring atoms, e.g. in molecules. Hence, the absorption edge of elements within a molecule is not exactly found at the theoretical absorption edge of the atom but can differ slightly in energy.

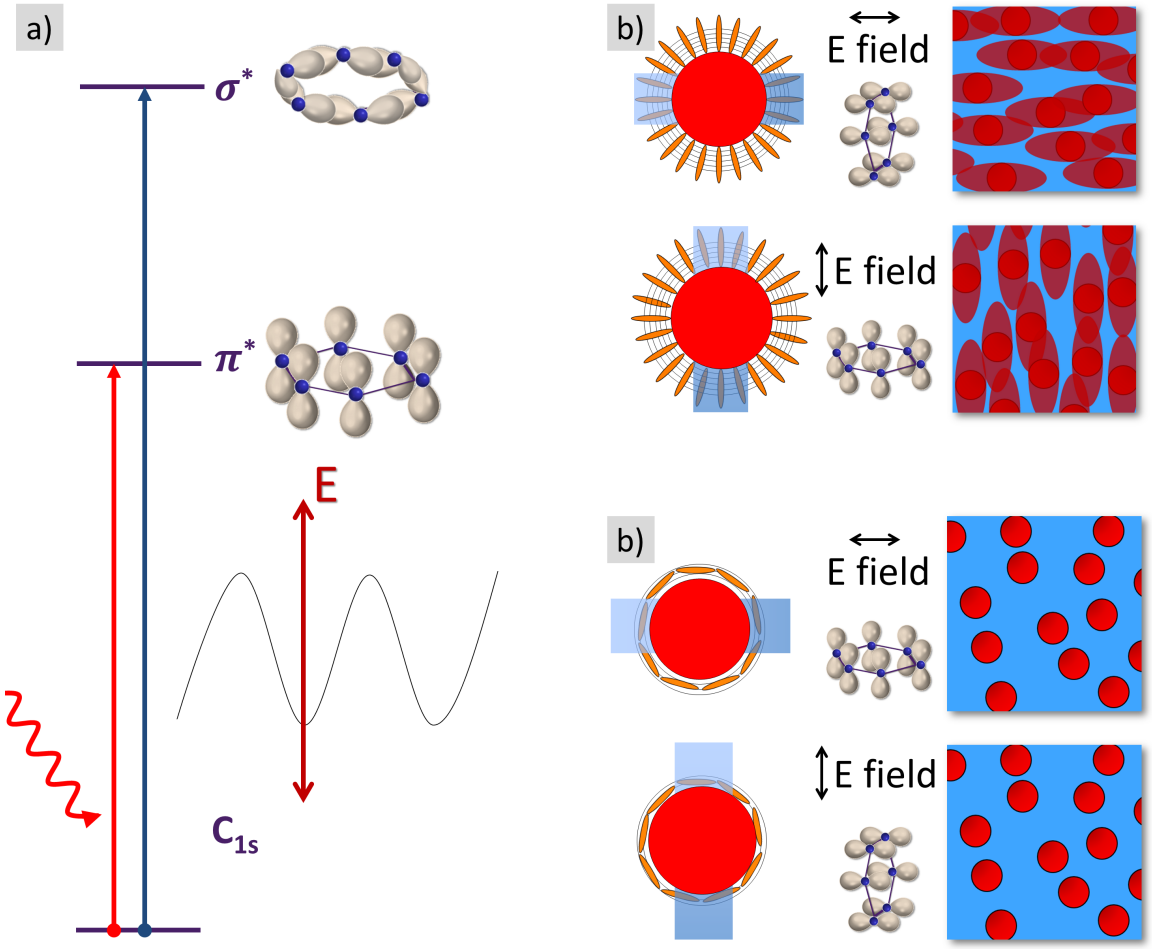

Figure 2.16: Schematic of resonant scattering with soft X-rays. In a) the resonant scattering is depicted with the excitation of core electrons to empty states. In b) and c) the influence of polarized electric fields on the contrast between two materials is depicted. In b) the contrast is smeared out since the electric field is oriented in the direction of the π-orbitals, which are excited as tiny dipoles. In c) the electric field is oriented perpendicular to the π-orbitals such that their excitation and with this the excitation of the tiny dipoles is prohibited. The 2D image illustrations in b) and c) are adapted from.[59]

In this thesis, thin films are investigated with polarized resonant soft X-ray scattering (PSoXS)in transmission geometry. The incident X-ray beam is thereby linear polarized, which can lead to anisotropic scattering in the 2D detector images. With this method, the orientation of molecules at the interface to domains of the other material can be revealed even for non-crystalline material domains. In figure 2.16b,c the situation for linearly polarized light at resonant energy is depicted. The red core depicts a material domain, whereas the orange bar-bells depict the π-orbitals of a benzene ring. The orbitals are excited as tiny dipoles if the linear polarized electric field is oriented parallel. If the orbitals are oriented parallel to the electric field at an interface of the material domain, the contrast in this direction is smeared out as depicted in the 2D sketch in figure 2.16b. In the case where the electric field is oriented perpendicular to the π-orbitals, the tiny dipoles are not excited, which leads to a strong contrast of the two materials as depicted in figure 2.16c. In total, linear polarized soft X-ray scattering can thereby reveal molecular orientation at interfaces for non-crystalline material by analysis of anisotropic scattering at resonant energy as shown in chapter 6, section 6.2.2.

Chapter 3

Characterization Methods

This chapter presents the methods that were used to characterize the spectroscopic and electronic properties of the investigated organic thin films (section 3.1). Further, various techniques that provide information on the film surface structure (section 3.2) and the film volume structure (section 3.3) are explained in detail. For all methods, the instrument specifications and working principles are given. Whenever meaningful, details on the data evaluation are included.
Section 3.1 includes the method of UV-Vis spectroscopy (section 3.1.1) which is used for investigation of the spectroscopic properties of materials, current-voltage characterization (section 3.1.2) for evaluating the performance of photovoltaic devices and the four point probe technique (section 3.1.3), which allows for electronic characterization of the film resistance and conductivity. Section 3.2 gives details on structure characterization methods for investigation of the film surface. These include profilometry (section 3.2.1) for determination of the film thickness as well as scanning electron microscopy (section 3.2.2), which is used to image the surface structure of the thin films in real space. Section 3.3 then provides detailed information on scattering techniques, which provide information on the structure of the measured film volume in reciprocal space. X-ray reflectivity (section 3.3.1) is used to determine the film thickness with high precision and to obtain information on the vertical composition of the thin films. In contrast, grazing incidence small angle X-ray scattering (section 3.3.2) provides information on the lateral structure inside the film volume on the mesoscale. For investigating the crystals within the thin films, grazing incidence wide angle X-ray scattering (section 3.3.3) is used to resolve structures on the scale of molecular distances. For this method, several important corrections apply to the obtained reciprocal images. As these corrections experience increasing attention within the field of scattering investigations for organic thin films, a special focus is put on these corrections in section 3.3.4. Finally polarized resonant soft X-ray scattering (section 3.3.5) is a scattering method, which is used to increase the contrast between two

materials present in the same film and to probe the orientation of molecules at domain and material interfaces.

3.1 Spectroscopic and electronic characterization

For the application of conducting organic thin films, the spectroscopic and electronic properties of the films need to be understood and hence investigated. Therefore, spectroscopic properties such as the film absorption and transmission are investigated for PEDOT:PSS and active layer thin films. The performance of photovoltaic devices is characterized in detail to provide insight to the complex processes of charge carrier generation, transport and recombination. In particular for the application of polymeric electrodes such as PEDOT:PSS, the electronic characterization of the film resistance and conductivity plays a crucial role.

3.1.1 UV-Vis spectroscopy

With the absorption of light, i.e. photons, electrons within the molecules of the measured organic thin film are excited to respective electronic, vibrational and rotational states. This provides the possibility to extract detailed information about the energetic levels of materials. Spectroscopic analysis of the samples is performed using two different UV-Vis spectrometers. Both instruments are supplied by *Perkin Elmer* and measure the light spectrum from unltraviolet (UV) to near infrared (IR). To cover this range, two lamps are used: a tungsten halogen lamp for the near infrared to visible range and a deuterium lamp for the UV range of the incoming light. In this thesis, the instruments are used in the transmission mode to measure the transmitted intensity using a photodiode as the detector. Hence, the films are fabricated and measured on glass substrates with the glass substrate taken as a reference. The first instrument is a Lambda 35 with a spectral range from 190 nm to 1100 nm with a lamp change at 326 nm, a measuring rate of 120 nm/min and slits of 1 nm. The transmission is measured here along the beam path which neglects the diffracted and reflected light from the surface and interfaces. Hence with this setup only films are measured which have a low reflection and diffraction. The contribution of the glass substrate is measured by a reference beam which is split from the measurement beam such that only the contribution of the thin film remains. The second instrument is a Lambda 650 with a spectral range from 250 nm to 950 nm with a lamp change at 319.3 nm, a measuring rate of 266.75 nm/min and slots of 2 nm. The important advantage of this instrument is the integrating sphere of 150 mm in diameter which allows to account for reflection and diffraction contribution at the film surface or at interfaces. Placing the sam-

ple before the sphere, the transmission is measured including the diffracted light while placing the sample after the sphere, the reflection from the film surface and from interfaces is measured. In combination, the complete spectral information of the film in the measured range is accessible. The contribution of the glass is measured prior to the thin film measurement. Choosing the so-called autozero calibration, before measuring the thin film, only the contribution of the thin film remains.

The fraction of absorbed light dI after passing the thin film of a thickness dx is given by

$$dI \;=\; -\alpha\, I\, dx. \tag{3.1}$$

Integrating this equation from $x = 0$ to $x = d$ with d the film thickness, the Lambert-Beer law is obtained with α being the absorption coefficient. The Lambert Beer law reads as follows:

$$I \;=\; I_0\, \mathrm{e}^{-\alpha d} \tag{3.2}$$

After measuring the transmission of the thin films, the absorbance of the thin film is given by:

$$A(\lambda) \;=\; \alpha(\lambda)\, d\, log_{10}\mathrm{e} \;=\; 2 - log_{10}\, I_T(\lambda) \;=\; -log_{10}\left(\frac{I_T}{I_0}\right) \;=\; -log_{10}T(\lambda) \tag{3.3}$$

Therein, I_0 is the incident light intensity, I_T is the transmitted light intensity and the transmission $T(\lambda)$. From this, the absorption coefficient α relates to the measured intensity of the transmission and the absorption as follows:

$$\alpha(\lambda) \;=\; \frac{2 - log_{10}\, I_T(\lambda)}{d\, log_{10}\mathrm{e}} \;=\; \frac{A(\lambda)}{d\, log_{10}\mathrm{e}} \tag{3.4}$$

From the equation it is clear, that $\alpha(\lambda)$ is a parameter which contains solely information of optical properties. Further it is a parameter which is normalized to the film thickness of the investigated materials and thereby provides good comparability between different measured films.

3.1.2 Current-voltage characterization

To measure the current-voltage (I-V) characteristic of photovoltaic devices, in this thesis the solar simulator Solar Constant 1200 from *K. H. Steuernagel Lichttechnik GmbH* is used. The solar simulator is based on a metal halogen lamp as the light source and a reflector system with parabolic reflectors and integrated borosilicate diffusor. In combination, this provides a good resembling of the 1.5 AM spectrum and a homogeneous illumination on a large area. Further, the spectra is cut by the diffusor at 290 nm. Before measuring

the photovoltaic devices, the halogen lamp is heated up for 1 h such that the condition, i.e. the intensity of the light source, remains constant within measurement series. For the calibration of the setup, i.e. the lamp intensity, the WPVS-ID3 calibration cell from the *Fraunhofer ISE* is used to tune the intensity such that it resembles the AM 1.5 spectrum with 1000 $\mathrm{W/m^2}$. The lamp-sample distance is kept at 32 cm for all measurements. Further, during the illumination of an individual pixel a mask slightly larger than the active area of the individually measured solar cell (so-called pixel), is used. Thereby the other solar cells (pixels) are kept in dark. The I-V characteristic is measured by applying a voltage to the device and measuring the current given by the device. After applying the voltage for the first time, a 0.1 s delay is programmed before the voltage is scanned from −1 V to 1 V with voltage steps of 0.002 V to 0.01 V using a Keithley 2400. The current is tracked depending on the applied voltage using the *LabView* based software Testpoint V6 (CEC Capital Equipment). The software allows further to program an integrated loop for degradation studies. The setup can be equipped additionally for angular dependent measurements with a measurement holder fixed to an axis containing a degree scale. It is noted that for the angular dependent measurements no sample mask is used.

Data analysis

From the measured IV curve, the performance of the photovoltaic device is characterized using typical parameters such as the short-current density at $V = 0$ (I_{sc}), the open-circuit voltage at $I = 0$ (V_{oc}), the fill factor (FF), the serial resistance at $I = 0$ (R_s) and the shunt resistance at $V = 0$ ($R_{sh}(R_s)$, also referred to as $R_p(R_s)$), which all have an impact on the resulting efficiency η. The efficiency is directly related to the maximum power point (MPP), where the power density $P = I\,V$ is maximized (P_{max}). At this point a photovoltaic device generates its maximum output. Therefore, a photovoltaic device is operated at the voltage of the MPP. In idealized photovoltaic devices, the MPP equals $P_{ideal} = V_{oc}\,I_{sc}$. In realistic devices the ratio between the maximal power density at the MPP (P_{max}) and the ideal power density (P_{ideal}) is the FF of the device given by

$$FF = \frac{P_{max}}{P_{ideal}} = \frac{V_{MPP}\,I_{MPP}}{V_{oc}\,I_{sc}} \tag{3.5}$$

With the FF, the efficiency η is given by

$$\eta = \frac{P_{out}}{P_{in}} = \frac{P_{max}}{P_{in}} = \frac{V_{MPP}\,I_{MPP}}{P_{in}} = FF\,\frac{V_{oc}\,I_{sc}}{P_{in}} \tag{3.6}$$

with $P_{out} = P_{max}$ and $P_{in}(AM\ 1.5) = 1000\,\mathrm{W/m^2}$.

A good measure for the diode behavior of a photovoltaic device are R_s and $R_{sh}(R_s)$. For an optimized device of high efficiency, the R_s is maximized (equal to a minimized slope)

and $R_{sh}(R_s)$ is maximized (equal to a minimized slope). R_s and $R_{sh}(R_s)$ are given by

$$R_s = \left(\frac{dI}{dV}\right)^{-1}_{V=V_{oc}} \tag{3.7}$$

and

$$R_{sh}(R_s) = \left(\frac{dI}{dV}\right)^{-1}_{V=0} - R_s \tag{3.8}$$

More information on the theory of photovoltaic devices is given in chapter 2, section 2.2.

3.1.3 Four point probe measurements

The sheet resistance was measured free of contact resistance with the four-point-probe setup Cascade Microtech (C4S-54/5). It consists of four equally spaced (1 mm) tungsten carbide test probes with radii of 125 μm and a weight of 40 g to 70 g. The current is applied at the outer two tips and the voltage drop is recorded between the inner two tips. By this, the sheet resistance is extracted from the current voltage characteristic. The setup is schematically shown in figure 3.1. The contacting tips are equipped with a spring such that the tips do not penetrate in to the film.

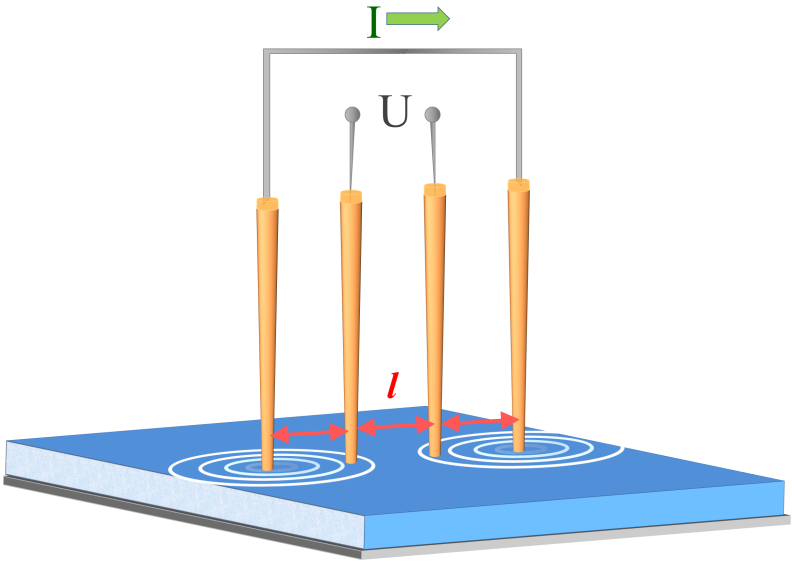

Figure 3.1: Schematic of a four point probe setup. The distance between the tips is constant. For sheet resistance measurements, a current is applied at the outer two tips which leads to a continuous potential drop along the direction of measurement. The potential drop is measured at the inner two tips as a function of the applied current.

The conductivity σ for a sample of any shape is given by

$$\sigma = \frac{1}{\rho} = \frac{I}{V}\frac{1}{2\,\pi\,l\,F} \tag{3.9}$$

with ρ the resistivity, l the distance between the contacting tips and F the correction factor for finite sample thicknesses. For the investigated samples in this thesis the film thickness d is much lower than the distance between the tips l, $d << l$. Therefore the sheet resistance of the sample is given by

$$R_{\square} = \frac{1}{\sigma\, d} = \frac{\rho}{d} = \frac{V}{I}\frac{\pi\, d}{ln(2)} \tag{3.10}$$

The sheet resistance is independent of the film thickness and thereby is a parameter, which is often used to compare films. It has a unit of $1\,\Omega/^2$, a dimension which is equal to $1\,\Omega$, i.e. the resistance through a square ($\square$) of any size perpendicular to the current flow has a resistance of $1\,\Omega$. Thereby, the $\square$ indicates that the given value is not a bulk material value.
In the field of organic electronics, often the sheet resistance of a material $R_{\square}$ is related to its transmission $T(\lambda)$ according to

$$T(\lambda) = \left(1 + \frac{188.5}{R_{\square}}\frac{\sigma_{op}(\lambda)}{\sigma_{dc}}\right)^{-2} \tag{3.11}$$

As the optical and direct current are not directly measurable, $\frac{\sigma_{op}(\lambda)}{\sigma_{dc}}$ is taken as a figure of merit for the quality of a transparent electrode, i.e. a transparent conducting thin organic film such as PEDOT:PSS.

3.2 Structural characterization of film surface

For thin films, acting as active layers, polymeric electrodes or interface layers in organic photovoltaic devices, the film thickness as well as the vertical film composition, e.g. enrichment layers, are important to obtain optimized devices without high energetic losses. Further, the structure of the film surface and the film volume can differ depending on the system. The surface structure is investigated using real space imaging tools.

3.2.1 Profilometry

The thickness of organic thin films in this thesis is measured by a profilometer as well as by XRR (see section 3.3.1). The profilometer instrument was a DEKTAK 150 surface profiler by *Veeco instruments Inc.* located at the cleanroom of the *Zentrum für Nanotechnology und Nanomaterialien* (ZNN) of the TU Munich. Profilometers are used to determine the thickness and the roughness of materials on a nanometer scale. In this thesis, it is used to determine the rough thickness of organic thin films. The instrument consists of three main components: a sample stage for high precision, a diamond tipped stylus of

12.5 μm in radius as the scanning cantilever and a linear variable differential transformer (LVDT) for moving the sample below the measurement cantilever. For measuring an organic thin film, the thin film is scratched using the edge of a cleaned tweezers such that the bare substrate is exposed. After placing the sample on the sample stage, it is moved below the stylus cantilever by applying a constant force onto the sample. The measured lateral deflection of the stylus is converted to a digital signal with the help of the LVDT. Thereby the resolution of the profilometer theoretically is 1 nm. The thickness is measured perpendicular to the scratch by scanning the vertical drop. For estimating a measurement error, the measurement is repeated at three different spots on the same sample. For all measurements the contact force of the stylus was set to 1 mg. Profilometry is widely used in literature to determine the thickness of organic thin films such as PEDOT:PSS. As the organic thin films measured in this thesis are rather soft, there is a certain risk to scratch the thin film during the measurements with the stylus. Hence, the thicknesses obtained with this method for such films are typically 10 nm to 20 nm lower than the actual film thickness (for an example see section 5.2.1). Therefore, additionally the thickness of thin polymeric films is obtained by the non-destructive and precise XRR technique (section 3.3.1).

3.2.2 Scanning electron microscopy

The surface structure of the investigated thin films was investigated with high resolution of 1 nm to 10 nm using scanning electron microscopes. Within this thesis two instruments of the same kind were used, the FESEM Gemini N-Vision 40 SEM and the Ultra 55 SEM by *Carl Zeiss*. This technique enables to investigate the surface of a thin film with high resolution and high depth of field. In contrast to optical microscopes where light waves are used for imaging, SEM uses electrons which have a much smaller wavelength and thereby enable a higher resolution of the obtained images. Further, the resolution can be adjusted by the acceleration voltage as the wavelength of the electrons depends on the applied acceleration voltage. The electrons are generated by field emission before they are accelerated by a voltage of several kV and focused on the sample surface by electromagnetic lenses. The electrons which hit the sample surface are either scattered back from the sample or secondary electrons are generated. The sample under investigation is scanned line by line while an InLense detector measures the secondary electrons released from the sample. The detected signal is then converted to a grey-scale image where the brightness depends on the height, inclination and conductivity of the probed material. Higher positions on the sample e.g. appear brighter in the detected image due to the shorter working distance. In the case of a two material system with materials of different conductivity, SEM enables to get a contrast between the two materials. When secondary

electrons are released from a material of low conductivity, the material charges up and further release of secondary electrons is hindered. The material thereby appears darker than more conductive materials. For all measurements shown in this thesis, an acceleration voltage of 1.5 kV to 2.0 kV and a working distance, i.e. the source-sample distance, of 1.0 mm to 1.5 mm is used. Further, the gun vacuum was in the order of 10^{-9} mbar and the system vacuum in the order of 10^{-6} mbar.
For the evaluation of the SEM images, the *ImageJ* software (by Wayne Rasband, National Institutes of Health, USA) was used to adjust the contrast and the brightness of the image. Further, the image can be Fourier transformed to reciprocal space where the power spectral density (PSD) is obtained by radial integration of the transformed image. The PSD gives information on the surface structure of the films which can then be compared to the volume structures obtained by GISAXS measurements. An example for this comparison is shown in section 5.2.3 and 5.2.4.

3.3 Structural characterization of film volume

> Parts of this section are based on the manuscript *Controlled morphologies by molecular design and nano-imprint lithography*, T. Pfadler, C. M. Palumbiny, Wojciech Pisula, Holger Hesse, Xinliang Feng, Klaus Müllen, Peter Müller-Buschbaum, Lukas Schmidt-Mende, which has been submitted for the final report of the DFG program SPP1355 as a book chapter in *Advances in Polymer Science*, Springer (in press).

To understand the self-assembly and spontaneous self-organization of conjugated molecules dedicated analytical techniques are required. In particular, it is challenging to detect the complex morphologies, which are crucial for organic solar cells. Structures need to be detected from the crystalline arrangement of the molecules to mesoscopic domain sizes, because conductivity is driven by the crystalline parts and the morphology is strongly linked to the device performance. Scattering experiments using X-rays have proven to be well suited for this task as they provide information of the structure within the film volume from a molecular to a mesoscopic scale. Since the devices make use of a thin-film geometry, which limits the scattering volume for measurements in transmission geometry, the use of a reflection geometry turned out to be beneficial for such investigations. The successfully applied X-ray scattering techniques used in this thesis are X-ray reflectivity (XRR), grazing incidence wide angle X-ray scattering (GIWAXS) and grazing incidence small angle X-ray scattering (GISAXS). With the GIWAXS technique the crystalline parts of the films are addressed. The orientation of molecules and polymer chains in the crystalline

domains with respect to the interfaces given by the electrodes is accessible. In addition, information about the size of the crystalline domains can be obtained. Conductivity in polymer crystals is typically anisotropic and strongly depends on the orientation of the crystalline domains in the film volume and is thus of fundamental importance for the understanding of the current flow in the device. Last but not least scattering investigations are not only performed using hard X-rays but also using polarized soft X-rays scattering (P-SoXS). With measurement energies typically below 2 keV the incidence photons are in the range of electronic transitions in atoms. This makes the technique tunable to specific bond types and thereby chemical sensitive. P-SoXS provides the possibility of contrast matching by the choice of measurement energy to detect lateral structure information and molecular orientation at interfaces.

3.3.1 X-ray reflectivity

The principle geometry that is used in scattering techniques to investigate the vertical and the lateral structure of a thin film in reflection geometry is shown in figure 3.2a. The incident beam k_i impinges onto the sample where it is reflected and diffracted. The reflection and diffraction depends on the nature of the material system from which the beam is scattered. In order to probe the vertical structure of a thin film, X-ray reflectivity (XRR) is used where the specular scattering q_z is measured as a function of the incident angle α_i on the condition that the incident angle equals the exit angle. The intensity of the reflection is measured with a point detector resulting in reflectivity curves such as shown in figure 3.2b. From the Kiessig fringes the film thickness can be determined and using refractive indices and related thicknesses, simulation of the data yields information on the vertical film composition.[60–62]

The XRR measurements presented in this thesis are carried out at a Bruker D8 ADVANCE diffractometer which is operated at room temperature. During the measurements the sample remains at a fixed position while the detector is rotated along with the source such that the condition for specular reflection is maintained (reflected angle equal to incident angle, $\alpha_i = \alpha_f$). The X-ray source of the diffractometer is a Cu-K_α line ($\lambda = 0.1541\,\mathrm{nm}$) provided by a copper X-ray tube. The X-ray beam is defined by a Goebel mirror, which monochromizes and focuses the beam. Further, slits between the source and the sample define the beam size and a tantalum knife edge at the sample position prevents over-illumination of the sample at small incident angles. Hence no footprint correction of the detected intensity is necessary. Further, absorbers are used to avoid saturation of the detector. The reflected photons are detected using a point detector. The organic thin films

are either prepared on silicon or glass substrates of at least 1 cm by 1 cm. For extracting the vertical film composition, the reflectivity curves are measured up to 10 ° with a typical data acquisition time of 8 h to 12 h depending on the resolution aimed for. This allows to fit the reflectivity using the software package *Motofit*[63] for *IGOR Pro* (by *WaveMetrics, Inc.*). Thereby the data is fitted with multilayers, taking their thickness, scattering length density (SLD), layer roughness and complex refractive index into account. The SLD profile versus the distance from the interface resembles the vertical film composition. For the purpose of pure thickness determination, reflectivity measurements with a lower angular range are sufficient shortening the data acquisition time to 3 h to 4 h. Figure 3.2b shows the reflectivity curve of a PEDOT:PSS thin film measured on glass. The PEDOT, PSS as well as the glass critical edges are highlighted by vertical lines. Further, the distance between two minimum Δq_z is used for film thickness determination and is highlighted in orange in figure 3.2b.

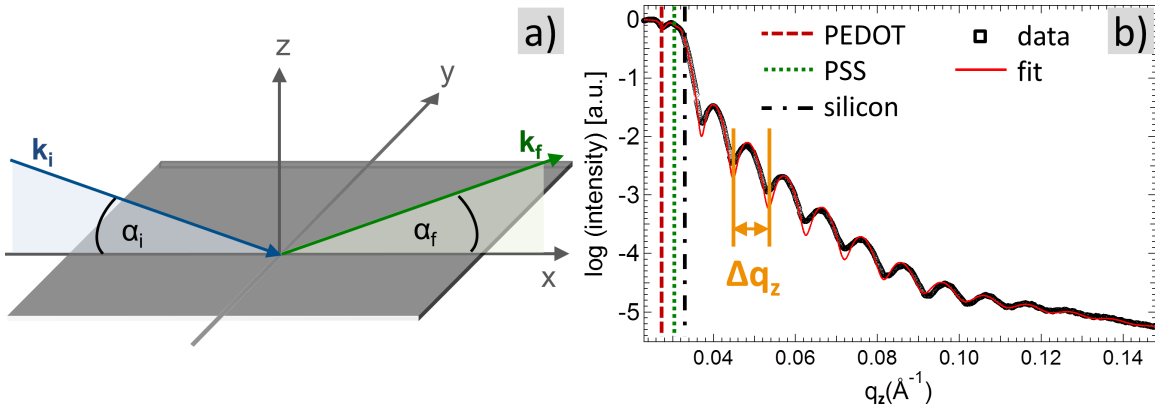

Figure 3.2: a) Principle scattering setup in reflection geometry with incident and exiting beam defined by k_i and k_f, respectively. The incident angle α_i and exit angle α_f lie in the scattering plane. b) Calculated reflectivity curve of a polystyrene (PS) film on a silicon substrate. The critical q_z values of PS and glass are highlighted. The distance between the minima of the Kiessig fringes is Δq_z.

3.3.2 Grazing incidence small angle X-ray scattering

For the application of polymeric or small molecule thin films in photovoltaic devices not only the vertical but also the lateral structures are of great importance. This holds for the structure in active layer blends where the exciton diffusion and separation strongly depends on the lateral structure as well as for polymeric electrodes where the lateral structure strongly determines the charge transport and film conductivity. Grazing incidence small angle X-ray scattering (GISAXS) is a non-destructive measurement technique that provides lateral structure information from the film volume with good statistics. In

grazing incidence geometry, the beam impinges onto the sample under a shallow angle. After the photons interact with the material probed, they are scattered elastically from the film volume. In contrast to XRR, in GISAXS the off-specular scattering is analyzed instead of the specular reflection which is blocked by a beamstop. As figure 3.3 shows, depending on the distance between the sample and the detector, different angles of the scattered beams are detected and with this different length scales of structures in the film. Small angle scattering provides information on structure sizes in the range of several nanometers to micrometers whereas wide angle scattering provides information on the size of molecular stacking distances. For further information on wide angle scattering, it is referred to section 3.3.3. In the following, small angle scattering, its experimental details and data analysis is describes.

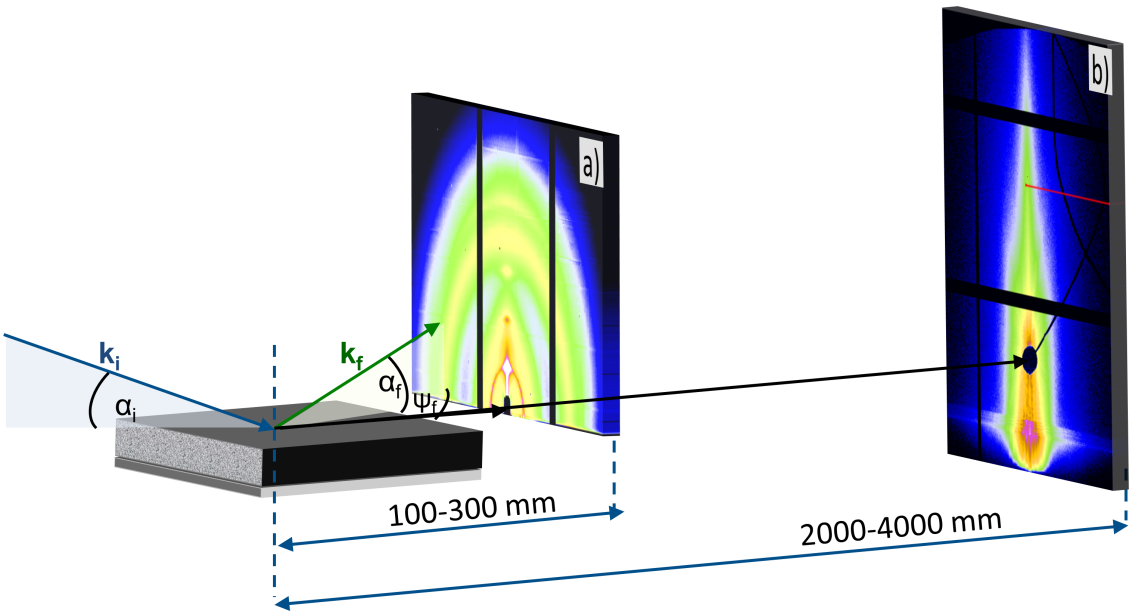

Figure 3.3: Schematic view of a grazing incidence small/wide angle X-ray scattering setup. The X-ray beam (blue line) impinges under a small incident angle (below 1°) onto the sample. The incident angle α_i and exit angle α_f lie in the scattering plane, the out-of plane angle ψ_f in the sample plane. After interaction of the incident beam with the sample, a 2D-detector records the scattered intensity. The sample-detector distance defines the resolvable length scales, e.g. for $SDD = 10\,\text{cm}$ molecular structures (GIWAXS) and for and $SDD = 2\,\text{m}$ mesoscopic structures (GISAXS) are resolved.

Experimental details

In the framework of this thesis, GISAXS experiments are performed at two synchrotron beamlines, the beamline P03 of the Deutsches Elektronen Synchrotron (DESY) in Hamburg, Germany and at the beamline 7.3.3. of the Advanced Light Source (ALS) of the

Lawrence Berkeley National Laboratory (LBNL) in Berkeley, USA. The beamline energies were slightly different with 12.6 keV to 13.3 keV at the P03 beamline (DESY) and 10 keV at the 7.3.3. beamline (ALS). Further, the beam size at the two beamlines is different. The P03 beamline (DESY) has a micro-focused beam size which is focused to a beam size of 22 μm in width and 12 μm in height at the sample position by an assembly of beryllium compound refractive lenses. The 7.3.3. (ALS) beamline has a beamsize of 30 μm in width and 50 μm in height. The beam size influences the probed volume of the measured film and thereby the data acquisition time. For GISAXS measurements, incident angles of 0.35 ° and above were used which is above the critical angle of the probed material and hence assures full penetration of the thin film. Further, for these incident angles, the footprint does not exceed the sample size. For the GISAXS experiments performed at both beamlines typical sample-detector distances (SDD) between 2 m and 4 m were used. The exact SDD of ascertained experiments are given in the corresponding chapters. For detecting the scattered photons from the measured thin film, two detector sizes are used within the thesis, namely the Pilatus 300k and 1M detector by the supplier *Dectris*. Both detectors are identical in their constitution and are distinguished by their different total area. The 1M detector has a total size of 981 px x 1043 px whereas the 300k has a total size of 487 px x 619 px. The Pilatus 300k and 1M are noise free detectors consisting of several modules with blind areas in between, the so-called inter detector or inter module gaps. The pixel sizes are 172 μm x 172 μm for both detector types. Owing to the absence of a noise and the fast readout time of 5 μs for this single photon counting detector, kinetic measurements as shown in chapter 7 are possible. The scattered photons are recorded by the detector with the amount of photons presented by intensities using a false color code. Further to avoid damage of the detector, the direct beam as well as the specular beam were blocked by beamstops.

Data evaluation

Figure 3.4a exemplary shows the 2D scattering pattern of a nanostructured P3HT:PCBM bilayer thin film. These 2D scattering pattern, vertical cuts such as shown in 3.4b provide information about the vertical film structure relative to the sample plane, e.g. the correlated roughness.[64] In this thesis, mainly horizontal cuts of the 2D scattering pattern are performed, such as depicted in figure3.4c. These profiles are typically performed at the Yoneda peak position of the investigated material and enables to extract quantitative information on the lateral structure of the measured thin film. For the evaluation of the data, the *Fit2D* software (by Andy Hammersley, 1987-2005, ESRF, Grenoble), the *DPDAK* program (by Gunthard Benecke, DESY Hamburg & MPIKG Potsdam) or the *NIKA* package[65] for *IGOR Pro* (by *WaveMetrics, Inc.*) is used. The latter two are

used in particular for batch processing of a large number of individual measurements, e.g. in-situ measurement. The horizontal line profiles are fitted to extract quantitative information on the lateral structures in the volume of the film. The custom-made model which is used to fit the scattering profiles, is based on a mathematical approach neglecting possible correlations between the interfaces (local monodisperse approximation). The extracted length scales are a good approximation of the lateral structure in the film volume of the system. The model is based on a 1d paracrystalline model in the framework of the local monodisperse and the distorted wave Born approximation (see section 2.3.3). The model considers the geometry and mean radii of the scattering objects by a form factor of cylindrical or spherical geometry following a Gaussian distribution. Further, the mean distance of the scattering objects is taken into account by the corresponding structure factors. The number of form and corresponding structure factors depends on the probed sample and the probed range of the out of plane scattering. Within this thesis, typically two to three form and structure factors are used to fit the scattering profiles. For scattering contributions in the horizontal direction near $q_y = 0\,\mathrm{nm}$, a Lorentzian resolution function takes the resolution of the experimental setup into account.

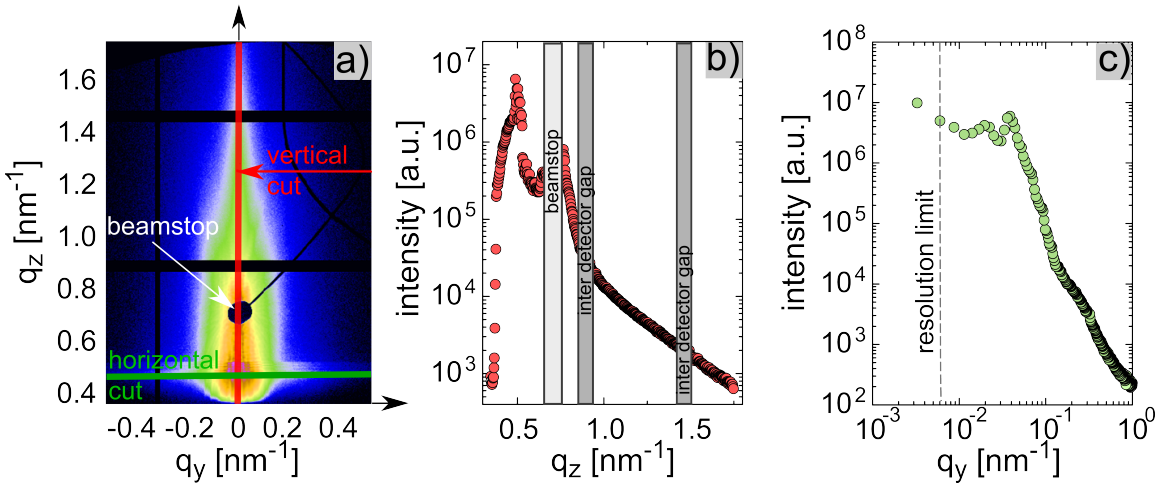

Figure 3.4: a) Exemplary 2D GISAXS data showing the relevant positions for typical analysis. b) Vertical cut which is depicted in a) in red. c) Horizontal cut which is depicted in a) in green.

3.3.3 Grazing incidence wide angle X-ray scattering

The charge transport and conductivity in polymeric systems is strongly correlated to the crystallization of the materials. Further the conductivity through a polymer is anisotropic with the best conductivity along the backbone, good conductivity along the $\pi-\pi$-stacking

direction and low conductivity along the side chains. In active layers and selective interface layers of OPV devices, the vertical conductivity is decisive. For polymeric electrodes, as investigated in this thesis, a good lateral conductivity is required. In such organic thin films, not only the intramolecular conductivity along a polymer chain is important but also the intermolecular conductivity between polymer chains within one crystal grain is important.[66] Hence, within this thesis the molecular orientation of crystals will be investigated in detail. To obtain this information, grazing incidence wide angle X-ray scattering (GIWAXS) is used to investigate the molecular stacking distances[66–70], crystal orientations[6,71,72] and the lower limit of crystal sizes[66,67,70,71,73–75]. A schematic of the principle setup is depicted in figure 3.3, section 3.3.2.

In figure 3.5 the two distinguishable polymer crystal orientations are exemplary shown for the polymer poly(3,4-ethylene-dioxythiophene) (PEDOT). The stacking distances are repeated within a crystal and hence result in diffraction peaks in the 2D image. In the figure, the $\pi-\pi$-stacking distance of the polymer crystal is marked as a and the side-chain stacking as b.

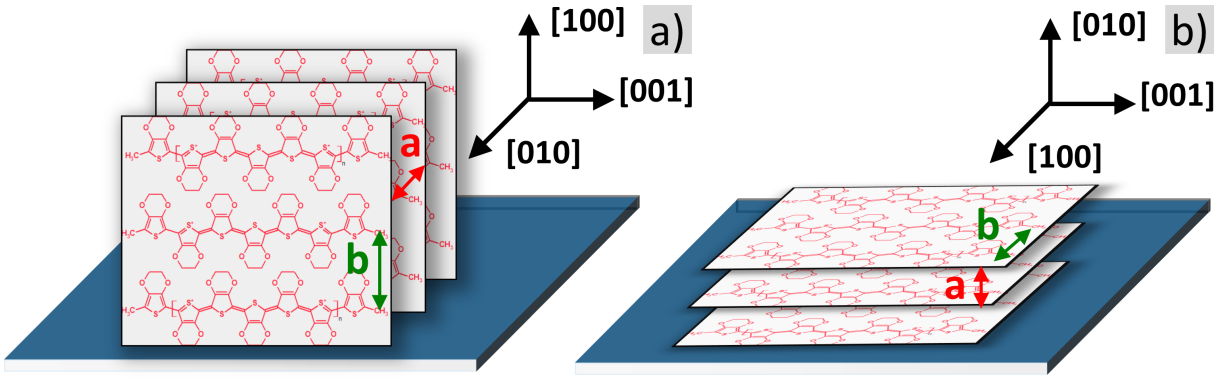

Figure 3.5: Schematic representation of PEDOT crystals in a) edge-on and b) face-on orientation with respect to the substrate. The lattice constants a and b as well as the crystal directions [100], [010] and [001] are depicted.

Small stacking distances within crystals result in diffraction peaks further away from the center of a 2D GIWAXS image, where a beam stop blocks direct beam, specular beam and most of the GISAXS signal. Consequently, large stacking distances correspond to diffraction peaks closer to the specular reflection. Figure 3.6a schematically shows the 2D diffraction pattern of crystals with full rotational disorder. According to the rotational disorder the diffraction peaks are widened and appear as semicircles in the 2D pattern. The semicircles correspond to the stacking distance of the crystal planes and

the higher interference orders of the same stacking distance. Scattering from crystals with preferred vertical or horizontal lamella stacking, leads to diffraction peaks in the vertical or horizontal plane, respectively. Both situations are depicted in figure 3.5b and c, respectively.

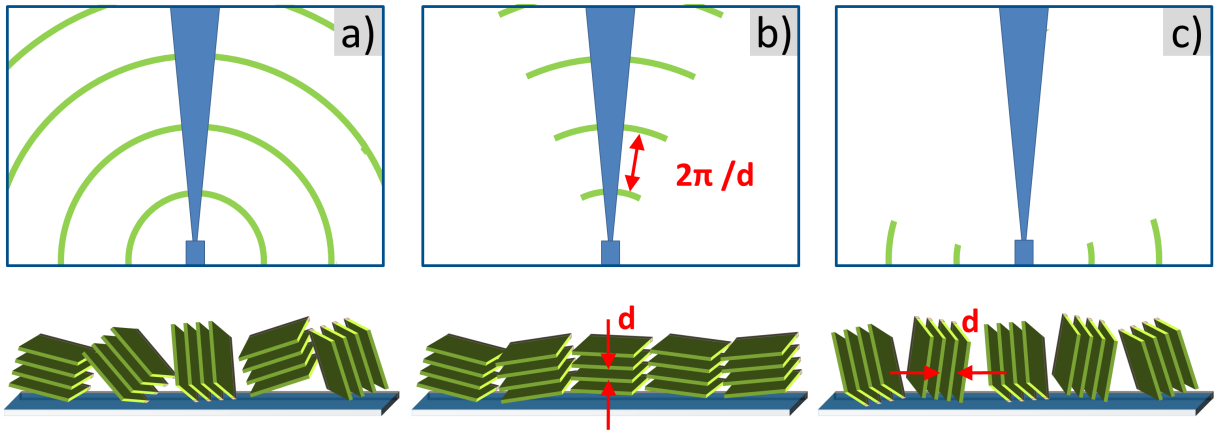

Figure 3.6: Sketch of film crystallinity and corresponding 2D GIWAXS data in case of a) full rotational disorder of crystallites, b) vertical lamella stacking and c) horizontal lamella stacking.

Experimental details

The molecular resolution in GIWAXS experiments of typically 0.2 nm to 6 nm is achieved with sample-detector distances of 100 mm to 300 mm. The GISAXS signal is typically blocked with a beam stop which is seen in the center of the diffraction circles of figure 3.7. By choosing the incident angle between the critical angle of the sample and the one of the substrate, scattering from the substrate material is prevented and no correction for the substrate scattering contribution is needed. However, as discussed in the following section (section 3.3.4), several corrections apply to the pristine 2D scattering pattern. As discussed in the previous section, two beamlines are used in the framework of this thesis, namely the beamline P03 of the Deutsches Electronen Synchrotron (DESY) in Hamburg, Germany and at the beamline 7.3.3. of the Advanced Light Source (ALS) of the Lawrence Berkeley National Laboratory (LBNL) in Berkeley, USA. For the beamline and detector specifications it is referred to the experimental detail paragraph of section 3.3.2.

Data evaluation

To extract structural length scales present in the volume of the measured film, sector and azimuthal integrals are taken as depicted in figure 3.7a, where the 2D scattering pattern of a PEDOT:PSS thin film is exemplary shown. The sector integral from 75 °-85 ° (figure 3.7) shows a strong scattering at 0.35 Å, which is attributed to vertical layering

within the PEDOT:PSS films (see the strong reflection in the vertical direction). The two following Bragg reflections originate from the $\pi - \pi$ stacking of PSS (1.3 Å) and $\pi - \pi$ stacking of the PEDOT (1.8 Å) crystallites in the film volume. From the scattering position, the lattice constant of the crystal in the corresponding direction can be estimated while from the full width half maximum (FWHM) of the reflection the lower limit of the crystal size can be estimated. Further, the intensity ratio of the horizontal sector integral (figure 3.7b) and a sector integral in the most vertical direction, e.g. 10 °-20 °, provides information on the main orientation of the polymer crystallites in the film volume. When comparing measurements under different incident angles, the recorded intensities need to be calibrated for footprints exceeding the sample size as well as for footprints smaller than the sample size. For details, it is referred to section 7.1.2, where this effect is shown for incident angle dependent GIWAXS measurements of PEDOT:PSS thin films.

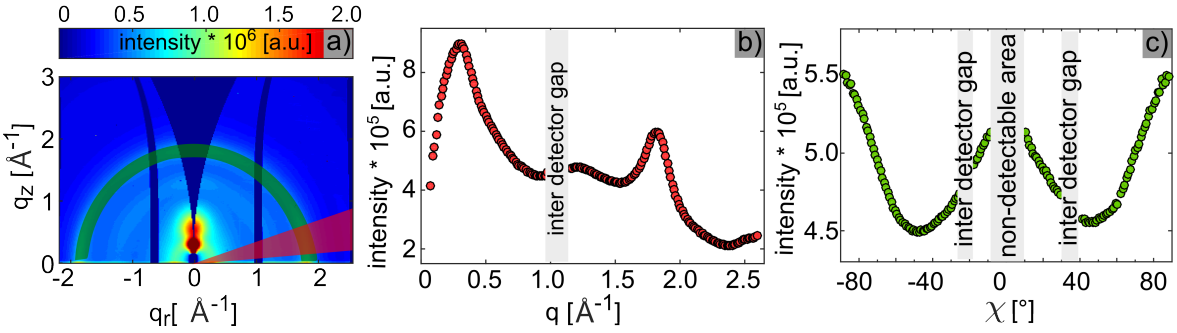

Figure 3.7: a) Exemplary 2D GIWAXS data of a PEDOT:PSS thin film. The GISAXS signal is blocked by a beam stop close to $q_{z,r} = 0$. Further, the the two inter-detector gaps are seen as dark stripes in the 2D image. b) Horizontal sector integral (75 °-85 °) and c) azimuthal integral of the $\pi - \pi$ scattering of the polymer. The horizontal sector integral and the azimuthal integral are highlighted by the red-shaded area and the green-shaded are in a).

Sector integrated profiles can be used to extract crystallite characteristics such as an estimation of the crystallite sizes. Beforehand, the 2D data is solid angle corrected and q-space converted according to following section 3.3.4. To extract the crystallite parameters, integrated sector profiles are fitted. Therein, the contribution of scattering from amorphous material is typically accounted for by a linear background. Further, the involved scattering characteristics, e.g. of PEDOT and PSS, are accounted for by fitting a Gaussian distribution to each observed peak. Exemplary fitted integrated sector profiles are shown in figure 3.8. To estimate the crystallite characteristics, the areas and the full width at half maximum (FWHM) of the two fitted Gaussian are used. Thereby, the peak center inversely relates with $\frac{2 \cdot \pi}{q}$ to the molecular stacking distance (interchain coupling) and the

full width at half maximum (FWHM) relates with $D = \frac{K \cdot \lambda}{\Delta\theta \cdot cos(\theta_0)}$ (Debye-Scherrer equation) to the crystallite size. Therefore, the profile is either fitted in the θ-representation or the q-space parameters are converted. D is the crystallite size parameter, K the Scherrer shape factor, λ the wavelength, $\Delta\theta$ the FWHM and θ_0 the center of the Gaussian term in the θ-representation. The ratio of the Gaussian areas of the same diffraction peak in the vertical and horizontal sector profile relate to the molecular orientation. The ration of diffraction peaks of two materials within the same sector profile however relates to the ratio of crystalline fraction of the corresponding materials.

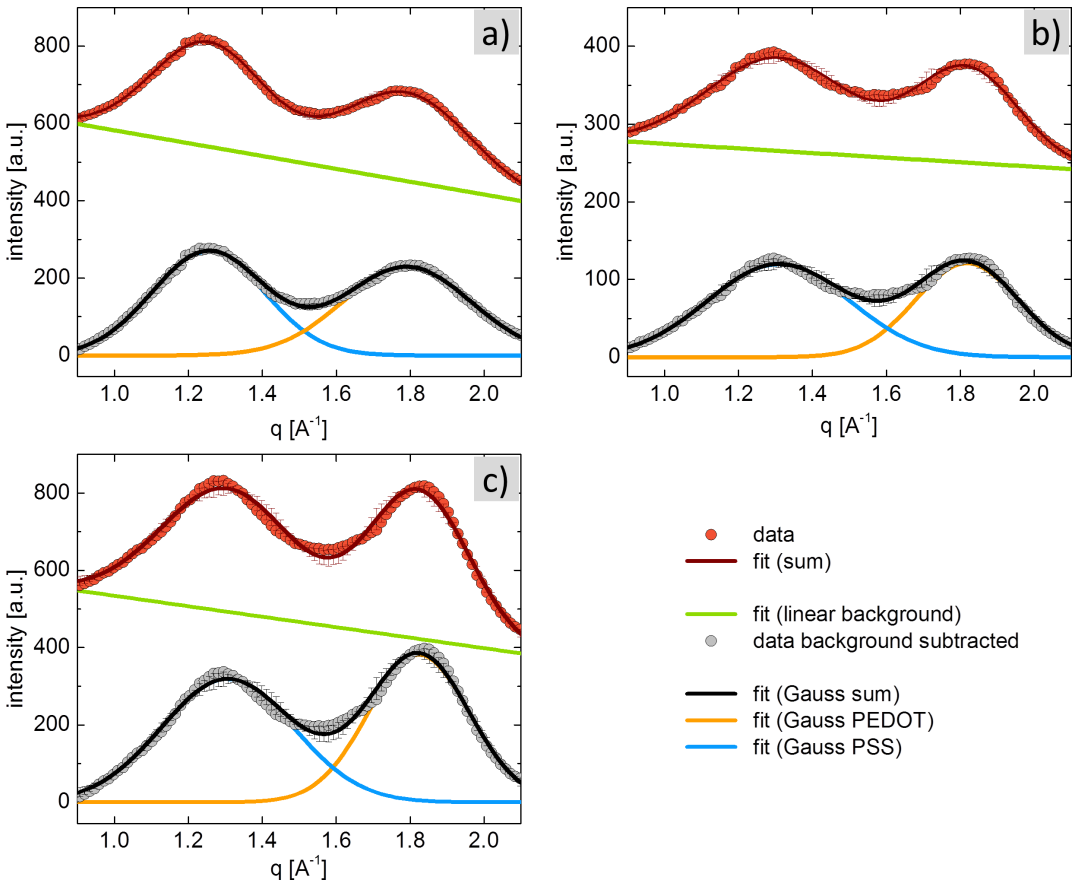

Figure 3.8: Fitted integrated sector profiles of pure, EG-doped and EG-post-treated films showing the key profiles of the fit (background and two Gaussian terms) exemplarily. Adapted from Palumbiny et al. [6]

The importance of the molecular orientations, stacking distances and the evolution of the latter on the conductivity of films is shown in detail in chapters 5,6 and 7 for PEDOT:PSS polymeric electrodes for application in ITO-free OPV. [6,66]

3.3.4 Correction of 2D GIWAXS data

Grazing incidence measurements with wide-angle detection (i.e. short sample-detector distances of centimeters) requires a number of corrections to the obtained 2D pattern. For GIWAXS measurements, typically a 2D detector is placed at a fixed sample-detector distance with the direct beam impinging normal to the detector plane. Each repeating distance in the sample results in diffraction rings of different cross sections of the sample, resulting in constructive scattering at different radial distances from the direct beam position. The analysis of the detected scattering requires a number of corrections, namely efficiency-, solid-angle- and χ-correction, that need to be applied to the 2D GIWAXS detector images obtained from the diffuse scattering of the sample. The geometry for diffuse scattering is shown in figure 3.9 including the used nomenclature. The corrections to the data are performed using the *GIXSGUI* 1.6.1 software of the Advanced Photon Source, X-ray Science Division - Argonne National Laboratory, developed by Zhang Jiang. [76,77] In the following each of the three corrections are explained in detail according and analogue to the manual of the *GIXSGUI* 1.6.1.

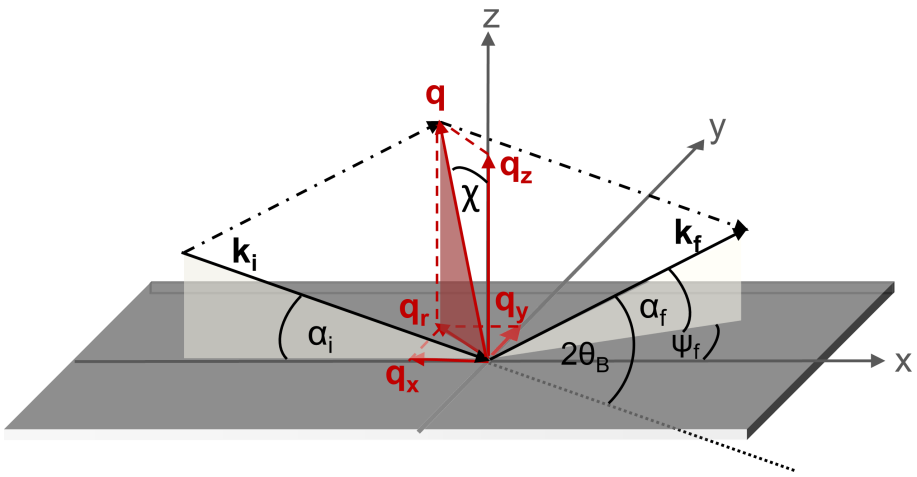

Figure 3.9: Geometric scheme of a scattering event under grazing incidence geometry.

Efficiency-corrections

Especially when detecting wide angle scattering, i.e. with short SDD, in grazing incidence geometry, the medium attenuation, e.g. from the air, and the detector sensor absorption need to be taken into account. Both effects increase as the sample-pixel distance increases. Pixels at different radial distances from the direct beam with different oblique angles 2Θ, have different effective sample-pixel distances and hence different medium attenuation and detector sensor absorptions. Consequently, the 2D GIWAXS data is efficiency-corrected

on a pixel by pixel basis according to[76,77]:

$$E_m = \frac{1}{exp\left[-\mu_m \, SDD/cos\left(2\Theta_i\right)\right]} \tag{3.12}$$

where E_m is unity for negligible medium attenuation, e.g. for measurements conducted in vacuum. μ_m $[1/mm]$ is the linear mass attenuation coefficient of the path medium, SDD $[mm]$ is the nominal sample-to-detector distance with respect to the direct beam pixel and $2\Theta_i$ is the oblique scattering angle of pixel $(x_i,\, y_i)$ given by[76,77]:

$$2\Theta_i = atan\left[\frac{\sqrt{L_x^2(x_i - x_0)^2 + L_y^2(y_i - y_0)^2}}{SDD}\right] \tag{3.13}$$

L_x and L_y are the horizontal and vertical pixel lengths, x_i and y_i the position of an individual pixel and x_0 and y_0 the direct beam position on the detector. In the study presented in chapter 7, the measurements are conducted under helium atmosphere where the medium attenuation can be neglected and is set to be unity.

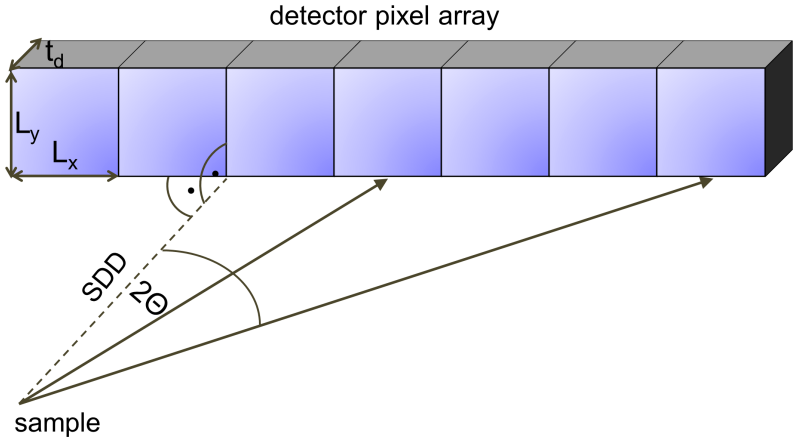

Figure 3.10: Photons scattered to larger oblique angles are more attenuated in the path medium and have increased absorption probability in the detector sensor.

In contrast to the medium attenuation described above, the detector sensor absorption depends on the properties of the detector, i.e. the variation of X-ray absorption probability across a pixel, and is not neglected here. Here, a Pilatus (Dectris Inc.) detectors are used which has a direct pixel-array detector. The X-ray photons impinging on the detector under different oblique angles have different path length through the detector sensor of the impinging pixel and hence have different probabilities to be stopped and detected. Concluding, with increasing oblique angle the absorption probability of the detector sensor absorption for X-rays is increased. To account for the detector sensor absorption variation,

the following efficiency-correction is applied[76,77]:

$$E_d \;=\; \frac{1}{1 - exp\left[-\mu_d\, t_d / cos\left(2\Theta_i\right)\right]} \tag{3.14}$$

μ_d [1/mm] is the linear mass attenuation coefficient of the sensor material, and t_d [mm] is the thickness of the sensor plate, here 0.32 mm. An illustration of the geometry for different oblique angle scattering is shown in figure 3.10. Further information on the efficiency-correction can be found in the $GIXSGUI$ 1.6.1. manual.

Solid angle correction

Contrary to the efficiency corrections, the solid angle correction is a solely geometric correction and therefore independent of the used detector. It can be calculated given valid setup parameter such as the sample-detector distance (SDD), the direct beam position (DB) and the pixel size (L_x, L_y). The origin of the solid angle correction lies in different effective pixel areas for different solid angles. The measured intensity on a pixel hence relates to the intersecting plane of the solid angle and the pixel area. To account for this effect, the intensity is normalized to the solid angle of the direct beam. The solid angle correction array C_s is hence given by[76,77]:

$$C_s \;=\; \frac{\Delta\Omega_0}{\Delta\Omega_i} \tag{3.15}$$

where $\Delta\Omega_i$ and $\Delta\Omega_0$ are given by[76,77]:

$$\Delta\Omega_i \;=\; \frac{A_i}{R_i^2} \;=\; \frac{L_x\, L_y\, cos\left(2\theta_i\right)}{\left(SDD/cos\left(2\theta_i\right)\right)^2} \quad \text{and} \quad \Delta\Omega_0 \;=\; \frac{A_0}{R_0^2} = \frac{L_x\, L_y}{SDD^2} \tag{3.16}$$

with[76,77]

$$A_0 \;=\; L_x\, L_y \;\;;\;\; A_i \;=\; L_x\, L_y\, cos\left(2\theta_i\right) \;\;;\;\; R_i \;=\; \frac{SDD}{cos\left(2\theta_i\right)} \;\;;\;\; R_0 \;=\; SDD. \tag{3.17}$$

Here, $\Delta\Omega_0$ is the solid angle of the direct beam pixel and $\Delta\Omega_i$ is the solid angle of the pixel $(x_i;\, y_i)$, where the beam impinges onto, and R is the sample-pixel distance. $L_x\, L_y$ is the area of a single pixel (see also figure 3.10).

To obtain the corrected data, the efficiency corrections (E_m and E_d) and the solid angle correction (C_s) are combined on a pixel by pixel basis. Therein, the combined efficiency correction is obtained by pixel by pixel multiplication of E_m and E_d and normalization to their maximum value. Taking into account the solid angle correction array, this leads to a correction on a pixel by pixel basis of[76,77]:

$$CorrectedData \;=\; RawData \cdot C_s \cdot \frac{E_d \cdot E_m}{max(E_d \cdot E_m)} \tag{3.18}$$

For measurements performed in a helium atmosphere such as shown in chapter 7, the air attenuation is set to be unity ($E_m = 1$) which leads to a correction of[76,77]:

$$CorrectedData \;=\; RawData \cdot C_s \cdot \frac{E_d}{max(E_d)} \tag{3.19}$$

with C_s the solid angle correction array and E_d detector sensor absorption, where $\cdot*$ stands for the pixel by pixel array multiplication.

Polarization correction

As synchrotron radiation is typically linear polarized in the horizontal plane, the detected scattering intensities are distorted in the 2D raw images, i.e. the distribution needs to be corrected in order to depict the true scattering from the sample. Figure 3.11 schematically shows this polarization of the synchrotron beam in a grazing incidence geometry. In GISAXS experiments with small scattering angles and hence small α_f and ψ_f angles, this polarization correction can be neglected. In GIWAXS experiments however, the polarization correction has a strong influence as shown in detail for the example of water at the end of this section.

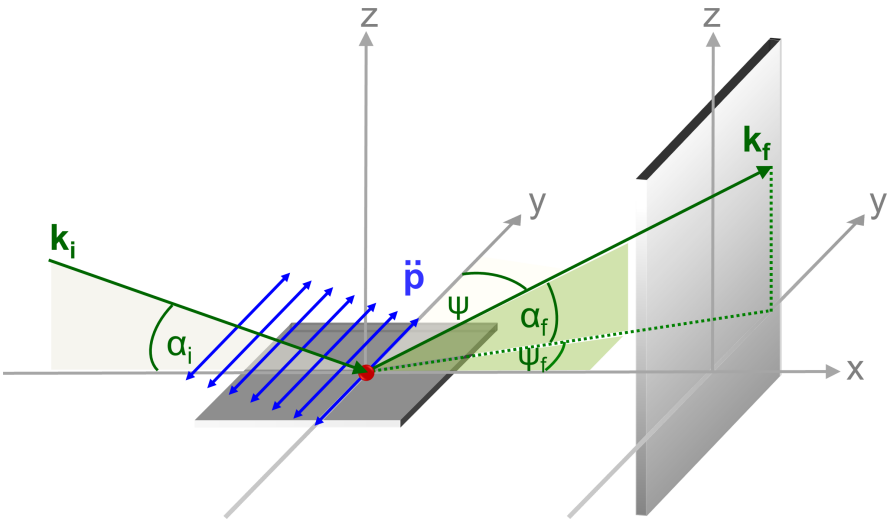

Figure 3.11: Schematic of a horizontally polarized X-ray beam interacting with and scattering from the material probed. Adapted from[76,77].

In a X-ray scattering experiment, the X-rays interact with the electrons of the material probed before they are scattered from the sample. The electrons in the sample thereby get excited with dipole oscillation in the direction of the X-ray polarization. The amplitude of this scattering is thereby proportional to the observed acceleration of the electron dipole moment and the scattering intensity in this direction is thereby reduced due to the energy

absorbed by the electron excitation. Only in the xz-plane the full acceleration whereas out of the xz-plane only part of the acceleration is detected. Hence, as ψ increases the detected scattering intensity decreases. As this is an effect that is solely attributed to the X-ray source and not to the material probed, the detected intensities need to be corrected accordingly by[76,77]

$$P_h = |sin\psi| = 1 - cos^2\,\delta\, sin^2\,\gamma. \tag{3.20}$$

where P_h is the polarization, ψ is the angle between the polarization and the exit wave vector k_f and δ and γ are the angles between the exit wave vector k_f and the xy-plane and the xz-plane, respectively.

On a pixel by pixel basis, the detected scattering intensities are corrected by dividing the 2D raw images by the corresponding polarization factor. The polarization correction is then superimposed to the efficiency and solid angle corrections. Note, that the polarization correction is the only correction with a non-radial correction and hence leads to a correction that is not constant for a certain scattering distance q. The effect becomes apparent for the example of water scattering at the end of this section.

χ-correction

The flat 2D detector which is typically used for data acquisition in GIWAXS experiments, can only detect a distorted and hence incomplete diffraction in grazing incidence geometry, i.e. no direct reciprocal space maps. As a consequence, the 2D detector patterns have to be corrected in χ. To understand the distortion and the resulting χ-correction, an illustration based on two spheres in reciprocal space is provided according to the publication of Baker et al.[78]:

First the Ewald sphere which connects the real space with the reciprocal space is very helpful to describe the diffraction condition for scattering. The surface of the sphere describes all possible scattering events that can be detected. Second, the crystallite orientation sphere describes a crystal orientation in reciprocal space with radius q_B of interest, for which the center for all crystal orientations spheres is $q = 0$. The two spheres relate to each other in a way that the center of the crystal orientation sphere is at the head of the incoming k vector and therefore is located at the surface of the Ewald sphere. The intersection of the two spheres, Ewald and crystal orientation sphere, leads to an intersection ring for each q_B as depicted in red and orange in figure 3.12. For a certain crystal orientation sphere $q_{B,a}$ (figure 3.12a), the intersection ring with the Ewald sphere describes the detectable diffraction for this $q_{B,a}$. Further, for each q_B, such an intersection ring with the Ewald sphere exists. Summing up all intersection rings (for all q_B of interest) yields in an intersection area with the Ewald sphere, which then describes all accessible diffractions in the grazing incidence geometry.

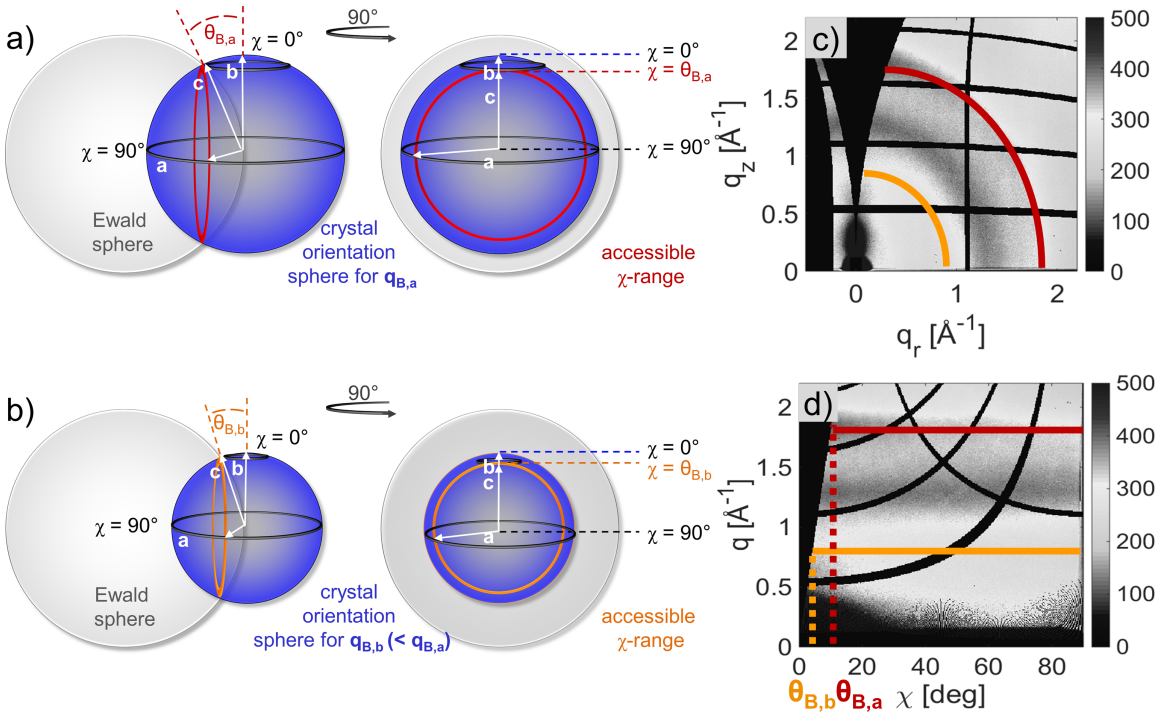

Figure 3.12: Illustration of the distortion of 2D scattering data arising from the intersection of the Ewald sphere and the crystal orientation spheres shown in a) and b), which are adapted from [78]. The area of intersection, depicted in red and orange, indicates possible diffraction events in grazing incidence geometry. In this geometry, the angle range is constrained in χ: $[-90°\ to\ -\theta_B]$ and $[\theta_B\ to\ 90°]$, such that the angle range between $\chi = 0$ and $\chi = \theta_B$ is not accessible. a is the in-plane scattering vector with solely horizontal scattering ($\chi = 90°$), $\vec{b}$ is the out out-of-plane scattering vector that is not detectable in the grazing incidence geometry shown ($\chi = 0°$) and c is the off-vertical scattering vector that results in pure vertical scattering on the detector in the grazing incidence geometry, however does not equal to the out-of-plane scattering vector. The intersections shown in a) and b) are highlighted as red and orange semicircles in the 2D scattering representations: c) q_z vs. q_r representation and in d) q vs. χ representation.

It is evident from figure 3.12, that for each crystal orientation sphere, crystallites with q_B near in-plane (figure 3.12, $\vec{a}$) with a polar angle χ between 90° and θ_B, will intersect with the Ewald sphere. In contrast, for the same crystal orientation sphere, crystallites with q_B near out-of-plane (figure 3.12, $\vec{b}$) with a polar angle χ between θ_B and 0°, will not intersect with the Ewald sphere. In total, rather than ranging from $[-90°\ to\ 0°\ to\ 90°]$, χ is constrained to $[-90°\ to\ -\theta_B]$ and $[\theta_B\ to\ 90°]$ in the grazing incidence geometry, which is important in particular for short sample-detector distances as typically used in GIWAXS. [78]

Comparing the situation for two q_B of interest with $q_{B,a} > q_{B,b}$ shows that the angle range which is not accessible in the grazing incidence scattering, is smaller for smaller $q_{B,b}$ (figure 3.12b) than for the larger $q_{B,a}$ (figure 3.12a). In figure 3.12c and d, the resulting data which corresponds to the two intersection rings in figure 3.12 a and b are represented by the colored pitch circles and lines. Note, that this also shows, that the intensity displayed along the z-direction of the detector images does not represent the specular diffraction as it is only accessible at $\alpha_i = \alpha_f$ near the beam stop. For all data positions above the specular angle, the diffraction is not detected due to the distortion described above. The black area close to the out-of-plane direction indicates this non-accessible angle range in the χ-corrected data in figure 3.12c and d.

Examples

In the following, two examples are given for the corrections discussed above, namely the corrections for the 2D data for water and PEDOT:PSS. The effect of the corrections becomes most apparent when looking at the scattering pattern of water. No preferred orientation of the water molecules with respect to the sample plane is expected and the scattering of the nearest neighbor distance should hence lead to homogeneously distributed intensities along one scattering distance, i.e. a scattering ring on the detector with homogeneous intensity distribution. The raw 2D detector image however does not show a homogeneous intensity distribution along one radial distance from the beam center. When applying the efficiency correction and polarization correction for the scattering of water, the observed distortion in the detector images are corrected to a large extend. The correction images for these two corrections are shown in figure 3.13.

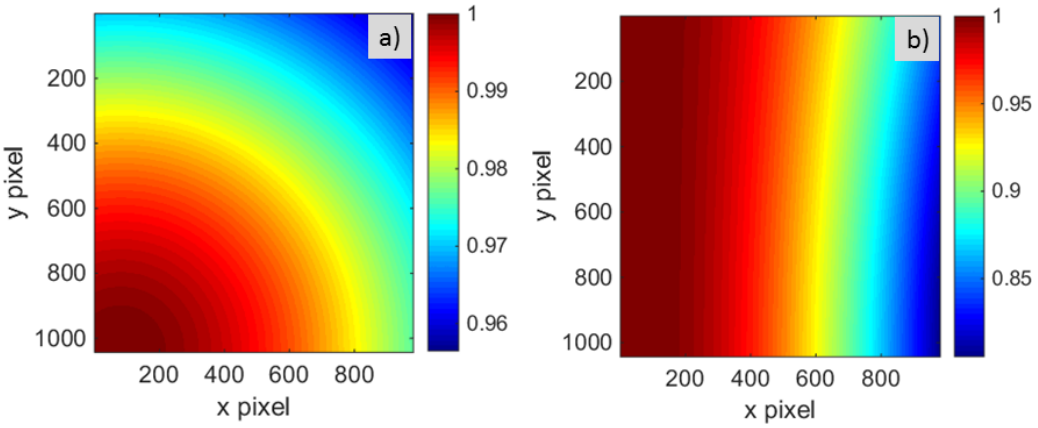

Figure 3.13: In a) the efficiency and in b) the polarization correction for horizontally polarized synchrotron radiation are shown. Correction images from [76,77].

Figure 3.14 shows raw data for water scattering before (figure 3.14a), after solid angle and efficiency correction (figure 3.14b) and after additional polarization correction for the horizontally polarized synchrotron beam of the measurement (figure 3.14c). It is evident from this comparison that the efficiency and solid angle correction adjusts the intensity distribution radial from the beam center. The polarization correction is the only one correcting the intensities non-radial from the direct beam. Consequently, the distribution of intensity along the water scattering ring, i.e. along one scattering distance, becomes homogeneously distributed after applying the polarization correction discussed above. Figure 3.14d and e show the q-space converted data after χ-correction for the 2D images without and with applied polarization correction, respectively.

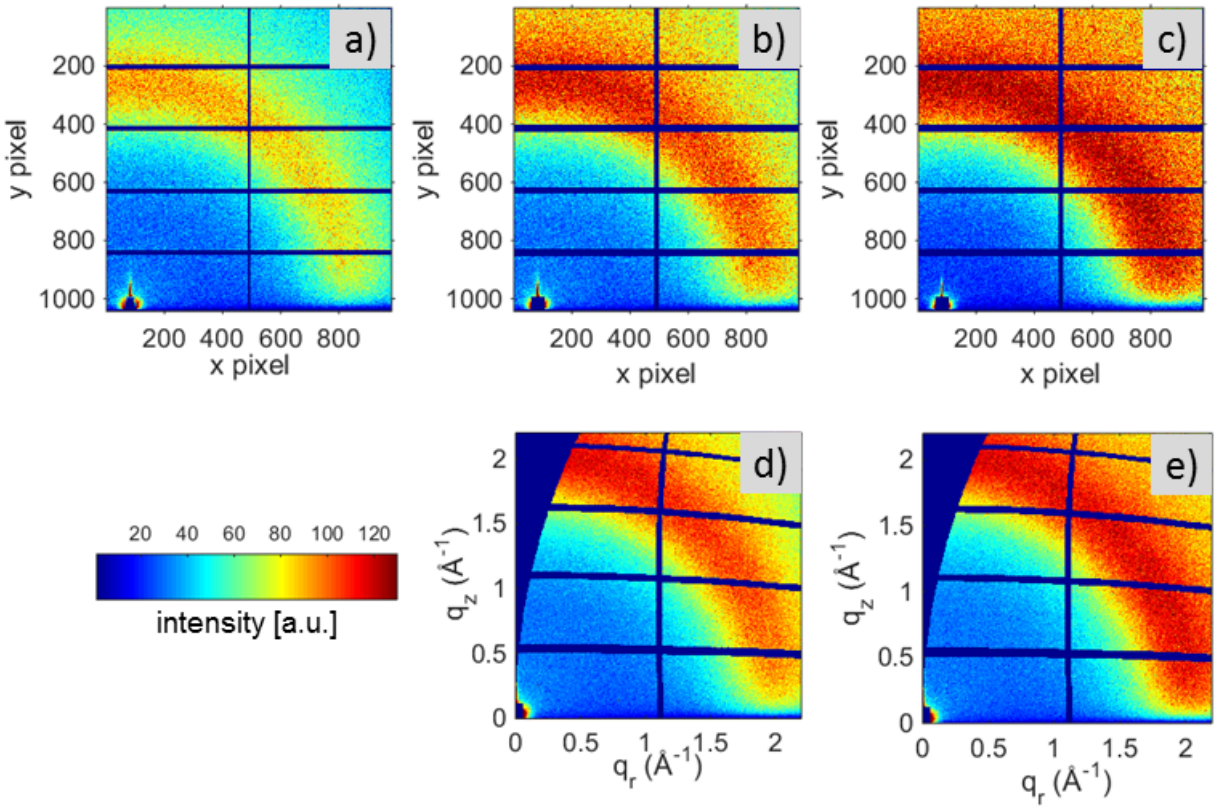

Figure 3.14: 2D GIWAXS scattering data of water a) before b) after efficiency and solid angle correction and c) after additional polarization correction of the 2D GIWAXS scattering data. d) and e) show the χ-correction of the 2D GIWAXS scattering data depicted in b) and c).

The homogeneous intensity distribution of water after full 2D GIWAXS correction (efficiency, solid angle and polarization) is demonstrated by intensity versus scattering vector profiles for vertical and horizontal scattering, shown in figure 3.15. It is evident from the comparison of the two profiles that the scattering intensity in both directions is nearly

identical after full correction.

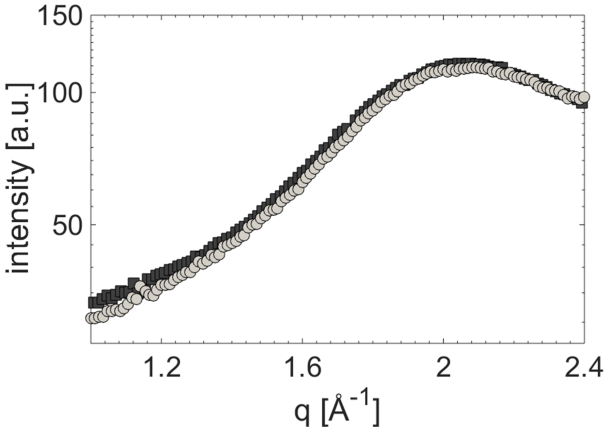

Figure 3.15: Intensity versus scattering vector for GIWAXS measurements of water after 2D data correction. The black and the gray profile correspond to the vertical and the horizontal cuts, respectively.

The effect of the efficiency and solid angle corrections for PEDOT:PSS is shown in figure 3.16. The gray squared and red circle symbols represent the scattering before and after 2D GIWAXS data correction, respectively. Figure 3.16a shows the detected q-range whereas figure 3.16b shows a close up to the scattering from the characteristic $\pi - \pi$ stacking. It can be clearly seen that the corrections lead to a much less pronounced intensity drop for higher q-values due to the intensity corrections described above.

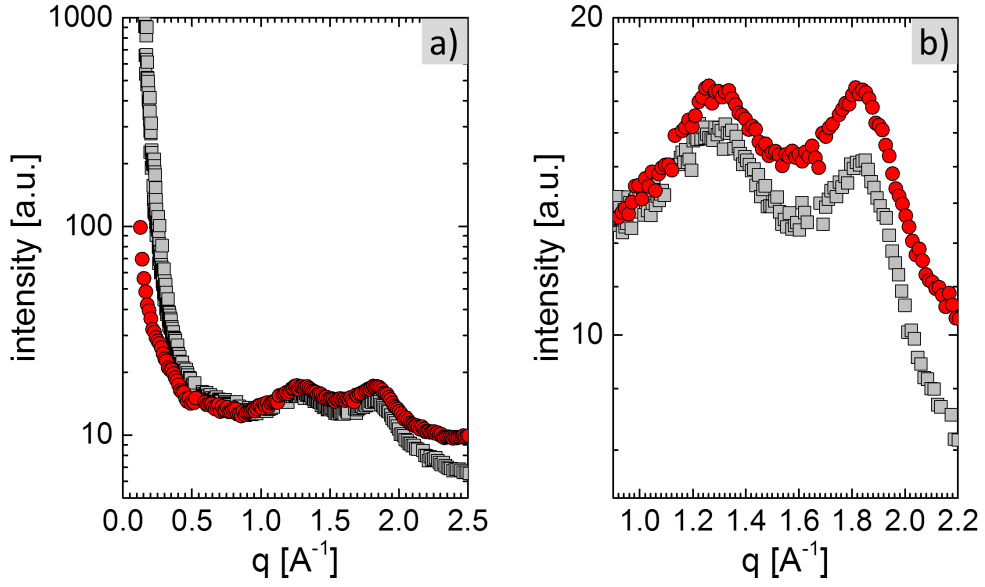

Figure 3.16: a) Intensity versus scattering vector for PEDOT:PSS before (gray squared symbols) and after (red circle symbols) 2D data correction. In b) a close up to the characteristic $\pi - \pi$ stacking is shown.

3.3.5 Polarized resonant soft X-ray scattering

Despite all the advantages of XRR, GISAXS and GIWAXS, especially for all-polymeric systems the contrast between materials can be insufficient. In such cases, polarized resonant soft X-ray scattering (P-SoXS) is a strong tool for tuning the contrast between materials. The basic principle of scattering with this technique is fundamentally different to hard X-ray scattering, a fact which can be exploited in order to enhance the scattering contrast between materials. In soft X-ray scattering experiments energies typically below 2 keV are used, which is much lower than for hard X-rays. Further the measurement energy is tunable within a certain range which depends on the individual setup. At these energies, the measured material, that is the polymeric system, is sensitive to the incident photon energy where fundamental electronic transitions in lighter atoms, e.g. carbon, take place.[79] This chemical sensitivity can be utilized to tune the scattering to specific bond types. Figure 3.17 exemplary shows a fundamental carbon transition, the C1s-π^* in aromatic carbon rings for a non-resonant photon energy (figure 3.17a) and a resonant photon energy (figure 3.17b) to the electron transition. The photon energy in the situation shown in figure 3.17b is absorbed by an electron located in the C1s shell and subsequently excited to the unoccupied molecular orbital π^*. Thereby, the measurement energy is resonant with the C1s-π^* transition. As a consequence, the aromatic molecules collectively act as tiny dipole antennas which are aligned parallel to the polarization of the incident photons. This material interaction with the incident photon results in a scattering which is dependent on the relative alignment of the electric field.[79] Figure 3.17 shows two 2D transmission scattering patterns obtained for such a P-SoXS measurement of the same PEDOT:PSS thin film. They clearly show how the scattering of the material changes from an isotropic scattering to an anisotropic scattering when the measurement energy is changed from a non-resonant energy to the resonant energy of the C1s-π^* transition. Furthermore, the scattering signal obtained with polarized R-SoXS corresponds to scales where the molecular orientation is preserved and can expand over several crystal grains and even to non-crystalline parts.[79]

P-SoXS measurements are performed at the synchrotron beamline 11.0.1.2 of the Advanced Light Source at the Lawrence Berkeley National Laboratory in Berkeley, USA. The energy of the incident photons is varied from 160 eV to 320 eV which corresponds to wavelength of 7.8 nm to 3.9 nm. Considering the long wavelength of the beamline, sample-detector distances of 80 mm to 130 mm were sufficient to probe length scales of a few tens of nm to a few μm, which is comparable to GISAXS experiments. On the basis of the fact that soft X-rays are subject to high absorption in air, all P-SoXS measurements are conducted in high vacuum. The setup at the beamline 11.0.1.2. allows for transmission

as well as grazing incidence measurements. The scattered photons are detected by a CCD camera with 2048 px x 2048 px and a pixel size of 13 μm x 13 μm. Depending on the scattering behavior of the probed material, typical measurement times range from 0.1 s to 10 s.

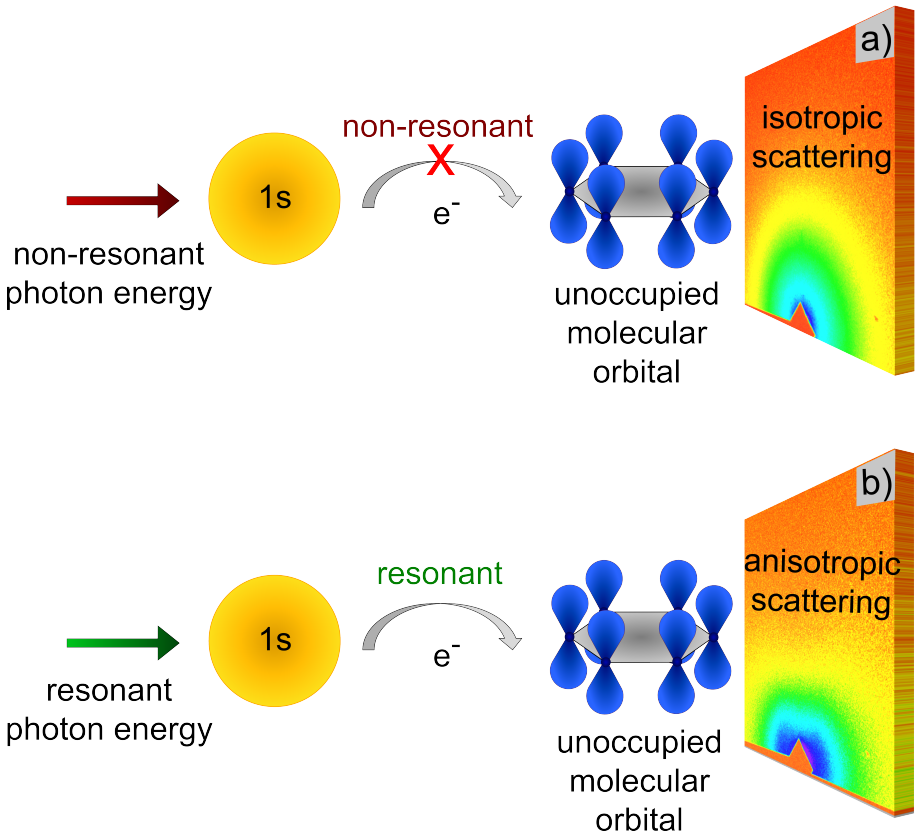

Figure 3.17: Basic principle of R-SoXS where e.g. the photon energy excites an electron from the 1s orbital to an unoccupied molecular orbital. R-SoXS is hence driven by electronic transitions of lighter atoms, e.g. carbon, leading to chemical sensitivity of this technique.

A project in collaboration with T. Pfadler et al. showed how the contrast in the all-polymeric system P3HT:P(NDI2OD-T2) is too low for hard X-ray investigation.[80] The interface between the two materials in this work was artificially nanostructured and therefore well-defined. With grazing incidence P-SoXS, the absence of scattering was proven to be caused by the lack of material contrast and the interface between the materials. Furthermore, the P-SoXS measurements proved the existence of the nanostructured polymer-polymer interface.

3.3.6 Summary

Concluding, the variety of grazing incidence scattering techniques enables structural investigations ranging from molecular size, e.g. molecular stacking distances, to mesoscopic size in the nanometer range, e.g. active layer domain sizes and artificial structures. With the help of the discussed methods, vertical and lateral structures which are relevant for the exciton separation and charge transport mechanisms in organic thin films can be investigated. Further, additional parameters that influence the conductivity in such films, such as molecular orientation, crystal sizes and stacking distances can be investigated in wide angle scattering. Last but not least, the possibility of applying the principles of XRR and GISAXS with hard X-rays to neutron or soft X-ray scattering, the contrast between materials can be tuned such that even materials with similar electron densities can be distinguished.

Chapter 4

Materials and Sample Preparation

The materials, thin film processing and solar cell assembly routes used to prepare the samples investigated within this thesis, are described in the present chapter. Specifications in the processing of particular investigations are explicitly mentioned in the respective chapters.
The specifications and characteristic properties of materials that were used to prepare samples are given in section 4.1. Therein, section 4.1.1 introduces functional materials used for the preparation of the polymeric electrodes and photovoltaic devices. Details on substrate materials are described in section 4.1.2. In section 4.2 the preparation of thin films is explained in detail. The processing of PEDOT:PSS by secondary doping is described in section 4.2.1. Therein, co-solvent modifications of PEDOT:PSS, i.e. doping and post-treatment, as well as surfactant modification of PEDOT:PSS are illustrated. Different deposition methods for polymeric electrode materials and photovoltaic active materials are elaborated in section 4.2.2, including spin-coating and slot-die printing. Lastly, section 4.3 illustrates the process of assembling the investigated photovoltaic devices.

4.1 Materials

Materials investigated in the present thesis are categorized into two groups. The first group of materials consists of functional materials, i.e. the polymeric electrode materials PEDOT:PSS, the structure-directing secondary dopants as well as the electron and hole conducting materials (section 4.1.1). The second group includes substrate materials and the molding materials for structuring (section 4.1.2).

4.1.1 Functional materials

Polymeric electrode material (PEDOT:PSS)

The polymeric material poly(3,4-ethylenedioxythiophene) blended with polystyrene sulfonate (PEDOT:PSS) is used in this work as a selective electron blocking layer as well as polymeric electrode. The chemical formula of the monomers are $C_6H_4O_2S$ and $C_8H_7O_3S$ for (P)EDOT and (P)SS, respectively. Blended in aqueous solution, the polymer blend is purchased with the trade name $HeraeusClevios^{TM}PH1000$ (order code M122) purchased from *Ossila Ltd.*, Sheffield, UK. According to the supplier, the formulation consists of 1 % to 1.3 % PEDOT:PSS (CAS. 155090-83-8) in H_2O, has a PEDOT to PSS blending ratio of 1 : 2.5 and a density of about ~1 g/ml in solution. In figure 4.1, the chemical structures of the two monomers as well as their interaction are shown.

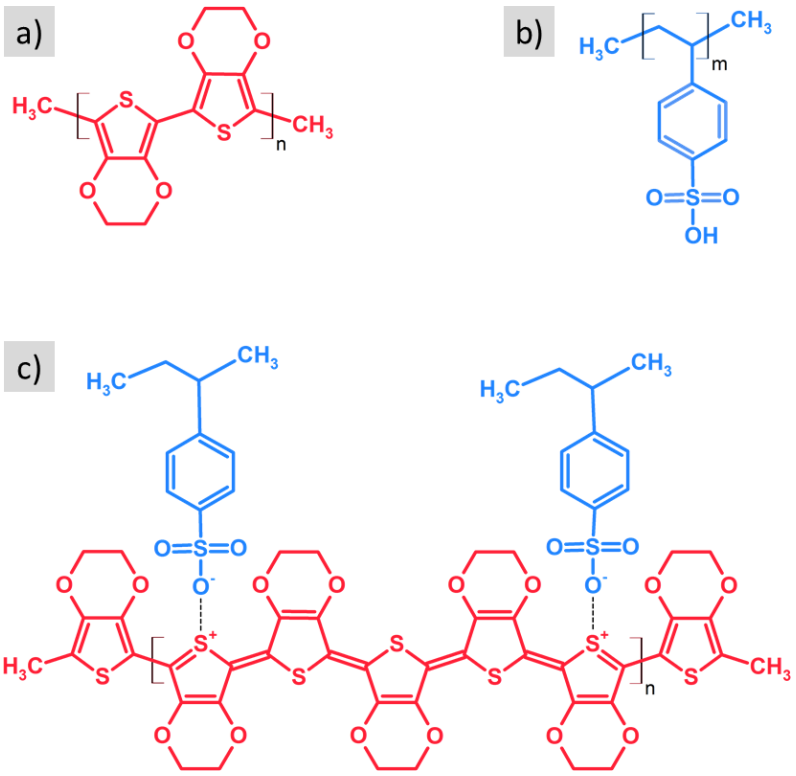

Figure 4.1: Chemical structures of PEDOT (a) and PSS (b) monomers as well as their blend (c).

For the scattering experiments presented in the present thesis, the critical angle determination of the material under investigation is essential. Therefore, in table 4.1 the parameters of PEDOT:PSS which are needed to estimating the critical angle of the materials for X-ray scattering experiments listed.

	PEDOT	**PSS**
MM [g/mol]	140.065	183.065
MD $[kg/m^3]$	1	1
δ	$2.15002 \cdot 10^{-6}$	$2.16859 \cdot 10^{-6}$
α	$2.00133 \cdot 10^{-8}$	$1.64466 \cdot 10^{-8}$
$f^0 = Z_k$	72	95
$f^{'}$	0.515	0.596
$f^{''}$	0.675	0.725

Table 4.1: Material parameters for the determination of scattering properties such as the critical angles of PEDOT and PSS. Values are calculated for the material monomers. Acronyms: molar mass (MM), assumed molar density (MD), dispersion coefficient (δ), absorption coefficient (α), dispersion correction factors ($f^0 = Z_k$, $f^{'}$, $f^{''}$). f^0, $f^{'}$ and $f^{''}$ are values for the copper K_α edge.

Structure-directing secondary dopants

A variety of secondary dopants for PEDOT:PSS is used in the present thesis. Secondary dopants modify the film structure and thereby the film properties. Chapters 5 to 7 discuss this effect in detail. In the following, characteristic values of the secondary dopants are listed in table 4.2.

dopant	**CF**	**BP** $[°C]$	**P** [%]	**D** $[g/cm^3]$	**MM [g/mol]**
G	$C_3H_8O_3$	290.0	≥99.5	1.261	92.09
EG	$C_2H_6O_2$	197.3	≥99.8	1.113	62.07
DMSO	C_2H_6OS	189.0	≥99.8	1.100	78.13
E	C_2H_6O	78.4	≥99.8	0.789	46.07
M	CH_3OH	64.7	≥99.0	0.792	32.04

Table 4.2: Characteristic parameter of secondary dopants used for PEDOT:PSS modification. Dopant Acronyms: glycerol (G), ethylene glycol (EG), dimethylsulfoxide (DMSO), ethanol (E), methanol (M). Further acronyms: chemical formula (CF), boiling point (BP), purity (P), density (D), molar mass (MM). Values taken from [81] and by the suppliers data sheets.

Dimethylsulfoxide, ethanol and methanol are purchased by *Carl Roth*, whereas glycerol and ethylene glycol are supplied by *Sigma Aldrich*. All chemical structures are depicted in figure 4.2a-e.

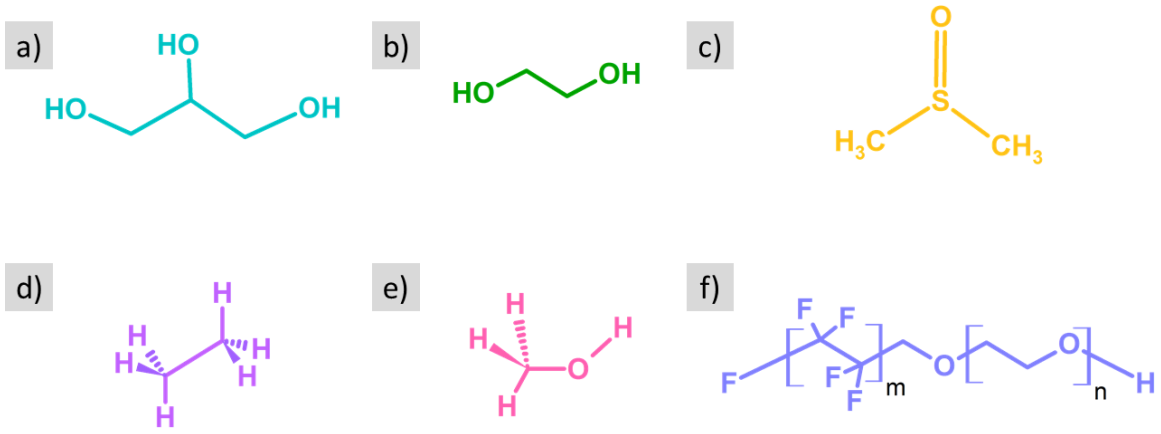

Figure 4.2: Chemical structure of the structure-directing solvent dopants used in the present thesis to modify the PEDOT:PSS. a) glycerol, b) ethylene glycol, c) dimethylsulfoxide, d) ethanol, e) methanol and f) the (fluoro)surfactant FS-300 Zonyl.

(Fluoro)surfactant (FS)

The surfactant used in this thesis for modification of PEDOT:PSS is Zonyl® FS-300, a non-ionic (fluoro)surfactant (CAS. 1974664-69-0). Zonyl® FS-300 is a registered trade mark of the company *E. I. du Pont de Nemours & Co.*, Wilmington, Delaware, USA. It is purchased from *Sigma Aldrich* who produce it through their subsidiary *Fluka* (Lot. BCBL2674V). Zonyl is supplied with 40 % (fluoro)surfactant in aqueous solution, has a density of 1.10 g/ml ± 0.05 g/ml at 20 °C, a boiling point of 80 °C. For the following thesis it is simply referred to as FS. Further, its chemical structure is shown in figure 4.2f.

Electron and hole conductors for photovoltaic active layers

The active layer of the photovoltaic systems presented in this thesis consists of two organic semiconducting materials blended in solution. Coated as solid thin films, the two materials behave relative to each other as hole and electron conducting materials. The polymer poly(3-hexyl-thiophene-2,5-diyl) (P3HT) with the chemical formula $(C_{10}H_{14}S)n$ is a conventional hole conductor that acts as a model system in organic photovoltaics when blended with the fullerene electron conductor (6,6)-phenyl C61 butyric acid methyl ester (PC71BM) with the chemical formula $C_{82}H_{14}O_2$. Figure 4.3 shows the chemical monomer structure of the two molecules which are described in detail in the following.

P3HT is, as above-mentioned, one of the most-studied photoactive polymers. With a HOMO of −5.2 eV, a LUMO of −3.3 eV and a band gap of 1.9 eV, it absorbs light with wavelength in the visible range between 500 nm and 650 nm. Its side chains (see figure 4.3a) are responsible for the high solubility of P3HT in organic solvents like chloro-

benzene. The thiophene backbone is responsible for the conductivity of P3HT, which is $10^{-9} - 10^{-7}$ S/cm^{-1} as declared by the supplier. The P3HT used in the present thesis is purchased from *1-material*, Dorval, Canada, with a regioregularity of 91 to 94 %, a molecular weight of 53 000 and a polydispersity of 2.3 (as declared by the supplier).

PC71BM is an alternation of the commonly used PC61BM (see figure 4.3b). Both molecules consist of a so-called buckyball which is modified by a side chain in order to make the molecule soluble in organic solvents. In contrast to the highly symmetric C60 molecule (60 carbon atoms arranged in 20 hexagons and 12 pentagons), also referred to as buckyball or Buckminster fullerene, the C70 molecule with its 25 hexagons is slightly elongated and hence less symmetric than its C60 relative. Owing to the lower symmetry of the C70 molecule, its electronic properties change and lead to better absorption in the visible range compared to C60. The π-orbitals of the C70 are, similar to C60, delocalized over the structure leading to a high electron affinity. The PC71BM used in the present thesis has a low HOMO of -6.1 eV and a LUMO of -3.7 eV resulting in a band gap of 2.4 eV. It is purchased from *Nano-C*, Westwood, USA.

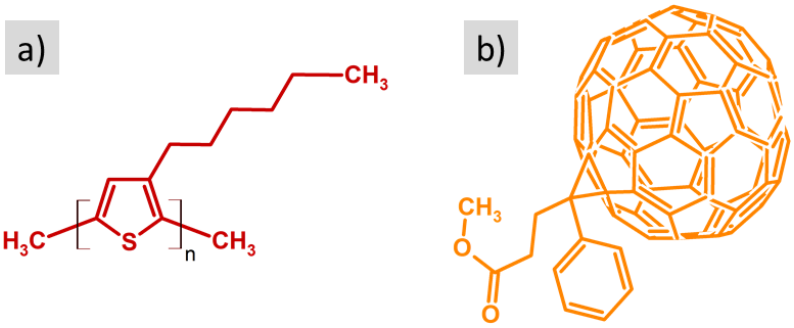

Figure 4.3: Chemical structure of the photoactive materials used in the present thesis. a) P3HT and b) PC71BM.

4.1.2 Substrates

In the present thesis a variety of substrate materials are used for the preparation of thin films and photovoltaic devices. In the following a short description of the most important substrates is given.

Glass

Glass substrates are use for the purpose of conductivity, absorption and some scattering measurements. For this purpose, microscope slides made of 1 mm thick soda-lime glass

are cut to the desired sample sizes. Before the organic thin films are coated onto the glass substrate, the latter are cleaned in a hot acid bath as described in section 4.2.2. Glass slides are purchased from *Carl Roth GmbH & Co. KG*, Karlsruhe, Germany.

Silicon
Scattering measurements are also performed on thin films coated onto silicon substrates. The silicon wafers are polished on one side, the (100) plane of the single crystal from which they are cut in their production cycle. The purchased wafers are particularly flat with a roughness of only 0.36 nm. All silicon wafers are supplied in the size of 5 cm in radius by *Silicon Materials Inc.*, Thornburg, USA. silicon substrates are cleaned via the same preparation routine as glass substrates. The cleaning procedure is detailed in section 4.2.2.

Indium tin oxide (ITO)
Photovoltaic devices are prepared on indium tin oxide (ITO) coated glass substrates of high transparency in the visible light spectrum. The ITO layer thickness is given by the supplier as 80 mm with a sheet resistance of 25 Ω/□-35 Ω/□. ITO has a work function of −4.7 eV. The ITO substrates are purchased from *SOLEMS*, Palaiseau, France pre-cut into samples of 300 mm^2 in size. Before their utilization, the substrates are subject to an extensive cleaning process as described in section 4.3.

4.2 Thin film processing

For the fabrication of highly conductive PEDOT:PSS films as an alternative for the brittle ITO, secondary doping processes are utilized. These are described in detail in section 4.2.1 followed by a description of the deposition methods used (section 4.2.2).

4.2.1 Secondary Doping

PEDOT:PSS is widely used in organic electronics as functional layer between the ITO electrode and the active layer. Furthermore, PEDOT:PSS can act as a substitute for the brittle ITO by enhancing its conductivity with secondary doping methods, i.e. doping via induced structural changes in the film morphology. In particular, PEDOT:PSS can be modified by high boiling point co-solvents, and surfactants as shown in the present thesis. This section provides an overview of the various methods of secondary doping used in this thesis.

Structure modification of PEDOT:PSS using co-solvents

Doping

PEDOT:PSS is a polymer blend immersed in aqueous solution. Hence, the addition of a dopant directly to the solution is feasible and is referred to in this thesis as doping.
The aqueous PEDOT:PSS solution (PH1000), stored at 4 °C, is sonicated and filtered prior to the addition of dopants to ensure a homogeneous solution exclusive of agglomerates. After the appropriate amount of PH1000 is transferred to a cleaned glass vial, the PH1000 is ultrasonicated in a water bath at room temperature for 15 min. Subsequently, the solution is filtered with a poly(vinyldifluoride) (PVDF) filter of 0.45 μm pore size. The dopants themselves are added to the PEDOT:PSS solution after the above-described filtering process.

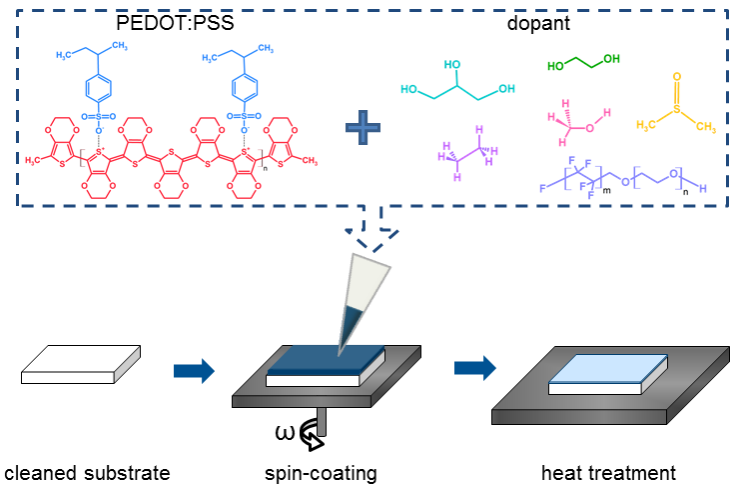

Figure 4.4: Direct doping process for PEDOT:PSS solution with dopant solutions.

Directly after spin-coating of the doped solutions, the samples are transferred to a heating plate, where they are annealed at 140 °C for 10 min if not stated different. The subsequent transfer of the samples to the heating plate has to be assured for the success of the doping process. A scheme illustrating the post-treatment process is shown in figure 4.4.

Post-treatment

Instead of direct doping of the PEDOT:PSS solution, post-treatment with the above-described co-solvents can be applied to modify the PEDOT:PSS layer. The effect of post-treatment on the PEDOT:PSS films differs from the solution doping as discussed in chapters 5, 6 and 7. Within the framework of this thesis, post-treatment via a variety of dopants is used to modify the structure and and thereby the electrical and optical prop-

erties of PEDOT:PSS films. Some of the most important properties of the additives are given in table 4.2. Post-treatment is applied to solidified and temperature-treated films. The post-treatment procedures differ depending on the deposition method used.

In the case of spin-coated films, two processes of exposing the solidified and annealed film to the dopant solution are used. Firstly, the films can be immersed in a solvent bath of the dopant for the desired time. In this case, subsequently after the immersion, the film is removed from the bath by lifting it up vertically from the dopant bath and dabbing the excess solution on the backside of the sample. The sample is placed on the spin-coater where the excess solvent is spun off with 1500 rpm (ACL9) for 30 s. Immediately after this step, the sample is transferred to the heating plate where it is annealed at 140 °C for 10 min.

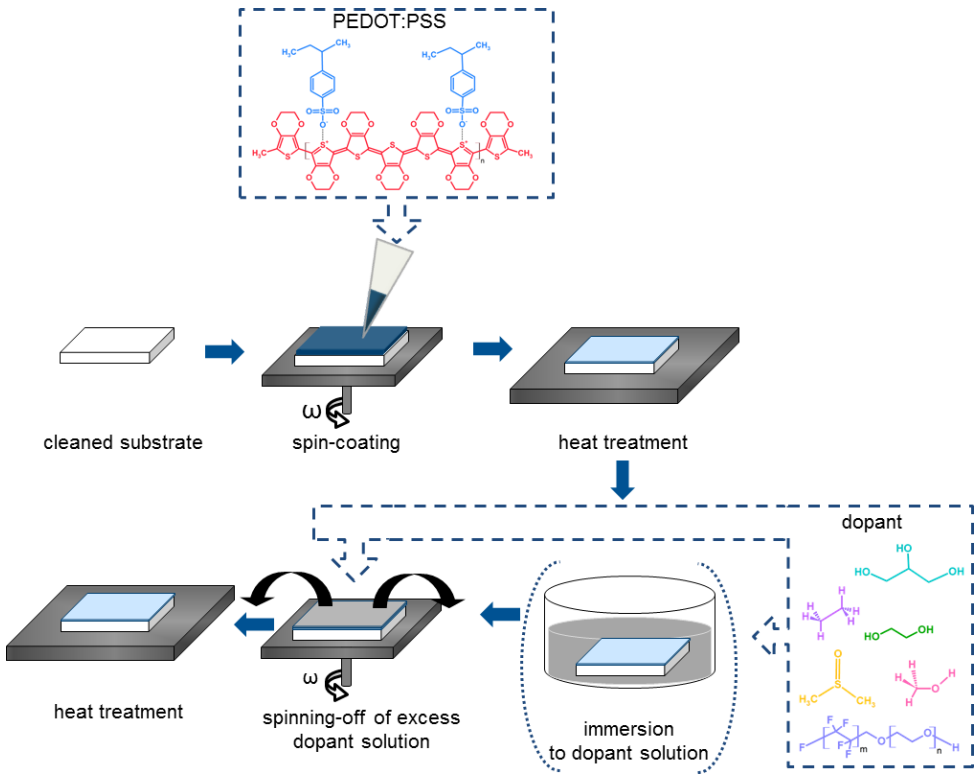

Figure 4.5: Post-treatment process for PEDOT:PSS with dopant solutions. Two ways of immersion to the dopant are depicted: immersion in a dopant solution bath and drop-casting of the dopant solution onto the sample prior to spin-coating.

Secondly, the film can also be post-treated by dropping a controlled amount of the dopant solution onto the PEDOT:PSS film. For this process, the solidified and annealed PEDOT:PSS film is placed on a spin-coater prior to drop-casting the dopant solution.

After the desired time of immersion, the excess dopant solution is spun off and the film is annealed as described above. In chapter 5, for the latter method the influence of the immersion time on the final film properties is investigated with the result of a sufficient immersion time of 3 min. Hence, the immersion time for post-treated films is 3 min if not stated different. A scheme illustrating the post-treatment process is shown in figure 4.5. In the case of PEDOT:PSS slot-die printing and subsequent post-treatment (see chapter 7), the dopant solution is slot-die coated directly onto the solidified and annealed PEDOT:PSS film at an elevated temperature of 90 °C. Details on this process are given in the corresponding chapter.

Structure modification of PEDOT:PSS using a surfactant

In this thesis, the (fluoro)surfactant (FS)Zonyl is shown to influence the electrical and optical properties of PEDOT:PSS. The surfactant induces a change in morphology by phase separation of the PEDOT:PSS polymer mixture, which leads to the increase in electrical conductivity. As described above for the co-solvents, the FS is added to the PEDOT:PSS solution after the latter has been sonicated and filtered. Due to the amphiphilic nature of the FS, it is found to be easiest to first weigh the desired amount of FS before adding the corresponding amount of PEDOT:PSS, in this thesis from 0.01 % to 10 %. After the FS is added, the solution is mixed on a shaker for one to two hours. Depending on the desired layer thickness, the spin-coating parameters differ and are hence given in the respective context. After deposition, the film is annealed at an elevated temperature of 140 °C for 10 to 15 min.

4.2.2 Deposition methods

PEDOT:PSS in all its variations as well as the active layers are deposited on solid substrates (see section 4.1.2) as thin films for characterization of the films or for practical applications such as solar cell assembly. For this purpose several deposition techniques have been developed for laboratory as well as for industrial use. For the investigations and applications shown in the present thesis the laboratory-scale technique of spin-coating is used to obtain thin films. In chapter 7 it is explained how the industrial-scale technique of slot-die coating can be used not only for thin film deposition, but also simultaneous X-ray investigations. The obtained results are then applicable for industrial processes.

Substrate cleaning

Prior to the deposition of thin films by the techniques described later, the solid substrates require a cleaning process for reproducible results. As all deposition techniques are highly

sensitive to the surface quality and properties of the substrate, e.g. the surface tension, the cleaning of the substrates is of utmost importance. For the case of silicon substrates the cleaning process defines the thickness of the native oxide layer on the substrate, which can influence the wetting and thereby the resulting film quality and thickness.

For all glass and silicon substrates used in the present thesis, the same hot acid bath (HAB) cleaning procedure applies according to[51]. The process is derived from the so-called piranha solution, which is a strong oxidizing agent. As a result, the surface of the substrate is free from organic residuals and by the addition of -OH groups becomes more hydrophilic. The hot acid bath is composed of 54 mL deionized water (H_2O), 84 mL hydrogen peroxide (H_2O_2, 30 %) and 198 mL sulfuric acid (H_2SO_4, 96 %), mixed in this order and heated to 80 °C before immersing the samples into the bath. As the solution exhibits an exothermic reaction, careful handling is required. For the same reason, the substrates are first placed in acid resistant holders and rinsed with deionized water. Once immersed into the HAB, the samples are kept there for exactly 15 min, before they are removed from the bath and directly transferred to a bath of deionized water. From there, each substrate is removed separately, rinsed immediately with deionized water (approximately 250 mL per sample) and dried under an oil-free nitrogen flow, starting in one corner of the sample. The HAB can be used for three times, when cleaning 10 samples per bath, before it is exchanged. The samples should be coated with the following thin organic film within the next six hours.

Spin-coating

One of the most common deposition methods for thin films from solution on a laboratory scale is spin-coating. Prior to the deposition process, the spin-coater is programmed to a defined rotation speed, time and acceleration. For this work, the acceleration is typically set to ACL9, which has an acceleration time of 6 s until the final rotation speed is reached and the counter of the rotation time starts.

At the beginning of the spin-coating process, a controlled amount of the solution (100 μl to 300 μl depending on the sample size), containing the dissolved organic molecules, is deposited fast and homogeneously onto the entire sample, which is placed in the center of a rotation disc, where the sample is held in place by vacuum. Spin-coating is a non-equilibrium deposition method consisting of a three-step process. First, with the start of the rotation, most of the deposited solution is driven to the brim by centrifugal force and flung off the sample. As a second step, convection of the solution starts. This process dominates the dynamic processes involved in the film formation. Third, the evaporation of the solution proceeds, whereby solvent molecules imbedded in the film volume diffuse

to the surface and evaporate.
The thickness of the resulting film can be estimated by an empirical formula giving a linear relation between its thickness and the concentration of the solution. This relation holds within the regime of negligible viscosity of the solution. Using this formula, the desired parameters can be calculated according to the Schubert equation:

$$d_\infty = A \left(\frac{1950\, min^{-1}}{\omega}\right)^{1/2} \left(\frac{c_0}{20\, g/l}\right) \left(\frac{M_{sp}}{100\, kg/mol}\right)^{1/4} \tag{4.1}$$

with d_∞ the thickness after infinite rotation time, ω the rotational velocity, c_0 the initial concentration, A a factor incorporating device specific parameters and M_{sp} the spin-coating molar mass. Most of the parameters are difficult to determine. Hence a more qualitative simplification of the formula is used to determine the resulting thickness d_2 of a film, which was coated with a rotational velocity of w_2 from a solution with concentration d_2. Therein, reference values for the system under investigation are utilized (d_2, w_2, d_2). It is noted, that factors such as moisture, temperature or solvent atmosphere are neglected.

$$\frac{d_1}{d_2} = \left(\frac{\omega_2}{\omega_1}\right)^{1/2} \left(\frac{c_1}{c_2}\right) \tag{4.2}$$

Slot-die printing

In the present thesis, slot-die coating is used to print the fluid PEDOT:PSS onto silicon substrates. The PEDOT:PSS solution was coated with a flow rate of 0.2 ml/min. In this process, the solution is inserted into an injection tube using an automated slider for the solution filled syringe pump. The solution is pumped through the injection tube, until it reaches the slot-die head. After wetting of the slot-die head and the sample surface, i.e. the formation of a meniscus, the printing process is started manually. During the printing process and throughout the film formation time, the substrate temperature is kept constant to assure controlled drying conditions. A sketch of the slot-die coater used is shown in figure 4.6

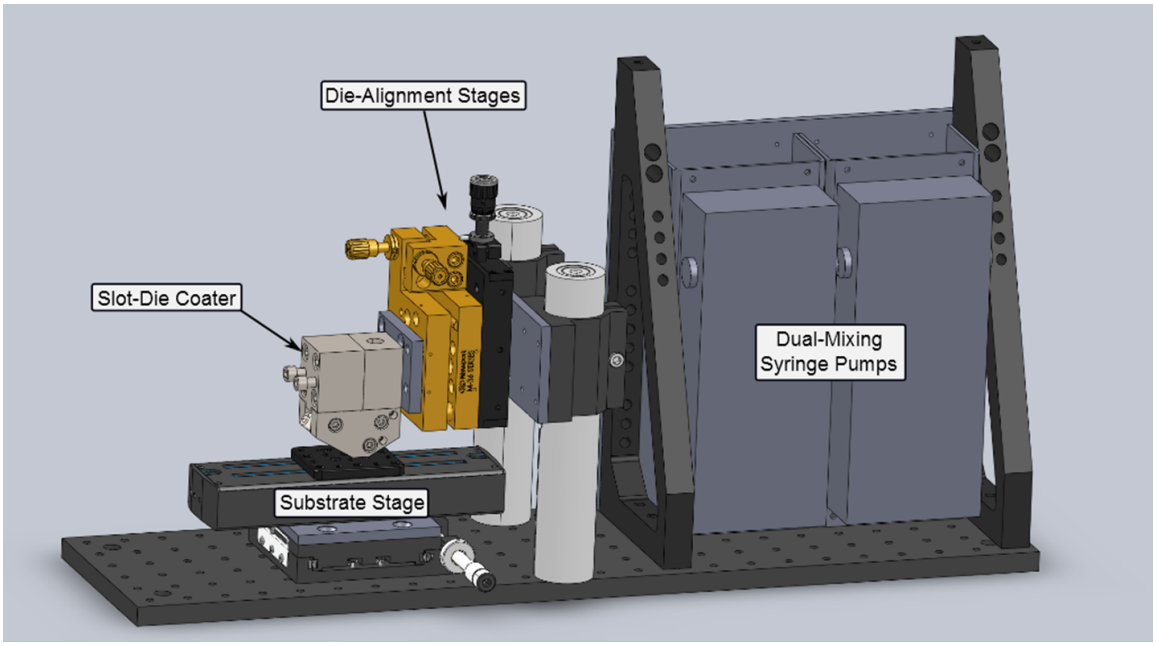

Figure 4.6: Schematic drawing of the slot-die coater used in the present thesis. The important components of the printer are highlighted. The solution to be printed is injected into the dual syringe pump from where it is injected through the slot die printer head onto the sample that is placed on the substrate alignment stage. For in-situ GIWAXS investigations that are shown in chapter 7, the die-alignment stage assures the alignment of the printers sample stage to the X-ray beam. The drawing is provided by Dr. Cheng Wang and Dr. Feng Liu from the ALS, LBNL in Berkeley.

4.3 Solar cell assembly

Organic photovoltaic devices have a sandwich-structure in which the active layer is sandwiched in between two electrodes. Additional functional layers, typically hole and electron blocking layers, are added in between the respective electrode and the active layer. The resulting work function alignment improves charge extraction and reduces charge recombination. For the photovoltaic devices produced in this thesis, the deposition methods described in section 4.2.2 apply. In the following, the individual steps involved in the fabrication of the devices are explained in detail.

Substrate preparation

In this thesis, ITO substrates are used for the fabrication of photovoltaic devices. Owing to the device geometry used, only one half of the surface remains coated with the transparent electrode material.

In the case of ITO, a part of the ITO layer is etched via a catalytic reaction. For this, one half is covered with an adhesive tape for protection whereas the other half is etched by exposing the ITO to the catalytic reaction using a cotton bud dipped into 37 % hydrochloric acid and zinc powder beforehand. Subsequently, the substrates are rinsed in deionized water and blow-dried under nitrogen flow before the protective tape is removed. Both, the etched ITO as well as the PET substrates are cleaned in a four step ultrasonic bath for 15 min each: Alkonox® detergent of 16 g/L in deionized water, (denaturated) ethanol (≥99.8 %, *Carl Roth*), aceton (≥99.9 %, *Carl Roth*) and 2-propanol (≥99.8 %, *Carl Roth*). After each cleaning step, the substrates, which are placed in a PTFE holder, are rinsed first with the previously used solvent and then with the following solvent without letting the samples dry in between. Further, the ultrasonic bath is filled with deionized water and processed without heating for all steps. After the final cleaning step, the substrates are taken individually from the solution bath and dried in a controlled manner under a constant flow of nitrogen.
Prior to the deposition of the PEDOT:PSS thin films from aqueous solution, the samples are exposed to an oxygen plasma. This step improves the hydrophilic properties of the surface and removes organic particles. The oxygen plasma is applied with a power of 200 W and a pressure of 0.4 mbar for 10 min.

Functional layer (PEDOT:PSS)

The aqueous PEDOT:PSS solution (PH1000) (see section 4.2.1) is stored at 4 °C. Prior to its deposition, the PEDOT:PSS solution is sonicated and filtered to ensure a homogeneous solution exclusive of agglomerates. After the appropriate amount of PH1000 is transferred to a cleaned glass vial, the PH1000 is ultrasonicated in a water bath without heating for 15 min. Subsequently, the solution is filtered with a poly(vinyldifluoride) (PVDF) filter of 0.45 μm pore size. After the above-described plasma treatment of the substrate, a 65 nm film of PEDOT:PSS is spin-coated with 2500 rpm for 60 s and an acceleration step (ACL) of 9. The films are subsequently transferred to a heating plate for 10 min at 140 °C. In the case of PET substrates, PEDOT:PSS is used directly as the transparent electrode. Therefore, half of the PEDOT:PSS layer is removed after spin-coating of the film and prior to the heat treatment. The film is removed with the help of a water-soaked cotton pad and a razor blade for a sharp edge.

Active layer

As active layer, the well-known and well-investigated P3HT:PC71BM system is used. Both materials are photoactive and there is evidence, that the materials degrade under oxygen and light exposure. Hence, all processing steps in which the two materials are

involved, are carried out in the dark. Both materials are weighed and dissolved separately with a concentration of 24 mg/ml in cholobenzene. After stirring the polymeric solutions separately for 1 h on a shaker, the P3HT solution is added to the PC71BM solution with a ratio of 1:0.8. Therein, it is important to add the solution of the the more soluble P3HT to the PC71BM solution and not vice versa to assure that the undissolved PC71BM is maintained. Prior to coating the blended solution of the two materials, the solution is prepared and stirred for approximately 12 h. The resulting solution is weighed at the beginning and at the end of the 12 h period in order to calculate the solvent loss by evaporation, which can be compensated by solvent addition prior to the film deposition (chlorobenzene density = 1.1 g/l). The active layer blend of P3HT andPC71BM is spin-coated as a 120 nm thick film with 1250 rpm for 30 s and an acceleration step (ACL) of 9, if not stated differently.

Counter electrode

For all photovoltaic devices investigated in this thesis, the counter metal electrode is deposited via a thermal evaporation setup, custom-built for the chair of functional materials (Lehrstuhl für funktionelle Materialien, TUM) by Dr. Robert Meier. After deposition of the active layer as described above, the samples are placed upside down into a shadow mask inside the evaporation setup. The mask defines the area onto which the metal is evaporated. Each substrate is evaporated with four so-called pixels. Under an atmospheric pressure of 2 mbar to 2.5 mbar and a working pressure of up to $8 \cdot 10^{-5}$ mbar, 100 nm thick metal contacts are evaporated. Before current-voltage characterization of the cells, the device is annealed at 150 °C for 30 min under constant nitrogen flow. For a correct current-voltage characterization, the area of the single pixel is evaluated from the microscope images via the ImageJ software. Further, to prevent short cuts during contacting of the cells, the pixels are contacted at the outer edges, where the ITO or PEDOT is removed from the substrate prior to film deposition, as described in the first step of the solar cell assembly description.

Chapter 5

Influence of Co-Solvents on Conductivity and Morphology of PEDOT:PSS Electrodes

Parts of the results shown in section 5.2 have been published in the article: *Molecular Reorientation and Structural Changes in Co-Solvent Treated Highly Conductive PEDOT:PSS Electrodes for Flexible ITO-Free Organic Electronics*[6] (C. M. Palumbiny et al., *The Journal of Material Chemistry C*, 118 (25): 13598–13606, 2014, DOI: 10.1021/jp501540y)

In the field of organic electronics and beyond, the polymer blend PEDOT:PSS is widely used as a functional electron blocking layer with high transparency and mechanical flexibility. The possibility to strongly increase its conductivity and the possibility to use PEDOT:PSS directly as an alternative to the brittle ITO electrode, has increased the amount of research activities in the field of organic electronics. Although strong effort is put into explaining the mechanism of conductivity and its increase, it yet remains unclear to a large extent. For most applications, the aqueous polymeric dispersion of PEDOT and PSS is used. Coated from this solution, PEDOT:PSS results in film conductivities in the range of 0.01 S/cm to 10 S/cm. As discussed in chapter 4, section 4.1.1, due to the hydrophobicity of the PEDOT part PEDOT:PSS blend in aqueous solution exhibits a core shell structure consisting of a PEDOT-rich core and a PSS-rich hydration shell. This structure also remains in the film to some extend. In the dissolved matrix, the short PEDOT chains ionically bind to the long PSS chains. Further, a PSS enrichment layer forms on the film surface. The addition of organic high boiling point co-solvents is known to increase the conductivity of PEDOT:PSS by up to three orders of magnitude. The

maximum conductivity value that can be reached with one specific solvent depends on the PEDOT:PSS formulation that is used. This effect can be traced back to different PEDOT to PSS ratios, particle sizes, distributions and molar masses.

Depending on the desired function of the PEDOT:PSS layer, either the conductivity perpendicular or the one in the thin film plane is more important. PEDOT:PSS is typically used as a functional selective electron blocking layer in OE devices. In this function, the hole blocking property perpendicular to the thin film plane, the so-called vertical conductivity, is important to transport the hole charge carriers to the external electrodes. For the application of highly conductive PEDOT:PSS directly as the main electrode in an ITO-free OE device as measured in this thesis, the conductivity along the thin film plane, the so-called lateral conductivity, becomes more important than the vertical conductivity. In this case, the charges are injected from the active layer directly to the PEDOT electrode, where they need to be transported in lateral direction to the external contacts. At this point it should be mentioned that the change in work function with co-solvents has to be kept in mind for application.[82–84] So far the increase in lateral conductivity by the use of co-solvents is explained in literature by different mechanisms listed in the following, partially contradicting each other:

- Screening effect: reduced coulombic attraction between PEDOT and PSS molecules[85]
- Enhanced electrostatic pairing resulting in enhanced conductivity by beneficial complex formation[21]
- Enhanced arrangement time for polymers by residual solvents in the film[86,87]
- Enhanced phase separation to smaller grains resulting in thinner isolating PSS phase and better intergrain transport[88,89]
- Larger PEDOT grains with better intragrain transport[83,90]
- Direct change of chain conformation[89,91]
- Enhanced crystallinity[92]
- Partial washing out of PSS from the matrix[93,94]

To understand the influence of co-solvents on the film conductivity of PEDOT:PSS, the films are treated with several solvents. The impact on the film properties is shown in the first part of the chapter (section 5.1). Section 5.1.1 shows the difference in treatment

parameters, i.e. the difference in doping and post-treatment. The influence of different high boiling point co-solvents on PEDOT:PSS film conductivity is investigated in section 5.1.2, before the influence of the treatment time (section 5.1.3) and the treatment cycles (section 5.1.4) is evaluated. Parts of section 5.1 were shown in the diploma thesis of C. Heller.[95] Although there are strong efforts to understand the mechanism of conductivity and its increase, the mechanism is not fully understood yet. The results listed above partially contradict each other and are so far based on investigations of the film surface with methods such as AFM, SEM or XPS. However, the conductivity of materials is in general strongly influenced by the structure of the inner film volume. Therefore, the second part of this chapter (section 5.2) combines different methods probing the electronic (section 5.2.1) and optical (section 5.2.2) properties, the surface morphology (section 5.2.3)as well as the inner film morphology (section 5.2.4) and molecular orientation (section 5.2.5) before introducing a model for the morphological changes upon doping and post-treatment of PEDOT:PSS films in section 5.2.6.

5.1 Processing parameters

PEDOT:PSS is processed from solution. The electrical and spectral properties of the final film depend very much on the film formation dynamics and thus on the processing parameters. Therefore, in the following, the influence of key processing parameters, such as the treatment method, the choice of co-solvent, the treatment time and cycles, on the final film characteristics are investigated systematically.

5.1.1 Doping and post-treatment

In this thesis, two methods of co-solvent treatment are investigated, namely co-solvent doping and co-solvent post-treatment. The experimental process is described in detail in section 4.2.1. It has been shown by Kim et al. that it is possible to increase the conductivity of PEDOT:PSS films by up to three orders of magnitude up to values comparable to indium thin oxide (ITO) which is the commonly used transparent electrode material for organic photovoltaics (OPV) or organic light emitting diodes (OLED).[5] Ethylene glycol (EG) is a common high boiling point co-solvent which is used in this this section as a model to prove the two above-mentioned treatment processes. For this purpose, PEDOT:PSS films coated from two commonly used concentrations of EG in aqueous PEDOT:PSS solution (4 wt% and 6 wt%) are compared to films coated from pure aqueous PEDOT:PSS solution. To compare the method of EG-doping to the method of EG post-treatment,

the three films are post-treated in an EG bath as shown in section 4.2.1. For all films, the sheet resistance (by four point probe) and the film thickness (by profilometry) was measured and the respective conductivities calculated as depicted in Figure 5.1. The conductivity clearly increases from pure PEDOT:PSS to 4 wt% to 6 wt%. The comparison to PEDOT:PSS films which are post-treated with EG shows that the conductivity for those films further increases independent of the initial EG-doping concentration. As the impact of the two methods on the final film conductivity is quite different, in section 5.2 the mechanism, which is responsible for the conductivity increase is investigated systematically.

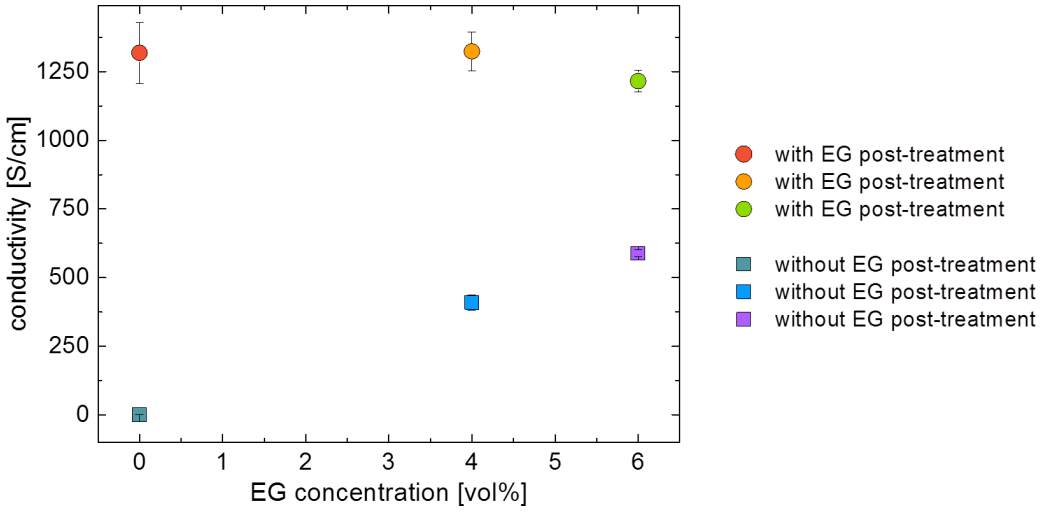

Figure 5.1: Conductvity of PEDOT:PSS films dependent on the ethylene glycol doping concentration and post-treatment.

For the method of EG post-treatment depending on the processing, the homogeneity varies and is hence examined in detail. To do so, the conductivity of three different EG post-treatment procedures are compared. In the first procedure, a solid PEDOT:PSS film is post-treated in an EG bath for 30 min. In the second procedure, the EG is dropped onto and subsequently spin-coated off the solid PEDOT:PSS film and in the third procedure, the PEDOT:PSS film is first post-treated in an EG bath for 2 min before the excess EG is subsequently spin-coated off. Figure 5.2 shows the conductivity of PEDOT:PSS films post-treated with these three procedures. As a reference the conductivity of pure PEDOT:PSS is given. Independent of the post-treatment processing, the conductivity of PEDOT:PSS is strongly improved compared to pure PEDOT:PSS. The highest values and smallest deviations are obtained for PEDOT:PSS films treated with a short EG bath plus subsequent spin-coating. Further, in contrast to the other two, this processing method results in homogeneous films on a large scale.

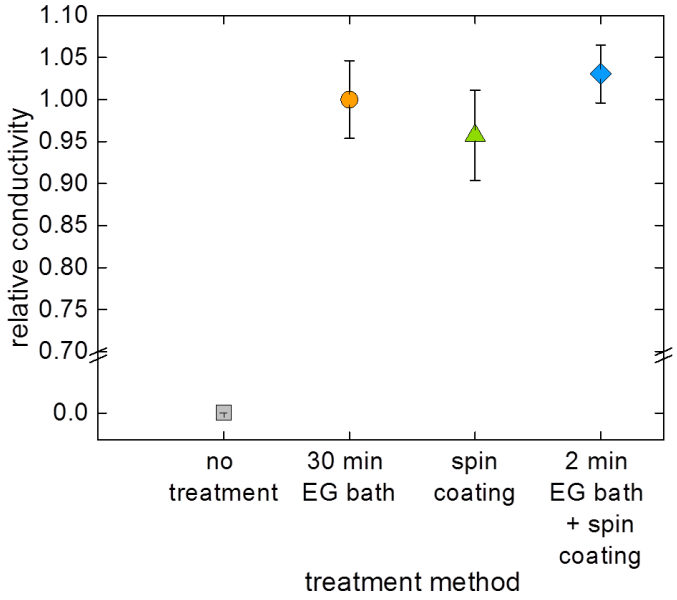

Figure 5.2: Relative conductvity of PEDOT:PSS films dependent on the procedure of EG post-treatment in comparison to pure PEDOT:PSS. Values are normalized to the conductivity ($\sigma = 962\,\mathrm{S/cm}$) of a PEDOT:PSS film treated in a 30 min EG bath.

5.1.2 Solvent

As shown above, post-treatment of PEDOT:PSS films with high boiling point co-solvents results in strongly increased conductivities of the film. So far, the effect has been shown in the last section for ethylene glycol (EG). In order to verify the choice of co-solvent, the effect of solvent post-treatment on the resulting film conductivity is compared for five organic co-solvents. Besides the already shown impact of EG, the co-solvents dimethylsulfoxide (DMSO), methanol (M), ethanol (E) and glycerol (G) are chosen. Table 4.2 of section 4.1.1 lists the basic physical-chemical properties of these solvents. In addition, table 5.1 lists properties by which the solvents are assumed to interact with the PEDOT:PSS and cause the morphological changes which are observed within this chapter. Table 5.1 hence compares the boiling point, polarity, dipole moment and viscosity of the chosen solvents. DMSO is a high boiling point co-solvent which possesses similar properties as EG. Further, M and E have similar characteristics. Glycerol has by far the highest boiling point in this comparison. Further G is a solvent which acts as a plasticizer for artificial micro-structuring and is hence added to the comparison. In order to give a valid comparison, the process of co-solvent post-treatment has to be comparable. Due to the various boiling points of the solvent, the post-treatment processing method of dropping the solution onto the solid PEDOT:PSS films and subsequent spin-coating is chosen. For this, the sample is placed onto the chuck of the spin-coater prior to dropping of the

solvent	**boiling point** [°C]	**dielectric constant**	**dipole moment** $[C \cdot m]$
ethylene glycol	197.0	41.0	2.28
dimethylsulfoxide	189.0	48.0	3.96
glycerol	290.0	42.0	2.60
methanol	64.7	32.0	1.70
ethanol	78.0	24.3	1.69

Table 5.1: Characteristic parameters of used solvents for PEDOT:PSS post-treatment: boiling point, dielectric constant and dipole moment. Values taken from [81].

solvents. Directly after spinning off the excess solvent, the samples are transferred immediately onto a heating plate ($T = 140\,°C$) where the co-solvents are evaporated according to procedure described in section 4.2.1. Only for G the annealing time is increased to 40 min in order to guarantee the sufficient evaporation of the solvent with a much higher boiling point compared to the other solvents. At this point it should be mentioned that even after annealing the samples, the high boiling point solvents remain in the film in a small concentration to not degrade the conductivity. Instead, the conductivity is increased by more than three orders in magnitude as as shown in this chapter. This shows clearly that residuals of co-solvent do not affect the conductivity of thin film PEDOT:PSS.

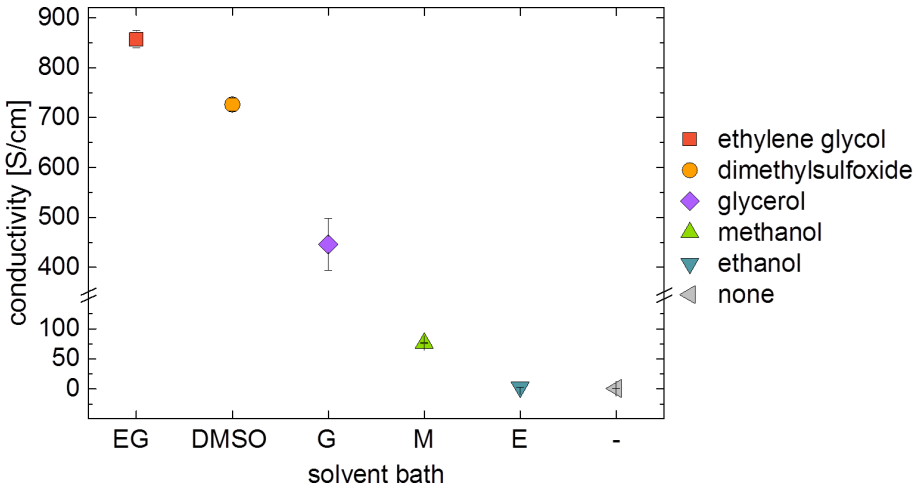

Figure 5.3: Conductivity of PEDOT:PSS films post-treated with different solvents.

Figure 5.3 compares the conductivity values of PEDOT:PSS films post-treated with the five different co-solvents. For comparison, the conductivity of pure PEDOT:PSS without post-treatment is given. The conductivity decreases for post-treatment with EG to

DMSO, G, M and E. The highest conductivity is shown for EG post-treated films. Films post-treated with DMSO, which is a co-solvent of similar physical-chemical properties, show a slightly lower conductivity. The PEDOT:PSS films which are post-treated with G show an increase in conductivity compared to pure PEDOT:PSS which is however lower than for EG or DMSO. The lower conductivity with co-solvent post-treatment are reached for M and E whereby the conductivity with M treatment is slightly higher. No direct correlation of the conductivity increase to one of the solvent properties given in table 5.1 is observed. Therefore, it is assumed that the boiling point and with it the film formation time as well as the dielectric constant and polarity of the solvent and with those the molecular interaction with PEDOT and PSS have an impact on the final film conductivity. The similarity of conductivity increase with EG and DMSO as well as with M and E resembles the similarity of their solvent properties and strengthens the above-mentioned explanation.

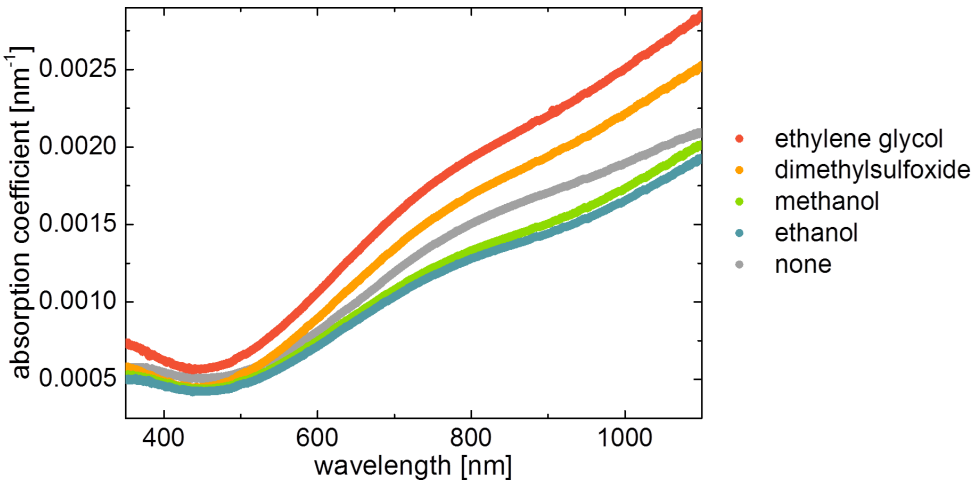

Figure 5.4: Absorption coefficient of PEDOT:PSS dependent on the post-treatment solvent.

The above-described conductivity is attributed to charge carrier transport along the polymer chain as well as by the hopping transport between polymers as discussed in section 3.9. The charge transport along polymer chains depends on the type of charge carriers. Depending on the oxidation of the PEDOT:PSS, the contribution of dication charge carriers (DC) and radical cation charge carriers (RC) varies. Neutral chains of PEDOT:PSS have been shown only when strong oxidizing agents are added to the system.[96] The other two charge carrier contributions can be investigated by UV-Vis spectroscopy. An absorption at wavelengths around 900 nm is attributed to RC charge carriers while absorption at wavelengths above 1000 nm is attributed to DC charge carriers. In general the absorption

coefficient, which is independent from the film thickness, increases for increasing conductivity. Figure 5.4 shows that the absorption coefficient for co-solvent post-treatment using EG or DMSO increases compared to pure PEDOT:PSS. This explains the strong increase in film conductivity shown in figure 5.3. For co-solvent treatment using M or E however, the absorption coefficient decreases compared to pure PEDOT:PSS for the observed wavelength range. According to the discussion above, the conductivity of these films should decrease which contradict the observation shown before. The absorption coefficient above 1000 nm however indicates an increase in absorption above 1000 nm and with this in DC charge carriers, which is assumed to continue beyond the measured range. By this, the slight increase in film conductivity compared to pure PEDOT:PSS is explained.

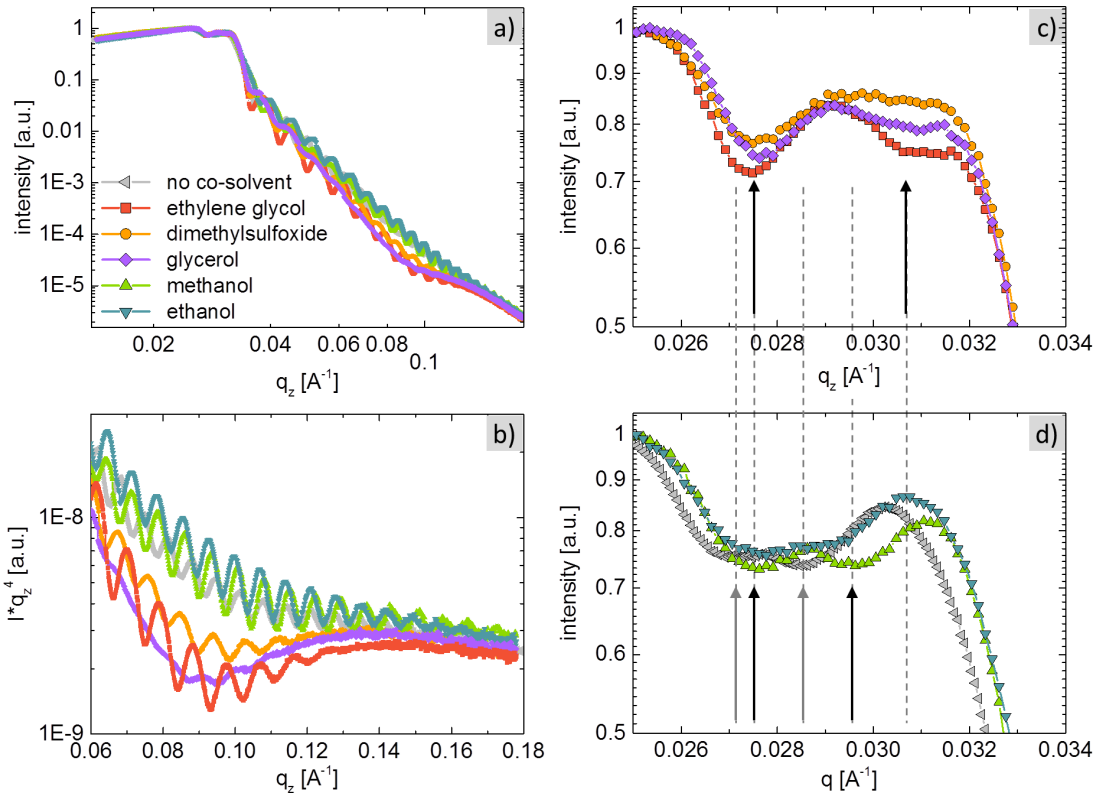

Figure 5.5: Normalized XRR data of PEDOT:PSS post-treated with different organic solvents. a) Reflectivity of all films shown for the measured q-range. b) Fresnel representation of the reflectivity at high q_z. c) Reflectivity of EG, DMSO and G post-treated films before the SiO_2 edge. d) Reflectivity of M and E post-treated films before the SiO_2 edge. In c) and d) the arrows and corresponding dashed lines show the critical edges of the vertical polymeric layers in the PEDOT:PSS thin films, which are a complex superposition of the scattering length density and the layer thickness.

The vertical composition of the PEDOT:PSS films is investigated by X-ray reflectivity

(XRR). The measured reflectivity curves of the five films post-treated with different co-solvents are depicted in figure 5.5. Figure 5.5a shows the total measured range with the strong drop in intensity at $0.0325\,\text{Å}^{-1}$, which originates from the critical angle of the glass substrate. At q_z-values above the critical angel of glass, the so-called Kiessig fringes are seen which originate from the interference of beams scattered at the air-polymer interface with beams scattered from the polymer-glass interface (see section 3.3.1). The less pronounced depth of the fringes for DMSO post-treatment and in particular for G post-treatment results from an increased surface roughness for these films. For high q_z-values an additional modulation of the intensity is observed. This modulation is particularly pronounced for the films post-treated with EG, DMSO and G. Figure 5.5b shows the high q_z-range in the Fresnel normalized representation where the generic decay of the reflectivity is removed by multiplying the intensity by the factor q_z^4. This representation is useful for highlighting features of the X-ray reflectivity curve by suppressing the generic decay. Hence, in this representation of the reflectivity in particular the modulation at high q_z-values is highlighted. These kind of modulations typically result from vertical thicknesses which are much smaller than the total film thickness, i.e an enrichment layer at the interface to air or the substrate.

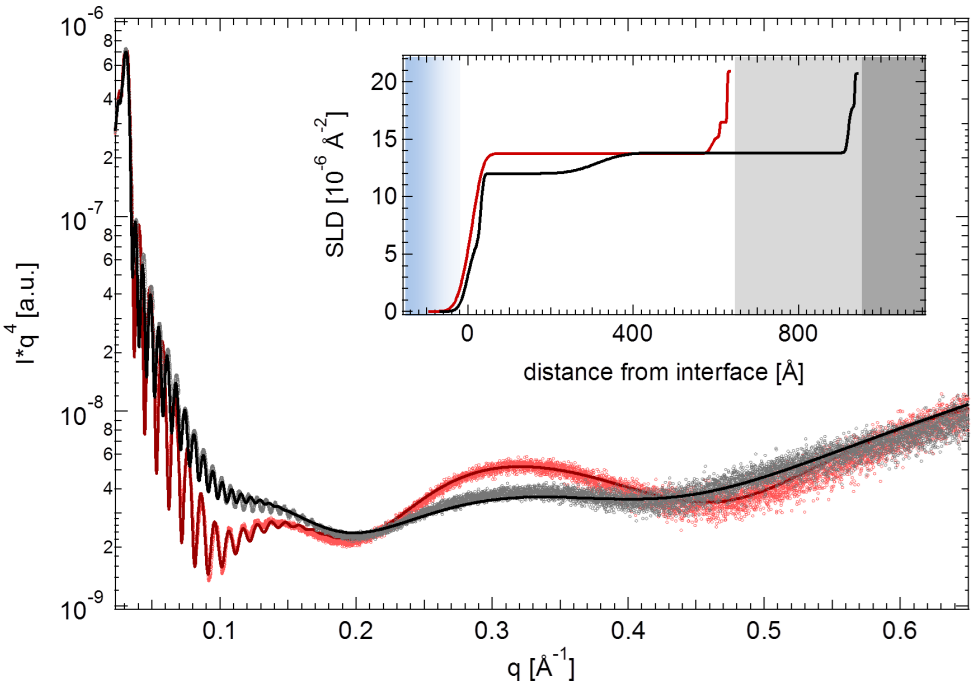

Figure 5.6: Simulation of the XRR data of PEDOT:PSS with and without ethylene glycol post-treatment. The inset depicts the scattering length density in dependence of the distance from the air-polymer interface for both films.

The modulation and thus the vertical film composition is similar for EG, DMSO and G post-treated PEDOT:PSS films. Post-treatment of the PEDOT:PSS films with M or E however results in a different vertical film composition as discussed later in this section. Figures 5.5c and 5.5d show a close-up to the small q-range where the observed intensity dips correspond to the vertical layers in the film. The first dip at $0.0275\,\text{Å}^{-1}$ is observed for all films in both figures. Its position originates from the thickness as well as from the scattering length density of the corresponding layer, the so-called critical edge, which is assigned to a PEDOT-rich layer. For larger q_z-values, the reflection is substantially different for the different solvent treatments. This dip shifts from $0.0305\,\text{Å}^{-1}$ for films treated with EG, DMSO or G (figures 5.5c) to $0.0295\,\text{Å}^{-1}$ for films treated with M or E (figures 5.5d).

The vertical film composition of a polymeric blend such as PEDOT:PSS consists of multiple layers of different scattering length densities (SLD). This is a consequence of changes in the material composition and density along the vertical film direction. Hence, the total reflectivity of the PEDOT:PSS polymeric films results from complex interference of reflected beams at multiple layers. In order to investigate the vertical film composition, the PEDOT:PSS films are simulated using the software Igor Pro 6 and the Motofit package for reflectivity data. The PEDOT:PSS films which are post-treated with EG, DMSO and G show similar reflectivity and by this similar vertical film composition. Further, the reflectivity of the pure PEDOT:PSS film is similar to the ones of M and E post-treated PEDOT:PSS films. The Fresnel representation in figure 5.6 exemplary shows the reflectivity of a pure and an EG post-treated PEDOT:PSS film together with the simulation of both films. The inset depicts the scattering length density as a depth profile corresponding to the two simulated reflectivity curves. Both reflectivity profiles are simulated by four polymeric layers between air and glass. The inset of figure 5.6 depicts the SLD profile and by this the simulated layer stratification starting from the air-polymer interface to the polymer-glass interface. For a pure PEDOT:PSS film an enrichment layer of 31 Å and a SLD of 6.3×10^{-6} Å at the film surface. This enrichment layer at the film surface is assigned to a PSS layer of low density. It is followed by a thick PEDOT:PSS layer with a density gradient. This gradient is simulated by two layers and a high interface roughness as depicted in the SLD profile. The 280 Å layer of SLD 12×10^{-6} Å just after the PSS surface enrichment layer is assigned to a PEDOT:PSS layer of low density. The PEDOT:PSS layer gradually becomes more dense (13.8×10^{-6} Å) towards the polymer-glass interface. At the interface to glass an 15 Å enrichment layer with a SLD as high as 17.8 Å is simulated. Assuming the same density for PEDOT and PSS, the theoretical SLD of a styrene sulfonate (SS) monomer is higher than of a 3,4-ethylenedioxythiophene

(EDOT) monomer. However, the EDOT monomers crystallize much stronger than the SS monomers which results in a higher density of PEDOT crystallites and by this a higher SLD. Therefore, the surface enrichment layer is allocated to a PSS-rich phase while the substrate enrichment layer is allocated to a PEDOT-rich phase. It is known that co-solvent treatment can wash off the PSS surface enrichment of PEDOT:PSS films. The reflectivity simulation of the EG post-treated films supports this fact. The total layer thickness is reduced by the removal of PSS from the film surface and volume. The surface enrichment layer is reduced to 22.5 Å and increased in SLD to 9×10^{-6} Å which is a clear indication toward a more PEDOT-rich phase at the surface compared to pure PEDOT:PSS films. Further, the thick PEDOT:PSS films does not show the gradient in SLD as seen for pure PEDOT:PSS films, but shows constant SLD of 13.8×10^{-6} Å. At the polymer-glass interface, the PEDOT enrichment layer is simulated by two layer (19 Å and 18.8 Å) which are gradually increasing in SLD from 15.0×10^{-6} Å to 16.5×10^{-6} Å.

5.1.3 Time

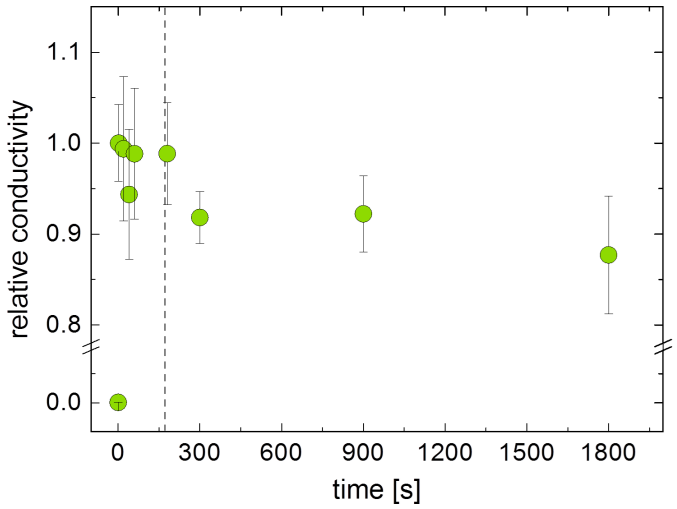

Figure 5.7: Relative conductivity of PEDOT:PSS dependent on the EG post-treatment time. Values are normalized to the conductivity value of PEDOT:PSS treated in an EG bath of 2 s ($\sigma = 1254$ S/cm).

As shown in figure 5.2 the post-treatment method of a short EG bath with subsequent spin-coating of the excess solvent results in the best conductivity values. For reproducible results, the time of the EG bath needs to be controlled and verified. Therefore, a series of PEDOT films post-treated with EG bath times ranging from 0 s to 1800 s is evaluated. The obtained conductivity values for all post-treatment times are normalized to the maximum conductivity as depicted in figure 5.7. This series clearly show the strong impact

of EG on PEDOT:PSS film conductivity, which shows to be independent on the EG bath time up to 180 s before the conductivity decays for the EG bath time of 300 s and beyond. To assure a reproducible process with high resulting conductivity, a bath time of 180 s is chosen as a standard recipe in the following, if not stated differently.

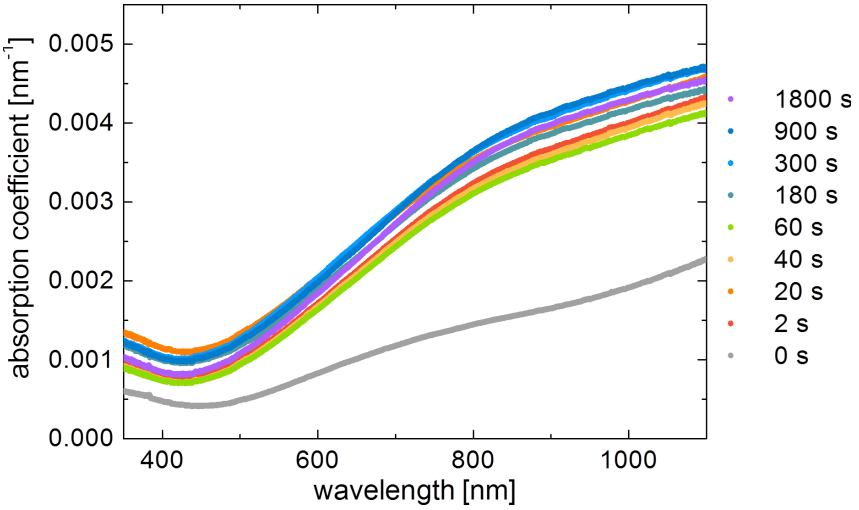

Figure 5.8: Absorption coefficient of PEDOT:PSS for different EG post-treatment time.

With the increase in EG bath time, a change in the film morphology or composition could occur which would impact the spectroscopic properties of the film and by this the quality of the transparent electrodes and their application. In order to exclude this effect, UV-Vis spectroscopy measurements of all films are performed. Figure 5.8 shows the absorption coefficient as a function of the wavelength for all EG bath times. The clear change between pure non-treated PEDOT:PSS and the EG post-treated films is obvious. An increased overall absorption coefficient as well as an increase in the 900 nm absorption is observed for EG-post-treated films. The overall increase leads to a general increase in charge carriers. The slight increase in the 900 nm absorption (change of the intensity distribution compared to pure PEDOT:PSS) results from a change in the molecular chain conformation by the interaction with the EG molecules and hence in more radical cation (RC) charge carriers compared to pure PEDOT:PSS. A more general discussion on the different charge carrier contributions can be found in sections 3.9 and 5.1.2. The decrease in conductivity for EG bath times above 300 s however cannot be explained by the absorption coefficients shown here. Based on the results obtained here, the general strong increase in conductivity with EG post-treatment is attributed to the general increase in charge carriers rather than to the increase in RC charge carriers.

5.1.4 Cycle

In this section, the influence of a multiple post-treatment with EG on PEDOT:PPSS thin films is investigated. Figure 5.9 shows the conductivity values for PEDOT:PSS films post-treated in multiple cycles compared to pure PEDOT:PSS. Contradicting perhaps the expectations, the conductivity decreases slightly from one to two to four treatment cycles. This however verifies that a single post-treatment procedure is sufficient to reach the maximum conductivity value.

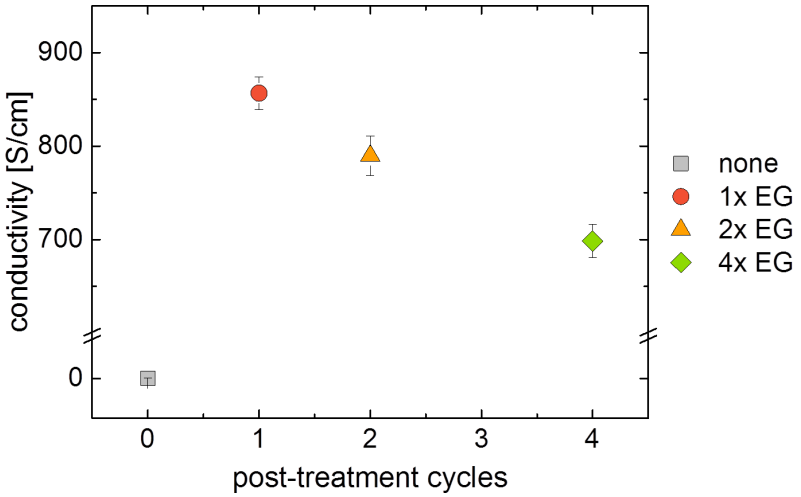

Figure 5.9: Conductivity of pure PEDOT:PSS compared to EG post-treatment and multiple cycles.

Similar to the investigations of different post-treatment solvents and times, UV-Vis spectroscopy of the films is used to investigate the absorption coefficient dependent on the wavelength of illumination. The dependence shown in figure 5.10 depicts an increase in total absorption coefficient as well as an increase in radial cation charge carriers with a maximum at 900 nm (see discussion in section 5). The increase in absorption coefficient would be an indication for an increase in charge carriers. This however is not in accordance with the conductivity trend observed. Multiple EG post-treatment leads to repeated interaction of the solvent molecules with the polymers. After this positive effect on the polymer film morphology at the beginning, reduction of the polymers sets in and by this to an enhancement of the RC charge carriers. Although the absorption coefficient for wavelength above 1200 nm could not be detected with the available UV-Vis spectrometer, based on the slope of the absorption curve at high wavelength a decrease in the dication charge carrier contribution is assumed. By this, the decrease in conductivity for multiple EG post-treatment could be explained.

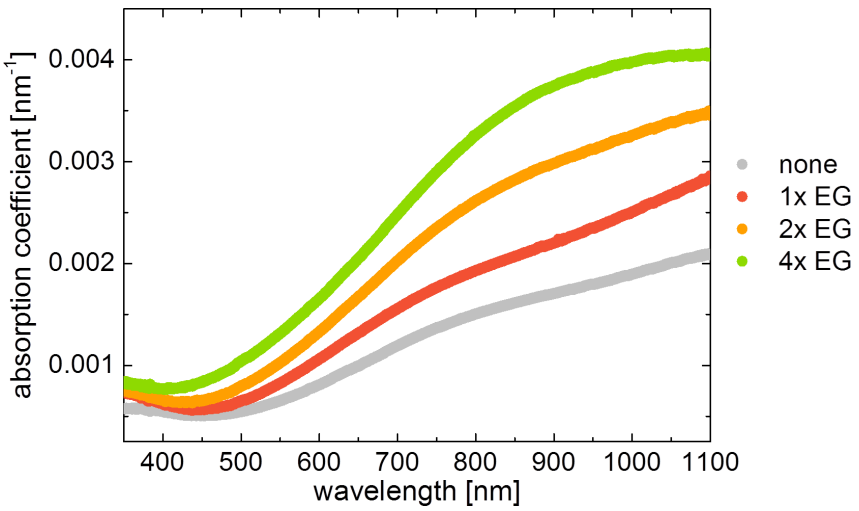

Figure 5.10: Absorption coefficient of pure PEDOT:PSS compared to one, two and four EG post-treatment cycles.

In order to investigate the vertical composition of the PEDOT:PSS films which are post-treated in multiple cycles, X-ray reflectivity measurements are performed. Figure 5.11a shows the reflectivity curve of the three PEDOT:PSS films for the measured q_z-range. The Kiessig fringes (see section 3.3.1) are modulated by fringes of much larger oscillation period (thinner layers) as seen by the shoulder at high q_z and more clear by the broad peak in the Fresnel representation (inset of figure 5.11a). This modulation results from enrichment layers at the air-polymer and polymer-glass interfaces as discussed already in section 5.1.2 and remains for all post-treatment cycles. Figure 5.11b shows a close-up to the low q-range where the observed dips correspond to the critical edges of the materials. For the critical edge at $\approx 0.0275\,\text{Å}^{-1}$, a shift towards higher q_z-values is observed for multiple post-treatment cycles. Further, the critical edge at $\approx 0.0305\,\text{Å}^{-1}$ becomes less pronounced with increasing post-treatment cycle. A shift in the critical edges can result from changes in the materials density and by this in the SLD as well as from the change in layer thickness.

To identify the reason for the above-discussed change in critical edges, the reflectivity of the three PEDOT:PSS films is simulated using the software Igor Pro 6 and the Motofit package for reflectivity data. In the Fresnel representation (figure 5.12) the reflectivity data is shown together with the simulated reflectivity curve. The inset depicts the scattering length density as a depth profile corresponding to the three simulated reflectivity curves. For the PEDOT:PSS film post-treated with EG in one cycle, the surface enrichment layer is 22.5 Å thick with a SLD of 9×10^{-6} Å which is a clear indication for

a more PEDOT-rich phase at the surface compared to pure PEDOT:PSS films (see section 5.1.2). The thick PEDOT:PSS film shows a constant SLD of 13.8×10^{-6} Å. At the polymer-glass interface, the PEDOT enrichment layer is simulated by two layers (19 Å and 18.8 Å) which are gradually increasing in SLD from 15.2×10^{-6} Å to 16.5×10^{-6} Å. The surface enrichment layer is allocated to a PEDOT:PSS phase of low density while the substrate enrichment layer is allocated to a PEDOT-rich phase. Further, for multiple post-treatment cycles the reflectivity data is simulated by simply changing the layer thickness of the thick PEDOT:PSS layer. This can be seen in the SLD profile shown in the inset of figure 5.12. It is concluded that the use of multiple EG post-treatment cycles changes the total film thickness, in this case from 690 Å to 570 Å, but not the enrichment layers at the air-polymer and polymer-glass interfaces.

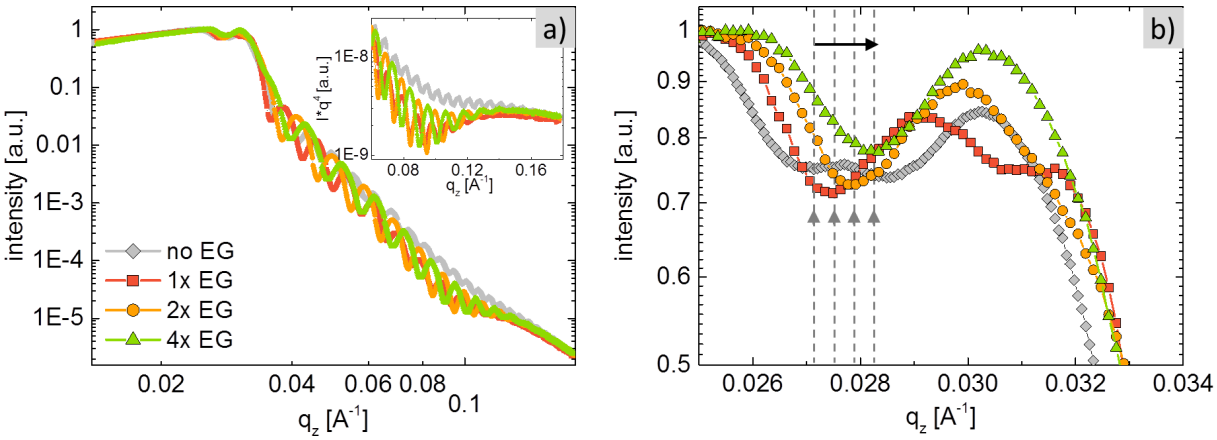

Figure 5.11: a) Normalized XRR data of PEDOT:PSS post-treated with ethylene glycol in dependence of the post-treatment cycle number. The inset depicts a close-up to the high q_z regime in the Fresnel representation b) Close-up to the low q_z regime.

In summary, as discussed for the UV-Vis spectroscopy above, the main reason for the decrease in conductivity with multiple post-treatment cycles is attributed to reduction of the PEDOT:PSS by EG which leads to the observed increase in RC charge carriers and to the expected decrease in DC charge carriers. Based on the obtained observations within the framework of this thesis a single post-treatment cycle of PEDOT:PSS with EG is used.

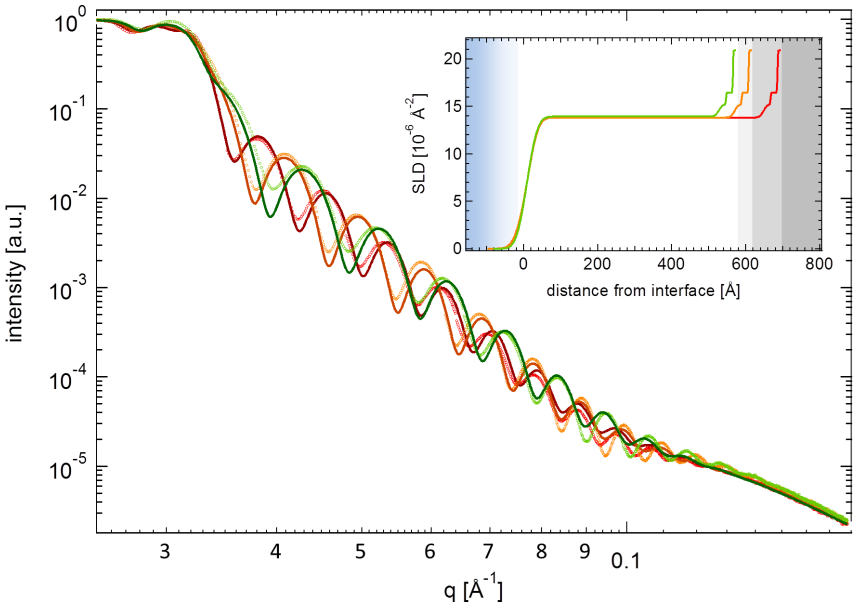

Figure 5.12: Simulation (solid line) of the measured XRR data (sympols) of PEDOT:PSS post-treated with ethylene glycol in dependence of the number of post-treatment cycle. The inset shows the corresponding scattering length density in dependence of the distance from the air-polymer interface for the three films of varying post-treatment cycles.

5.2 Ethylene glycol and glycerol treated PEDOT:PSS

To address the correlation between inner film structure and conductivity, the changes of the inner film structure of PEDOT:PSS films that arise with ethylene glycol post-treatment are investigated. As discussed in section 5.2, using this method the conductivity is increased reaching values comparable to those of ITO.[5] Additionally, a comparison is drawn to glycerol doping. Co-solvent addition of glycerol is also known to enhance the conductivity of the resulting layer.[97] Furthermore, glycerol acts as a plasticizer for the application of structuring methods on PEDOT:PSS for enhanced light absorption and efficiency enhancement in OPV devices as shown in contiguous studies[98] Secondary doping, as shown in this thesis using high boiling point co-solvents, allows the molecules to rearrange within the thin film.

In order to systematically investigate the effect of glycerol doping and EG post-treatment, six different concentrations of glycerol, ranging from 0 mg/ml to 50 mg/ml, were used. For each glycerol concentration the comparison is drawn to additional co-solvent post-treatment using EG. The routine for doping and post-treatment was shown and discussed in detail in section 4.2.1. In the following sections, glycerol and EG post-treatment of

PEDOT:PSS films are compared by investigating their influence on basic thin film properties such as the film conductivity 5.2.1 and absorption coefficient 5.2.2. Further, the effect of glycerol additive and EG post-treatment on the PEDOT:PSS surface 5.2.3 and inner film morphology 5.2.4 as well as PEDOT molecular orientation 5.2.5 is investigated. Section 5.2.6 combines the result in a suggested model explaining the conductivity increase by morphological changes.

5.2.1 Electronic characterization

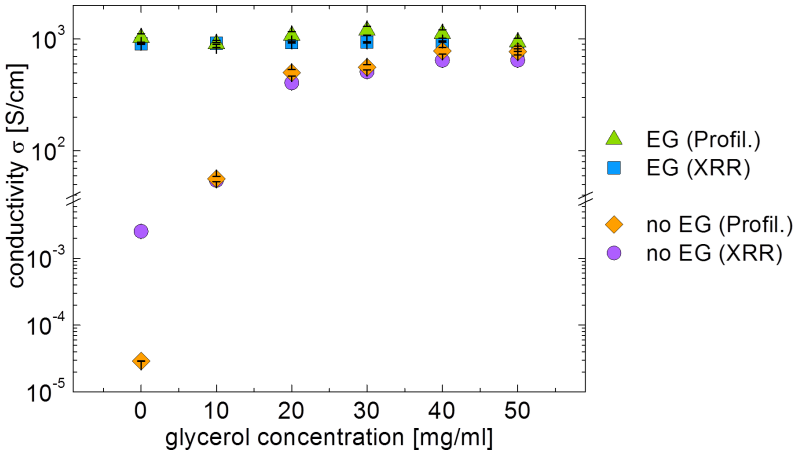

Figure 5.13: Conductivity of PEDOT:PSS films with different glycerol concentration. The conductivity is shown for all films with as well as without additional EG-post-treatment.

As motivated before, in order to use PEDOT:PSS as an electrode, its conductivity needs to be enhanced to the level of ITO (10^3 S/cm). Figure 5.13 shows the lateral conductivity of the PEDOT:PSS films doped with glycerol in concentrations from 0 mg/ml to 50 mg/ml. Moreover, the conductivity of all these films after additional post-treatment with ethylene glycol is shown. It is evident from figure 5.13 that EG-post-treatment increases the lateral conductivity dramatically independent of the initial G-additive concentration. With this, conductivity values as high as 1000 S/cm are reached. Pure glycerol doping however, increases the conductivity steadily with increasing doping concentration. Finally, high concentrations of glycerol result in a similar conductivity to that for EG-post-treatment.

For the calculation of film conductivity, the film thickness is needed. The conductivity values shown above are calculated from the sheet resistance (obtained by four-point-probe measurements, see section 3.1.3) and the thickness. The correct determination of the polymer film thickness directly influences the calculated conductivity and therefore

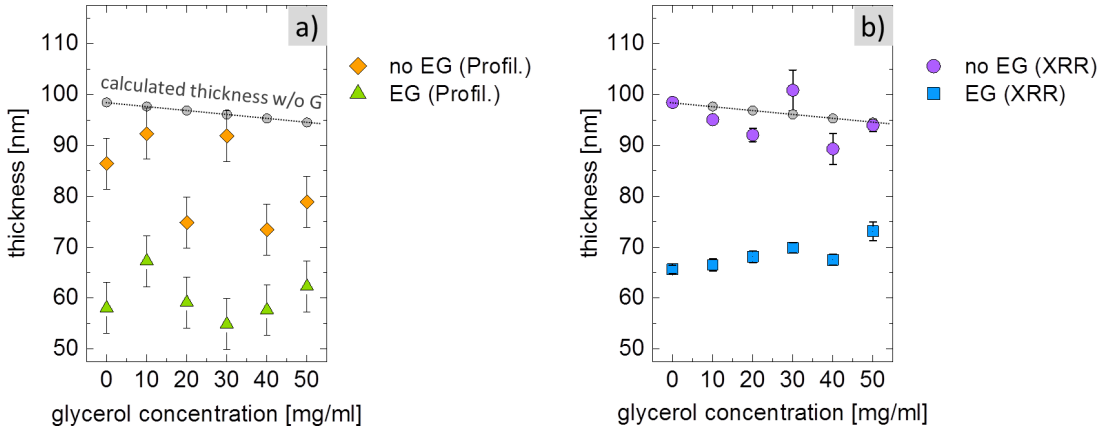

Figure 5.14: Thickness of PEDOT:PSS films with different glycerol concentration. Thicknesses determined with a) profilometry and b) XRR. The thicknesses are shown for all films with as well as without additional post-treatment with ethylene glycol (see legend).

has to be handled with care. As the film thickness can be determined by various methods, in this case profilometry (section 3.2.1) and X-ray reflectivity (XRR) (section 3.3.1), the conductivity values shown above are calculated with thicknesses measured by both methods. Supplementary, the thicknesses for all films determined with both techniques are shown in figure 5.14. Figure 5.14a shows the values obtained from profilometry and figure 5.14b shows the values obtained from XRR. Profilometry is the faster and easier to use method compared to the more time-consuming XRR method. However, for the relatively soft polymer films, the determination of the thickness with the non-destructive XRR method is more precise. Comparing the data shown in figures 5.14a and b, an offset of approximately 15 nm to 20 nm is observed. Further, comparing the measured values to the calculated thicknesses without glycerol, the better matching of the XRR values with the calculated values is evident.

5.2.2 Spectroscopic characterization

To address the optical properties of PEDOT:PSS films as a function of the modification method used, the absorption coefficients of PEDOT:PSS with and without EG post-treatment are determined from the UV-Vis spectroscopy and the thickness for all glycerol concentrations (section 3.1.1). All absorption coefficients are depicted together in figure 5.15 in comparison to pure PSS. A higher absorption coefficient of the same material composition, in this case PEDOT and PSS, indicates an optically denser film morphology. It is obvious from figure 5.15 that the EG-post-treated PEDOT:PSS films are optically more dense than films that are solely doped with glycerol. For the case of EG post-

treatment, the PSS molecules are partially washed from the polymer matrix. Thereby the PEDOT molecules gain space and collapse as proven and discussed in section 5.2.4. This observation explains the decrease in film thickness with EG post-treatment as well as the increase in optical density for higher wavelengths, since at these wavelengths PSS hardly contributes to the absorption.

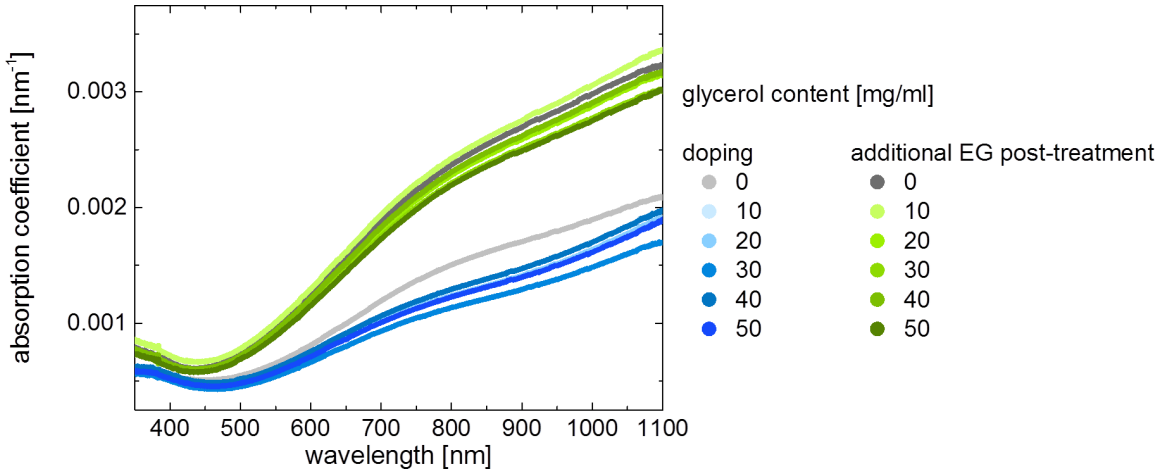

Figure 5.15: Absorption of PEDOT:PSS films doped with different glycerol content together with the absorption with additional ethylene glycol post-treatment.

5.2.3 Structural characterization of the surface

In section 5.2.1 it was shown that a high concentration of glycerol results in similar conductivity values to that of EG-post-treatment. As the film properties in polymeric blends, such as the conductivity or the absorption, depend on the film morphology, it is assumed that high glycerol doping concentration results in a similar film morphology than EG-post-treatment. In order to investigate the morphology of the PEDOT:PSS films, scanning electron microscopy images (SEM) are analyzed. Figure 5.16 shows the surface morphology of pure PEDOT:PSS compared to EG-post-treatment of the same film on the left and the morphology of G-doped PEDOT:PSS in comparison to additional EG-post-treatment of the same films on the right. Comparing the SEM images, a more pronounced contrast of the surface structure is seen for all co-solvent treatments (b-d).

For investigation of the surface morphology more quantitatively, power spectral density functions (PSD) are extracted from the micrographs. To obtain the PSD function, the 2D images are first Fourier transformed as shown for all films in the lower row of figure 5.16. Second, the Fourier transformed images are radially integrated resulting in the PSD func-

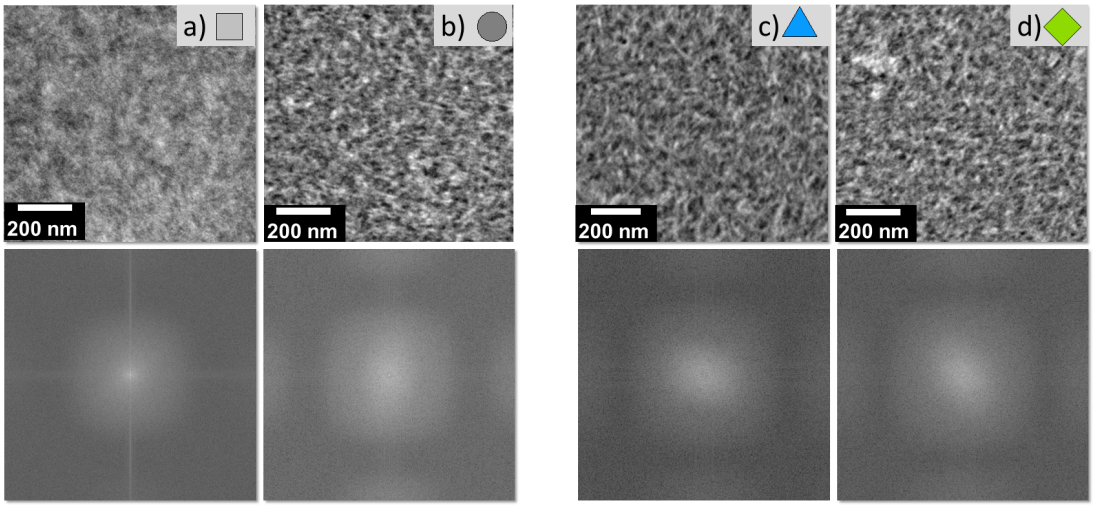

Figure 5.16: Scanning electron microscopy (SEM) images (top row) of PEDOT:PSS films with and without glycerol doping and ethylene glycol post-treatment. The Fourier transformation of the SEM images is shown in the lower row.

tions (section 3.2.2). The PSD function thereby represents the lateral scattering of the surface. For the q_y-range of interest (q_y =0.1 nm^{-1} to q_y =0.8 nm^{-1}), figure 5.17 shows the PSD function of glycerol-doped and pure PEDOT:PSS films, both with and without EG-post-treatment. An enhanced scattering intensity is observed for the glycerol doped, EG-post-treated and both glycerol doped and EG-post-treated films. The enhanced intensity thereby indicates a structural change at the surface in the presence of co-solvents. Since SEM provides only information about the film surface, in the following section, the inner film structure is investigated with grazing incidence small angle scattering.

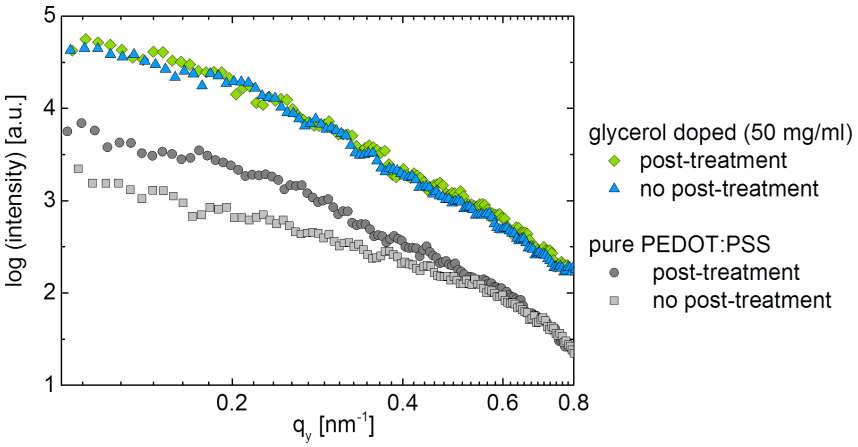

Figure 5.17: Power spectral density (PSD) function obtained by Fourier transformation and radial integration of SEM images. PSD for PEDOT:PSS films with and without glycerol doping and ethylene glycol post-treatment.

5.2.4 Structural characterization of the film volume

To investigate the inner film morphology, grazing incidence small angle X-ray scattering (GISAXS) is used (section 3.3.2). Scattering signals are detected as two-dimensional (2D) patterns for the pure and the glycerol-doped films, both without and with EG-post-treatment as depicted in figure 5.18. From the 2D scattering images, a clear change in the scattering pattern from the pure film to all co-solvent treated films is observed.

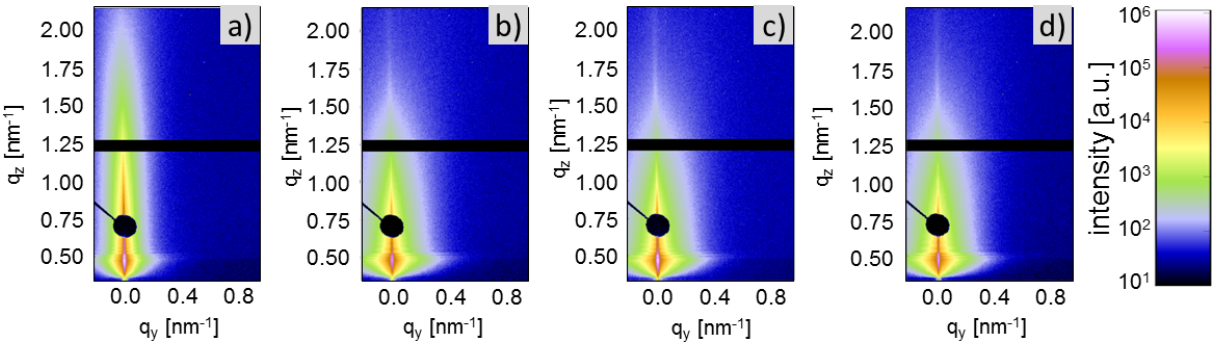

Figure 5.18: 2D grazing incidence small angle X-ray scattering (GISAXS) patterns of pure (a,b) and glycerol doped (c,d) PEDOT:PSS films, both without (a,c) and with (b,d) additionally ethylene glycol post-treatment.

The lateral scattering along q_y at the material sensitive Yoneda peak position[99] is enhanced for all modifications of the pristine film. This is shown in the horizontal line cuts of the 2D GISAXS data that are taken at the Yoneda scattering of PEDOT. Figure 5.19 shows the cuts together with their fits. It is evident that the difference of the scattering intensity that can be seen between non-post-treated and EG post-treated films (black and green symbols), decreases with increasing G-additive concentration. This trend follows the trend of the conductivity which is shown in section 5.2.1.

The horizontal line cuts are modeled with two form and two corresponding structure factors. The domain radii (form factor), distances (structure factor), distributions and shape of domains (used model) are extracted from the fitting model used. In figures 5.20 and 5.21 the radii and distances, as extracted from the form and structure factors respectively, are plotted. The dashed lines, together with the gray arrows, act as guide to the eye for the observed changes in the lateral scattering and show how the radius and the distance of the small domains decrease with EG-post-treatment.

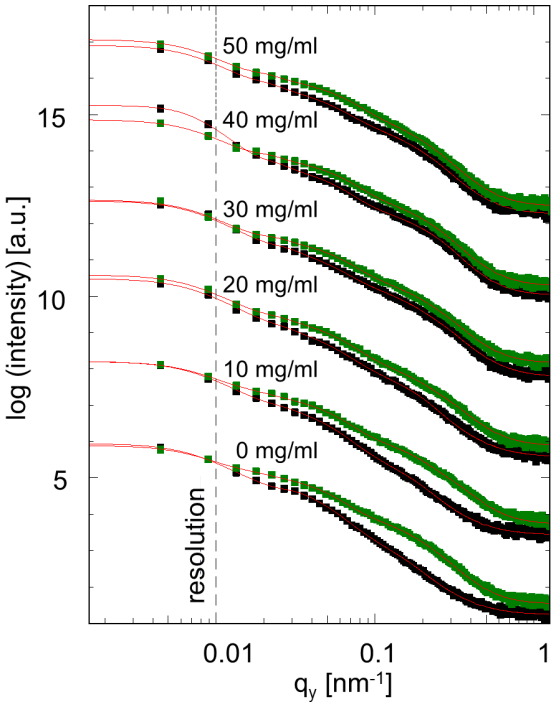

Figure 5.19: Horizontal line cuts of the grazing incidence small angle X-ray scattering (GISAXS) data of PEDOT:PSS films doped with glycerol (0 mg/ml-50 mg/ml) (black symbols) in comparison to the same films additionally post-treated with ethylene glycol (green symbols).

For the larger domains shown in figure 5.20 the distance, meaning the distance between PEDOT grains, increases for higher glycerol concentration. Further, the difference in distance between glycerol doping and additional EG-post-treatment decreases with increased glycerol concentration. The radius on the other hand decreases with increasing glycerol concentration and decreases further by a constant factor for additional EG-post-treatment. This means that with higher glycerol concentration the large PEDOT domains shrink in size while their distance increases.

For the small domains shown in figure 5.21, no clear trend in the structure size or structure distance is observed for the different glycerol concentrations. With additional EG post-treatment however, both the structure size and structure distance decrease. The small PEDOT grains hence decrease in size and distance. This indicates a trend towards denser domain packing. Together with the above discussed trend for the larger domains, a rupture of the large domains into smaller and denser packed domains is likely.

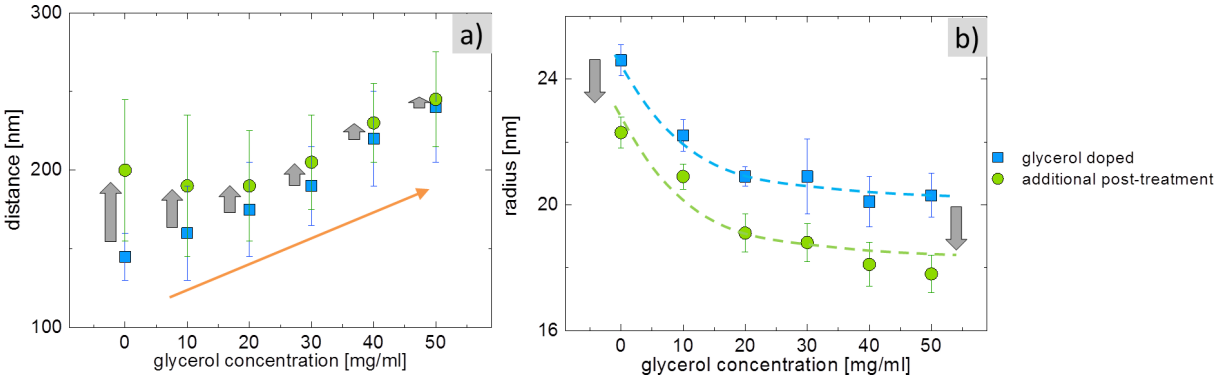

Figure 5.20: Distance and radius of large PEDOT domains in films doped with glycerol (0 mg/ml-50 mg/ml) in comparison to the same films additionally post-treated with ethylene glycol.

In total a clear tendency towards smaller domains and domain rupture at high additive concentration as well as post-treatment is observed. For the latter, the domains are additionally denser packed. It is noted that a different film treatment can lead to different observations due to different film formation times.[100] The films are transferred onto a heating plate, T = 140 °C subsequently after each spin-casting step as explained in section 4.2.1. Thereby aggregation of the domains within the films after solvent treatment is suppressed and therefore unlikely.

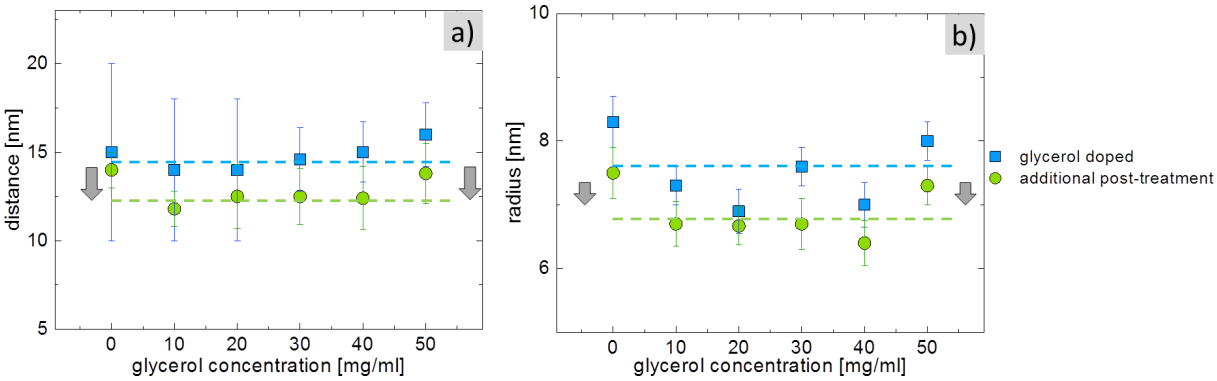

Figure 5.21: Distance and radius of small PEDOT domains in films doped with glycerol (0 mg/ml-50 mg/ml) in comparison to the same films additionally post-treated with ethylene glycol.

Comparison of surface and inner film morphology

To draw a direct comparison between the surface and the inner film structures, the GISAXS-derived horizontal line cuts (figure 5.19) are compared to the SEM-derived PSD

function (section 5.2.3, figure 5.17). The enhanced intensity for the three co-solvent treated films compared to the pristine PEDOT:PSS film is similar in the PSD and the horizontal line cuts. It is concluded that the structural changes observed on the film surface upon co-solvent treatment are similar to the changes in the inner film volume of the PEDOT:PSS. Furthermore, the structure information of the inner film volume (from GISAXS) is a statistical information of a large volume while the structure information of the surface (from SEM) is a local information. It is hence confirmed that the local picture also represents the inner morphology of the whole film and, in turn that the local topography is similar on the whole sample. This similarity of the surface and inner film structure is not always given and needs to be confirmed for other systems when using these techniques. Further, from the GISAXS fits detailed information on shape, size and distribution of domains present in the inner film volume can be extracted as shown in figures 5.20 and 5.21.

5.2.5 Molecular orientation

Besides the morphological changes on larger scale shown in sections 5.2.3 and 5.2.4, also the orientation of the PEDOT chains is expected to have great impact on the lateral conductivity of the film as the conductivity in polymeric systems is anisotropic (section 3.9).[101] Grazing incidence wide angle X-ray scattering (GIWAXS) measurements, as exemplary shown in figure 5.22 are performed in order to investigate the crystalline nature of PEDOT:PSS in detail (section 3.3.3). Due to the shorter sample-detector distance used for GIWAXS measurements compared to GISAXS, smaller length scales are detected, which are in the order of molecular stacking distances.

From the scattering signal corresponding to the π-π stacking of the PEDOT polymer[92,101] the orientation of the PEDOT stacking planes is determined. The integrated intensity along the azimuthal scattering from the π-π stacking is shown in figure 5.23. In this representation, the edge-on molecular orientation, with the polymer chain and the π-π stacking in the plane, can be distinguished from the face-on orientation, with the π-π stacking vertical to the plane. The orientation of the molecules is thereby distinguished by the scattering angle represented by the x-axis in figure 5.23. Scattering intensities detected between $0\,^\circ$ and $45\,^\circ$ as well as $135\,^\circ$ and $180\,^\circ$ results from edge-on oriented crystals whereas intensities between $45\,^\circ$ and $135\,^\circ$ results from face-on oriented crystals.

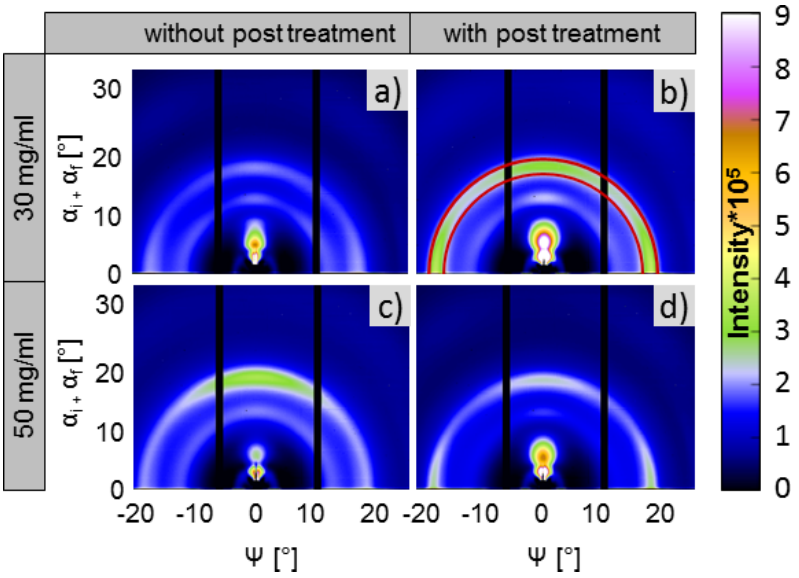

Figure 5.22: 2D grazing incidence wide angle X-ray scattering (GIWAXS) patterns of PEDOT:PSS films. 30 mg/ml (a,b) and 50 mg/ml (c,d) glycerol doped PEDOT:PSS films, both without (a,c) and with (b,d) additionally ethylene glycol post-treatment. Images are corrected for background scattering.

Figure 5.23 shows the angular-dependent scattering intensities resulting from π-π stacked PEDOT molecules. Figure 5.23a shows the intensity distribution of PEDOT:PSS films doped with different glycerol concentrations compared to pure PEDOT:PSS. The pure PEDOT:PSS film exhibits edge-on as well as face-on orientation with an overall low intensity compared to the other films. This indicates an expected lower crystallinity of the pure PEDOT:PSS film. The addition of glycerol to the PEDOT:PSS system leads to a reorientation of the molecules towards more face-on oriented crystals as the strongly enhanced intensity at χ =90 ° and the suppressed intensity at χ =0 ° and χ =180 ° indicates. The trend towards face-on orientation is further enhanced for increased glycerol concentrations. Additionally, the overall intensity and hence the overall crystallinity is enhanced for increased glycerol concentration.

Figure 5.23b shows the intensity distribution of PEDOT:PSS films with additional EG post-treatment of the glycerol doped PEDOT:PSS films shown in figure 5.23a. Comparing the two figures, a clear reorientation of the PEDOT crystallites towards enhanced edge-on orientation independent of the initial G-additive concentration is observed. Further, the scattering intensity and thereby the overall crystallinity for EG post-treated films is independent of the initial glycerol concentration before the EG post-treatment.

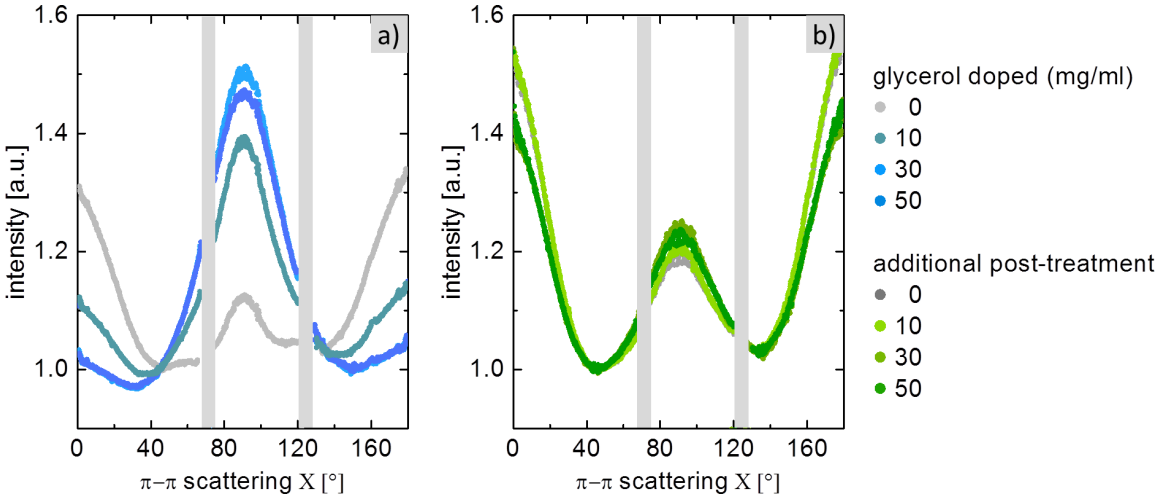

Figure 5.23: Angular scattering profile along one the π-π scattering distance of PEDOT molecules. Data shown for different glycerol doping concentrations (a) and additional ethylene glycol post-treatment (b).

For a more quantitative evaluation of the molecular orientation, the edge-on to face-on ratio is calculated. To obtain the edge-on to face-on ratio, first the areas under the partial curves corresponding to the molecular orientations are calculated. Second, the specific areas are divided by each other. The edge-on to face-on orientation is determined by dividing the area corresponding to the edge-on orientated crystals by the area corresponding to the face-on oriented crystals. The estimated edge-on to face-on ratio for all PEDOT:PSS film parameters are shown in figure 5.24.

The orientation of PEDOT crystallites is assumed to influence the film conductivity. This valid assumption is based on the anisotropic conductivity in PEDOT molecules and crystallites with the highest conductivity along the backbone chain of the PEDOT, the second highest conductivity along the π-π stacking of the PEDOT molecules and a low conductivity along the side chain of the molecule side chains.[101] Therein, charge transport along the backbone is described by delocalized charges whereas the charge transport along the π-π stacking is described by charge hopping transport.

To understand the conductivity of the PEDOT:PSS film on the molecular level, the conductivity of the film is related to the molecular orientation of crystals. With respect to pure PEDOT:PSS, the EG-post-treated films show an enhanced edge-on orientation of PEDOT crystallites as shown above. In edge-on oriented crystals the backbone as well as the π-π stacking is oriented parallel to the substrate surface. Therefore, the lateral conductivity within one edge-on oriented crystallite and most likely also between two crystallites

is improved by an enhanced edge-on orientation. This enhancement of the edge-on orientation gives rise to the assumption that the increase in lateral conductivity (section 5.2.1) is not only caused by the formation of small and densely packed PEDOT domains as shown in section 5.2.4 or the known removal of PSS [85,102] discussed in section 5.2.2 but also the reorientation of the molecules within the crystallites to enhanced edge-on orientation increases the lateral conductivity. The reorientation of PEDOT molecules from face-on to edge-on due to EG-post-treatment is observed in the corresponding publication for the very first time, to the best of our knowledge. [6]

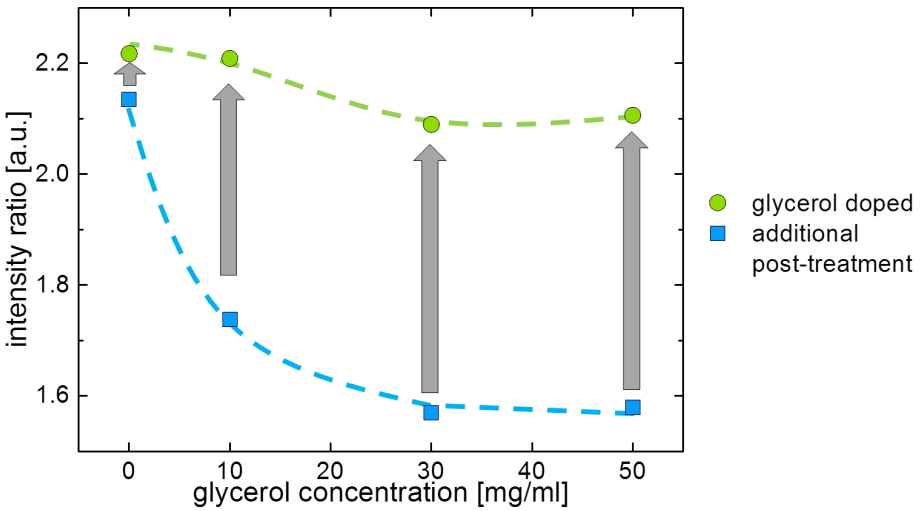

Figure 5.24: Estimation of edge-on to face-on ratio of PEDOT molecules. Data shown a) for different glycerol doping concentrations and b) additional ethylene glycol post-treatment.

The addition of glycerol to PEDOT:PSS leads to an enhanced face-on orientation of the crystallites which becomes stronger by increasing the glycerol concentration. In face-on oriented crystals the backbone of PEDOT molecules is oriented parallel to the substrate, the π-π stacking however is oriented perpendicular to the substrate. Therefore a reduced lateral conductivity within the crystallites and between crystrallites is expected. Figure 5.13 in section 5.2.1 shows that the conductivity of the strong glycerol doped film (50 mg/ml) is comparable to the ones of EG-post-treated films. At first glance this observation conflicts with the expectation. However, by increasing the glycerol concentration, the overall crystallinity in glycerol doped films increases, strongly reducing the amorphous PEDOT:PSS between the PEDOT crystallites. Hence, the increase of conductivity is additionally caused by better charge transport between crystallites in more crystallized systems.

It is concluded that the increase in conductivity by glycerol doping and by EG-post-treatment results from two different effects. For glycerol doped PEDOT:PSS the conductivity is enhanced by overall strongly increased crystallinity with face-on oriented crystals. In the case of EG post-treated films the crystals have an enhanced edge-on orientation compared to the glycerol doped films. In this case the pathway for charge transport is more direct along the lateral plane. Therefore the increased conductivity of EG post-treated films is explained by the improved edge-on orientation of PEDOT:PSS and more direct percolation paths for the charges. The enhancement in conductivity for glycerol doped films is therefore dominated by the structural changes and the enhanced overall crystallinity together with the known removal of PSS. Further enhancement in conductivity for additional EG post-treatment however is influenced additionally by the edge-on improvement within the crystals.

5.2.6 Model

To explain the strong increase in lateral conductivity by exposure to co-solvents, a model is proposed which relates the changes in conductivity to changes in the film morphology, i.e. PEDOT domain size and distance and molecular orientaion and crystallinity. The model for the morphological changes with glycerol (G) doping and ethylene glycol (EG) post-treatment is based on the information obtained by UV-Vis, SEM, GISAXS and GIWAXS in sections 5.2.2 to 5.2.5.

In the proposed model, the sizes and distances of the PEDOT domains are obtained from GISAXS measurements as shown in section 5.2.4. In order to estimate a ratio of small to large scattering domains, the scattering intensities of the corresponding form factors are compared to each other. One large domain leads to more intense scattering compared to one small domain for an equal exposed volume. Based on the general relation between the scattering intensity I and the mass m of spherical objects, the following estimation is made. The intensity of a form factor relates to the radius of the structure according to

$$I(FF) \propto n\, m^2 = n(\rho\, V)^2 \propto (\rho\, 4\,\pi R^3)^2 \propto (R^3)^2 \propto R^6. \tag{5.1}$$

For two different radii with

$$R_1 = x\, R_2 \;;\; x \geq 1 \tag{5.2}$$

the corresponding intensities relate to each other according to

$$I_1(R_1) = I_2(R_2)\, x^6. \tag{5.3}$$

The ratio of domains can then be estimated by

$$\frac{I_1(FF_1)}{x^6} : I_2(FF_2) \tag{5.4}$$

where n is the particle concentration, ρ the scattering length density, V the volume of a particle, and R the radius of the scattering objects extracted from the fits and x the scaling factor for the domain ratio. From this, a model is developed which contains the relative distances and radii from the fit and the estimated number ratio of scattering objects per volume.

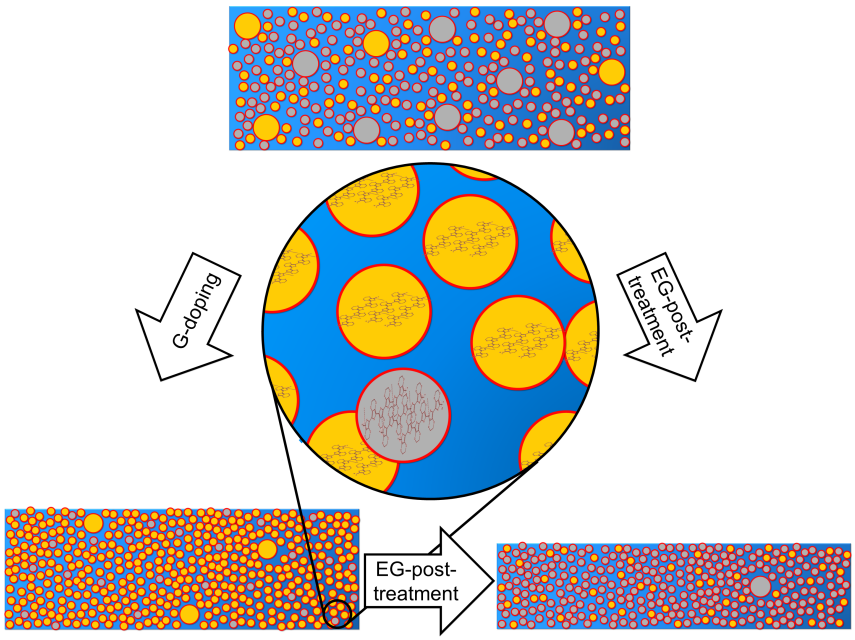

Figure 5.25: Schematic of the structural changes in PEDOT:PSS films that result from glycerol doping and ethylene glycol post-treatment.

In figure 5.25 a graphical representation for the structural and molecular changes with co-solvent treatment is shown. Derived from the above described estimation for morphological changes are depicted together with the molecular reorientation of the molecules within the PEDOT crystallites as discussed in section 5.2.5. The representation illustrates how the inner film structure changes towards smaller and more densely packed domains. Thereby the amount of insulating PSS between the conducting PEDOT domains is reduced. Further, as discussed in section 5.2.5 the reorientation of the molecules within the domains has an impact on the conductivity since the conductivity within a crystal of conjugated molecules is anisotropic. Although EG post-treatment and G doping both lead to a strong conductivity increase, the molecular reorientation opposites. The conductivity increase is of different nature for the two treatments and is explained by different

dominating effects, i.e. beneficial edge-on orientation of PEDOT molecules within crystallites in the case of EG post-treatment and enhanced overall crystallinity in the case of G doping. The change of inner film morphology, molecular orientation and crystallinity together with the removal of PSS, explains the increase in conductivity of PEDOT:PSS.

5.3 Summary

In the first part of this chapter (section 5.1) it was shown how the conductivity of PEDOT:PSS films increases upon doping and post-treatment with high boiling point co-solvents. In section 5.1.1, the processing method of doping was compared to the method of post-treatment with ethylene glycol (EG), i.e. the most commonly used solvent for this purpose. A steady increase in conductivity was shown for increasing EG doping concentration. The method of post-treatment was shown to result in a very strong conductivity increase of up to three orders of magnitude. When the method of doping was combined with the method of additional post-treatment, the resulting conductivity increases to similar values to that of pure post-treatment, which was shown to be independent of the initial doping concentration. Further, the method of post-treatment led to the best results when the film was first dipped into a EG bath for a short time (120 s to 180 s) and the excess solution was subsequently spin-coated off the substrate. In section 5.1.2 several promising solvents were compared in their impact on PEDOT:PSS film conductivity, absorption and vertical film composition. Depending on a combined effect of solvent properties, i.e. boiling point, dielectric constant and polarity, the resulting conductivity increase by post-treatment varied. In general the conductivity increase was shown to go along with an increase in absorption coefficient and with this in the amount of available charge carriers. Further, a strong change in vertical film composition was shown to influence the film conductivity as determined from XRR. Besides the removal of PSS surface enrichment layers and the formation of PEDOT enrichment layers at the polymer-substrate interface, with EG, DMSO and G denser PEDOT:PSS films result in a higher conductivity of the films. As EG was shown to be the solvent with the strongest impact on the resulting film conductivity, the time of the EG bath was verified to further optimize the processing protocol. In section 5.1.3 it was shown that a bath time of 180 s first results in the best conductivity values and second in a reproducible process. As the effect of the bath time on the resulting conductivity is quite low, the changes in the absorption coefficient are negligible. To further verify the processing protocol, in section 5.1.4 multiple post-treatment cycles on PEDOT:PSS films were compared in terms of electronic, spectral and morphological variations. The highest conductivity value was reached for a single cycle of post-treatment with EG. The decrease in conductivity for multiple post-treatment cy-

cles went along with a change in absorption coefficient indicating an increase in radial cation charge carriers and an assumed decrease in dication charge carriers. Further, by investigating the vertical film composition, it was shown that the observed changes in the reflectivity curves are simply caused by the change in film thickness and no changes, e.g. in the enrichment layers is observed. Summarizing, in the first part of this chapter various parameters which influence the film conductivity of PEDOT:PSS polymeric electrodes were tested, verified and characterized for an optimized and reproducible processing based on profound knowledge of the influencing parameters which is important for optimization of organic electronic devices. Further, the investigations strongly suggest that the inner film morphology of the PEDOT:PSS films is crucial for the charge transport and the resulting conductivity as shown in the second part of this chapter.

The second part of this chapter (section 5.2) provides a detailed investigation on the morphological structure of co-solvent modified PEDOT:PSS films. A contiguous study of glycerol (G) doped PEDOT:PSS films of varying initial doping concentration and subsequent EG post-treatment of these films provided deep insight into the structure formation of highly conductive polymeric PEDOT:PSS films. Based on the electronic (section 5.2.1), spectroscopic (section 5.2.2) and morphological (section 5.2.4 and section 5.2.4) investigations presented in this section, it is concluded that the enhancement in conductivity of co-solvent treated films is ascribed to partial removal of the non-conductive PSS molecules, morphological changes towards smaller and more densely packed PEDOT-rich domains with improved inter-chain and inter-grain conductivity. For G-additive, an enhanced crystallinity with face-on oriented molecules within the crystals was observed as shown in section 5.2.5. Moreover a reorientation of the conjugated molecules towards improved edge-on orientation was found for EG-post-treatment. Together these molecular and structural changes lead to the highly improved lateral conductivity which is important for the application of PEDOT:PSS as an electrode. Particularly the reorientation of the PEDOT molecules with EG-post-treatment which is observed in the corresponding publication for the very first time requires consideration.[6] It is remarkable that the molecular orientation for G-additive and EG-post-treatment is drastically different, however leading to comparable enhanced conductivities. This indicates that the structural changes on the mesoscale together with the removal of PSS and the enhanced crystallinity might have a stronger influence than the molecular orientation within the crystalline domains. Correlating the inner film morphology and the molecular orientation within the crystalline domains to the film conductivity, these results assist in directed modifications of PEDOT:PSS thin films with optimized properties for practical devices.

Chapter 6

Influence of Surfactant on PEDOT:PSS Morphology and Photovoltaic Devices

This results shown in this chapter have been published in the article: *The Morphological Power of Soap: How Surfactants Lower the Sheet Resistance of PEDOT:PSS by Strong Impact on Inner Film Structure and Molecular Interface Orientation*[103] (C. M. Palumbiny et al., *Advanced Electronic Materials*, 2 (4): 2016, DOI: 10.1002/aelm.201500377)

Poly(3,4-ethylenedioxythiophene) blended with polystyrene sulfonate (PEDOT:PSS) is often used as an additional functional layer in organic electronics (OEs), typically in between the indium tin oxide (ITO) electrode and the active layer in organic light emitting diodes (OLED) and organic photovoltaic (OPV) applications. Addressing the limitations for OEs such as the cost, scarcity and lack of flexibility by the use of ITO, PEDOT:PSS can also be used directly as the transparent electrode (TE) when it is processed from a co-solvent modified solution. This supersedes the use of an ITO electrode[104]. As established in the previous chapter, it is necessary to tune the morphology of PEDOT:PSS in thin films to improve its conductivity for the use of PEDOT:PSS as a TE. In this context, besides high boiling point co-solvents as investigated in the previous chapter (chapter 5), also surfactants play an important role as structuring agents for the film morphology of PEDOT:PSS. For instance Zhang et al. have spin-coated glycerol monostearate (GMS) on top of a PEDOT:PSS film and have obtained conductivities over 1000 S/cm.[105] The authors attribute the improvement in conductivity to a phase separation between the hydrophobic PEDOT and the hydrophilic PSS molecules induced by the preferred in-

teractions of the GMS end groups with the PSS and PEDOT molecules.[105] The (fluoro)surfactant Zonyl (FS) for instance is a surfactant which enhances the conductivity of PEDOT:PSS as well as its wetting properties on hydrophobic surfaces. Zonyl consists of a hydrophilic and a hydrophobic end which interact with the PSS and PEDOT molecules, respectively. This chapter now aims for combining the benefits of the (fluoro)surfactant Zonyl (FS) and the ethylene glycol (EG) post-treatment (section 5) on the PEDOT:PSS properties. In section 6.1 it is shown how the surfactant and the co-solvent EG influence the electrical (section 6.1.1) and optical properties (section 6.1.2) of the film, namely the sheet resistance, the transmission, and the figure of merit (FOM) for transparent electrodes (TE). Together with additional treatments, the surfactant causes a change in morphology and by this an increase in electrical conductivity.[4] Therefore, the intrinsic relation between electronic properties and morphology is investigated with grazing incidence small angle X-ray scattering (GISAXS) (section 6.1.3). Consequently, in section 6.2 the impact of the morphological changes on device characteristics is investigated in organic solar cell devices (section 6.2.1). The polarized resonant soft X-ray scattering (P-SoXS) measurements shown in section 6.2.2 explain the improved photovoltaic characteristics by an observed phase separation of the PEDOT:PSS polymer mixture induced by the surfactant. P-SoXS shows how the FS influences the relative molecular orientations at the polymer interfaces. Their impact on phase separation and work function is discussed in section 6.2.3, and related to the corresponding solar cell characteristics.

6.1 Influence of (fluoro)surfactant on film properties

For the application of surfactant and co-solvent modified PEDOT:PSS layer, it is important to understand the film properties such as their electronic, spectral and morphological characteristics. With this, the reproducibility of preparation can be guarantied and controlled. Further, it helps to understand the performance of the photovoltaic devices where the films are applied.

6.1.1 Electronic characterization

It is known that high boiling point co-solvents and surfactants decrease the sheet resistance of PEDOT:PSS. For the application of PEDOT:PSS as TE in OEs, a detailed characterization of the film properties such as the sheet resistance, is essential. In the following, the effect of a surfactant ((fluoro)surfactant Zonyl FS-300, see section 4) and a high boiling point co-solvent (EG) on the sheet resistance $R_{\square}$ of PEDOT:PSS is examined as a function of the applied voltage U and the resulting current I according to

$$R_{\square} = \frac{\pi}{ln(2)} \frac{U}{I}. \tag{6.1}$$

Various amounts of the (fluoro)surfactant Zonyl FS-300 (section 4.1 and 4.2.1) are added to the PEDOT:PSS solution, i.e. in amounts of 0 wt% to 10 wt%. Despite a slight increase in film thickness, FS-doping increases the sheet resistance as shown in figure 6.1.[6] This at first glance contradicts a previous study by Vosgueritchian et al.[4], although it is explained by the manufacturer changing the formulation of the Zonyl. The effect can be traced back to the FS solvent which included 50 % isopropyl alcohol when Vosgueritchian et al. conducted their study, thereby differing the suppliers composition of the surfactant that is used here (see chapter 4, section 4.1).

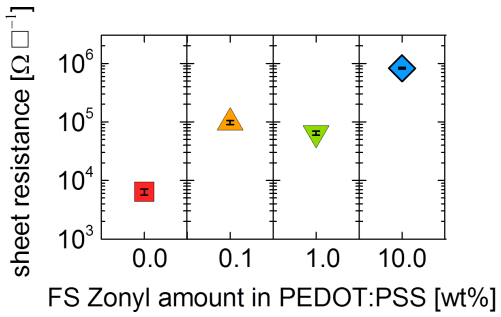

Figure 6.1: Sheet resistance of PEDOT:PSS films in dependence of FS Zonyl concentration (different symbols) ranging from 0 wt% to 10 wt%.

Doping PEDOT:PSS with FS plus additional EG-post-treatment, leads to a lowering of the sheet resistance by several orders of magnitude as shown in figure 6.2. Within a certain range of FS-addition (see 1 % of Zonyl), combining FS-doping plus EG-post-treatment surprisingly decreases the sheet resistance as evident when comparing one layer (1x) for 0 wt%, 0.1 wt%, 1 wt% and 10 wt% in figure 6.2. This observed trend for $R_{\square}$ with the addition of FS opposes the trend observed for increased FS-content without EG-post-treatment. The effect of multilayers is shown for 0.1 wt% and 1 wt% FS in figure 6.2. It is evident from the graph, that multilayers (2x,3x,4x) of PEDOT:PSS further reduce the sheet resistances as expected when increasing the total film thickness. For the thickness dependent conductivity values of the PEDOT:PSS films it is referred to[6].

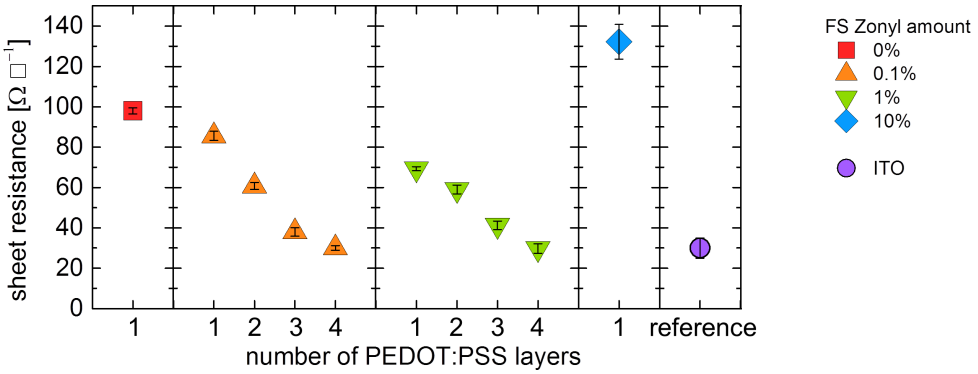

Figure 6.2: Sheet resistance of EG post-treated PEDOT:PSS films in dependence of FS Zonyl concentration (different symbols) ranging from 0 wt% to 10 wt%. The multilayer series for 0.1 wt% and 1 wt% show a trend towards reduced sheet resistance. Lowest sheet resistances are reached for a 4-layer PEDOT:PSS film with 1 wt% Zonyl. The sheet resistance of ITO is depicted as reference.

Pure PEDOT:PSS is known to form a capping layer of electrically insulating PSS on top of the film which is expected lead to to charge transport blocking layers in the stack of a multilayer PEDOT:PSS film. However, EG-post-treatment is known to remove this PSS capping layer. Therefore, all multilayer samples are EG-post-treated before applying additional layers. Thereby the PSS layer is removed from the surface prior to the following coating cycle. As a result, the PSS barrier layer blocking the charge transport is minimized before applying the second layer. Besides the positive effect of FS and EG on the sheet resistance of PEDOT:PSS, the addition of FS results in good surface wetting even on hydrophobic surfaces. Furthermore, only with the addition of FS it is possible to realize homogeneous PEDOT:PSS multilayers. The improved wetting properties of FS-doped PEDOT:PSS makes the material attractive for a wide range of additional applications. Concluding, controlled tuning of the PEDOT:PSS sheet resistance is possible by careful selection of surfactant, co-solvent and film assembly. Furthermore, the right combination of (fluoro)surfactant concentration, EG post-treatment and multilayers leads to conductivities similar to the one of ITO. Here, a multilayer stack of four (fluoro)surfactant-doped PEDOT:PSS layers and EG post-treatment of each layer, leads to the lowest sheet resistance which is the same as for ITO within the errors.

6.1.2 Spectral characterization

Besides the sheet resistance discussed above, for the application of the polymeric PEDOT:PSS electrodes e.g. in photovoltaic devices, the film transmission, that is a measure for the transparency of the film, plays a crucial role. In figure 6.3a, the transmission for one and

four FS-doped PEDOT:PSS layers is shown. As expected, the transmission decreases for multilayers, however, still shows reasonably good transmission properties of up to 80 % in the visible wavelength range.

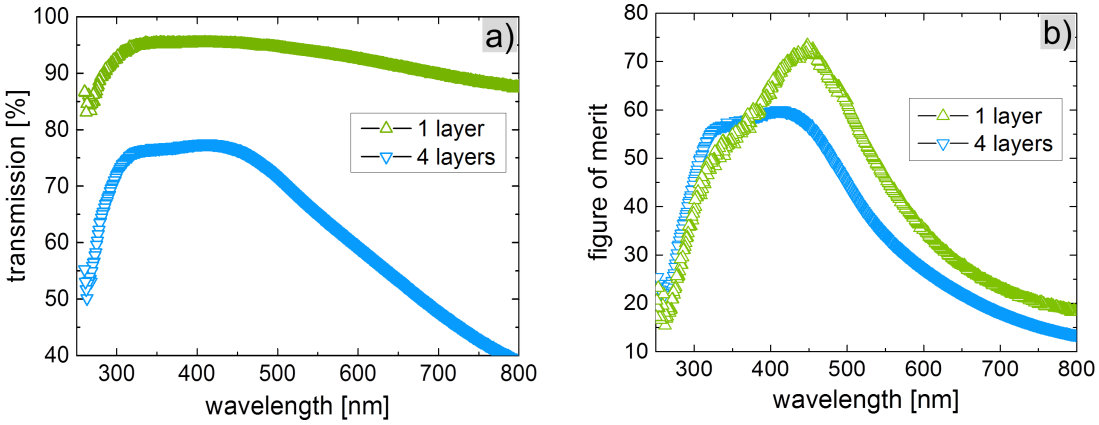

Figure 6.3: a) Transmission and b) figure of merit for one and four layers of PEDOT:PSS (0.18 wt% Zonyl and EG post-treatment of each layer).

In order to evaluate the quality of a transparent electrode, a common way is to relate its transmission $T(\lambda)$ to its sheet resistance $R_{\square}$ in dependence of the wavelength λ. Thus, the relation of direct current σ_{dc} to optical current $\sigma_{oc}(\lambda)$ acts as a figure of merit (FOM) (equation 6.2) relating the sheet resistance (equation 6.1) to the spectral transmission (equation 6.3).[106] As shown in the previous section, the sheet resistance of the PEDOT:PSS films is strongly decreased by the combination of FS additive and EG-post-treatment. In figure 6.3, the transmission (a) and the FOM (b) for a FS-doped plus EG-post-treated single layer are compared to a four-layer PEDOT:PSS film. The value of the FOM gives a limit for industrial applications of electrodes. Most devices require a FOM larger than 35 for a certain wavelength range which depends on the application. For touch screens for instance a FOM of 10 is sufficient, whereas for LCDs a FOM of 50 is essential.[4] Based on this comparison, the PEDOT:PSS electrodes shown in this study are suitable for a wide range of applications.

$$FOM = \frac{\sigma_{dc}}{\sigma_{oc}(\lambda)} \tag{6.2}$$

$$T(\lambda) = \left(1 + \frac{188.5}{R_{\square}} \frac{\sigma_{oc}(\lambda)}{\sigma_{dc}}\right) = \left(1 + \frac{188.5}{R_{\square}} \frac{1}{FOM}\right) \tag{6.3}$$

6.1.3 Structure characterization

For the application of TEs, the above-discussed transmission and FOM play a crucial role. These electric and spectral properties of PEDOT:PSS systems are strongly related to the inner film morphology as shown bofore in the previous chapter for high boiling point co-solvents. OEs can benefit from this intrinsic relation if applied in a well-targeted manner. In the previous chapter, it has been shown by grazing incidence small angle X-ray scattering (GISAXS) measurements, that the conductivity of PEDOT:PSS is strongly related to its inner film morphology. In order to examine the influence of FS on the inner film morphology of PEDOT:PSS, different FS-doping concentrations in PEDOT:PSS solution prior to spin-coating are investigated with and without additional EG-post-treatment of the PEDOT:PSS solid films (see chapter 5, sections 5.1.2 and 5.2). For the purpose of studying the inner film structure GISAXS measurements are performed and the results are related to the film conductivities of the corresponding films. The lateral information is extracted from the GISAXS measurementa using a 1D paracrystalline model and the local monodisperse approximation within the distorted wave Born approximation (DWBA) (see section 3.3.2) to model the measured data. From this approach, the form and structure factors of scattering domains are extracted. Dependent on the FS doping content in the film, figure 6.4 shows the form factors, corresponding to PEDOT domain sizes in the film, as well as the structure factors, corresponding to domain spacings in the film. In total, three form and corresponding structure factors are observed within the measured range.

The first form factor, referred to in the following as $FF1$, originates from an agglomeration of smaller PEDOT grains which form large network-like structures with a structure radius of 160 nm (green rectangles in figure 6.4a). These large percolation paths for charge carrier transport were observed before by Kim et al. at the film surface.[5]. The green dashed line in figure 6.4a shows that the addition of FS to the PEDOT:PSS solution prior to spin-coating has no influence on this structure size. However, for EG-post-treatment of pure PEDOT:PSS films (no FS addition), these structures grow to structure radii of 220 nm (first orange rectangle of $FF1(EG)$). The structure growth is explained by the removal of PSS from the films by EG post-treatment (chapter 5) and the subsequent additional aggregation of PEDOT grains. The structure distances ($SF1$) as well as their distribution(green shaded area in figure 6.4b) increase with increasing FS Zonyl content in the PEDOT:PSS solution prior to spin-coating which is attributed to the enhanced phase separation of PEDOT and PSS. When the film coated from FS doped PEDOT:PSS solution are additionally post-treated with EG, the above-described additional agglomeration of PEDOT grains (structure radius $FF1(EG)$) is reduced. The orange dashed line

in figure 6.4a indicates how $FF1(EG)$ decreases with increasing FS content down to the radius which is measured in PEDOT:PSS films without EG post-treatment. The structure distance after EG post-treatment ($SF1(EG)$) and moreover its distribution (orange shaded area in figure 6.4) is reduced compared to the structure distance before EG post-treatment (SF1) and its distribution (green shaded area in figure 6.4b). The removal of PSS between the PEDOT grains causes an agglomeration of the film and the PEDOT-rich domains which leads to the reduced structure distance between the domains as well as to its reduced distribution.

The large network structures of conducting PEDOT domains are expected to decrease the sheet resistance of the PEDOT:PSS film. With mere EG post-treatment the $FF1(EG)$ is increased compared to pure PEDOT:PSS which could explain the strong reduction of the sheet resistance after EG post-treatment. The PEDOT:PSS films which are FS-doped before EG post-treatment show a further decrease in sheet resistance. However, in this context, the structure radii for these films decrease which contradicts the expectation stated at the beginning of the paragraph. Even though large PEDOT structures are expected to decrease the sheet resistance by improved percolation paths for charge carriers, the observed trends for the $FF1(EG)$ alone do not support this assumption.

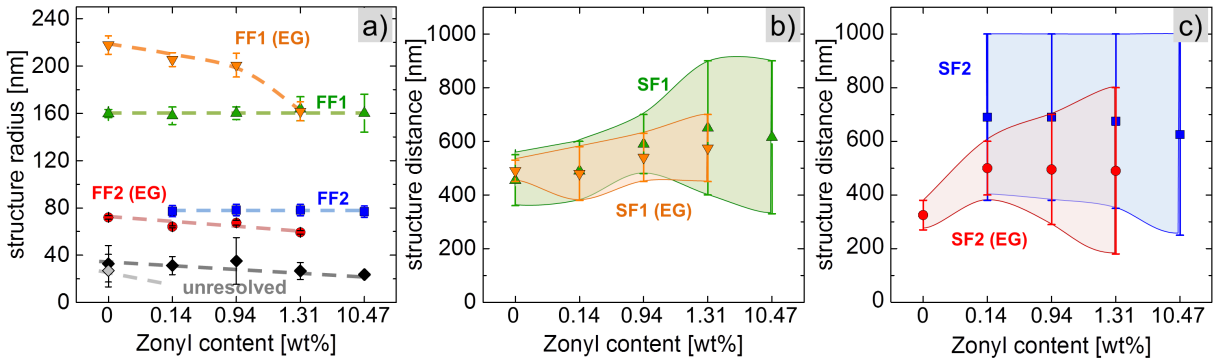

Figure 6.4: a) Form factors for different Zonyl content with and without EG post-treatment. Dashed lines act as guide to the eyes. b) Structure factor 1 and c) structure factor 2 shown together with their distribution indicated by the shaded areas. (The PEDOT:PSS film with 10.47 wt% FS Zonyl content is not stable after EG post-treatment and is hence not depicted here.)

The second form factor corresponds to domain sizes of 60 nm to 80 nm in radius and is referred to in the following as $FF2$. In this paragraph it is shown how this structure size is closely linked to the third domain size of 20 nm to 40 nm ($FF3$ and $FF3(EG)$). Figure 6.4a shows the second form factor for FS-doped films in blue squares and for ad-

ditional EG post-treated films in red spheres. The third form factor is depicted in black and gray rhombs for PEDOT:PSS films with and without EG post-treatment. The $FF2$ structure is only observed when FS or EG interact with PEDOT:PSS and does not exist for pure PEDOT:PSS films. As will be discussed in the following, the two structure sizes relate to the length and width of elongated PEDOT domains which form in particular by the addition of the (fluoro)surfactant.

An earlier hypothesis by Vosgueritchian et al. is based on AFM measurements of FS-doped PEDOT:PSS films and shows that the addition of surfactant results in an elongation of PEDOT-rich grains.[4] Xia and Ouyang investigated this elongation of grains by testing a series of different solvent additives on PEDOT:PSS films, including ethylene glycol and amphiphilic fluorinated molecules.[7,107–109] The solvent additives with polar groups interfere with the Coulombic interactions between the sulfonate side groups of the PSS and the PEDOT backbone. The much longer and hydrophilic PSS molecules usually coil around the shorter and hydrophobic PEDOT molecules to shield them from the aqueous surroundings. The screening effect induced by the surfactant however favors a phase separation between PEDOT and PSS that goes along with PSS molecules changing to a stretched coil (linear conformation). A similar, yet more pronounced effect is expected upon addition of surfactants with highly fluorinated end groups, such as the FS Zonyl, to the PEDOT:PSS solution prior to spin-coating.

Figure 6.5 shows a model that depicts the structure formation, aggregation and transformation without FS (figure 6.5a) and with FS (figure 6.5b). The effect of the surfactant on the PEDOT:PSS structure in aqueous solution changing the core-shell structure of PEDOT:PSS to a stretched coil (linear conformation) is shown in the left column. Figure 6.5b further shows how the stretched coils of PEDOT aggregate and form elongated grains with two lateral lengths, i.e. the length and the width of the elongated grains as depicted on the bottom right of the image. Further, the elongated PEDOT-rich grains are randomly oriented inside the film. Consequently, in scattering experiments two lateral structure sizes are seen which correspond to the two form factors $FF2$ and $FF3$. They are appendant to the length and the width of the same elongated PEDOT domain and hence are seen for all PEDOT:PSS films which are treated with FS. With the addition of FS to the PEDOT:PSS solution prior to spin-coating, the distance of these elongated domains ($SF2$) as well as the distribution of the distances (blue shaded are in figure 6.4c) remain constant for all FS doped PEDOT:PSS films. With the additional processing step of EG post-treatment, PSS is washed from the PEDOT:PSS polymer matrix. By this the structure distance ($SF2(EG)$) as well as the distribution of the structure distance (red

shaded are in figure 6.4b) decreases after EG post-treatment of the PEDOT:PSS films while also the structure size itself decreases slightly ($FF2(EG)$ and $FF3(EG)$). The decrease in structure size ($FF2(EG)$ and $FF3(EG)$) and structure distance ($SF2(EG)$) is caused by the removal of the PSS between the PEDOT-rich grains and the removal of PSS from the volume of the individual PEDOT-rich grains, respectively. Note, that the pure PEDOT:PSS film does not show this elongation of the PEDOT grains as the PEDOT domains are spherical in these films as depicted on the right of figure 6.5a. The third form factor $FF3$ that is modeled for the GISAXS scattering profiles, originates from PEDOT domains with a radius of 35 nm. With pure EG post-treatment, these domains decrease in amount and size due to domain rupture as shown and discussed in detail in the previous chapter 5, section 5.2.4 and published in [6]

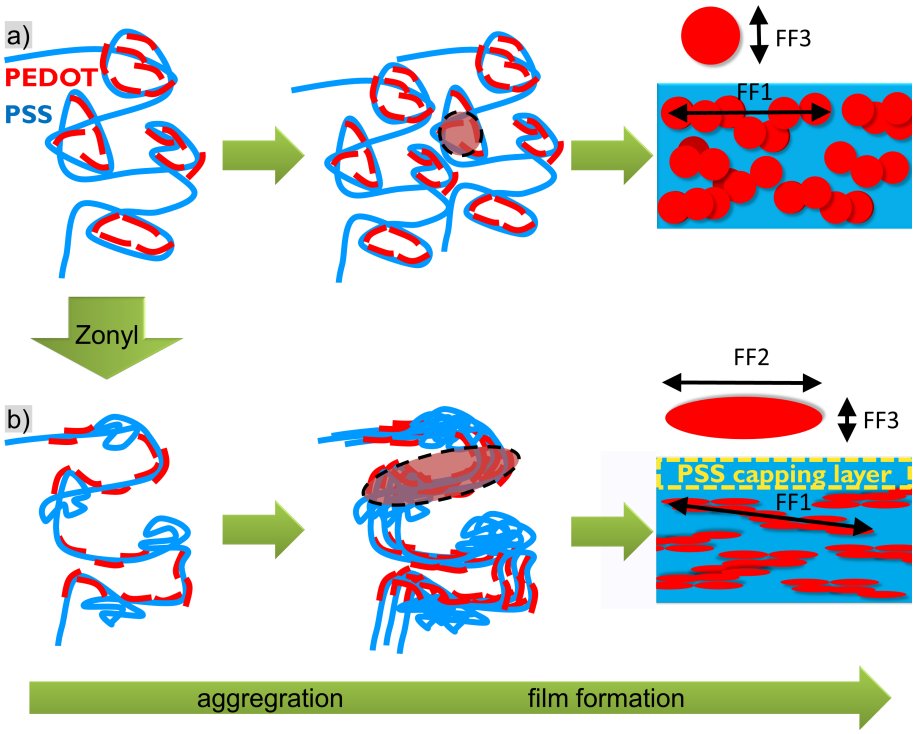

Figure 6.5: Schematic presentation a) of the film formation of pure PEDOT:PSS and b) of (fluoro)surfactant doped PEDOT:PSS. Addition of the surfactant leads to stretching of the chains in aqueous solution and thereby consequently different aggregation and film formation, depicted by the red-shaded areas.

6.2 The origin of interface tuning via surfactants in photovoltaic devices

As the results from the GISAXS measurements show, the addition of FS to the PEDOT:PSS system changes the inner film morphology. The structural changes lead to changes in the electronic properties, i.e. the sheet resistance discussed in section 6.1.1. In the following, the effect of structural and electronic changes in the PEDOT:PSS layer is investigated by photovoltaic device characteristics with and without FS in section 6.2.1. Furthermore, the observed impact of FS on photovoltaic characteristics is explained by phase separation caused by molecular reorientation of PSS molecules at the interface of PEDOT domains (section 6.2.2). Special focus is put on the phase separation of PEDOT and PSS on the surface. As it is known that co-solvents and surfactants can have an impact on the work function which in turn depends on the PEDOT:PSS composition. Section 6.2.3 therefore discusses the possibility of tuning the interface between electrode and active layer by surfactant treatments.

6.2.1 Photovoltaic devices with surfactant-modified PEDOT:PSS electrodes

In order to investigate the effect of FS-doped PEDOT:PSS on solar cell characteristics, the well-known and well-investigated material system of poly(3-hexyl-thiophene-2,5-diyl) and [6,6]-phenyl-C71-butyric acid methyl ester (P3HT:PC71BM) is used as active layer with a thickness of 120 nm. The total thicknesses of the PEDOT layers are chosen to be 65 nm for all its variations, as determined by profilometry, to exclude an influence of the film thickness on the device performance. All solar cells are built in a stack using ITO as anode and aluminum as cathode (see chapter 3, section 3.1.2). In order to investigate the effect of FS-doping and additional EG-post-treatment on the performance of photovoltaic devices, solar cells with a pure PEDOT:PSS electrode are compared to solar cells with one and two layers of FS-doped PEDOT:PSS electrodes (each doped with 0.5 wt% FS and EG post-treatment of the lower layer). The solar cell stratification are depicted in figure 6.6. Further it is investigated why EG post-treatment of the topmost PEDOT:PSS layers leads to a strong decrease of the device efficiency as shown by the diode characteristics seen in figure 6.7a. The characteristics of the devices shown in figure 6.7 possess clear tendencies, particularly regarding their fill factor FF, shunt (parallel) resistance R_p and power conversion efficiency η. A summary of the before-mentioned characteristics is shown in figure 6.7b-c. Within the set of photovoltaic devices investigated, FS-doped electrodes

show an improved efficiency. This efficiency increase by 2.6 % by the use of surfactant modified PEDOT:PSS is subject to a 115 % increase in parallel resistance (R_{sh}) and an up to 13 % increase in fill factor (FF). However, the open circuit voltage (V_{oc}) and the serial resistance (R_s) remain constant within the accuracy of the experiment. The efficiency (η) is further improved by additional 2.5 % for two layers of FS-doped PEDOT:PSS of same total film thickness which is referred to an increase in short circuit current density (I_{sc}) together with a 4 % improved FF and a 96 % improved R_{sh} compared to the reference. In total, by the use of two layers FS doped PEDOT:PSS films, the efficiency is improved by 5 % compared to the reference.

Figure 6.6: Schematic of the the investigated photovoltaic layer compositions with varying PEDOT:PSS electrodes depicted in red (a), green (b) and blue (c). a) Reference with a single pure PEDOT:PSS layer, b) solar cell with one layer of Zonyl doped PEDOT:PSS and c) solar cell with two layers of Zonyl doped PEDOT:PSS. The total PEDOT:PSS thickness is 65 nm for all PEDOT:PSS variations.

However, additional EG-post-treatment, leads to a strong decrease in efficiency owing to strongly deteriorated fill factor, open circuit voltage, parallel and serial resistance. This drastic decrease using EG-post-treated PEDOT:PSS layers, is due to leakage current and recombination losses (R_s and R_p) that are attributed to a change in work function by the known removal of the PSS capping layer by EG post-treatment.[83,84] A work function shift below the HOMO of the P3HT results in a short cut of the corresponding device. The removal of PSS from the PEDOT:PSS system by EG enhances for FS-doped PEDOT:PSS. As shown with GISAXS (section 6.1.3), the surfactant induces a phase separation between PEDOT and PSS. Additional post-treatment with EG in this case is expected to remove the PSS more efficiently than for pure PEDOT:PSS films. In the following section (section 6.2.2) the phase separation and the molecular orientation at the PEDOT to PSS interface is discussed in detail by P-SoXS.

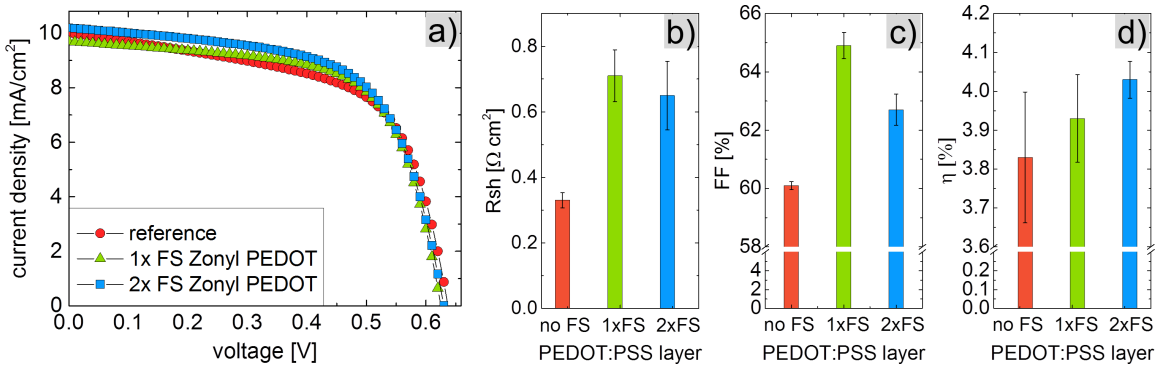

Figure 6.7: Photovoltaic current-voltage performance of P3HT:PC70BM bulk heterojunction devices with different FS-doped PEDOT:PSS selective electrodes in comparison to the reference with pure PEDOT:PSS selective electode.

6.2.2 Phase separation and molecular interface orientation

In thin polymer films, particularly in blend systems consisting of two materials, the charge transport is strongly influenced by the final phases in the matrix as these act as pathways for charge percolation. Furthermore, evidence for the molecular arrangement at interfaces will help to unravel some of the currently poorly understood structural complexities and factors that govern electrical performance. Pioneering work in exploring the molecular orientation at polymer interfaces for a photovoltaic active layer system was presented by Collins et al.[59] In order to investigate the purity of polymer phases and molecular arrangements at the interface between PEDOT-rich and PSS-rich domains, resonant scattering of polarized soft X-rays (P-SoXS) by the molecules was used (chapter 2, section 2.3.4 and chapter 3, section 3.3.5). This technique is sensitive to inter-facial interactions, providing insight into the molecular arrangements at interfaces. Its sensitivity to chemical composition thus reveals orientations of molecules at domain interfaces even for non-crystalline parts of the polymers.

By P-SoXS at the off-resonant energy of 280 eV, the influence of FS-doping on the structure of the film is investigated. Pure PEDOT:PSS films are compared to Li:PSS films as well as to films with 0.1 wt% and 1 wt% of FS added to the PEDOT:PSS solution. Li:PSS was chosen as a PSS reference. It is closest to a pure PSS scattering signal, because the system does not contain PEDOT. In figure 6.8, a clear tendency towards an enhanced scattering for increased FS concentration in PEDOT:PSS is observed. It is further evident that the scattering behavior for 1 wt% of FS and for Li:PSS is similar. This, at first glance, surprising result indicates a phase separation between PEDOT and PSS. The scattering of the evolving PSS bulk structure thereby increases with increased FS concentration.

The observed phase separation originates from the fact that the FS migrates between the hydrophobic PEDOT and water mitigating the Coulombic interaction. With this, the resulting stretched conformation of PSS allows PSS molecules to move more freely during film formation. The increase in PSS bulk-like phases leads to the observed similar scattering as for Li:PSS films. Hence, it is assumed that the PSS-enriched capping layer, too, becomes more pure with increasing FS concentration. As a more pure PSS top layer will have an impact on the work function of the PEDOT:PSS layer, this assumption can be proven by comparing the P-SoXS results to the solar cell characteristics. In particular the parallel resistance R_{sh} and the open circuit voltage V_{oc} will be affected by a work function shift. In fact, R_{sh} increases upon addition of FS as shown in the previous section 6.2.1. After EG-post-treatment however, R_{sh} strongly decreases, as does the V_{oc}. This is due to the known removal of the PSS capping layer with EG-post-treatment and reinforces the assumed effect of FS and EG on the work function and the related solar cell characteristics.

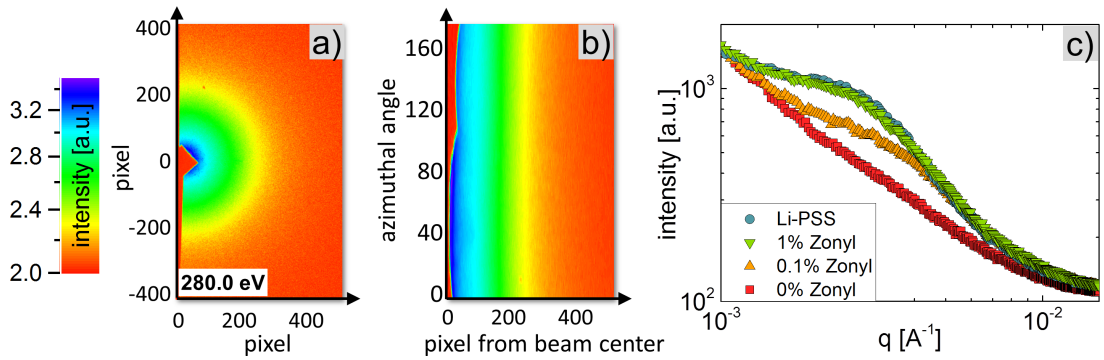

Figure 6.8: Resonant scattering statistics for pure PEDOT:PSS films compared to Li:PSS films and 0.1 wt% and 1 wt% of (fluoro)surfactant added to the PEDOT:PSS solution used for preparing the films. All films are measured the the off-resonant energy of 280.0 eV.

In the following, it is shown how resonant scattering at 285.3 eV reveals the molecular orientation of PSS molecules at the interface to PEDOT crystallites. It is shown that the mechanism of phase separation of PEDOT and PSS discussed above, is induced by the FS molecules causing molecular reorientation of the PSS molecules at the PEDOT interface. Interestingly, at the measurement energy of 285.3 eV, an anisotropic scattering is observed. The measurement energy of 285.3 eV corresponds to an excitation of a $1s$ electron into the π^* orbital of the PSS benzene ring. With the electric field being polarized in the direction of the π^* orbitals, perpendicular to the benzene plane, the electrons excited with 285.3 eV absorb exactly the energy they need to oscillate resonantly within the π^* orbital, similar to dipole oscillations. This leads to an anisotropic scattering of the film at resonance energy of the $1s$ π^* excitation in the PSS benzene ring (285.3 eV).

Due to the aforementioned absorption and oscillation, the observed scattering in the 2D images is reduced in the direction of the electric field as depicted in figure 6.9.

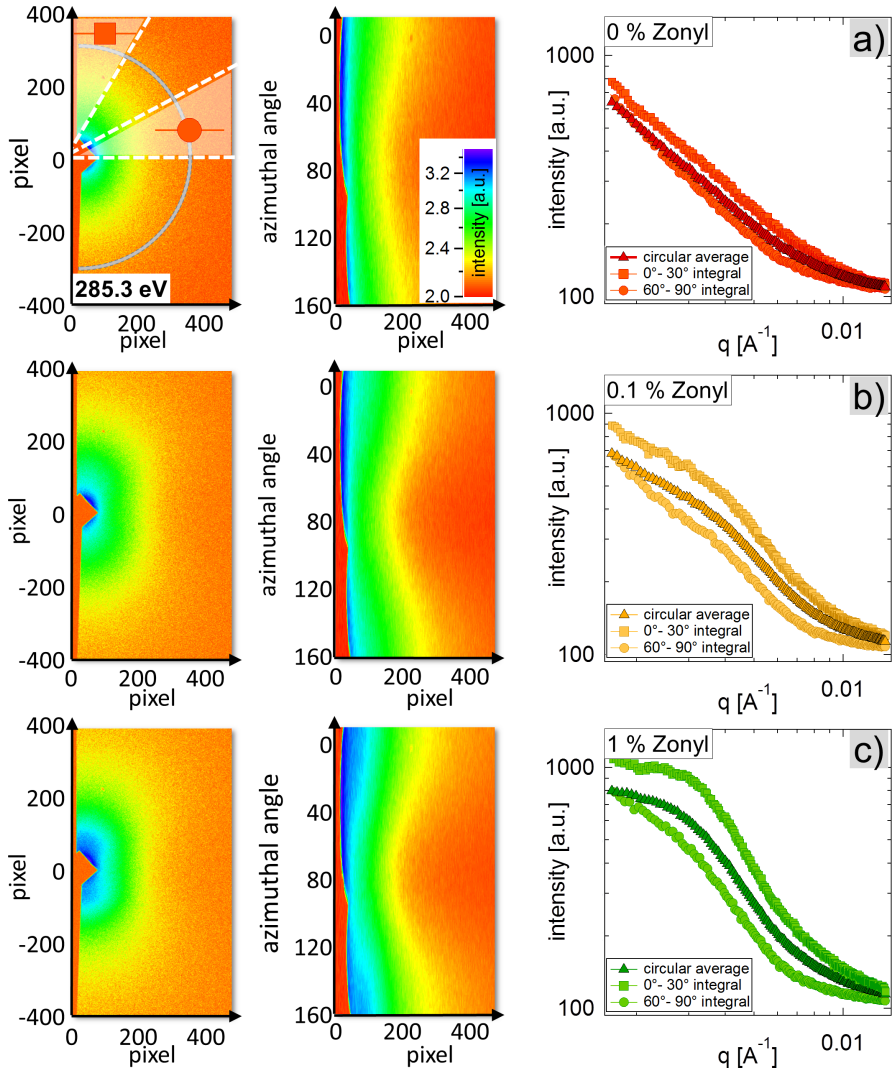

Figure 6.9: 2D polarized resonant soft X-ray (P-SoXS) scattering patterns and 2D P-SoXS angle vs. q-representation together with radial scattering profiles for PEDOT:PSS films measured at the resonant energy of 285.3 eV. a) Pure PEDOT:PSS films, b) 0.1 wt% Zonyl in PEDOT:PSS solution used to prepare the measured films and c) 1 wt% Zonyl in PEDOT:PSS solution used to prepare the measured films. Black symbols are circular averaged over the azimuth. Colored symbols are 30 ° integrated sector profiles along the azimuth as indicated in a).

Figure 6.10a shows the scattering profiles in vertical and horizontal directions exemplary for 1 wt% of FS. The striking anisotropy in the scattering profiles is only observed for resonant scattering at the energy of 285.4 eV whereas the scattering for the off-resonant

energy of 280 eV is isotropic. In order to depict the scattering anisotropy, sector integrals of 30 ° are compared to 180 ° integrated scattering profiles in figure 6.9. All profiles are shown for pure PEDOT:PSS (figure 6.9a), 0.1 wt% (figure 6.9b) and 1 wt% (figure 6.9c) of FS. The difference in the angular scattering profiles show that the anisotropy increases with the amount of FS in the system.

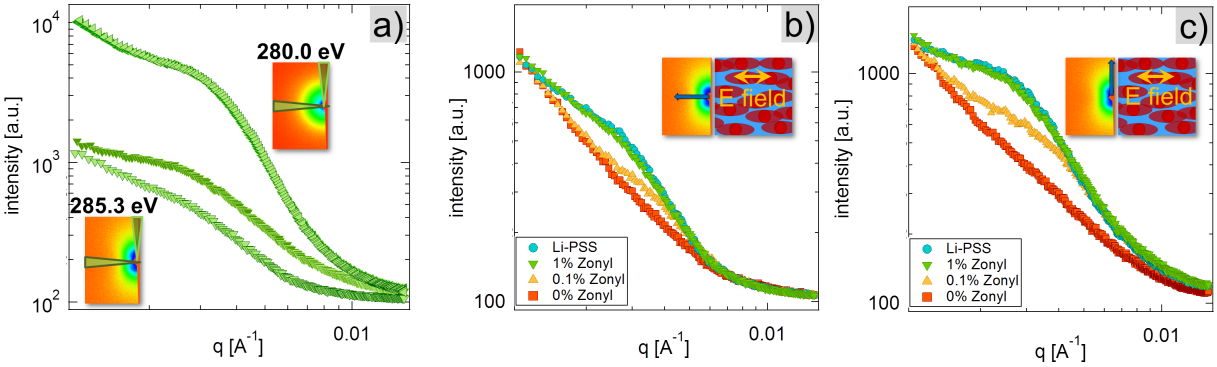

Figure 6.10: a) Resonant and off-resonant scattering of 1 wt% Zonyl doped PEDOT:PSS solution used to prepare the measured films. Anisotropic behavior for resonant scattering is observed. The inset shows 2D scattering images with the two profile directions for each measurement energy highlighted by the green triangles. b) Resonant scattering profiles and in electric field direction and c) perpendicular to electric field direction for pure PEDOT:PSS films, Zonyl doped PEDOT:PSS films and Li:PSS films.

As first shown by Collins et al. anisotropic scattering in P-SoXS experiments indicates an orientation at the interface between two materials [59], in this case at the interface of PSS to PEDOT. Therefore, the origin of the anisotropic scattering in PEDOT:PSS systems is discussed. If the plane of the PSS benzene ring is aligned perpendicular to the interface, the π-orbitals of the ring are aligned parallel to the interface. In this situation, the π^*-excitation is not in resonance if the orbital is not aligned with the electric field. As a result, the scattering will be isotropic for all electric field orientations. If the benzene rings of the PSS molecules, however, are aligned parallel to the interface, the π orbitals are oriented perpendicular to the interface. In this case the $1s$ π^* excitation of the orbitals at the interface is in resonance at the energy of 285.3 eV and the dipole oscillation of the electrons in the π^* orbitals is excited. This resonant scattering leads to a decreased contrast between PEDOT and PSS in the direction of the electric field. The phenomenon is depicted schematically in the inset of figure 6.11a. For the different investigated PEDOT:PSS variation, an enhanced anisotropic scattering with increased FS content in the film is observed. The anisotropy is calculated as the vertical scattering over the horizontal scattering and is plotted versus q in figure 6.11a. A clear increase in

the anisotropy factor is seen for the addition of FS as the percentage of anisotropy indicates. The anisotropic scattering thereby indicates that the normal configuration of the PEDOT to PSS molecules is disturbed and the PSS molecules at the PEDOT interface are reoriented compared to pure PEDOT:PSS.

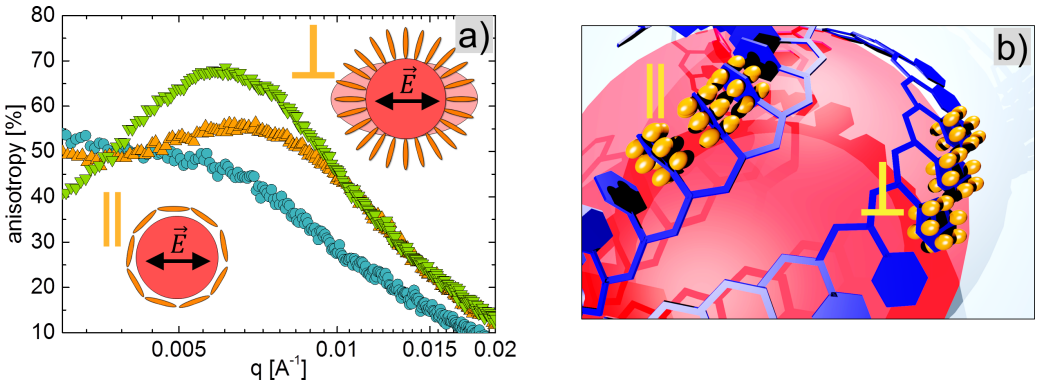

Figure 6.11: a) Anisotropy of the P-SoXS data showing increasing anisotropy for different (fluoro)surfactant (Zonyl) content from 0 wt% (blue circles), 0.1 wt% (green triangle up) and 1 wt% (orange triangle down). The insets depict how the polarized X-ray beam resonantly excites only the π^* orbitals perpendicular to the domain interface resulting in anisotropic scattering. b) Schematic representation of the respective orientation of the benzene rings on the PSS molecules (blue) towards the surface of a PEDOT grain (red). Yellow symbols indicate the direction of excitation of π orbitals (orange).

The two molecular orientations at the PSS-PEDOT domain interface are depicted schematically in figure 6.11b. In a pure PEDOT:PSS film, the PEDOT and the PSS molecules lie in one plane. Thereby the sulfonate groups that are attached to the PSS benzene ring, point to the PEDOT molecules and interact with the backbone of the PEDOT molecule by Coulombic interaction. The benzene rings of the PSS molecules are bound by a C-C bond to the backbone and can only rotate around this axis. In this configuration, the π orbitals of the PSS benzene rings are always parallel to the PEDOT interface. Consequently, no anisotropy can be observed in the 2D scattering patterns at the $1s$ π^* resonance energy. With addition of FS to the system, the interaction between the PSS and PEDOT molecules changes and anisotropic scattering is observed. Being a FS with a hydrophilic and a hydrophobic end, Zonyl intersects between PEDOT and PSS. The hydrophobic part interacts with the PEDOT whereas the hydrophilic part interacts with the sulfonate group attached to the PSS benzene ring. Hence, the FS shields Coulombic interaction between PEDOT and PSS. Only in this case a perpendicular orientation of the π orbitals from the PSS benzene ring is allowed. Our results strongly suggest a reorientation of the PSS molecules at the interface to PEDOT grains. Furthermore, the screening

effect of the FS between PEDOT and PSS is assumed to favor the phase separation which is observed with P-SoXS in-resonance as well as off-resonance and is indicated by the enhanced scattering contrast.

6.2.3 Electron blocking interface tuning

In the previous sections, the impact of phase separation and molecular orientation on solar cell characteristics was discussed in detail. P-SoXS shows on one hand an enhanced phase separation and on the other hand a molecular reorientation at the interface of PSS to PEDOT which is induced by the (fluoro)surfactant Zonyl. Referring to photovoltaic application, it is known that PEDOT:PSS forms a PSS-enriched capping layer. With the observed phase separation in the thin PEDOT:PSS films, a more PSS-pure enrichment layer on the PEDOT:PSS film surface is expected by the addition of FS to the PEDOT:PSS solution prior to spin-coating. PSS is an electrical isolating material and hinders the injection of electrons from the P3HT to the electrode which would result in a strong recombination at the P3HT-PEDOT:PSS interface. The purification of the PSS enrichment layer by phase separation, leads to enhanced electron blocking of the PEDOT:PSS layer and thereby, similar to a Schottky barrier, reduces recombination effects at the P3HT-PEDOT:PSS interface. With this, a beneficial PSS interface layer evolves for reducing leakage current as well as interface recombination as shown in section 6.2.1. As shown in literature a similar effect can be achieved by the adding an extra buffer layers which acts as a selective barrier for charge transport, such as ethoxylated polyethylenimine (PEIE), fenoprofen (PFN) or electropolymerized polythiophene (ePT).[110,111] Here it is shown that a thin PSS enriched layer between the PEDOT:PSS and the active layer is beneficial for the device performance of P3HT:PCBM solar cells. Further, it explains the dramatic decrease in efficiency of P3HT:PCBM solar cells with EG post-treated PEDOT:PSS layer where the PSS capping layer is removed. Nevertheless, EG post-treatment strongly decreases the sheet resistance and if combined with active layer materials of matching HOMO and LUMO levels, these polymeric electrodes have great potential. Concluding, with the results discussed in this section, the impact of FS-doped PEDOT:PSS on the solar cell characteristics can be explained.

6.3 Summary

The results of this chapter show, that modified PEDOT:PSS electrodes are suitable for industrial applications as transparent electrodes. For surfactant and co-solvent modified films as well as for multilayer films, an 80 % transmission in the visible range and

an unprecedented low sheet resistance comparable to commercially available ITO makes PEDOT:PSS a highly promising electronic material. The results presented in this chapter show how and why the structures of such films matter, by relating structure sizes, phase separation and molecular orientation at material interfaces to their electrical properties and the impact on the performance of photovoltaic devices. Although large network structures of radii 160 nm to 220 nm form favorable percolation paths for charge transport, the GISAXS measurements show that with EG post-treatment as well as with FS addition the sheet resistance is more likely lowered due to the formation of additional PEDOT domains of radii 60 nm to 80 nm. The resonant scattering experiments performed at the excitation energy of 285.3 eV reveal the molecular orientation of PSS molecules at the interface to PEDOT crystallites. The enhanced scattering for higher FS concentration indicates a phase separation between PEDOT and PSS owing to the screening effect due to the amphiphilic nature of the surfactant. The observed phase separation results in a PSS-enriched capping layer at the surface and hence in a change of work function as indicated by the increase of parallel resistance by 96 % to 115 % in the corresponding P3HT:PC70BM photovoltaic devices. Thus, the use of FS-treated PEDOT:PSS blocking layers in solar cells leads to an increase in fill factor of 4 % to 13 % and improved power conversion efficiency by up to 5 %. EG post-treatment is known to remove the PSS capping layer. This removal changes the surface properties such as the energy levels and thereby strongly deteriorates the parallel resistance as well as the open circuit voltage, fill factor and series resistance of the corresponding photovoltaic devices. This drastic decrease due to leakage current and recombination losses is attributed to the expected change in work function after PSS removal by EG-post-treatment. Further, the anisotropic scattering at 285.3 eV in the P-SoXS measurements reveal that the normal configuration of the PEDOT to PSS molecules is disturbed and the PSS molecules at the PEDOT interface are reoriented compared to pure PEDOT:PSS by the FS intersecting between PEDOT and PSS.

In summary, the results discussed in this chapter prove a reorientation of PSS molecules at the interface to PEDOT grains. Further, the screening effect of the FS between PEDOT and PSS is assumed to favor a phase separation which was observed with P-SoXS in-resonance and off-resonance. With the structural information obtained from GISAXS and P-SoXS the influence of the FS on PEDOT:PSS films is explained and their favorable impact on solar cell characteristics is demonstrated. These results, pave the way for controlled tuning of the polymeric electrode properties for a range of versatile applications, like an intrinsic buffer layer at the active layer interface in OE devices without the need of additional interface layers or the use of TEs with low sheet resistance.

Chapter 7

In-Situ GIWAXS Investigation of Printed Polymeric PEDOT:PSS Electrodes

Parts of the results shown in this chapter have been published in the article *The Crystallization of PEDOT:PSS Polymeric Electrodes Probed In-Situ During Printing* ([112] C. M. Palumbiny et al., Adv. Mater., 2015, DOI: 10.1002/adma.201500315).

Water soluble PEDOT:PSS is already widely used in organic electronic devices (OE) as a selective charge blocking layer. As discussed in the previous chapters, it can be modified by a secondary dopants, i.e. high boiling point co-solvents or surfactants, to increase its conductivity. In the previous two chapters the influence of co-solvents (chapter 5) and surfactants (chapter 6) on the electrical performance, i.e. the conductivity, of the polymeric system PEDOT:PSS are discussed and related to the inner film morphology. The conductivity increase by more than three orders of magnitude, from ∼0.1 S/cm to ∼1000 S/cm, makes PEDOT:PSS one of the most promising electrode materials for the production of cheap and flexible OEs.[3,4,6,113] Ethylene glycol (EG), which is miscible with water is one of the most commonly used co-solvents for this purpose.[6,7,113] So far, investigations on the structure-conductivity relation of PEDOT:PSS are based on spin coating as film deposition technique. However, one of the strongest motivations for OEs lies in the fabrication of flexible devices that can be scaled-up for industrial processing. For that purpose, laboratory-based processes, such as spin coating, are not always practical anymore. Industrial techniques for large scale coating, such as spray coating, rotary screen printing, flexographic printing, or slot-die coating, were shown to be applicable for

processing thin films for OEs.[114–116] In particular, slot-die coating is a very cost-effective production technique that offers the possibility of large scale manufacturing and custom-designed pattern coating.[116,117] Therefore, slot-die coating is used to study the dynamic processes during the printing and structure evolution process of PEDOT:PSS.

In this chapter, it is shown that the conductivity of printed PEDOT:PSS thin films is strongly related to molecular π-π-stacking distances (interchain coupling) and the size of crystallites. To investigate this relation, the film formation and structure evolution is followed during the drying process by in-situ GIWAXS measurements. The slot-die coating technique and the in-situ GIWAXS characterization technique, including the instrument specifications and procedures, are described in the first part of this chapter (section 7.1). In the second part (section 7.2) the structure evolution and molecular dynamics in printed PEDOT:PSS thin films are discussed. It is shown how co-solvents influence the evolution of the films and the interchain coupling within the films. The crystallite charactersitics of the final films are discussed in details, including the molecular orientation, PEDOT to PSS ratio and crystallite sizes. Therein also the influence of processing temperature on crystallite sizes is discussed. Further, a model for the film formation is presented on the basis of these results. The relation of film conductivity to the discussed crystallite characteristics identifies the dominating parameters that influence the conductivity of the final film, i.e. the interchain coupling together with the orientation and size of PEDOT crystallites (section 7.3), before concluding the chapter by a summary (section 7.4).

7.1 Simultaneous slot-die coating and structure observation

During slot-die coating, the initial fluid film is deposited on the substrate with controlled elevated temperature, making the process highly dynamic. Hence, real-time monitoring of the structure evolution with high temporal resolution is required. State-of-the-art imaging techniques such as AFM or TEM, face severe limitations in this context. To address this challenge, GIWAXS is used to investigate the slot-die coating of PEDOT:PSS in terms of the evolution of the film morphology, drying time and molecular arrangement. In the following, the slot-die coating setup is described (section 7.1.1) and the experimental procedure for the in-situ GIWAXS measurements is explained (section 7.1.2).

7.1.1 Slot-die coater

The parameters used for the application of the thin film on the substrate have a fundamental impact on the resulting film characteristics, such as the film thickness, the morphology and the crystallinity. Hence, the deposition method controls to a large extent the film formation and the final film characteristics. A variety of methods is available for coating of thin films from solution. Among these techniques, slot-die printing evolved as high quality application, using a linear printing process to coat thin fluid films onto substrates. This technique was first introduced by A. Beguin in the year 1954 with its breakthrough in 1970. Thanks to the high production output and the good final film quality, slot-die coating is e.g. used for the fabrication of flexible electronics.

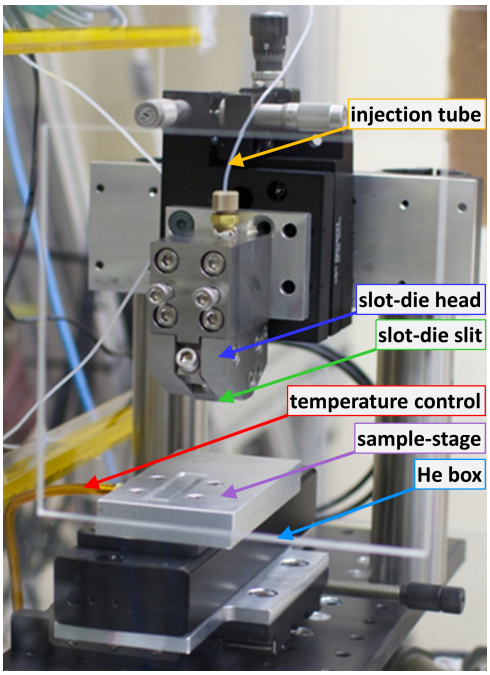

Figure 7.1: Photograph of the miniature slot-die coater implemented at the beamline 7.3.3. of the Advanced Light Source, Berkeley. Photograph provided by Dr. Feng Liu, ALS, LBNL Berkeley.

The slot-die coater used for the experiment presented in this chapter was custom-designed for the implementation in a synchrotron beamline, in this case the beamline 7.3.3. of the Advanced Light Source (ALS) of the Lawrence Berkeley National Laboratory (LBNL). It was designed by the group of A. Hexemer and C. Wang from the ALS together with the group of T. P. Russell from the University of Massachusetts in Amherst. A photograph of the slot-die printer setup as implemented at the beamline is shown in figure 7.1.

At the beginning of the in-situ measurements, the PEDOT:PSS solution is coated with a flow rate of 0.2 ml/min as described in 4.2.2. During the printing process and throughout the film formation the substrate temperature is kept constant. Further, to suppress background scattering with atoms in the air, the experiment was performed in a helium atmosphere. A chamber was filled with helium before and during the experiment to accomplish the desired atmosphere. The window of the He-chamber (shown in figure 7.1) was sealed with a Kapton foil. In the following, details on the sample preparation are given and the in-situ GIWAXS experiment procedure is described in detail.

7.1.2 In-situ GIWAXS

Performing in-situ experiments to determine the real-time evolution of the morphology is difficult for most investigation techniques. Grazing incidence scattering however provides a powerful tool for in-situ investigation of soft matter materials.[118] E.g., Chou et al.[68] and Perez et al.[119] investigated the development of film morphology during spin-coating of bulk heterojunction photoactive layers, Sanyal et al.[120] investigated the structural evolution of bulk heterojunction photoactive films processed by doctor blading and Sarkar et al.[114] reported on the dynamics of spray coating of metal oxide layers for photovoltaic applications by using high-resolution X-ray scattering. In addition, Liu et al.,[121] Zawacka et al.[122] and Rossander et al.[123] compared the morphology of dry films with the morphology of wet films during slot-die coating and roll-to-roll processing, and Gu et al.[124] reported on morphology changes under solvent vapor annealing. Further, Schaffer et al. were able to relate the degradation of solar cell performance to morphological changes by in-situ GISAXS investigations.[125] The emergence of these advanced characterization tools, e.g. in-situ GISAXS and GIWAXS, enable the real-time characterization of the structure evolution and consequent device optimization.

Here, focus is put on comparing the structure evolution of PEDOT:PSS films, which are printed with different routes. Printed films of PEDOT:PSS (pure PEDOT:PSS) are compared with EG doped PEDOT:PSS films and films that are treated with EG after printing and annealing (EG post-treated PEDOT:PSS). For pure and and for EG doped PEDOT:PSS, the substrate temperature was set to 50 °C. For EG post-treatment however, the substrate temperature had to be elevated to 95 °C to assure a final homogeneous film. The experimental procedures are shown in figure 7.2 for all three printing routes. The three PEDOT:PSS solutions were slot-die coated onto cleaned silicon substrates after the standard preparation of the PEDOT:PSS solution, as explained in chapter 4, section 4.2.1. For the EG doped PEDOT:PSS additionally 6 vol% of EG was added to the

filtered PEDOT:PSS solution prior to printing. For the EG post-treated PEDOT:PSS, first the pure PEDOT:PSS film was printed and subsequently annealed to 140 °C for 10 min in air. After the annealing process, EG was coated onto the pure PEDOT:PSS film, which is referred to as EG-post-treatment.

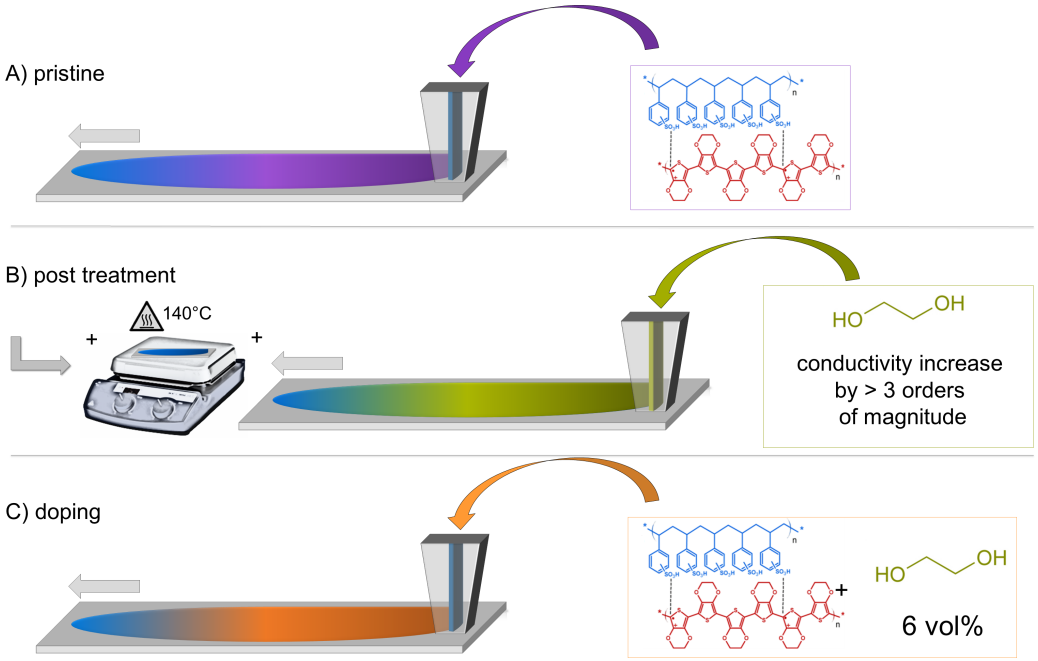

Figure 7.2: Sketch of the slot die coating to obtain printed PEDOT:PSS films: (A) pure PEDOT:PSS films, (B) pure PEDOT:PSS films with additional EG-post-treatment after annealing and (C) PEDOT:PSS films with EG-doping.

The in-situ GIWAXS investigation during the printing process became feasible by three contributions, i.e. the implementation of a custom-designed slot-die coater to the synchrotron beamline, the high brilliance X-ray beam at the synchrotron facilities of the LBNL (ALS) and the performance of the experiment in helium atmosphere. A schematic illustration of the experiment is shown in figure 7.3. For details on theoretical aspects and the experimental method of GIWAXS, it is referred to section 2.3 and section 3.3.3, respectively. During the measurements of the results shown here, the X-ray beam had a photon energy of 1.24 Å (10 keV). If not stated different, the incident angle was chosen to be 0.16 °, which is between the critical angles of the substrate and the material at this photon energy as shown in the following paragraph. The scattered signal was detected with a Pilatus 1M detector and the sample-detector distance was chosen to be 314.6 mm. Each detected in-situ GIWAXS measurement has an integration time of 5 s. Further, for all in-situ measurements series of 120 measurements are taken. With this,

the investigated film evolution time sums up to 600 s. It is important to note that the first measurement starts as soon as the slot-die coater head passes the beam footprint on the sample, which is kept at a fixed position on the film throughout the measurements. Thereby the structure evolution of the just coated film was detected right after the sample, i.e. the position of the footprint of the X-ray beam on the sample, intersected with the slot die head. The in-situ GIWAXS measurements enable to follow the evolution of film characteristics such as the film composition and intermolecular stacking during the drying process (see section 7.2). Further, the influence of the printing parameters, e.g. the addition of co-solvents or the processing temperature, on the final film characteristics is investigated in static measurements with acquisition times of 120 s (see section 7.2.3).

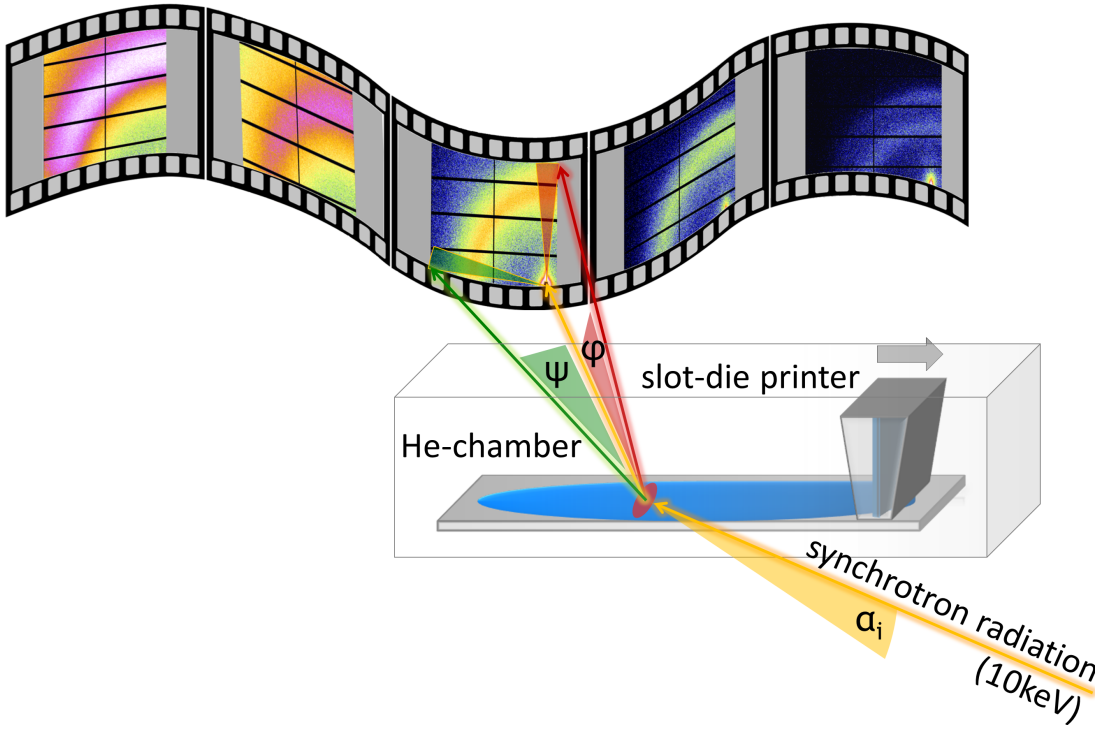

Figure 7.3: Schematic of the in-situ GIWAXS setup. The miniature slot-die coater, which was implemented at the synchrotron beamline, is additionally mounted in a He-chamber to minimize the background scattering.

Incident angle and penetration depth

Typically, the incident angle α_i for GIWAXS measurements is set to a value between the critical angle of the investigated material α_c and the critical angle of the substrate $\alpha_{c,Si}$. Above the incident angle of the investigated material, the film penetration depth increases rapidly. Several incident angles are compared in their influence on the scattering behavior.

To proof the assumption that the crystallite sizes are independent from the choice of the incident angle above $\alpha_i = \alpha_c$, GIWAXS measurements with four different incident angles are performed on a PEDOT:PSS film printed at a processing temperature of 70 °C. The choice of incident angle is thereby shown to only influence the scattering intensity as seen in figure 7.4a. Thereby, the observed difference in scattering intensities for varying angles is explained by geometric effects. For GIWAXS typically very small incident angles are used. At the same time the beam dimensions of the X-ray source are rather large, in this case 30 μm in height and 50 μm in width. Consequently for small incident angles the sample is probed by only a fraction of the beam, i.e. $h/(w \sin(\alpha_i))$ where α_i is the incident angle, h is the beam height and w is the length of the sample in the direction of the beam, in this case 1 cm. The intensity correction applies up to the incident angle, where the beam height equals $w \sin \alpha_i$ and the full beam height probes the sample, in this case $\alpha_i = 0.172°$. Hence the correction is applied for the incident angles 0.12 °, 0.14 ° and 0.16 ° but not for 0.18 °. The correction factors are shown for incident angles of the measured range in figure 7.4b. Consequently, in figure 7.4c the intensity corrected scattering profiles are shown. After correction, the difference in scattering intensities between 0.14 ° and 0.16 ° incident angle is negligible as expected.

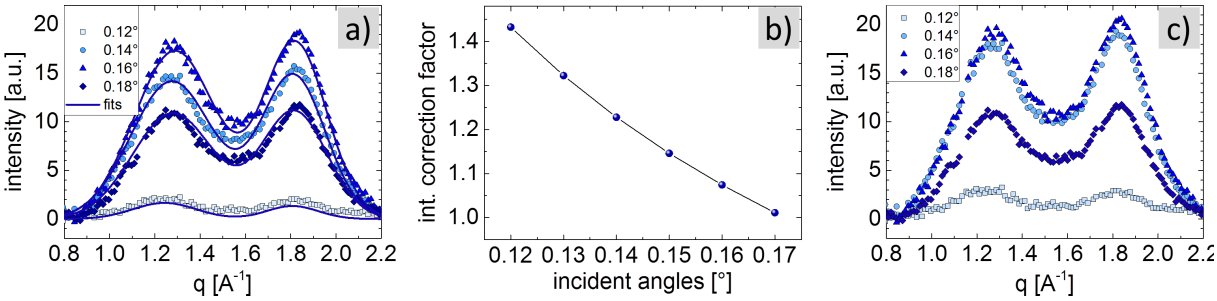

Figure 7.4: a) Influence of incident angle shown by integrated 10 ° - 20 ° and baseline subtracted sector profiles for printed EG-doped PEDOT:PSS films measured for incident angles from 0.12 ° to 0.18 °. The substrate temperature during the printing and drying process was 70 °C and the data aquisition time 10 s for each measurement. b) Intensity correction factor based on the beam height fraction probing the sample. c) Intensity corrected profiles.

This observation of dissenting intensities for 0.12 ° and 0.18 ° are explained in detail in the following. For 0.12 °, which is the critical angle of the polymers, the low intensities are caused by the lower penetration depth and waveguide effects which occur at this angle. It is noted that at $\alpha_f = \alpha_c$ (exit angle equals the critical angle), the waveguide effect in GISAXS experiments leads to strong intensity enhancement at $\alpha_f = \alpha_c$ and a decrease in intensity for other exit angles α_f. For the incident angle 0.18 °, the intensities are strongly

reduced as this angle is at the critical angle of the silicon substrate (0.18 °) and above the one of silicon dioxide (0.174 °) for the measurement photon energy. Thus, a fraction of the incident photons is not reflected back but penetrates the substrate. This leads to the detected decreased scattering intensities.

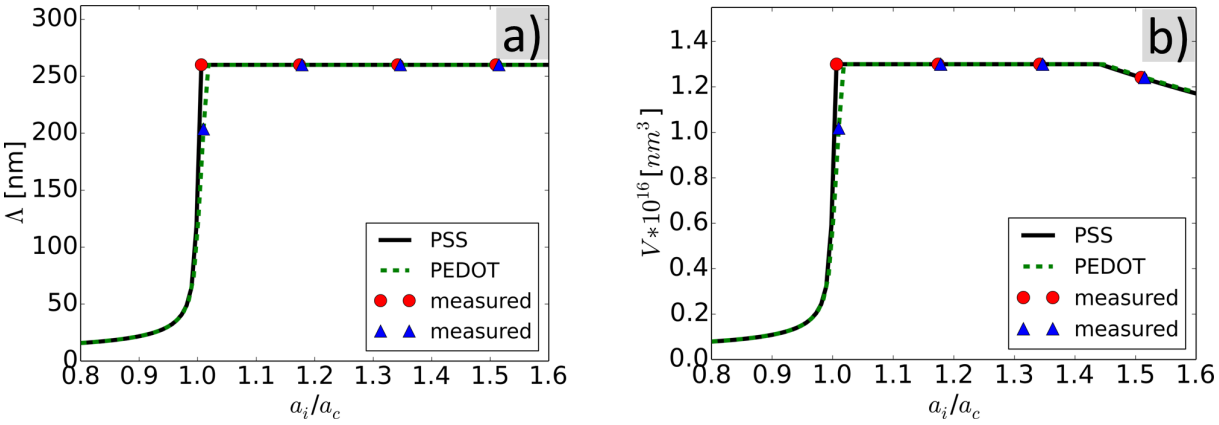

Figure 7.5: a) Penetration depth calculated for pure PSS (black solid line) and pure PEDOT (green dashed line), both investigated with X-rays of 10 keV in energy. Red circles and blue triangles indicate the measured angles on the theoretical line of PSS and PEDOT penetration depth, respectively. b) Effective volume probed by the X-ray beam taking into account the penetration depth as well as the decrease in footprint by increasing incident angle.

Additional to the influences on scattering intensities discussed above, the scattering depth (see section 2.3) and the related effective volume that is probed, varies with the incident angle. As figure 7.5a shows, with the choice of incident angle, the scattering depth increases dramatically before reaching a plateau where the scattering depth equals the film thickness. A similar effect originates from the probed volume which is a measure for the amount of scattering objects contributing to the detected signal (figure 7.5b). This volume increases with the increase in scattering depth, $V(\alpha_i) = h\,w\,\Lambda(\alpha_i)/sin(\alpha_i)$, where h and w are the height and width of the X-ray beam and $\Lambda(\alpha_i)$ is the scattering depth dependent on the incident angle. Starting from the incident angle where the footprint length is equal to the sample length, the footprint becomes shorter than the sample and consequently the probed sample volume decays as seen in figure 7.5b.

angle [°]	**PSS (FWHM)** [nm^{-1}]	**PEDOT (FWHM)** [nm^{-1}]
0.12	3.30 ± 0.17	2.68 ± 0.18
0.14	4.27 ± 0.11	3.34 ± 0.08
0.16	4.23 ± 0.10	3.32 ± 0.08
0.18	4.21 ± 0.11	3.41 ± 0.09

Table 7.1: Full widths at half maximum of PSS and PEDOT dependent on the incident angle of the impinging X-rays exemplary for printed EG-doped PEDOT:PSS films.

Above the critical angle, in this case for measurement angles of 0.14 ° to 0.18 °, the FWHM of the Gaussian terms that are used to model the scattering profile, do not change significantly. This is shown in table 7.1. Correspondingly, the estimated crystallite sizes remain constant for measurement angles of 0.14 ° to 0.18 ° within the accuracy of the estimation as shown in figure 7.6. As a consequence, the angular measurements confirm the assumption that the change in crystallite size is independent of the chosen incident angle above a certain value, here above 0.14 °. Further, it shows that the choice of an incident angle of 0.16 ° results in the best statistics and is therefore chosen for all measurements shown in this chapter if not stated different.

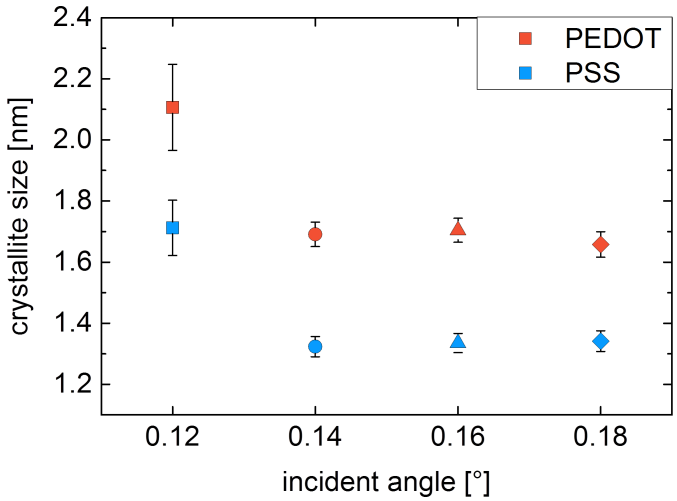

Figure 7.6: Crystallite sizes for printed EG-doped PEDOT:PSS films measured for incident angles from 0.12° to 0.18°. The substrate temperature during the printing and drying process was 70°C.

7.2 Structure evolution in printed PEDOT:PSS thin films

Due to the rapid film formation, typically over tens of seconds, the resulting morphology of the thin films is a delicate balance between multiple kinetic processes: solvent evaporation, diffusion of the constituents, phase separation and ordering. Consequently, real-time monitoring as introduced above, is used to follow the structural evolution with sufficient time resolution. The film formation of PEDOT:PSS films is monitored for the three introduced solution compositions as discussed in section 7.2.1. Special focus is put on the evolution of interchain coupling in section 7.2.2 before the crystallite characteristics are discussed in detail. Therein, the molecular orientation, PEDOT to PSS ratio and and crystallite sizes are evaluated before introducing a film formation model for highly conductive slot-die printed PEDOT:PSS films in section 7.2.4.

7.2.1 Film evolution

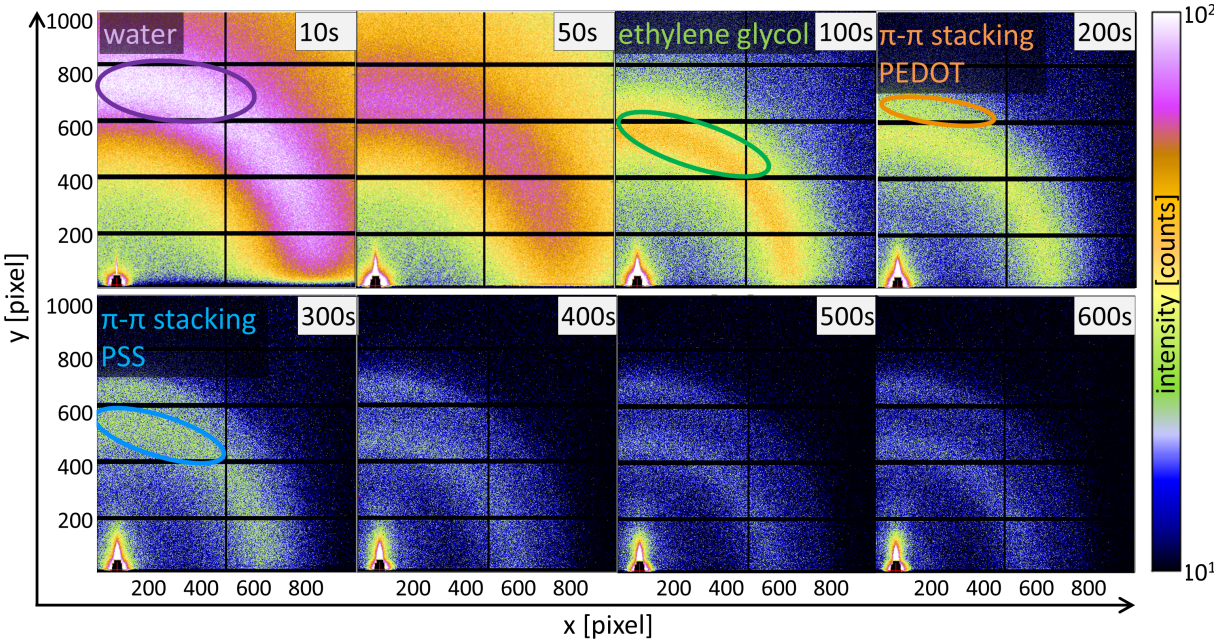

Figure 7.7: Selection of 2D GIWAXS detector images for different times after printing of an EG doped PEDOT:PSS solution. The time series shows the scattering pattern during formation and solidification of the film with the dominating and arising diffraction contributions marked.

In the following, the film formation of pure PEDOT:PSS is compared to EG doped PEDOT:PSS and EG post-treated PEDOT:PSS by in-situ GIWAXS. Figure 7.7 shows

representative detector images as recorded for the EG-doped film. These show how the intensity of the strong diffuse scattering at the beginning of the film evolution (marked in the 10 s and 100 s images) decreases with time in favor of two defined scattering rings, which can be clearly seen at a later stage of the film evolution (highlighted in the 200 s and 300 s images). At the beginning of the film evolution the printed film is still liquid. Therefore, the initially intense and diffuse scattering is assigned to the solvent, in figure 7.7 to water at the initial state followed by EG after water evaporation. The two scattering rings observed for the final solidified film result from the repeated π-π stacking of PEDOT and PSS molecules in their crystallites.

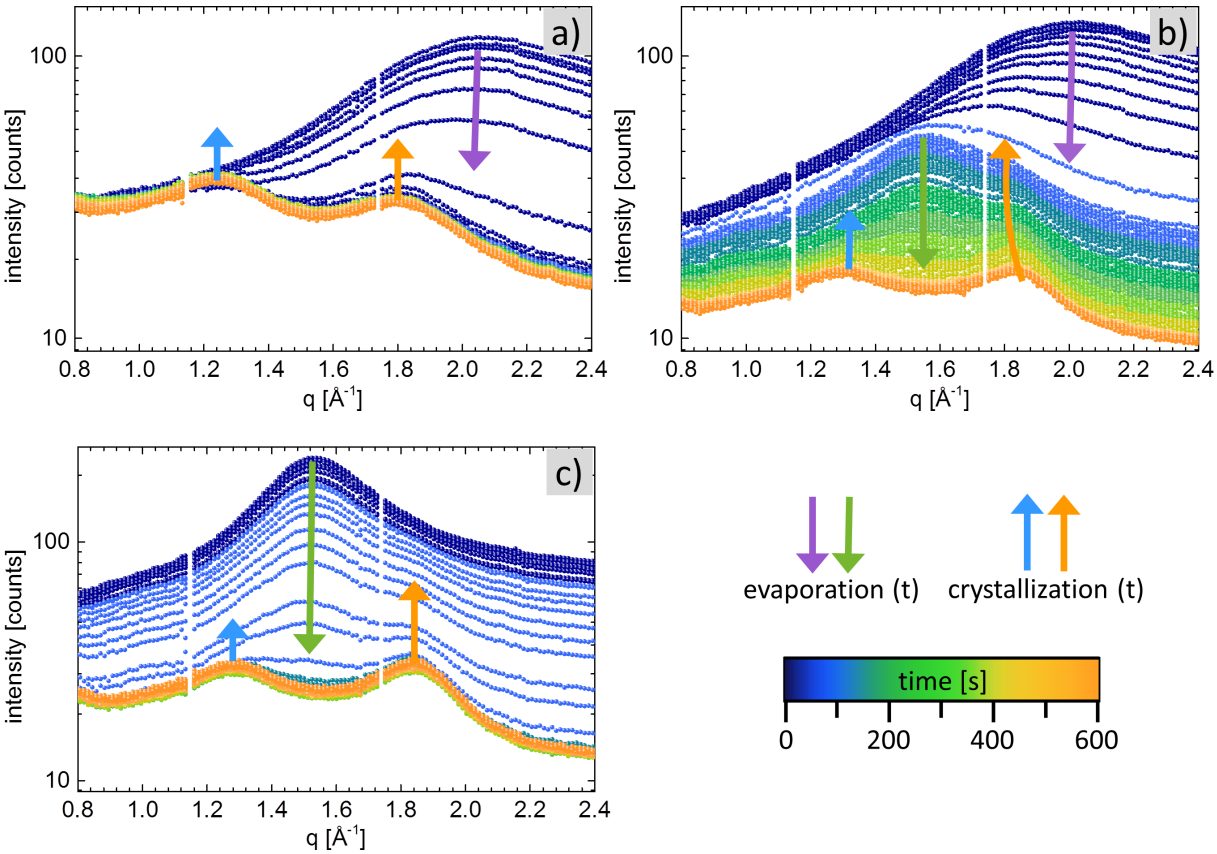

Figure 7.8: Time-resolved vertical (10 ° - 0 °) sector integrals of the 2D GIWAXS data of a) pure, b) EG doped and c) EG post-treated films. Purple and green arrows indicate the solvent evaporation of water and EG, respectively. Blue and red arrows indicate the crystallization of PSS and PEDOT molecules.

To follow the evolution of the structure with time, the in-situ GIWAXS measurements are analyzed via sector averaged integrals, depicted as the intensity versus the scattering vector q. All 2D GIWAXS data were solid angle corrected[78,126] and q-space converted[127]

according to the explanation in section 3.3.4. The sector integrals after 2D GIWAXS correction are performed for all times of the in-situ experiment. Theses are shown in figure 7.8 for (a) pure, (b) EG-doped and (c) EG post-treated PEDOT:PSS films. Within the figure, the solvent evaporation of water and ethylene glycol (EG) is indicated by arrows pointing downwards and the crystallization of the polymers indicated with arrows pointing upwards.

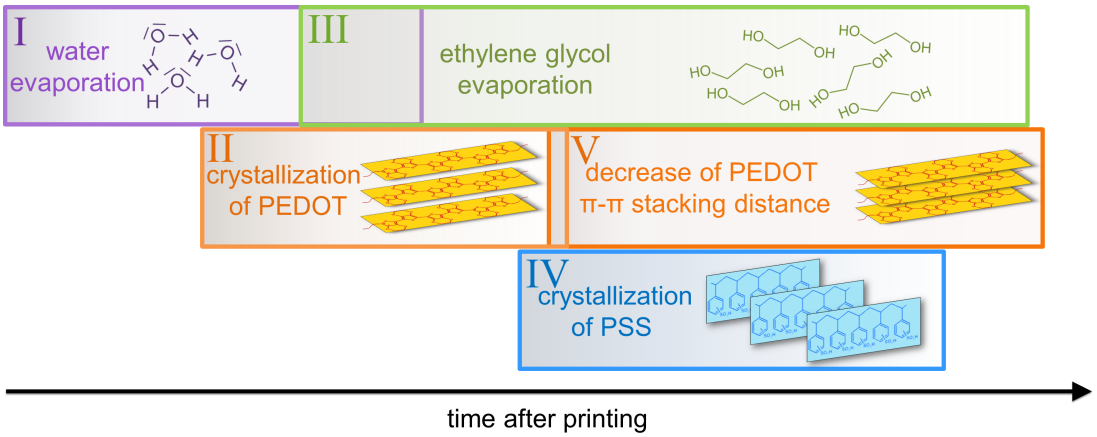

Figure 7.9: Qualitative representation of the five film formation stages identified during the drying process of EG doped PEDOT:PSS after printing. *Stage I*: water evaporation. *Stage II*: crystallization of PEDOT. *Stage III*: ethylene glycol evaporation. *Stage IV*: crystallization of PSS. *Stage V*: decrease of PEDOT interchain distance.

The observed peaks which are highlighted in figure 7.8 are interpreted here for the three PEDOT:PSS films:

- *Pure PEDOT:PSS*: The scattering peak at 2.06 Å^{-1}, which is observed in the initial film (figure 7.8a) corresponds to a real space distance of 3.05 Å. This value is in very good agreement with the scattering observations by Sellberg et al.[128] and arises from the average separation distance between water molecules. As the water evaporates, the intensity of this reflection decreases as shown by the purple arrow. At the same time, the crystallization of PEDOT and PSS molecules lead to two diffraction peaks at $q = 1.78\,\text{Å}^{-1}$ and $q = 1.23\,\text{Å}^{-1}$, respectively, which originate from the π-π stacking distance of the molecules.[92,101] The intensity of these diffraction peaks increase in intensity as the PEDOT crystallizes further as indicated by the orange and blue arrows in figure 7.8.

- *EG doped PEDOT:PSS*: The scattering from the water molecules dominates the scattering profile in figure 7.8b initially. As the water evaporates, the concentration

of EG increases as it features a higher boiling point than water. The scattering arising from EG is observed at $q = 1.55\,\text{Å}^{-1}$ and decreases in intensity as the EG evaporates. With further evaporation, the crystallization of PEDOT can be observed by the diffraction from its π-π stacking. The diffraction center (q-value) for this peak increases from $1.73\,\text{Å}^{-1}$ to $1.82\,\text{Å}^{-1}$ as indicated by the orange arrow. This increase in scattering vector corresponds to a decrease in stacking distance and thereby a resulting enhanced interchain coupling of PEDOT molecules triggered by the presence of EG during the film formation. The scattering diffraction which originates from the π-π stacking of the PSS molecules thereby remains constant at $q = 1.30\,\text{Å}^{-1}$ and increases in intensity with increasing film formation time. This five-step process for EG doped PEDOT:PSS films is depicted qualitatively in figure 7.9.

- *EG post-treated PEDOT:PSS*: The only solvent which is present in this case, is EG. Therefore, the scattering profile is clearly dominated by the post-treatment solvent. While the EG evaporates, the intensity increases for the diffraction from PEDOT and PSS π-π stacked molecules at $1.83\,\text{Å}^{-1}$ and $1.28\,\text{Å}^{-1}$.

7.2.2 Interchain coupling evolution

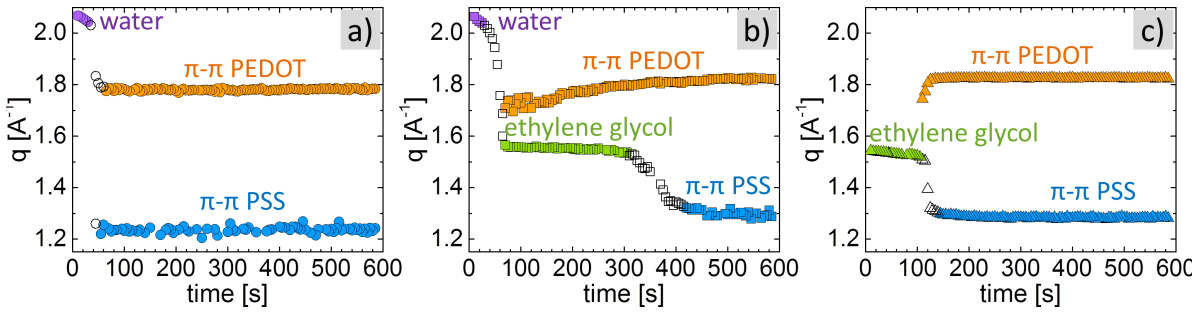

Figure 7.10: Scattering peak positions for a) pure, b) EG doped and c) EG post-treated PEDOT:PSS followed during film evolution. The different peaks can be assigned to different materials as indicated by different colors.

The center of the diffraction peaks in the scattering profiles (figure 7.8) are assigned to the nearest neighbor distance of solvent molecules in the case of diffraction from water and EG, or to the π-π stacking distance of molecules in the case of diffraction from PEDOT and PSS. Gaussian terms are used to follow the temporal evolution of the peaks in the sector averaged integrals of figure 7.8a-c. Figure 7.10a shows the peak positions with time for pure PEDOT:PSS, figure 7.10b for EG-doped PEDOT:PSS and figure 7.10c for

EG-post-treatment of PEDOT:PSS electrodes. The different materials that interplay in the film formation process are highlighted with different colors in the graphs. The solvents water and EG are indicated in purple and green, whereas the polymers PEDOT and PSS are highlighted in red and blue color. During the transition i.e. during evaporation from solvent dominated scattering to polymer dominated scattering, the sector integral profile is a superposition of these scattering contributions. For the period of transition, the peak positions cannot be assigned clearly to one or the other contribution and are therefore indicated with open symbols in figure 7.10. The scattering peak positions for the four materials before and after the transitions remain constant in the case of pure (figure 7.10a) and EG post-treated films (figure 7.10). Only the peak position assigned to π-π stacking of PEDOT molecules in EG doped films (figure 7.10c), shows a clear increase in the scattering vector q between 100 s and 450 s.

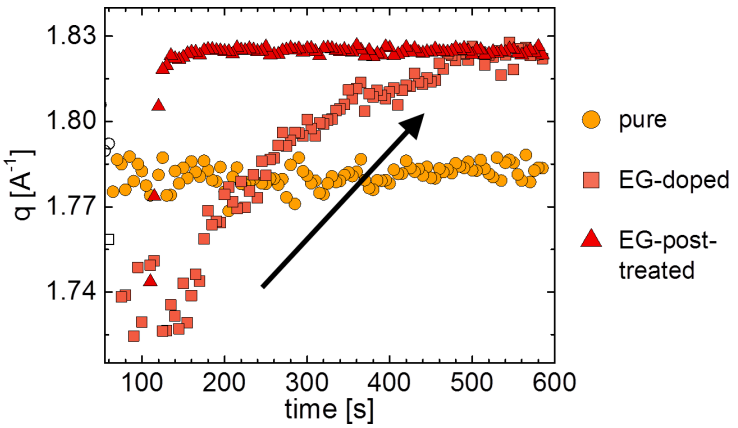

Figure 7.11: Close-up to the time evolution of the PEDOT π-π scattering position for all three PEDOT:PSS films under investigation. The gradual shift in EG doped PEDOT:PSS films is indicated by the arrow.

To compare the drying processes, a close-up to the evolution of the PEDOT π-π scattering peak is depicted in figure 7.11. It shows the evolution of the PEDOT peak for all three films. The peaks in pure and EG post-treated PEDOT:PSS films remain at a constant q-position after a film formation time of 150 s. In comparison, the evolution in the EG doped PEDOT:PSS film clearly shows a gradual shift in the π-π reflection from $q = 1.76\,\text{Å}^{-1}$ to $q = 1.83\,\text{Å}^{-1}$, where the latter is the same final peak position as in EG post-treated films. This trend in the film formation of EG doped PEDOT:PSS is indicated by an arrow in figure 7.11. For the EG doped film, the EG is evaporated after 450 s, while for EG post-treated films, the EG is evaporated after 150 s (figure 7.10) due to the higher processing temperature. After EG evaporation, the PEDOT scattering peak po-

sition remains constant in both films and moreover reaches the same q value. Therefore, the shift in peak position for EG doped films and the increased final peak position in both EG modified films, compared to pure PEDOT:PSS, is attributed to the presence of EG during film formation. This decrease in the π-π stacking distance is only observed in the presence of EG and is associated with a stronger interchain coupling of the PEDOT molecules triggered by a shielding effect of the EG during film formation.

film	**peak position** [Å^{-1}]				
	water	EG	PEDOT initial	PEDOT final	PSS final
pure	2.06 ± 0.01	-	-	1.78 ± 0.01	1.23 ± 0.02
EG doped	2.05 ± 0.01	1.55 ± 0.01	1.73 ± 0.02	1.82 ± 0.01	1.30 ± 0.01
EG post-treated	-	1.54 ± 0.01	1.76 ± 0.02	1.83 ± 0.01	1.28 ± 0.01

Table 7.2: Summary of characteristic peak positions for the involved materials during film formation of the three printed films. The values relate inversely to the nearest neighbor distances in the case of the solvents (water and EG) and to the and π-π stacking distances (molecular interchain coupling) in the case of the polymers (PEDOT and PSS).

In addition to the stronger interchain coupling between PEDOT molecules, the PSS stacking is also influenced by the presence of EG. Scattering from the PSS molecules is ascribed to the π-π stacking of PSS side groups. The resulting PSS π-π scattering vector is $1.30\,\text{Å}^{-1}$ and $1.28\,\text{Å}^{-1}$ in EG doped and EG post-treated films, respectively. In pure PEDOT:PSS films, the π-π scattering vector is with $1.23\,\text{Å}^{-1}$ lower than in the EG modified films. This indicates, that the presence and evaporation of EG not only influences the PEDOT, but also the PSS π-π stacking distances. Thus, it is concluded that EG modification of PEDOT:PSS films leads to stronger interchain coupling of both molecules and to denser films (reduced PEDOT and PSS π-π stacking distances). This observation is in agreement with the investigations shown in chapter 5.[6]

By fitting a Gaussian term to each scattering peak, the position is determined by the center of the Gaussian terms. In table 7.2 a summary of all peak positions is given. It lists the peak positions assigned to the nearest neighbor distance of the solvents, the initial stacking distances of PEDOT as well as the final stacking distances of PEDOT and PSS.

film	**characteristic distance** [Å]				
	water	EG	PEDOT initial	PEDOT final	PSS final
pure	3.05 ± 0.02	-	-	3.53 ± 0.02	5.11 ± 0.08
EG doped	3.07 ± 0.02	4.05 ± 0.03	3.63 ± 0.04	3.45 ± 0.02	4.83 ± 0.04
EG post-treated	-	4.08 ± 0.03	3.57 ± 0.04	3.43 ± 0.02	4.91 ± 0.04

Table 7.3: Summary of real space distances present in the three printed PEDOT:PSS films: solvent nearest neighbor distances and molecular interchain coupling (π-π stacking distances).

Calculated from the peak positions summarized in table 7.2, table 7.3 lists the converted real space distances. From the comparison of the initial to the final state, a decrease in PEDOT π-π stacking distance as well as the slight decrease in PSS stacking distance is evident. Further, a clear trend towards smaller stacking distances with co-solvent treatment is evident.

7.2.3 Crystallite characteristics

After completed film evolution, the data acquisition time was increased to 120 s for enhanced statistics. The corresponding 2D scattering patterns are shown in figure 7.12 for the three investigated PEDOT:PSS films.

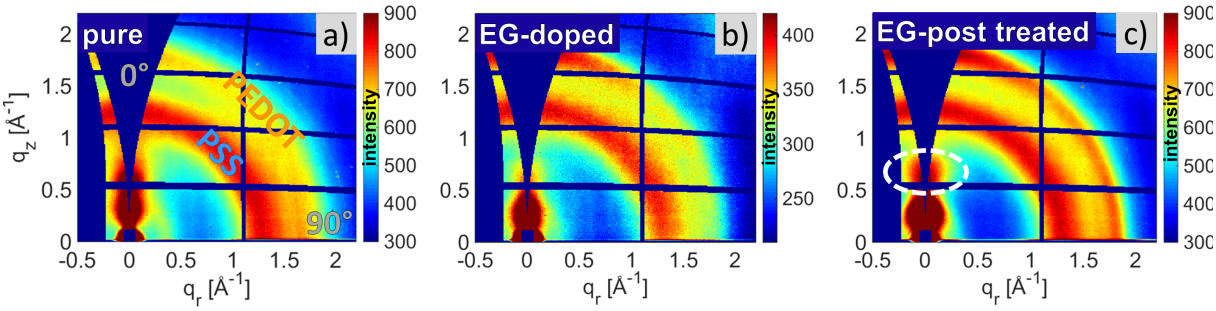

Figure 7.12: 2D GIWAXS measurements of dry PEDOT:PSS films: a) pure, b) EG-doped and c) EG-post-treated.

As discussed in the last section, two observed scattering rings in the 2D pattern originate from the π-π stacking of the two remaining materials, PSS and PEDOT as indicated in figure 7.12a. In addition, the films show a significant scattering in vertical direction, which

is indicated by the circle in figure 7.12c. This scattering peak is centered at a momentum transfer of 0.69 $Å^{-1}$, which corresponds to a real space distance of 0.9 nm. The structure is least pronounced for the EG-doped film and most pronounced for the EG-post-treated film, as seen in contiguous studies for spin coated films (supporting information of reference [6]). This scattering diffraction originates from a vertical layering in EG post-treated PEDOT:PSS films. [94]

For all evaluations the 2D data are solid angle corrected and q-space converted according to section 3.3.4. GIWAXS. Figure 7.13 shows the sector profiles for angles integrated in ranges of 5 °-15 ° to 75 °-85 ° for pure Figure 7.13, EG doped figure 7.13b and EG post-treated figure 7.13c PEDOT:PSS films. To extract the crystallite characteristics, the sector profiles are fitted by a linear background and a Gaussian term for each peak according to section 3.3.3. The obtained crystallite characteristics are summarized in the following.

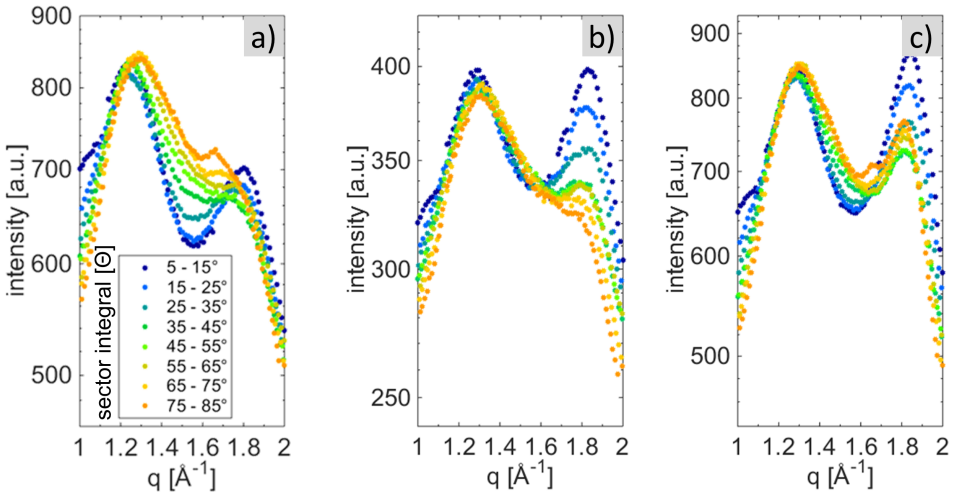

Figure 7.13: Sector integrals for a) pure, b) EG-doped and c) EG-post-treated films from 5 °-15 ° to 75 °-85 °.

Molecular orientation

Scattering from the π-π stacking of the molecules in horizontal and vertical directions, characterize the edge-on and face-on orientations of the molecules relative to the substrate. To investigate the molecular orientation, sector integrals in the horizontal scattering direction (5 °-15 °) are compared to sector integrals in the vertical scattering direction (75 °-85 °). The scattering intensity from the PSS π-π-stacking at ∼1.3 $Å^{-1}$ (figure 7.13a-c) shows only small variations for the different sector integrals and the PSS crystallites thus show no preferred molecular orientation. The scattering intensity from the PEDOT

π-π stacking at 1.8 $Å^{-1}$ (figure 7.13a-c) is stronger in the vertical than in the horizontal direction. Thus, it can be concluded that PEDOT crystallites have a preferred face-on molecular orientation, with slight differences in the edge-on to face-on ratios, especially in EG-post-treated films. To investigate the relative differences in the molecular orientation the edge-on to face-on ratios of the three different films are given by the ratio of the fitted Gaussian areas (table 7.4). The listed values show a clear tendency towards an enhanced edge-on orientation of PEDOT molecules in EG treated films.

film	Edge-on to face-on ratio
pure	0.51
EG-doped	0.94
EG-post-treated	0.96

Table 7.4: Edge-on to face-on orientation for printed PEDOT:PSS films estimated by the ratio of the Gaussian areas.

Estimation of the PEDOT to PSS ratio

Since PEDOT is conductive and PSS is insulating, the PEDOT to PSS ratio influences the conductivity.[7,113] GIWAXS provides information on the volume fraction of crystallites in the film. A trend towards a higher PEDOT to PSS ratio of the crystalline fraction of the films from pure to EG-doped to EG-post-treated PEDOT:PSS is apparent when comparing the two full width at half maximum (FWHM) if the fitted Gaussian terms in figure 7.14.

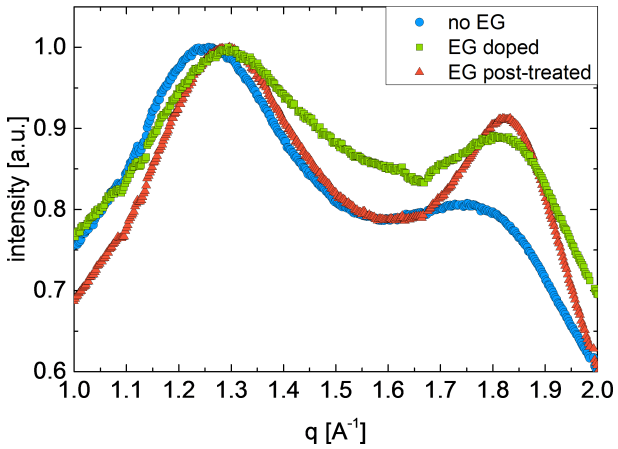

Figure 7.14: Comparison of the three films in terms of PEDOT to PSS ratio. Data is normalized to the PSS scattering peak.

Crystallite sizes

The conductivity within the film is the highest within crystallites of PEDOT molecules. Therefore, the size of the crystallites directly influences the complete film conductivity. In order to estimate the PEDOT and PSS crystallite sizes from the scattering of the π-π stacking, the FWHM of the fitted Gaussian terms is used. The FWHM scales inversely with the crystallite size and therefore can be used as an inverse measure of the size of crystallites. The sizes are derived by the Scherrer formula and the FWHM of the fitted Gaussian terms as shown in section 3.3.3. Therein, peak broadening due to the paracrystalline nature of organic semiconductors and setup related peak broadening are not taken into account. Further, the Scherrer K-factor is estimated to be $K = 0.9$, as in most major publications.[129] Therefore, the determined crystallite size parameters are a lower limit for the actual crystallite sizes and act as comparison parameters and not as exact crystallite sizes.

film	**crystallite size [nm]**			
	PSS (face-on)	PSS (edge-on)	PEDOT (face-on)	PEDOT (edge-on)
pure	1.58 ± 0.02	1.93 ± 0.07	1.38 ± 0.03	0.56 ± 0.02
EG-doped	1.25 ± 0.04	1.20 ± 0.02	1.72 ± 0.03	1.40 ± 0.03
EG-post-treated	1.29 ± 0.04	1.17 ± 0.02	1.78 ± 0.03	1.68 ± 0.03

Table 7.5: Summary of the PEDOT and PSS crystallite parameters.

The values determined by the Scherrer analysis correspond to 3–5 stacked molecules in one crystallite, which is in agreement with literature.[92] The estimated PEDOT crystallite sizes along the π-π stacking direction are summarized in table 7.5. In comparison to pure PEDOT:PSS films the PEDOT crystallite sizes in EG-doped films are larger for face-on as well as edge-on oriented molecules. By EG post-treatment the largest crystallite sizes are obtained for both face-on and edge-on oriented crystallites. Consequently, EG appears to enhance the growth of PEDOT crystallites. With EG-doping, face-on crystallites increase by 20 % and the edge-on crystallites increase by 23 %, relative to the pure films. With EG-post-treatment, face-on crystallites increase by 51 % and edge-on crystallites increase by 67 %, relative to the pure films.

Influence of processing temperature on crystallite sizes

For printing PEDOT:PSS films from the water-based solution, a certain elevated temperature is needed to obtain homogeneous films. Therefore, films printed with 50 °C substrate temperature are compared to film printed with 60 °C and 70 °C. It is evident from the

integrated sector profiles shown in figure 7.15, that the characteristic π-π scattering peaks of PSS and PEDOT (see section 7.2.1) show variations in their scattering intensity and above all in their FWHM. According to the Debye-Scherrer formula (see section 3.3.3), the change of the FWHM of the scattering peaks indicates that the crystallite sizes of the polymers change with the substrate temperature chosen for the printing process.

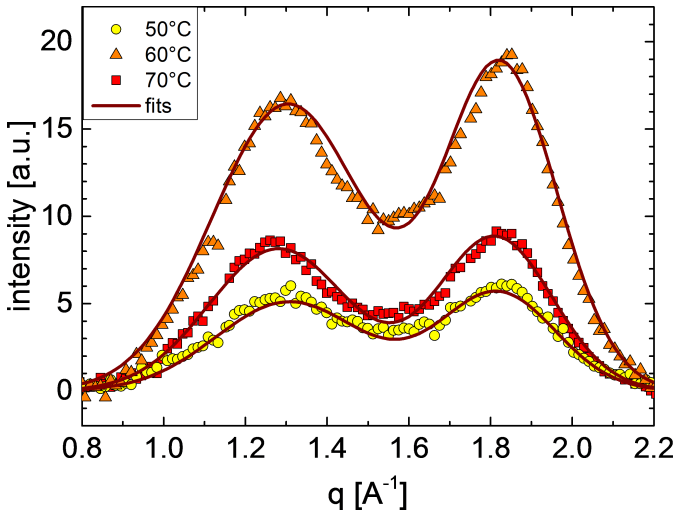

Figure 7.15: Influence of different processing temperatures shown by integrated 10 ° - 20 ° and baseline subtracted sector profiles for PEDOT:PSS electrodes printed on substrates of elevated temperatures of 50 °C, 60 °C and 70 °C.

To extract an estimation of the crystallite sizes from the scattering data, sector integrals from 10 °-20 ° were modeled as shown in section 3.3.3. The FWHM that are extracted from the two Gaussians for PSS and PEDOT scattering are shown in table 7.1. A decrease of the FWHM corresponds to an increase of crystallite size according to the Debye-Scherrer formula (see section 3.3.3).

temperature [°C]	**PSS (FWHM)** [nm^{-1}]	**PEDOT (FWHM)** [nm^{-1}]
50	4.61 ± 0.16	3.12 ± 0.09
60	4.37 ± 0.09	3.27 ± 0.06
70	4.02 ± 0.11	3.31 ± 0.08

Table 7.6: Full width half maximum (FWHM) of PSS and PEDOT dependent on the processing temperature for printed EG-doped PEDOT:PSS films.

Figure 7.16 shows that increasing the substrate temperature from 50 °C to 60 °C leads

to a slight decrease in the estimated PEDOT crystallite sizes and an increase in the PSS crystallite sizes. The center positions of the scattering peaks however do not show significant changes, which means that the polymer stacking distance is independent of processing temperature.

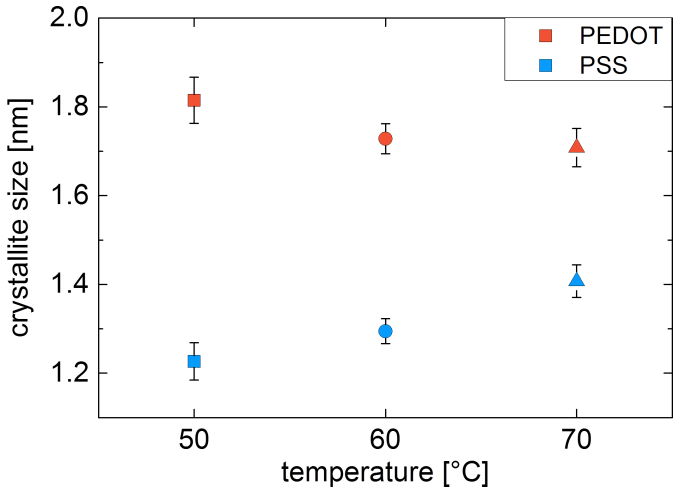

Figure 7.16: Crystallite sizes for PEDOT:PSS electrodes printed on substrates of elevated temperatures of 50 °C, 60 °C and 70 °C.

7.2.4 Film formation model

Based on the results discussed above, a model is developed, which describes the competing kinetic processes by which the films are formed and modified due to the EG co-solvent. Figure 7.17 shows the initial situation before film evolution for each of the three printing processes.

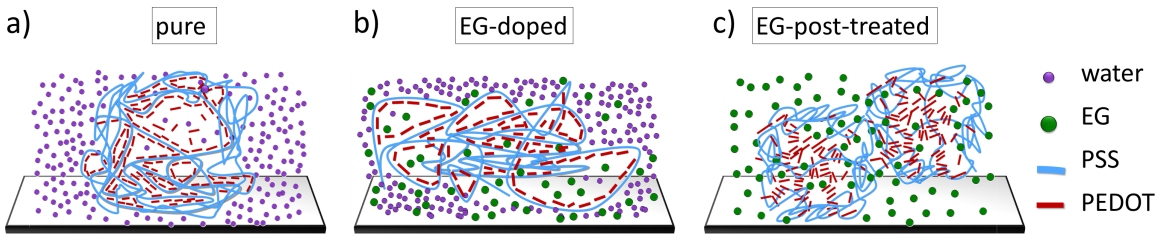

Figure 7.17: Model for the film composition at the beginning of the printing process for a) pure PEDOT:PSS, b) EG-doped PEDOT:PSS and c) EG-post-treated PEDOT:PSS. Solvents are indicated by the purple (water) and green (EG) circles and polymers by the blue (PSS) and red (PEDOT) lines and dashes.

Due to the hydrophobic nature of the PEDOT molecules, PEDOT:PSS in pure aqueous

solution forms a core-shell structure with a PEDOT core and a PSS shell. With the addition of EG into the aqueous solution, the co-solvent diffuses into the core partly dissipating the core-shell structure. The effect of diffusion of EG into the PEDOT core is even more enhanced for EG-post-treatment. In this case, the EG is the only involved solvent and is hence not hindered to diffuse into the PEDOT core by the water-enriched PSS shell as it is the case for EG-doping.

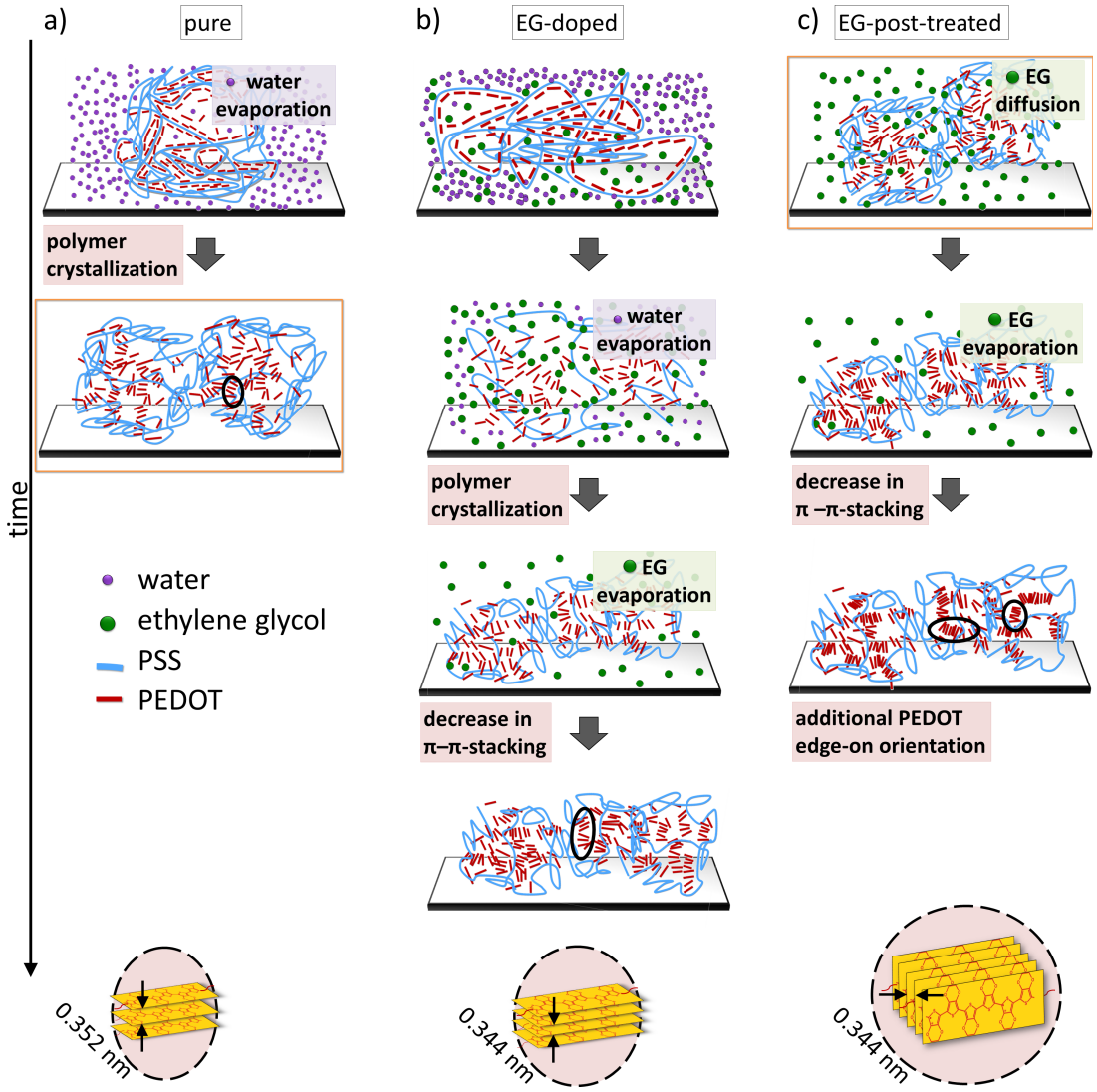

Figure 7.18: The model summarizes the findings derived from the in-situ and ex-situ GIWAXS investigation. It shows the film formation process for a) pure PEDOT:PSS, b) EG-doped PEDOT:PSS and c) EG-post-treated PEDOT:PSS films. The lower row depicts the changes in the molecular stacking distance, orientation and crystallite size upon EG treatment.

The difference in the film morphology evolution between pure doped and post-treated films therefore originates from the fundamentally different environments of the PEDOT:PSS. Due to the hydrophobicity of PEDOT, PEDOT:PSS forms a core-shell structure in aqueous solutions and enables fast film formation as shown in figure 7.18a. Adding EG to the aqueous PEDOT:PSS solution leads to a transition into more extended chains,[7] based on the assumption that water preferentially dissolves the PSS-rich shell, as shown in figure 7.18b. Hence, it is difficult for the organic solvent to diffuse into the PEDOT-rich grain through the water-solvated PSS-rich shell. As the water evaporates, diffusion of the high boiling point EG into the PEDOT-rich grain is favored. Additionally, with the formation of more extended chains, the interchain interaction of PEDOT is enhanced. Together, both processes lead to the observed smaller π-π-stacking distances, larger crystallites and higher film conductivities when compared to pure PEDOT:PSS films. In the case of EG-post-treatment the situation for film formation kinetics is fundamentally different. The PEDOT:PSS film is dry and annealed before the EG is coated onto the film. Therefore, the organic solvent can diffuse into the film and reach the pre-formed PEDOT crystallites more easily, as in the case of EG-doping. The diffusion of EG into the crystallites leads to a recrystallization of the film (see film formation process in figure 7.18c). Molecular reorientation with enhanced edge-on orientation, as well as larger crystallites with closer π-π stacking distances, are observed after the films have been exposed to the pure EG environment. At this point it is worth mentioning that the higher substrate temperature for EG-post-treatment could also have an impact on the film formation kinetics. Higher temperature lowers the activation energy for a PSSH phase separation from PEDOT:PSS as shown by Xia et al.[7] Moreover, the penetration of EG into PEDOT-rich grains has to overcome an energy barrier and will be favored at higher temperatures.

7.3 Conductivity-structure relation

Upon the results discussed above, the characteristic film structures are related to the film conductivities. Table 7.7 shows a strong conductivity enhancement from pure (0.2 S/cm) to EG-doped (990 S/cm) and to EG-post-treated films (1200 S/cm). Since the PEDOT molecules act as the conducting polymer in the system, their arrangement influences the charge transport in the film. One key factor that leads to the improved conductivity, is the improved intergrain conductivity. Equally important is the interchain coupling in the homogeneous model, as shown by Kim et al.[130] The addition of EG into the aqueous solution lowers the dissociation of PSSH into PSS anions and protons as reported by Xia et al.[7] A less dissociated PSSH chain experiences much less coulombic interactions with PEDOT and hence, its interaction with PEDOT is much weaker when leaving

the PEDOT:PSS film. The reduced isolating PSS shell around the PEDOT grains improves the intergrain conductivity. It is noted that for measuring the conductivity, the PEDOT:PSS thin films were printed onto cleaned glass substrates using the same printing parameters as for the in-situ GIWAXS measurements on silicon substrates.

film	**conductivity [S/cm]**	
	pre annealing	post annealing
pure	0.20 ± 0.01	0.5 ± 0.01
EG-doped	990 ± 80	640 ± 50
EG-post-treated	1200 ± 200	1300 ± 300

Table 7.7: Film conductivities prior and post an annealing of 10 min at 140 °C

Figure 7.19 shows that with increasing conductivity (figure 7.19a), the face-on and even more important for the conductivity, the edge-on oriented crystallites increase in their sizes (figure 7.19b). Thereby the intergrain conductivity is increased. Further, the distance between the conducting PEDOT molecules along the π-π stacking direction is reduced (figure 7.19c), increasing the interchain coupling of PEDOT molecules. By this, the interchain conductivity is further optimized. Concluding, the conductivity enhancement in EG-doped and EG-post-treated PEDOT:PSS films is caused by the enhanced PEDOT interchain coupling together with increased edge-on molecular orientation with larger PEDOT crystallites (figure 7.19). [6,113]

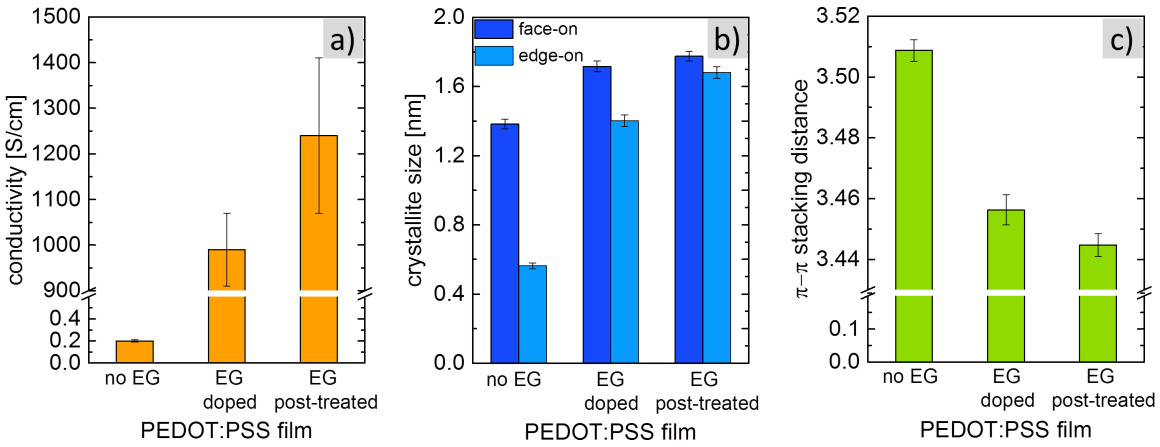

Figure 7.19: Film properties of PEDOT:PSS films printed from three solutions: pure PEDOT:PSS (no EG), EG doped PEDOT:PSS and EG post-treated PEDOT:PSS. The film conductivity (a) is compared to the PEDOT crystallite sizes (b) and the PEDOT stacking distances (c).

7.4 Summary

The morphological evolution of PEDOT:PSS is monitored during printing by in-situ GIWAXS measurements. The different stages and the effect of the solvent additive EG were examined during film formation and post-treatment. It was found, that the crystallization of PEDOT molecules was directly correlated to the evaporation of water. Furthermore, the subsequent evaporation of the EG induces a closer packing of the PEDOT and the PSS crystallites via a reduction of their π-π stacking distances and thus stronger interchain coupling. The solid films showed an enhanced PEDOT crystallinity. Furthermore, additional edge-on orientation of PEDOT was found for EG-post-treated PEDOT:PSS films. Together, the results obtained from the in-situ and ex-situ GIWAXS measurements show the impact of EG on the molecular arrangement and give reasons for the improved charge transport between molecules and the enhanced conductivity of the PEDOT:PSS films. Additionally, understanding the film evolution during the printing process allows for tailored modifications of the solutions and printed films thereby gaining further enhanced OE device performance. By controlling the π-π stacking distance of PEDOT with the amount of EG in the system the conductivity of PEDOT:PSS films could be controlled.

Chapter 8

Summary and outlook

In the present thesis, the conductivity-structure relation of highly conductive PEDOT:PSS thin films is investigated for their application in organic electronics (OE). The results obtained in the framework of this thesis provide answers to the questions that are raised at the beginning (chapter 1) regarding the optimized processing parameters, the conductivity-structure relation of the thin films, their optical properties and their potential application in organic photovoltaic (OPV) devices. Therein, this thesis covers three research highlights which are directed towards processing highly conductive PEDOT:PSS electrodes by a profound understanding of the underlying influences on the spectral and electronic thin film properties and towards tailoring polymeric electrodes in OPV devices:

(1) Processing of PEDOT:PSS electrodes by secondary doping of the initially low-conducting polymeric blend PEDOT:PSS. Using high boiling point co-solvents, highly conductive thin films are obtained. Therefore, the processing parameters are optimized and the inner film structure is related to the film conductivity. (chapter 5)

(2) Investigation of phase separation and molecular reorientation at phase boundaries of PEDOT and PSS, which is shown to be caused by secondary doping using surfactants. The influence of surfactant-modified PEDOT:PSS on photovoltaic device is examined by relating the inner film structure of different PEDOT:PSS films to the corresponding device characteristics. (chapter 6)

(3) Monitoring of the inner film structure in-situ during printing and during film evolution of highly conductive PEDOT:PSS thin films. Therein, structural parameters that influence the intragrain conductivity are tracked as a function of film formation time and related to the final film conductivity. (chapter 7)

In the first research highlight of this thesis (chapter 5), it is shown how the conductivity of PEDOT:PSS thin films can be successfully increased upon secondary doping methods, i.e. solution-doping and post-treatment. With these methods, it is possible to raise the lateral conductivity of PEDOT:PSS from 0.1 S/cm by three orders of magnitude to 1000 S/cm. Additionally, it is demonstrated that the method of post-treatment leads to the highest increase of conductivity. For this method, the film conductivity was found to be increased to a fixed value, independent of the initial state, notably the conductivity. This secondary doping method was optimized in terms of the choice of co-solvent and the treatment process, time and cycle. In terms of conductivity increase the best result is achieved by post-treatment of a solidified and heat-treated PEDOT:PSS thin film with the co-solvent ethylene glycol (EG) for 2 min in a bath and subsequent spinning off of the excess solvent followed by a second heat-treatment cycle. For the first time it is shown that a high PEDOT:PSS film conductivity relates to a vertical film composition with a PEDOT enrichment layer at the substrate interface and an overall increased density. Also, this structural change has been proven to lead to an increase in the number of dication charge carriers. By grazing incidence X-ray investigations of PEDOT:PSS films co-solvent treated with EG and glycerol, the conductivity of PEDOT:PSS was shown to not depend not only on the vertical, but also on the lateral inner film structure. For highly conductive films, a change in inner film morphology towards smaller and more densely packed PEDOT grains is shown for the first time, caused by removal of the insulating PSS.[6] Thereby, the intergrain conductivity is improved. Further, the crystalline structure influences the intragain conductivity by two factors, which depend on the choice of co-solvent and which are of different nature. An enhanced crystallinity, as well as an enhanced edge-on orientation of PEDOT molecules within crystalline grains lead to the observed increase in lateral conductivity. The latter was shown for the first time in literature.[6]

The large-scale usability of highly conductive PEDOT:PSS electrodes is promoted by its tunability to application on surfaces of different nature, i.e. hydrophilic and hydrophobic. The application of the water-based PEDOT:PSS solution on hydrophobic surfaces can be realized by the modification of the PEDOT:PSS solution via surfactants. In chapter 6 the applicability of these surfactant-modified films as transparent electrodes, i.e. with a sufficient conductivity, is proved by extending the processing to additional EG post-treatment step. Thereby for multilayers a transmission of up to 80 % with an unexpected low sheet resistance of down to $30\,\Omega/^2$ is achieved, which is comparable to the widely used ITO electrode.[103] The surfactant is shown to lead to a change in inner film morphology containing elongated conductive PEDOT grains of 60-80 nm in length. These elongated grains are formed as a consequence of the screening effect of the surfactant between the

hydrophilic PSS and the hydrophobic PEDOT molecules. For the first time in literature, this screening effect is proved to enable PSS molecules to reorientate themselves at the interface to PEDOT, consequently favoring their phase separation and the elongation of PEDOT domains.[103] Furthermore, the phase separation is shown to increase the efficiency of P3HT:PCBM organic photovoltaic devices by up to 5 % to power conversion efficiencies above 4 %. The efficiency increase arises out of the phase separation, which causes PSS to enrich at the interface to the active layer. This PSS enrichment layer leads to a reduction of charge carrier recombination at the interface of active layer and electrode, and hence a strong increase in the photovoltaic fill factor and parallel resistance. The results presented in this thesis pave the way towards a versatile application of PEDOT:PSS electrodes with tunable OE properties, i.e. sheet resistance and transmission, and tunable application on different surfaces.

Last but not least, a step towards industrial realization of PEDOT:PSS electrodes is made by successfully transferring the process of PEDOT:PSS co-solvent modification to the deposition method of slot-die printing. Contrary to the typically used deposition method of spin-coating, printing is applicable for the production of large-scale flexible OEs. In chapter 7 of this thesis, it is shown that in principle, the process can be transferred obtaining similar results in terms of PEDOT:PSS film conductivity. Still, the film formation is shown to be fast and complex, which makes it strongly dependent on the processing conditions and deposition methods used. For the first time in literature, the fast film formation kinetics of PEDOT:PSS are successfully monitored by in-situ grazing incidence wide angle X-ray scattering (in-situ GIWAXS) immediately after printing and during the whole film formation.[66] Thereby, new insight into the kinetic processes and their impact on the arrangement of the conducting PEDOT molecules is obtained. As PEDOT crystals exhibit an asymmetric conductivity, not only their backbone structure, but also their π-π stacking influences the intragrain conductivity as the charge transport along the π-π stacking direction is thereby more efficient. The investigations shed light on the evolution of the π-π stacking distance and reveal its dependence on the presence of solvent and co-solvent molecules during the film formation.[66] Therein, the presence of EG during the film formation is shown to decrease the resulting π-π stacking distance within the PEDOT crystallites, which results in an enhanced interchain coupling and thus an enhanced intrachain conductivity. In total, the results presented in this chapter relate the enhanced PEDOT:PSS film conductivity to stronger PEDOT interchain coupling, molecular orientation and crystallite sizes.[66]

In conclusion, the bundling of the research highlights discussed in this thesis presents the applicability of PEDOT:PSS thin films as polymeric electrodes for OEs. The inner film morphology is shown to be tunable by secondary doping. With this method, it is possible to obtain highly conductive polymeric electrodes. The characteristic structure sizes in PEDOT:PSS electrodes influence the electronic performance of the thin films and thus the respective photovoltaic device characteristics. Hence, this thesis demonstrates how the inner film structure of PEDOT:PSS thin films can be tailored by secondary doping and how this can be utilized to tune the electrical properties. Understanding the conductivity-structure relation in the developed PEDOT:PSS electrodes enables optimization and tuning the properties of polymeric electrodes and thus OEs.

As an outlook the light weight and ultra-thin polymeric electrodes, which were developed in the framework of this thesis, pave the way to fully transparent and ultra-thin electronic circuits of just several tens to hundreds of nanometers in thickness. With their scalability using e.g. roll-to-roll printing and their low cost, these plastic electrodes have a great potential in the field of OEs, but also beyond. PEDOT:PSS is a bio-compatible material and thus could be used in bio-compatible electronics for medical applications such as imperceptible health monitoring or bio-compatible electronics in medical instruments. Furthermore, the high flexibility and light weight of PEDOT:PSS electrodes is favorable for application in smart clothes and e-textiles, where digital components are embedded.

Bibliography

[1] C. K. Chiang, C. R. Fincher, Y. W. Park, A. J. Heeger, H. Shirakawa, E. J. Louis, S. C. Gau, and A. G. MacDiarmid, "Electrical conductivity in doped polyacetylene," *Physical Review Letters*, vol. 39, no. 17, pp. 1098–1101, 1977.

[2] H. Shirakawa, E. J. Louis, A. G. MacDiarmid, C. K. Chiang, and A. J. Heeger, "Synthesis of electrically conducting organic polymers: halogen derivatives of polyacetylene, (ch)x," *Journal of the Chemical Society, Chemical Communications*, no. 16, p. 578, 1977.

[3] K. Fehse, K. Walzer, K. Leo, W. Lövenich, and A. Elschner, "Highly conductive polymer anodes as replacements for inorganic materials in high-efficiency organic light-emitting diodes," *Advanced Materials*, vol. 19, no. 3, pp. 441–444, 2007.

[4] M. Vosgueritchian, D. J. Lipomi, and Z. Bao, "Highly conductive and transparent pedot:pss films with a fluorosurfactant for stretchable and flexible transparent electrodes," *Advanced Functional Materials*, vol. 22, no. 2, pp. 421–428, 2012.

[5] Y. H. Kim, C. Sachse, M. L. Machala, C. May, L. Müller-Meskamp, and K. Leo, "Highly conductive pedot:pss electrode with optimized solvent and thermal post-treatment for ito-free organic solar cells," *Advanced Functional Materials*, vol. 21, no. 6, pp. 1076–1081, 2011.

[6] C. M. Palumbiny, C. Heller, C. J. Schaffer, V. Körstgens, G. Santoro, S. V. Roth, and P. Müller-Buschbaum, "Molecular reorientation and structural changes in cosolvent-treated highly conductive pedot:pss electrodes for flexible indium tin oxide-free organic electronics," *The Journal of Physical Chemistry C*, vol. 118, no. 25, pp. 13598–13606, 2014.

[7] Y. Xia and J. Ouyang, "Pedot:pss films with significantly enhanced conductivities induced by preferential solvation with cosolvents and their application in polymer photovoltaic cells," *Journal of Materials Chemistry*, vol. 21, no. 13, p. 4927, 2011.

[8] F. C. Krebs, J. Fyenbo, and M. Jørgensen, "Product integration of compact roll-to-roll processed polymer solar cell modules: methods and manufacture using flexographic printing, slot-die coating and rotary screen printing," *Journal of Materials Chemistry*, vol. 20, no. 41, p. 8994, 2010.

[9] G. Strobl, *The Physics of Polymers: Concepts for Understanding Their Structures and Behavior*. Berlin, Heidelberg: Springer-Verlag Berlin Heidelberg, third revised and expanded edition ed., 2007.

[10] G. Strobl, "Colloquium: Laws controlling crystallization and melting in bulk polymers," *Reviews of Modern Physics*, vol. 81, no. 3, pp. 1287–1300, 2009.

[11] R. Becker, "Die keimbildung bei der ausscheidung in metallischen mischkristallen," *Annalen der Physik*, vol. 424, no. 1-2, pp. 128–140, 1938.

[12] W. Hu, "Intramolecular crystal nucleation," in *Progress in Understanding of Polymer Crystallization* (G. Reiter and G. R. Strobl, eds.), vol. 714 of *Lecture Notes in Physics*, pp. 47–63, Springer Berlin Heidelberg, 2007.

[13] G. Reiter and G. R. Strobl, eds., *Progress in Understanding of Polymer Crystallization*. Lecture Notes in Physics, Berlin, Heidelberg: Springer Berlin Heidelberg, 2007.

[14] P. J. Flory, "Thermodynamics of high polymer solutions," *The Journal of chemical physics*, vol. 10, no. 1, pp. 51–61, 1942.

[15] M. L. Huggins, "Theory of solutions of high polymers1," *Journal of the American Chemical Society*, vol. 64, no. 7, pp. 1712–1719, 1942.

[16] H. Lee, H. Jung, M. Han, C. Lee, and W. Kim, "Compatibility studies of blends of a thermotropic liquid crystalline polymer and flexible chain polymers by application of florys lattice theory.," *Polymer*, vol. 42, no. 5, pp. 2177–2184, 2001.

[17] B. B. Renker, R. Comes, and H. E. Keller, "Phenomena, low-dimensional cooperative," 1975.

[18] J. L. Bredas and G. B. Street, "Polarons, bipolarons, and solitons in conducting polymers," *Accounts of Chemical Research*, vol. 18, no. 10, pp. 309–315, 1985.

[19] M. Schott, M. Nechtschein, and J. P. Farges, "Organic conductors," 1994.

[20] L. Rothberg, M. Yan, and T. E. Kobayashi, *Relaxation in Polymers*. World Scientific, 1993.

[21] B. D. Martin, N. Nikolov, S. K. Pollack, A. Saprigin, R. Shashidhar, F. Zhang, and P. A. Heiney, "Hydroxylated secondary dopants for surface resistance enhancement in transparent poly(3,4-ethylenedioxythiophene)–poly(styrenesulfonate) thin films," *Synthetic Metals*, vol. 142, no. 1-3, pp. 187–193, 2004.

[22] A. Elschner, S. Kirchmeyer, W. Lovenich, U. Merker, and K. Reuter, *PEDOT: principles and applications of an intrinsically conductive polymer*. CRC Press, 2010.

[23] W. P. Su, J. Schrieffer, and A. J. Heeger, "Solitons in polyacetylene," *Physical Review Letters*, vol. 42, no. 25, p. 1698, 1979.

[24] M. Niedermeier, *Novel structuring routines of titania films for application in photovoltaics*. PhD thesis, Technische Universität München, 2013.

[25] M. Schwoerer and H. C. Wolf, *Organic molecular solids*. John Wiley-VCH Verlag, Weinheim, 2007.

[26] M. Pope and C. E. Swenberg, *Electronic processes in organic crystals and polymers*, vol. #56 of *Monographs on the physics and chemistry of materials*. New York: Oxford University Press, 2nd ed. ed., 1999.

[27] M. C. Scharber and N. S. Sariciftci, "Efficiency of bulk-heterojunction organic solar cells," *Progress in Polymer Science*, vol. 38, no. 12, pp. 1929–1940, 2013.

[28] J. Nelson, "Polymer:fullerene bulk heterojunction solar cells," *Materials Today*, vol. 14, no. 10, pp. 462–470, 2011.

[29] R. A. Segalman, B. McCulloch, S. Kirmayer, and J. J. Urban, "Block copolymers for organic optoelectronics," *Macromolecules*, vol. 42, no. 23, pp. 9205–9216, 2009.

[30] P. E. Shaw, A. Ruseckas, and Samuel, Ifor D. W., "Exciton diffusion measurements in poly(3-hexylthiophene)," *Advanced Materials*, vol. 20, no. 18, pp. 3516–3520, 2008.

[31] D. Kurrle and J. Pflaum, "Exciton diffusion length in the organic semiconductor diindenoperylene," *Applied Physics Letters*, vol. 92, no. 13, p. 133306, 2008.

[32] L. LUER, "Oxygen-induced quenching of photoexcited states in polythiophene films," *Organic Electronics*, vol. 5, no. 1-3, pp. 83–89, 2004.

[33] L. Onsager, "Initial recombination of ions," *Physical Review*, vol. 54, no. 8, pp. 554–557, 1938.

[34] C. L. Braun, "Electric field assisted dissociation of charge transfer states as a mechanism of photocarrier production," *The Journal of Chemical Physics*, vol. 80, no. 9, p. 4157, 1984.

[35] C. Deibel and V. Dyakonov, "Polymer–fullerene bulk heterojunction solar cells," *Reports on Progress in Physics*, vol. 73, no. 9, p. 096401, 2010.

[36] R. A. Marcus, "Electron transfer reactions in chemistry. theory and experiment," *Reviews of Modern Physics*, vol. 65, no. 3, pp. 599–610, 1993.

[37] R. A. Marcus, "On the theory of oxidation-reduction reactions involving electron transfer. i," *The Journal of Chemical Physics*, vol. 24, no. 5, p. 966, 1956.

[38] Miller, Allen and Elihu Abrahams, "Impurity conduction at low concentrations," *Physical Review*, vol. 120, no. 3, pp. 745–755, 1960.

[39] H. Bässler, "Charge transport in disordered organic photoconductors a monte carlo simulation study," *phys. status solidi b*, vol. 175, no. 1, pp. 15–56, 1993.

[40] V. Kažukauskas, M. Pranaitis, L. Sicot, and F. Kajzar, "Negative mobility dependence in different regioregular polythiophenes revealed by the charge extraction by linearly increasing voltage method," *Molecular Crystals and Liquid Crystals*, vol. 447, no. 1, pp. 141/[459]–153/[471], 2006.

[41] S. M. Tuladhar, M. Sims, J. Kirkpatrick, R. C. Maher, A. J. Chatten, Bradley, Donal D. C., J. Nelson, P. G. Etchegoin, C. B. Nielsen, P. Massiot, W. N. George, and Steinke, Joachim H. G., "Influence of alkyl chain length on charge transport in symmetrically substituted poly(2,5-dialkoxy-p-phenylenevinylene) polymers," *Physical Review B*, vol. 79, no. 3, p. 035201, 2009.

[42] C. Westermeier, M. Fiebig, and B. Nickel, "Mapping of trap densities and hotspots in pentacene thin-film transistors by frequency-resolved scanning photoresponse microscopy," *Advanced Materials*, vol. 25, no. 40, pp. 5719–5724, 2013.

[43] C. Westermeier, A. Cernescu, S. Amarie, C. Liewald, F. Keilmann, and B. Nickel, "Sub-micron phase coexistence in small-molecule organic thin films revealed by infrared nano-imaging," *Nature Communications*, vol. 5, 2014.

[44] J. Scott and G. G. Malliaras, "Charge injection and recombination at the metal–organic interface," *Chemical Physics Letters*, vol. 299, no. 2, pp. 115–119, 1999.

[45] M. Gopal, W. Moberly Chan, and L. d. Jonghe, "Room temperature synthesis of crystalline metal oxides," *Journal of Materials Science*, vol. 32, no. 22, pp. 6001–6008, 1997.

[46] M. Tolan, *X-Ray Scattering from Soft-Matter Thin Films*, vol. 148. Berlin, Heidelberg: Springer Berlin Heidelberg, 1999.

[47] L. G. Parratt, "Surface studies of solids by total reflection of x-rays," *Physical Review*, vol. 95, no. 2, pp. 359–369, 1954.

[48] H. Kiessig, "Interferenz von röntgenstrahlen an dünnen schichten," *Annalen der Physik*, vol. 402, no. 7, pp. 769–788, 1931.

[49] P. Müller-Buschbaum, "Structure determination in thin film geometry using grazing incidence small-angle scattering," in *Polymer Surfaces and Interfaces* (M. Stamm, ed.), pp. 17–46, Springer Berlin Heidelberg, 2008.

[50] Y. Yoneda, "Anomalous surface reflection of x rays," *Physical Review*, vol. 131, no. 5, pp. 2010–2013, 1963.

[51] P. Müller-Buschbaum, "Influence of surface cleaning on dewetting of thin polystyrene films," *The European physical journal. E, Soft matter*, vol. 12, no. 3, pp. 443–8; discussion 448, 2003.

[52] A. Naudon, D. Babonneau, D. Thiaudière, and S. Lequien, "Grazing-incidence small-angle x-ray scattering applied to the characterization of aggregates in surface regions," *Physica B: Condensed Matter*, vol. 283, no. 1-3, pp. 69–74, 2000.

[53] Holý, V. and Baumbach, T., "Nonspecular x-ray reflection from rough multilayers," *Physical Review B*, vol. 49, no. 15, pp. 10668–10676, 1994.

[54] Sinha, S. K. and Sirota, E. B. and Garoff, S. and Stanley, H. B., "X-ray and neutron scattering from rough surfaces," *Physical Review B*, vol. 38, no. 4, pp. 2297–2311, 1988.

[55] P. Müller-Buschbaum, "A basic introduction to grazing incidence small-angle x-ray scattering," in *Applications of Synchrotron Light to Scattering and Diffraction in Materials and Life Sciences* (M. Gomez, A. Nogales, M. C. Garcia-Gutierrez, and T. Ezquerra, eds.), vol. 776 of *Lecture Notes in Physics*, pp. 61–89, Springer Berlin Heidelberg, 2009.

[56] R. Hosemann, W. Vogel, D. Weick, and F. J. Baltá-Calleja, "Novel aspects of the real paracrystal," *Acta Crystallographica Section A*, vol. 37, no. 1, pp. 85–91, 1981.

[57] A. Guinier, *X-ray Diffraction in Crystals, Imperfect Crystals, and Amorphous Bodies*. Dover, 1994.

[58] H. Ade and A. P. Hitchcock, "Nexafs microscopy and resonant scattering: Composition and orientation probed in real and reciprocal space," *Polymer*, vol. 49, no. 3, pp. 643–675, 2008.

[59] B. A. Collins, J. E. Cochran, H. Yan, E. Gann, C. Hub, R. Fink, C. Wang, T. Schuettfort, C. R. McNeill, M. L. Chabinyc, and H. Ade, "Polarized x-ray scattering reveals non-crystalline orientational ordering in organic films," *Nature Materials*, vol. 11, no. 6, pp. 536–543, 2012.

[60] M. Gruber, M. Rawolle, J. Wagner, D. Magerl, U. Hörmann, J. Perlich, S. V. Roth, A. Opitz, F. Schreiber, P. Müller-Buschbaum, and W. Brütting, "Correlating structure and morphology to device performance of molecular organic donor–acceptor photovoltaic cells based on diindenoperylene (dip) and c60," *Advanced Energy Materials*, vol. 3, no. 8, pp. 1075–1083, 2013.

[61] M. A. Ruderer, S. Guo, R. Meier, H.-Y. Chiang, V. Körstgens, J. Wiedersich, J. Perlich, S. V. Roth, and P. Müller-Buschbaum, "Solvent-induced morphology in polymer-based systems for organic photovoltaics," *Advanced Functional Materials*, vol. 21, no. 17, pp. 3382–3391, 2011.

[62] M. Rawolle, E. V. Braden, M. A. Niedermeier, D. Magerl, K. Sarkar, T. Fröschl, N. Hüsing, J. Perlich, and P. Müller-Buschbaum, "Low-temperature route to crystalline titania network structures in thin films," *ChemPhysChem*, vol. 13, no. 9, pp. 2412–2417, 2012.

[63] A. Nelson, "Co-refinement of multiple-contrast neutron/x-ray reflectivity data using motofit," *Journal of Applied Crystallography*, vol. 39, no. 2, pp. 273–276, 2006.

[64] M. Rawolle, M. A. Ruderer, S. M. Prams, Q. Zhong, D. Magerl, J. Perlich, S. V. Roth, P. Lellig, J. S. Gutmann, and P. Müller-Buschbaum, "Nanostructuring of titania thin films by a combination of microfluidics and block-copolymer-based sol-gel templating," *Small*, vol. 7, no. 7, pp. 884–891, 2011.

[65] J. Ilavsky, "Nika: Software for two-dimensional data reduction," *Journal of Applied Crystallography*, vol. 45, no. 2, pp. 324–328, 2012.

[66] C. M. Palumbiny, F. Liu, T. P. Russell, A. Hexemer, C. Wang, and P. Müller-Buschbaum, "The crystallization of pedot:pss polymeric electrodes probed in situ during printing," *Advanced Materials*, vol. 27, no. 22, pp. 3391–3397, 2015.

[67] M. A. Ruderer and P. Müller-Buschbaum, "Morphology of polymer-based bulk heterojunction films for organic photovoltaics," *Soft Matter*, vol. 7, no. 12, p. 5482, 2011.

[68] K. W. Chou, B. Yan, R. Li, E. Q. Li, K. Zhao, D. H. Anjum, S. Alvarez, R. Gassaway, A. Biocca, S. T. Thoroddsen, A. Hexemer, and A. Amassian, "Spin-cast bulk heterojunction solar cells: A dynamical investigation," *Advanced Materials*, vol. 25, no. 13, pp. 1923–1929, 2013.

[69] Y.-C. Huang, C.-S. Tsao, C.-M. Chuang, C.-H. Lee, F.-H. Hsu, H.-C. Cha, C.-Y. Chen, T.-H. Lin, C.-J. Su, U.-S. Jeng, and W.-F. Su, "Small- and wide-angle x-ray scattering characterization of bulk heterojunction polymer solar cells with different fullerene derivatives," *The Journal of Physical Chemistry C*, vol. 116, no. 18, pp. 10238–10244, 2012.

[70] E. Verploegen, C. E. Miller, K. Schmidt, Z. Bao, and M. F. Toney, "Manipulating the morphology of p3ht–pcbm bulk heterojunction blends with solvent vapor annealing," *Chemistry of Materials*, vol. 24, no. 20, pp. 3923–3931, 2012.

[71] N. D. Treat, M. A. Brady, G. Smith, M. F. Toney, E. J. Kramer, C. J. Hawker, and M. L. Chabinyc, "Interdiffusion of pcbm and p3ht reveals miscibility in a photovoltaically active blend," *Advanced Energy Materials*, vol. 1, no. 1, pp. 82–89, 2011.

[72] W.-R. Wu, U.-S. Jeng, C.-J. Su, K.-H. Wei, M.-S. Su, M.-Y. Chiu, C.-Y. Chen, W.-B. Su, C.-H. Su, and A.-C. Su, "Competition between fullerene aggregation and poly (3-hexylthiophene) crystallization upon annealing of bulk heterojunction solar cells," *ACS Nano*, vol. 5, no. 8, pp. 6233–6243, 2011.

[73] P. Kohn, Z. Rong, K. H. Scherer, A. Sepe, M. Sommer, P. Müller-Buschbaum, R. H. Friend, U. Steiner, and S. Hüttner, "Crystallization-induced 10-nm structure formation in p3ht/pcbm blends," *Macromolecules*, vol. 46, no. 10, pp. 4002–4013, 2013.

[74] M. A. Niedermeier, M. Rawolle, P. Lellig, V. Körstgens, E. M. Herzig, A. Buffet, S. V. Roth, J. S. Gutmann, T. Fröschl, N. Hüsing, and P. Müller-Buschbaum, "Low-temperature sol-gel synthesis of nanostructured polymer/titania hybrid films based on custom-made poly(3-alkoxy thiophene)," *ChemPhysChem*, vol. 14, no. 3, pp. 597–602, 2013.

[75] J. T. Rogers, K. Schmidt, M. F. Toney, E. J. Kramer, and G. C. Bazan, "Structural order in bulk heterojunction films prepared with solvent additives," *Advanced Materials*, vol. 23, no. 20, pp. 2284–2288, 2011.

[76] Z. Jiang, "Gixsgui: a matlab toolbox for grazing-incidence x-ray scattering data visualization and reduction, and indexing of buried three-dimensional periodic nanostructured films," *Journal of Applied Crystallography*, vol. 48, no. 3, pp. 917–926, 2015.

[77] Zhang Jiang, "Documentation for gixsgui - 1.6.1,"

[78] J. L. Baker, L. H. Jimison, S. Mannsfeld, S. Volkman, S. Yin, V. Subramanian, A. Salleo, A. P. Alivisatos, and M. F. Toney, "Quantification of thin film crystallographic orientation using x-ray diffraction with an area detector," *Langmuir*, vol. 26, no. 11, pp. 9146–9151, 2010.

[79] S. C. B. Mannsfeld, "X-ray scattering: In tune with organic semiconductors," *Nature Materials*, vol. 11, no. 6, pp. 489–490, 2012.

[80] T. Pfadler, M. Coric, C. M. Palumbiny, A. C. Jakowetz, K.-P. Strunk, J. A. Dorman, P. Ehrenreich, C. Wang, A. Hexemer, R.-Q. Png, P. K. H. Ho, P. Müller-Buschbaum, J. Weickert, and L. Schmidt-Mende, "Influence of interfacial area on exciton separation and polaron recombination in nanostructured bilayer all-polymer solar cells," *ACS Nano*, p. 141125091002001, 2014.

[81] D. R. Lide, *Handbook of organic solvents*. Boca Raton: CRC Press, 1995.

[82] J. Huang, P. F. Miller, J. S. Wilson, Mello, A. J. de, Mello, J. C. de, and Bradley, D. D. C., "Investigation of the effects of doping and post-deposition treatments on the conductivity, morphology, and work function of poly(3,4-ethylenedioxythiophene)/poly(styrene sulfonate) films," *Advanced Functional Materials*, vol. 15, no. 2, pp. 290–296, 2005.

[83] S.-I. Na, G. Wang, S.-S. Kim, T.-W. Kim, S.-H. Oh, B.-K. Yu, T. Lee, and D.-Y. Kim, "Evolution of nanomorphology and anisotropic conductivity in solvent-modified pedot:pss films for polymeric anodes of polymer solar cells," *Journal of Materials Chemistry*, vol. 19, no. 47, p. 9045, 2009.

[84] A. M. Nardes, M. Kemerink, M. d. Kok, E. Vinken, K. Maturova, and R. Janssen, "Conductivity, work function, and environmental stability of pedot:pss thin films treated with sorbitol," *Organic Electronics*, vol. 9, no. 5, pp. 727–734, 2008.

[85] J. Y. Kim, J. H. Jung, D. E. Lee, and J. Joo, "Enhancement of electrical conductivity of poly(3,4-ethylenedioxythiophene)/poly(4-styrenesulfonate) by a change of solvents," *Synthetic Metals*, vol. 126, no. 2-3, pp. 311–316, 2002.

[86] H. J. Snaith, H. Kenrick, M. Chiesa, and R. H. Friend, "Morphological and electronic consequences of modifications to the polymer anode 'pedot:pss'," *Polymer*, vol. 46, no. 8, pp. 2573–2578, 2005.

[87] L. A. Pettersson, S. Ghosh, and O. Inganäs, "Optical anisotropy in thin films of poly(3,4-ethylenedioxythiophene)–poly(4-styrenesulfonate)," *Organic Electronics*, vol. 3, no. 3-4, pp. 143–148, 2002.

[88] X. Crispin, Jakobsson, F. L. E., A. Crispin, Grim, P. C. M., P. Andersson, A. Volodin, C. van Haesendonck, van der Auweraer, M., W. R. Salaneck, and M. Berggren, "The origin of the high conductivity of poly(3,4-ethylenedioxythiophene)−poly(styrenesulfonate) (pedot−pss) plastic electrodes," *Chemistry of Materials*, vol. 18, no. 18, pp. 4354–4360, 2006.

[89] M. Fabretto, C. Hall, T. Vaithianathan, P. C. Innis, J. Mazurkiewicz, G. G. Wallace, and P. Murphy, "The mechanism of conductivity enhancement in poly(3,4-ethylenedioxythiophene)–poly(styrenesulfonic) acid using linear-diol additives: Its effect on electrochromic performance," *Thin Solid Films*, vol. 516, no. 21, pp. 7828–7835, 2008.

[90] S. Timpanaro, M. Kemerink, F. J. Touwslager, Kok, M. M. de, and S. Schrader, "Morphology and conductivity of pedot/pss films studied by scanning–tunneling microscopy," *Chemical Physics Letters*, vol. 394, no. 4-6, pp. 339–343, 2004.

[91] D. Bagchi and R. Menon, "Conformational modification of conducting polymer chains by solvents: Small-angle x-ray scattering study," *Chemical Physics Letters*, vol. 425, no. 1-3, pp. 114–117, 2006.

[92] T. Takano, H. Masunaga, A. Fujiwara, H. Okuzaki, and T. Sasaki, "Pedot nanocrystal in highly conductive pedot:pss polymer films," *Macromolecules*, vol. 45, no. 9, pp. 3859–3865, 2012.

[93] S. Jönsson, J. Birgerson, X. Crispin, G. Greczynski, W. Osikowicz, Denier van der Gon, A.W, W. Salaneck, and M. Fahlman, "The effects of solvents on the morphology and sheet resistance in poly(3,4-ethylenedioxythiophene)–polystyrenesulfonic acid (pedot–pss) films," *Synthetic Metals*, vol. 139, no. 1, pp. 1–10, 2003.

[94] A. M. Nardes, M. Kemerink, Janssen, R. A. J., Bastiaansen, J. A. M., Kiggen, N. M. M., Langeveld, B. M. W., A. van Breemen, and de Kok, M. M., "Microscopic understanding of the anisotropic conductivity of pedot:pss thin films," *Advanced Materials*, vol. 19, no. 9, pp. 1196–1200, 2007.

[95] J. C. Heller, *Kontrollierte Morphologien durch molekulares Design und Nanostrukturierung für die Anwendung in der organischen Photovoltaik*. PhD thesis, Technische Universität München, München, 2013.

[96] N. Massonnet, A. Carella, O. Jaudouin, P. Rannou, G. Laval, C. Celle, and J.-P. Simonato, "Improvement of the seebeck coefficient of pedot:pss by chemical reduction combined with a novel method for its transfer using free-standing thin films," *J. Mater. Chem. C*, vol. 2, no. 7, pp. 1278–1283, 2014.

[97] S. L. Lai, M. Y. Chan, M. K. Fung, C. S. Lee, and S. T. Lee, "Concentration effect of glycerol on the conductivity of 5pedot6 film and the device performance," *Materials Science and Engineering: B*, vol. 104, no. 1–2, pp. 26–30, 2003.

[98] R. Meier, C. Birkenstock, C. M. Palumbiny, and P. Müller-Buschbaum, "Efficiency-improved organic solar cells based on plasticizer assisted soft embossed pedot:pss layers," *Physical Chemistry Chemical Physics*, vol. 14, no. 43, p. 15088, 2012.

[99] M. Reyes-Reyes, I. Cruz-Cruz, and R. López-Sandoval, "Enhancement of the electrical conductivity in pedot:pss films by the addition of dimethyl sulfate," *The Journal of Physical Chemistry C*, vol. 114, no. 47, pp. 20220–20224, 2010.

[100] H. J. Snaith, H. Kenrick, M. Chiesa, and R. H. Friend, "Morphological and electronic consequences of modifications to the polymer anode 'pedot:pss'," *Polymer*, vol. 46, no. 8, pp. 2573–2578, 2005.

[101] K. E. Aasmundtveit, E. J. Samuelsen, L. Pettersson, O. Inganäs, T. Johansson, and R. Feidenhans'l, "Structure of thin films of poly(3,4-ethylenedioxythiophene)," *Synthetic Metals*, vol. 101, no. 1-3, pp. 561–564, 1999.

[102] D. Alemu, H.-Y. Wei, K.-C. Ho, and C.-W. Chu, "Highly conductive pedot:pss electrode by simple film treatment with methanol for ito-free polymer solar cells," *Energy Environ. Sci.*, vol. 5, no. 11, pp. 9662–9671, 2012.

[103] C. M. Palumbiny, J. Schlipf, A. Hexemer, C. Wang, and P. Müller-Buschbaum, "The morphological power of soap: How surfactants lower the sheet resistance of pedot:pss by strong impact on inner film structure and molecular interface orientation," *Advanced Electronic Materials*, vol. 2, no. 4, p. doi: 10.1002/aelm.201500377, 2016.

[104] H. Shi, C. Liu, Q. Jiang, and J. Xu, "Effective approaches to improve the electrical conductivity of pedot:pss: A review," *Advanced Electronic Materials*, vol. 1, no. 4, 2015.

[105] F. Zhang, A. Petr, H. Peisert, M. Knupfer, and L. Dunsch, "Electrochemical variation of the energy level of poly(3,4-ethylenedioxythiophene):poly(styrenesulfonate)," *The Journal of Physical Chemistry B*, vol. 108, no. 45, pp. 17301–17305, 2004.

[106] M. Dressel and G. Grüner, *Electrodynamics of solids: Optical properties of electrons in matter*. PhD thesis, Cambridge and New York, 2002.

[107] Y. Xia and J. Ouyang, "Highly conductive pedot:pss films prepared through a treatment with geminal diols or amphiphilic fluoro compounds," *Organic Electronics*, vol. 13, no. 10, pp. 1785–1792, 2012.

[108] J. Ouyang, Q. Xu, C.-W. Chu, Y. Yang, G. Li, and J. Shinar, "On the mechanism of conductivity enhancement in poly(3,4-ethylenedioxythiophene):poly(styrene sulfonate) film through solvent treatment," *Polymer*, vol. 45, no. 25, pp. 8443–8450, 2004.

[109] J. Ouyang, C.-W. Chu, F.-C. Chen, Q. Xu, and Y. Yang, "High-conductivity poly(3,4-ethylenedioxythiophene):poly(styrene sulfonate) film and its application in polymer optoelectronic devices," *Advanced Functional Materials*, vol. 15, no. 2, pp. 203–208, 2005.

[110] S. Bom, *Cyclic potential growth mechanism for electropolymerized polythiophenes as anode buffer layers in P3HT-PCBM solar cells*. PhD thesis, DPG Frühjahrstagung, Dresden, 2014.

[111] Y. Zhou, C. Fuentes-Hernandez, J. W. Shim, T. M. Khan, and B. Kippelen, "High performance polymeric charge recombination layer for organic tandem solar cells," *Energy & Environmental Science*, vol. 5, no. 12, p. 9827, 2012.

[112] C. M. Palumbiny, F. Liu, T. P. Russell, A. Hexemer, C. Wang, and P. Müller-Buschbaum, "The crystallization of pedot:pss polymeric electrodes probed in situ during printing," *Advanced Materials*, vol. 27, no. 22, pp. 3391–3397, 2015.

[113] Y. H. Kim, C. Sachse, M. L. Machala, C. May, L. Müller-Meskamp, and K. Leo, "Highly conductive pedot:pss electrode with optimized solvent and thermal post-treatment for ito-free organic solar cells," *Advanced Functional Materials*, vol. 21, no. 6, pp. 1076–1081, 2011.

[114] K. Sarkar, E. V. Braden, S. Pogorzalek, S. Yu, S. V. Roth, and P. Müller-Buschbaum, "Monitoring structural dynamics of in situ spray-deposited zinc oxide films for application in dye-sensitized solar cells," *ChemSusChem*, vol. 7, no. 8, pp. 2140–2145, 2014.

[115] J. John, Y. Tang, J. P. Rothstein, J. J. Watkins, and K. R. Carter, "Large-area, continuous roll-to-roll nanoimprinting with pfpe composite molds," *Nanotechnology*, vol. 24, no. 50, p. 505307, 2013.

[116] F. C. Krebs, J. Fyenbo, and M. Jørgensen, "Product integration of compact roll-to-roll processed polymer solar cell modules: methods and manufacture using flexographic printing, slot-die coating and rotary screen printing," *Journal of Materials Chemistry*, vol. 20, no. 41, p. 8994, 2010.

[117] F. C. Krebs, N. Espinosa, M. Hösel, R. R. Søndergaard, and M. Jørgensen, "25th anniversary article: Rise to power - opv-based solar parks," *Advanced Materials*, vol. 26, no. 1, pp. 29–39, 2014.

[118] A. Hexemer and P. Müller-Buschbaum, "Advanced grazing-incidence techniques for modern soft-matter materials analysis," *IUCrJ*, vol. 2, no. 1, pp. 106–125, 2015.

[119] L. A. Perez, K. W. Chou, J. A. Love, T. S. van der Poll, D.-M. Smilgies, T.-Q. Nguyen, E. J. Kramer, A. Amassian, and G. C. Bazan, "Solvent additive effects on small molecule crystallization in bulk heterojunction solar cells probed during spin casting," *Advanced Materials*, vol. 25, no. 44, pp. 6380–6384, 2013.

[120] M. Sanyal, B. Schmidt-Hansberg, Klein, Michael F. G., A. Colsmann, C. Munuera, A. Vorobiev, U. Lemmer, W. Schabel, H. Dosch, and E. Barrena, "In situ x-ray study of drying-temperature influence on the structural evolution of bulk-heterojunction polymer-fullerene solar cells processed by doctor-blading," *Advanced Energy Materials*, vol. 1, no. 3, pp. 363–367, 2011.

[121] F. Liu, S. Ferdous, E. Schaible, A. Hexemer, M. Church, X. Ding, C. Wang, and T. P. Russell, "Fast printing and in situ morphology observation of organic photovoltaics using slot-die coating," *Advanced Materials*, vol. 27, no. 5, pp. 886–891, 2015.

[122] N. K. Zawacka, T. R. Andersen, J. W. Andreasen, L. H. Rossander, H. F. Dam, M. Jørgensen, and F. C. Krebs, "The influence of additives on the morphology and stability of roll-to-roll processed polymer solar cells studied through ex situ and in situ x-ray scattering," *J. Mater. Chem. A*, vol. 2, no. 43, pp. 18644–18654, 2014.

[123] L. H. Rossander, N. K. Zawacka, H. F. Dam, F. C. Krebs, and J. W. Andreasen, "In situ monitoring of structure formation in the active layer of polymer solar cells during roll-to-roll coating," *AIP Advances*, vol. 4, no. 8, p. 087105, 2014.

[124] X. Gu, I. Gunkel, A. Hexemer, W. Gu, and T. P. Russell, "An in situ grazing incidence x-ray scattering study of block copolymer thin films during solvent vapor annealing," *Advanced Materials*, vol. 26, no. 2, pp. 273–281, 2014.

[125] C. J. Schaffer, C. M. Palumbiny, M. A. Niedermeier, C. Jendrzejewski, G. Santoro, S. V. Roth, and P. Müller-Buschbaum, "A direct evidence of morphological degradation on a nanometer scale in polymer solar cells," *Advanced Materials*, vol. 25, no. 46, pp. 6760–6764, 2013.

[126] D. M. DeLongchamp, R. J. Kline, and A. Herzing, "Nanoscale structure measurements for polymer-fullerene photovoltaics," *Energy & Environmental Science*, vol. 5, no. 3, p. 5980, 2012.

[127] A. El Labban, J. Warnan, C. Cabanetos, O. Ratel, C. Tassone, M. F. Toney, and P. M. Beaujuge, "Dependence of crystallite formation and preferential backbone orientations on the side chain pattern in pbdttpd polymers," *ACS Applied Materials & Interfaces*, vol. 6, no. 22, pp. 19477–19481, 2014.

[128] J. A. Sellberg, C. Huang, T. A. McQueen, N. D. Loh, H. Laksmono, D. Schlesinger, R. G. Sierra, D. Nordlund, C. Y. Hampton, D. Starodub, D. P. DePonte, M. Beye, C. Chen, A. V. Martin, A. Barty, K. T. Wikfeldt, T. M. Weiss, C. Caronna, J. Feldkamp, L. B. Skinner, M. M. Seibert, M. Messerschmidt, G. J. Williams, S. Boutet, L. G. M. Pettersson, M. J. Bogan, and A. Nilsson, "Ultrafast x-ray probing of water structure below the homogeneous ice nucleation temperature," *Nature*, vol. 510, no. 7505, pp. 381–384, 2014.

[129] J. Liu, L. Chen, B. Gao, X. Cao, Y. Han, Z. Xie, and L. Wang, "Constructing the nanointerpenetrating structure of pcdtbt:pc70bm bulk heterojunction solar cells induced by aggregation of pc70bm via mixed-solvent vapor annealing," *J. Mater. Chem. A*, vol. 1, no. 20, p. 6216, 2013.

[130] N. Kim, B. H. Lee, D. Choi, G. Kim, H. Kim, J.-R. Kim, J. Lee, Y. H. Kahng, and K. Lee, "Role of interchain coupling in the metallic state of conducting polymers," *Physical Review Letters*, vol. 109, no. 10, 2012.

List of publications

Publications related to this work

- C. M. Palumbiny, J. Schlipf, A. Hexemer, C. Wang, P. Müller-Buschbaum: "The Morphological Power of Soap: How Surfactants Lower the Sheet Resistance of PEDOT:PSS by Strong Impact on Inner Film Structure and Molecular Interface Orientation"; *Adv. Electronic Mater.* **2016**, *4*, DOI: 10.1002/aelm.201500377.
- T. Pfadler, C. M. Palumbiny, Wojciech Pisula, Holger Hesse, Xinliang Feng, Klaus Müllen, Peter Müller-Buschbaum, Lukas Schmidt-Mende: "Controlled morphologies by molecular design and nano-imprint lithography"; book chapter in *Advances in Polymer Science*, Springer (in press).
- C. M. Palumbiny, F. Liu, T. P. Russell, A. Hexemer, C. Wang, P. Müller-Buschbaum: "The Crystallization of PEDOT:PSS Polymeric Electrodes Probed In Situ during Printing"; *Adv. Mater.* **2015**, *22*, 3382-3391.

  associated front cover:
  C. M. Palumbiny, F. Liu, T. P. Russell, A. Hexemer, C. Wang, P. Müller-Buschbaum: "The Crystallization of PEDOT:PSS Polymeric Electrodes Probed In Situ during Printing (Adv. Mater. 21/2015)"; *Adv. Mater.* **2015**, *22*, 3382-3391.
- C. M. Palumbiny, C. Heller, C. J. Schaffer, V. Körstgens, G. Santoro, S. V. Roth, P. Müller-Buschbaum: Molecular reorientation and structural changes in cosolvent-treated highly conductive PEDOT:PSS electrodes for flexible indium tin oxide-free organic electronics; *J. Phys. Chem. C* **2014**, *118*, 13598-13606.

Further publications

- C. Wehrenfennig, C. M. Palumbiny, H. J. Snaith, M. B. Johnston, L. Schmidt-Mende, L. M. Herz: Fast charge-carrier trapping in TiO2 nanotubes; *J. Phys. Chem. C* **2015**, *119*, 9159-9168.

- T. Pfadler, M. Coric, C. M. Palumbiny, A. C. Jakowetz, K.-P. Strunk, J. A. Dorman, P. Ehrenreich, C. Wang, A. Hexemer, R.-Q. Png, P. K. H. Ho, P. Müller-Buschbaum: Influence of interfacial area on exciton separation and polaron recombination in nanostructured bilayer all-polymer solar cells; *ACS Nano* **2014**, *8*, 12397-12409.

- C. J. Schaffer, C. M. Palumbiny, M. Niedermeier, C. Jendrzejewski, G. Santoro, S. V. Roth, P. Müller-Buschbaum: A direct evidence of morphological degradation on a nanometer scale in polymer solar cells; *Adv. Mater.* **2013**, *25*, 6760-6764.

- P. Docampo, A. Ivaturi, R. Gunning, S. Diefenbach, C. M. Palumbiny, J. Kirkpatrick, H. Geaney, V. Sivaram, L. Schmidt-Mende, M. E. Welland, H. J. Snaith: The influence of 1D, meso- and crystal structures on charge transport and recombination in solid-state dye-sensitized solar cells; *J. Mater. Chem.* **2013**, *1*, 12088-12095.

- C. Wehrenfennig, C. M. Palumbiny, L. Schmidt-Mende, M. B. Johnston, H. J. Snaith, L. M. Herz: Fast electron trapping in anodized TiO2 nanotubes ; *Infrared, Millimeter, and Terahertz Waves (IRMMW-THz)* **2013**, *38th International Conference*, 01/2013.

- R. Meier, C. Birkenstock, C. M. Palumbiny, P. Müller-Buschbaum: Efficiency-improved organic solar cells based on plasticizer assisted soft embossed PEDOT:PSS layers; *Phys. Chem. Chem. Phys.* **2011**, *14*, 15088-15098.

- J. Weickert, C. Palumbiny, M. Nedelcu, T. Bein, L. Schmidt-Mende: Controlled growth of TiO(2) nanotubes on conducting glass; *Chem. Mater.* **2011**, *23*, 155-162.

- J. Weickert, H. Sun, C. Palumbiny, H. C. Hesse, L. Schmidt-Mende: Spray-deposited PEDOT:PSS for inverted organic solar cells; *Sol. Energ. Mater. Sol. Cells* **2011**, *94*, 2371-2374.

Press releases and awards related to this work

- Press release of the Technische Universität München (TUM), „Optimized printing process enables custom organic electronics: Designer electronics out of the printer“, https://www.tum.de/en/about-tum/news/press-releases/short/article/32446/; 16 June 2015

- Press release of the Nano Initiative Munich (NIM), „Designer electronics out of the printer: Optimized printing process enables custom organic electronics“, https://

www.nano-initiative-munich.de/press/press-releases/meldung/n/designer-electronics-out-of-the-printer/; 18 June 2015

- ALS Best Poster Award (3rd Price), in recognition of the poster „Highly conductive PEDOT:PSS as electrode for flexible structured ITO-free organic electronics: A morphological study“, *Advanced Light Source (ALS) User Meeting*, Berkeley (USA), 7–9 October 2013.

- TUM.ENERGY Best Presentation Award 2013, in recognition of the presentation „Highly conductive PEDOT:PSS as electrode for flexible structured ITO-free organic electronics: A morphological study“, *3rd Colloquium of the Munich School of Engineering*, Garching (Germany), 4 July 2013.

Scientific reports

- C. M. Palumbiny, F. Liu, T. P. Russell, A. Hexemer, C. Wang, P. Müller-Buschbaum: „Enhanced interchain coupling in co-solvent modified PEDOT:PSS polymeric electrodes“; *Lehrstuhl für Funktionelle Materialien, Annual report 2014.*

- C. M. Palumbiny, F. Liu, A. Hexemer, T. P. Russell, C. Wang, P. Müller-Buschbaum: „In-situ GIWAXS study of slot-die coated highly conductive PEDOT:PSS“; *Lehrstuhl für Funktionelle Materialien, Annual report 2013.*

- J. Schlipf, C. M. Palumbiny, P. Müller-Buschbaum: „Reduced sheet resistance in poly(3,4-ethylendioxythiophene):poly(styrenesulfonate) with surfactant additive and multilayers“; *Lehrstuhl für Funktionelle Materialien, Annual report 2013.*

- C. M. Palumbiny, C. Heller, G. Santoro, S. V. Roth, P. Müller-Buschbaum: „Structural analysis of highly conductive PEDOT:PSS for ITO-free flexible solar cells“; *Lehrstuhl für Funktionelle Materialien, Annual report 2012.*

- C. Heller, C. M. Palumbiny, P. Müller-Buschbaum: „Increased conductivity of PEDOT:PSS for ITO free solar cells“; *Lehrstuhl für Funktionelle Materialien, Annual report 2012.*

- D. Moseguí Gonzáles, C. M. Palumbiny, J. Perlich, P. Müller-Buschbaum: „Influence of imprinting processes on crystallinity of P3HT thin films“; *Lehrstuhl für Funktionelle Materialien, Annual report 2012.*

- C. M. Palumbiny, M. Schindler, K. Sarkar, T. Geue, J. Stahn, P. Müller-Buschbaum: „Neutron reflectivity on PCBM enrichment in P3HT-PCBM blend films on PEDOT-PSS for applications in organic photovoltaics“; *SINQ/AMOR Experimental Report 2012*.

- C. M. Palumbiny, S. Lindner, L. Schmidt-Mende, P. Müller-Buschbaum: „Nanostructured interfaces and degradation in PCBM:HBC(CuPc) solar cells“; *Lehrstuhl für Funktionelle Materialien, Annual report 2011*.

Conference talks

- C. M. Palumbiny, F. Liu, T. P. Russell, A. Hexemer, C. Wang, P. Müller-Buschbaum: „Following the evolution of nanomorphology in PEDOT:PSS electrodes in-situ“; *DPG Frühjahrstagung*, Berlin (Germany), 15–20 March 2015.

- C. M. Palumbiny, F. Liu, T. P. Russell, A. Hexemer, C. Wang, P. Müller-Buschbaum: „Following the evolution of nanomorphology: In-situ GIWAXS on slot die coated PEDOT:PSS polymeric electrodes“; *EuroTech Meeting*, Brussels (Belgium), 27–28 October 2014.

- C. M. Palumbiny, J. Lebert: „Conducting polymers“; *Polymer Physics Summer School*, Obertauern (Austria), 24–27 June 2014.

- C. M. Palumbiny, F. Liu, T. P. Russell, A. Hexemer, C. Wang, P. Müller-Buschbaum: „In-situ GIWAXS on slot die coated highly conductive PEDOT:PSS as electrode for ITO-free organic electronics: Crystallinity and molecular orientation“; *DPG Frühjahrstagung*, Dresden (Germany), 30 March – 4 April 2014.

- C. M. Palumbiny, F. Liu, T. P. Russell, A. Hexemer, C. Wang, P. Müller-Buschbaum: ”Polymeric electrode by co-solvent treatment: „Molecular reorientation, structural changes and artificial structuring“; *EuroTech Meeting*, Neuchâtel (Switzerland), 23–24 January 2014.

- C. M. Palumbiny, C. Heller, C. J. Schaffer, V .Körstgens, G. Santoro, S. V. Roth, P. Müller-Buschbaum: „Highly conductive PEDOT:PSS as electrode for flexible structured ITO-free organic electronics: A morphological study“; *EuroTech ISPV meeting*, Garching (Germany), 17 July 2013.

- C. M. Palumbiny, C. Heller, C. J. Schaffer, V .Körstgens, G. Santoro, S. V. Roth, P. Müller-Buschbaum: „Highly conductive PEDOT:PSS as electrode for flexible

structured ITO-free organic electronics: A morphological study“; *3rd Colloquium of the Munich School of Engineering*, Garching (Germany), 4 July 2013.

- C. M. Palumbiny, C. Heller, C. J. Schaffer, V. Körstgens, G. Santoro, S. V. Roth, P. Müller-Buschbaum: „Highly conductive PEDOT:PSS for flexible structured ITO-free solar cells“; *DPG Frühjahrstagung*, Regensburg (Germany), 10–15 March 2013.
- C. M. Palumbiny, D. Moseguí Gonzáles, J. C. Heller, T. Pfadler, K. Sarkar, V. Körstgens, S. Yu, M. Al-Hussein, L. Schmidt-Mende, S. Roth, P. Müller-Buschbaum: „Structured interfaces for organic photovoltaics“; *3rd TUM-HASYLAB Colloquium*, Garching (Germany), 10–11 September 2012.
- K. Schaber, C. M. Palumbiny, J. Anderson: „Energy independence in Bavarian villages: Local level solutions and their contribution to local and national sustainability targets“; *Rio+20, United Nations Conference on Sustainable Development*, Rio de Janeiro (Brasil), 13–24 June 2012.

Conference poster presentations

- C. M. Palumbiny, T. Pfadler, D. Moseguí González, C. Heller, G. Santoro, S. V. Roth, A. Hexemer, C. Wang, J. Weickert, K. Müllen, L. Schmidt-Mende, P. Müller-Buschbaum: „Inner structure of thin films for organic PVs: Advanced scattering investigations“; *Final Meeting of the DFG Priority Programme SPP 1355 Elementarprozesse der Organischen Photovoltaik*, Bad Honnef (Germany), 22–24 January 2015.
- C. M. Palumbiny, C. Heller, C. J. Schaffer, V. Körstgens, G. Santoro, F. Liu, C. Wang, A. Hexemer, T. P. Russell, S. V. Roth, P. Müller-Buschbaum: „Conductivity in polymeric electrode for roll-to-roll printed organic electronics: Evolution of nanostructure and molecular orientation in PEDOT:PSS“; *CeNS Workshop "Walk and talk at the nanoscale"*, Venice (Italy), 22–26 September 2014.
- C. M. Palumbiny, F. Liu, T. P. Russell, A. Hexemer, C. Wang, P. Müller-Buschbaum: „Polymeric electrode for all-printed organic electronics: Following film formation and crystallization in-situ“; *4th Colloquium of the Munich School of Engineering*, Garching (Germany), 3 July 2014.
- C. M. Palumbiny, T. Pfadler, F. Liu, C. Heller, J. Schlipf , C. J. Schaffer, S. V. Roth, T. P. Russell, A. Hexemer, C. Wang, L. Schmidt-Mende, P. Müller-Buschbaum: „A glance into the inner life of thin films for organic PVs: In-situ and ex-situ advanced

scattering investigations“; *Third 'Solar Technologies Go Hybrid' Workshop*, Wildbad Kreut (Germany), 27–30 April 2014.

- C. M. Palumbiny, C. Heller, C. J. Schaffer, V. Körstgens, G. Santoro, S. V. Roth, P. Müller-Buschbaum: „Highly conductive PEDOT:PSS as electrode for flexible structured ITO-free organic electronics: A morphological study“; *MRS*, Boston (USA), 1–6 Dezember 2013.

- C. M. Palumbiny, C. Heller, C. J. Schaffer, V. Körstgens, G. Santoro, S. V. Roth, P. Müller-Buschbaum; „Highly conductive PEDOT:PSS as electrode for flexible structured ITO-free organic electronics: A morphological study“, *Advanced Light Source (ALS) User Meeting*, Berkeley (USA), 7–9 October 2013.

- C. M. Palumbiny, C. Heller, C. J. Schaffer, V. Körstgens, G. Santoro, S. V. Roth, P. Müller-Buschbaum: „Highly conductive PEDOT:PSS as electrode for flexible structured ITO-free organic electronics: A morphological study“, *Solar Technologies Symposium: Nanosystems for Solar Energy Conversion*, LMU, München-Großhadern (Germany), 24–26 July 2013

- C. M. Palumbiny, C. Heller, C. J. Schaffer, V. Körstgens, G. Santoro, S. V. Roth, P. Müller-Buschbaum: „Highly conductive PEDOT:PSS as electrode for flexible structured ITO-free organic electronics: A morphological study“; *Tag der Physikerin*, Garching (Germany), 8 Februar 2013.

- C. M. Palumbiny, R. Meier, H. C. Hesse, R. Dunbar, L. Schmidt-Mende, P. Müller-Buschbaum: „Structured interfaces for organic photovoltaics“; *2nd Colloquium of the Munich School of Engineering*, Garching (Germany), 28 June 2012.

- C. M. Palumbiny, R. Meier, L. Schmidt-Mende, P. Müller-Buschbaum: „Micro- and nanostructuring of thin layers for the application in organic photovoltaics“; *DPG Frühjahrstagung*, Berlin (Germany), 25–30 March 2012.

- C. M. Palumbiny, R. Meier, L. Schmidt-Mende, P. Müller-Buschbaum: „Micro- and nanostructuring of thin layers for the application in organic photovoltaics“; *Tag der Physikerin*, Garching (Germany), 15 February 2012.